PL-TR-97-2161

AN INTEGRATED STUDY OF LITHOSPHERIC STRUCTURE, REGIONAL SEISMIC WAVE PROPAGATION, AND SEISMIC DISCRIMINATION CAPABILITY IN THE MIDDLE EAST

Keith Priestley

University of Cambridge
Department of Earth Sciences
Madingley Rise, Madingley Road
Cambridge CB3 0EZ, UK

8 December 1997

19980303 018

DEPARTMENT OF ENERGY
OFFICE OF NON-PROLIFERATION
  AND NATIONAL SECURITY
WASHINGTON, DC 20585

AIR FORCE RESEARCH LABORATORY
Space Vehicles Directorate
29 Randolph Road
AIR FORCE MATERIEL COMMAND
HANSCOM AFB, MA 01731-3010

DTIC QUALITY INSPECTED 3

This technical report has been reviewed and is approved for publication.

_____   _____
JAMES C. BATTIS   CHARLES P. PIKE, Deputy Director
Contract Manager   Integration and Operations Division

REPORT DOCUMENTATION PAGE

1. AGENCY USE ONLY *(Leave blank)*	2. REPORT DATE 8 December 1997	3. REPORT TYPE AND DATES COVERED Final Technical Report (14 Aug 95–14 Nov 97)	

4. TITLE AND SUBTITLE
An integrated study of lithospheric structure, regional seismic wave propagation, and seismic discrimination capability in the Middle East

5. FUNDING NUMBERS

PE 69120H

PR DENN TA GM WU AD

Contract F19628-95-K-0017

6. AUTHOR(S)
Keith Priestley

7. PERFORMING ORGANIZATION NAME(S) AND ADDRESS(ES)
University of Cambridge
Department of Earth Sciences
Madingley Rise, Madingley Road
Cambridge, CB30EZ
United Kingdom

8. PERFORMING ORGANIZATION REPORT NUMBER

9. SPONSORING/MONITORING AGENCY NAME(S) AND ADDRESS(ES)
Air Force Research Laboratory
29 Randolph Road
Hanscom AFB, MA 01731-3010

Contract Manager: James Battis/VSB

10. SPONSORING /MONITORING AGENCY REPORT NUMBER

PL-TR-97-2161

11. SUPPLEMENTARY NOTES
This research was sponsored by the Department of Energy, Office of Non-Proliferation and National Security, Washington, DC 20585

12a. DISTRIBUTION/AVAILABILITY STATEMENT

approved for public release; distribution unlimited.

12b. DISTRIBUTION CODE

13. ABSTRACT *(Maximum 200 words)*

This report covers a number of studies relevant to seismic verification of the CTBT in Asia. The south Caspian basin anomalously affects regional seismic wave. Mangino and Priestley (1998) use teleseismic receiver functions and deep seismic sounding data to determine a crustal model of the basin and the surrounding region. Priestley, Patton and Schultz (1998) use this crustal structure to model the anomalous surface wave propagation across the basin seen in data from the Caspian Seismic Network (Mangino et al,1998). The attenuation of the intermediate frequency surface waves is primarily affected by the thick, low Q sediments. Cipar and Priestley (1997) have used reflectivity modeling of seismograms from three nuclear explosions along the RIFT profile to form a quasi-2-D cross section of the crust and upper mantle structure beneath the Siberian platform. This model shows considerable complexity above 250 km depth. Mangino, Priestley and Ebel (1998) have determined the receiver structure beneath six Chinese Digital Network stations and find these crustal thickness estimates agree well with those published in the Chinese literature. Priestley and Patton (1997) use broadband seismograms from the Chinese Digital seismograph at Urumqi (WMQ) to develop Mo:mb relationships for earthquakes and explosions in central Asia. The results show that Mo:mb(Pn) relationships for central Asian earthquakes and explosions are in excellent agreement with relationships for western United States and that the Mo:mb discriminate is transportable to other regions and support previous observations at the Nevada Test Site showing Mo:mb are comparable for explosions detonated in different media.

14. SUBJECT TERMS
Caspian basin   China   Crustal structure   Regional discriminate

15. NUMBER OF PAGES
208

16. PRICE CODE

17. SECURITY CLASSIFICATION OF REPORT unclassified	18. SECURITY CLASSIFICATION OF THIS PAGE unclassified	19. SECURITY CLASSIFICATION OF ABSTRACT unclassified	20. LIMITATION OF ABSTRACT SAR

CONTENTS

The crustal structure of the southern Caspian region

S. Mangino[1] and K. Priestley

Bullard Laboratories, Department of Earth Sciences

University of Cambridge

Madingley Rise, Madingley Road

Cambridge, CB3 0EZ, UK

SUMMARY

The south Caspian basin appears to behave as a relatively rigid aseismic block within the otherwise deforming Alpine–Himalayan orogenic belt. This anomalous character suggests that there is a fundamental compositional difference between the crust of the south Caspian basin and that of the surrounding region. Five new estimates of crustal velocity structure beneath the southern Caspian region are determined by the teleseismic receiver function method. These models show that the crust in Turkmenia along the trend of the Apshceron–Balkhan Sill — Kopet Dag Mountains is 50 km thick. In the southwestern part of the Caspian basin the crust is 33 km thick and consists of a 13 km thick sedimentary section lying on a high velocity ($V_p \sim 7.1$ km s^{-1}) lower crustal section. In the southeastern part of the basin the crust is 30 km thick and consists of a 10 km thick sedimentary section overlying a 20 km thick low velocity ($V_p \sim 5.8$ km s^{-1}) crystalline crust. The receiver function models are combined with velocity models from previous Russian Deep Seismic Sounding studies into a $\sim$1800 km long ESE–WNW trending crustal cross–section across the Kura Depression, the south Caspian basin and the Kopet Dag Mountains. The most significant features of this crustal model are the 20 km variation in thickness of Cenozoic sedimentary basin deposits, the absence of a "granitic" ($V_p \sim 5.8$–6.5 km s^{-1}) crustal layer in the central part of the south Caspian basin, and 20 km of crustal thinning beneath the central part of the basin. The Moho beneath the south Caspian basin has a broad arch–like structure whose western boundary is a relatively narrow zone across which the crust thins rapidly ($\sim$20 km thinning over a 100 km zone) and whose eastern boundary has a more gradual change in crustal

---

[1]Now at: Center for Monitoring Research, Arlington VA, USA

thickness (~20 km thinning over a 400 km zone). The velocity–depth profiles derived from the receiver functions are compared to laboratory velocity estimates made at pressures and temperatures appropriate for the lower crust in Turkmenia, but the seismic P–wave data alone do not permit differentiation between the various possible rock types. The crustal model developed for the south Caspian basin is consistent with the hypothesis that the crystalline crust of the basin is a section of oceanic crust that is being overthrust by the continental crust around much of its margins. However, we cannot rule out the possibility that the crystalline crust beneath the basin is a section of lower continental crust whose upper crustal section has been removed by erosion or faulting.

Key words: Crustal structure, South Caspian basin, Anomalous crust

1 INTRODUCTION

The Caspian Sea straddles the boundary between the stable Russian Platform to the north and the tectonically active Alpine – Himalayan orogenic belt to the south (Fig. 1). The Caspian can be divided into northern and southern basins separated by the Apshceron–Balkhan Sill, a structural high which is collinear with the trend of the Greater Caucasus Mountains to the west and the Kopet Dag Mountains to the east. The south Caspian basin, which is the focus of this study, is anomalous in a number of respects. Russian Deep Seismic Sounding (DSS) surveys conducted in this region primarily in the late 1950's and 1960's show that the crust of the south Caspian basin is very different from that of the surrounding region. Russian seismologists divided the continental crust into three main sections. Below the sedimentary layer, the upper or "granitic" crust is characterized by V_p in the range 5.8–6.5 $km\,s^{-1}$. The lower or "basaltic" crust is characterized by V_p in the range 6.5–7.8 $km\,s^{-1}$. The DSS studies of Gal'perin *et al.*, (1962), Neprochnov (1968), Rezanov & Chamo (1969), Neprochnov *et al.*, (1970), and Yegorkin & Matushkin (1970) show that the crust of the south Caspian basin lacks the "granitic" layer seen in the surrounding region. Instead, the crust of the south Caspian basin consists of a 15–25 km thick sedimentary layer with a V_p of 3.5–4.8 $km\,s^{-1}$ overlying a 12–18 km thick "basaltic" layer having a V_p of 6.8–7.0 $km\,s^{-1}$. However, the thickness of this "basaltic" crust is not well constrained in the central part of the basin.

2

There is little agreement as to the origin of the anomalous south Caspian crust. Rezanov & Chamo (1969) and Shikalibeily & Grigoriants (1980) indicate that the region was uplifted during the Mesozoic by a mantle diapir and the upper continental crust was eroded, thus exposing lower continental crustal rocks with velocities more typical of basalt. This was followed by a period of subsidence and sedimentation, thus the missing "granitic" layer is an artifact of erosion. Berberian & King (1981) and Berberian (1983) suggest that the south Caspian basin is either an unsubducted crustal remnant of an ocean that closed in the Triassic or Cretaceous, or of a marginal sea that developed behind an island arc in the late Mesozoic or Paleogene. Zonenshain & Le Pichon (1986) and Philip et al. (1989) argue that both the Black and Caspian Seas are fragments of a larger, late Mesozoic back arc basin which lies north of the late Mesozoic – Paleogene subduction zone of the Tethys Ocean. After the Tethys Ocean closed, the Red Sea Rift opened and as the Arabian plate moved northwards relative to the Eurasian plate, subduction shifted to the northern boundary of the marginal sea. Closure of this marginal sea ~3.5 Ma resulted in uplift and crustal thickening of the Caucasus and left relic oceanic crust underlying part of the Black Sea and south Caspian basin. Şengör (1990) suggests that the south Caspian basin opened as a large pull–apart structure along a major late Cretaceous strike–slip fault zone collinear with the Kopet Dag – Alborz – Greater Caucasus mountain belts.

Focal mechanism studies of earthquakes in the bordering seismogenic belts (M[c]Kenzie, 1972; Jackson & M[c]Kenzie, 1984; Priestley et al., 1994) demonstrate that the south Caspian region is dominated by compressional deformation resulting from the ~30 mm/yr (DeMets et al., 1990; Jestin et al., 1994) convergence between the Arabian and Eurasian plates. However, the south Caspian basin itself is a relatively aseismic block within this compressional regime. Priestley et al. (1994) show that the convergence between northwestern Iran and the south Caspian basin is partitioned into left–lateral strike–slip and pure thrust motion in the Alborz Mountains, resulting in the northward thrusting of the Iranian continental crust over the south Caspian basin. Shallow thrust events along the Apshceron–Balkhan Sill suggest that the Eurasian continental crust is also overriding the crust of the south Caspian basin from the north. Shallow earthquake thrust mechanisms beneath the Talesh Mountains along the southwest Caspian show that this region is being thrust over the south Caspian basin from the west. The closing of the south Caspian basin is also inferred from the presence of folding in the sedimentary layer of the basin (Neprochnov, 1968; Neprochnov et al., 1970; Zonenshain

& Le Pichon, 1986; Şengör, 1990).

A wide range of P_n velocities for the south Caspian region has been reported in the literature; however, the term P_n in these studies has been used to refer both to the average velocity of the upper mantle part of the lithosphere in earthquake studies and to the phase velocity of the compressional head wave directly below the Moho in refraction studies. Kadinsky–Cade et al. (1981) measured a P_n velocity beneath the south Caspian basin of 8.0 ± 0.9 km s^{-1} from the travel time – distance relationship of regional earthquake records at the WWSSN seismograph station at Tabriz in northern Iran. Hearn & Ni (1994) found a P_n velocity of 8.1 ± 0.1 km s^{-1} for the same region by tomographic inversion of regional distance range arrival time data from the Bulletin of the International Seismological Centre. Rezanov & Chamo (1969) obtained a P_n velocity of 8.5 ± 0.1 km s^{-1} beneath the Turkmenian lowlands using data from one DSS profile whereas most other DSS studies indicate the P_n velocity is 8.1 ± 0.1 km s^{-1} (Gal'perin et al., 1962; Neprochnov, 1968; Ryaboy, 1969; Yegorkin & Matushkin, 1970; Bulin, 1978; Khalilov et al., 1987) in the region within and surrounding the south Caspian basin.

The crust and upper mantle structure of the south Caspian has anomalous effects on seismic waves propagating across the basin. L_g is blocked for paths across the basin (Savarensky & Valdner, 1960; Mindeli et al., 1965; Kadinsky–Cade et al., 1981) but propagates in the surrounding regions. L_g is known to be sensitive to changes in crustal structure along its propagation path and is absent in seismograms after propagation across 100–200 km of oceanic crust (Press & Ewing, 1952; Knopoff et al., 1973). Intermediate period surface waves of teleseismic earthquakes are severely attenuated for propagation paths across the south Caspian basin (Priestley et al., 1996). On the other hand, S_n propagates efficiently for paths across the south Caspian but inefficiently for propagation paths beneath the Alborz and Talesh Mountains (Molnar & Oliver, 1969; Kadinsky–Cade et al., 1981). Observations of L_g blockage and efficient S_n propagation across the south Caspian basin have been cited as evidence in support of an "oceanic" crust beneath the basin.

The aim of this study is to determine the main features of the crustal structure beneath the south Caspian basin and the adjacent areas in southern Azerbaijan and southern Turkmenia. We first summarize an analysis of teleseismic P–wave receiver functions we conducted to determine the crustal structure beneath the seismograph stations we installed around the south Caspian basin in Turkmenia and Azerbaijan and beneath the broadband seismograph

4

operated by the Incorporated Research Institute for Seismology (IRIS) located about 300 km east of the Caspian Sea. The receiver function results are combined with published DSS results to construct a ~1800 km, ESE–WNW trending crustal cross–section across the eastern Kura depression, the south Caspian basin, the west Turkmenian lowlands, and the Kopet Dag Mountains (Fig. 1). A more detailed model of the crustal structure of this region will help resolve questions concerning: 1) the origin of the anomalous crust of the south Caspian basin, 2) the present style of deformation in this part of the Alpine–Himalayan Belt, and 3) the anomalous seismic wave propagation characteristics for paths across the south Caspian basin.

2 VELOCITY STRUCTURE OF THE SOUTH CASPIAN CRUST FROM TELESEISMIC RECEIVER FUNCTIONS

The seismograms we used in the receiver function analysis come from two sources. The data from the immediate vicinity of the south Caspian basin were obtained from four stations (LNK, KRF, NBD, and KAT – Fig. 1) of the seismic network we installed in May 1993 in Turkmenia and Azerbaijan. Details of the installation, operation, and calibration of these stations are given in Mangino (1997). These seismographs have Guralp CMG–3T broadband sensors recording on Refraction Technology 72a–02 16 bit data loggers at 10 samples/sec. Data from the IRIS seismograph ABKT (Fig. 1) were obtained from the IRIS Data Management Center. ABKT has a Streckeisen STS–1 broadband sensor and a 32 bit IDA MK6b data acquisition system; the ABKT data are sampled at 20 samples/sec.

The use of receiver functions to determine crust and upper mantle structure beneath three–component broadband seismograph stations is a well–established technique (*see* Langston, 1979; Owens *et al.*, 1984; Ammon *et al.*, 1990). We have determined true amplitude radial and tangential receiver functions (Langston, 1979; Ammon, 1991) for the events listed in Table A1 and determined 1–D velocity models using the time–domain linearized inversion procedure of Ammon *et al.* (1990). We inverted the receiver function at each station for those azimuths which appeared least affected by off–azimuth arrivals and then simplified the models and tested the significance of their features by forward modelling. In this way, we have determined the main crustal features beneath each of the stations while minimizing the effects of the lateral variations in structure. In the following discussion, we summarize

the receiver function results; details of these analyses are given in Appendix A. Although receiver functions are primarily sensitive to the S–wave velocity structure, all models in this study are described in terms of the P–wave velocity assuming a Poisson's ratio of 0.25 so that these results can be directly compared with the DSS results.

Fig. 2 summarizes the receiver function modelling results which show considerable variation over fairly short horizontal distances. The crustal features with which we have the most confidence are the thickness of the sedimentary surface layer, the average velocity of the mid–crust, and the depth to the Moho. KRF, NBD, and ABKT are located along the Apshceron–Balkhan Sill – Kopet Dag trend and all show similar crustal structure. All three models show a 2–3 km thick, low velocity surface layer and a ~50 km deep gradational Moho. The Moho may be slightly deeper beneath KRF but the main difference in these models is in the lower velocities in mid–crust beneath NBD.

The models for stations LNK and KAT indicate that the crust is significantly thinner (30–33 km) in the south part of the basin. Beneath LNK there is a ~13 km thick accumulation of sediment which overlies a high velocity mid– to lower crust. The high velocity layer beneath LNK may correspond to the "oceanic–like" basaltic layer described in previous DSS studies. The KAT model shows an 8–9 km thick sedimentary layer. The forward modelling tests for the LNK and KAT receiver functions show that large amplitude converted phases generated at the base of and within the sedimentary layer dominate the early part of the radial receiver function. Large amplitude tangential waveforms at these stations can be attributed in part to near–surface dipping interfaces, but the exact structure of the lateral heterogeneity at both stations is not constrained. The crust – mantle transition beneath KAT occurs over ~ 6 km whereas at LNK the data could not distinguish between a single step or a gradational Moho.

3 CRUSTAL CROSS–SECTION FOR THE SOUTH CASPIAN BASIN REGION

We next combine the receiver function results with published DSS results to form a ~1800 km long ESE–WNW trending crustal cross–section across the south Caspian basin from 46° to 62°E (Fig. 3). The DSS profiles used to construct the crustal cross–section were recorded from the late 1950's to 1960's using 1–4 Hz geophones and analogue recorders. Their locations

are shown in the upper part of Fig. 3. Published interpretation of the DSS data has been made using analysis of travel–time curves obtained by trace–to–trace correlation of reflected and refracted P–waves (Zveryev & Kosminskaya, 1978). Some caution is required in using the published DSS results for two reasons. Map coordinates are usually missing from the published figures, leading to some ambiguity in the profile locations. A more serious concern is that the seismic data are rarely published and it is therefore difficult to tell how well various features of the sometimes quite complex DSS crustal models are constrained by the data.

In constructing the crustal cross–section shown in Fig. 3 we have used the published DSS crustal models but have simplified the velocity structure considerably using our receiver function models as a guide. The crustal cross–section in Fig. 3 consists of three crustal layers corresponding to unconsolidated and consolidated sediments with velocities less than 4.8 $km\,s^{-1}$, the "granitic crust" with velocities in the 4.8 to 6.4 $km\,s^{-1}$ range, and the "basaltic crust" with velocities in the 6.4 to 7.4 $km\,s^{-1}$ range. These velocities correspond roughly to those of the "granitic" and "basaltic" crust of the Soviet literature from which we have taken the information on the DSS profiles and to those of the similar terms "upper" and "lower" crust in the western literature. However, it is important to emphasize that there are no real compositional implications to these terms. All of the DSS profiles with the exception of Rezanov & Chamo (1969) show that the P_n velocity decreases from $\sim$8.2 $km\,s^{-1}$ in south central Turkmenia to $\sim$8.0 $km\,s^{-1}$ in south central Azerbaijan. Rezanov & Chamo (1969) find the anomalously high P_n velocity of 8.5$\pm$0.1 $km\,s^{-1}$ beneath the West Turkmenian lowlands. We define the upper mantle at depths where the velocities are greater than 8.0 $km\,s^{-1}$.

3.1 Turkmenia

The crustal cross–section beneath Turkmenia is constrained by results from six DSS profiles and two receiver function models. Yegorkin & Matushkin (1970) have interpreted the Dushak–NE profile (#1 – Fig. 3) data in terms of a crustal model consisting of a sub-horizontally layered 50 km thick crust. Their model shows a change in velocity from 3.5 to 5.95 $km\,s^{-1}$ at 8 km depth corresponding to the top of the granitic layer, a step in velocity from 6.4 to 6.7 $km\,s^{-1}$ at $\sim$27 km depth corresponding to the top of the basaltic layer, and

7

a 7.65 to 8.25 km s^{-1} boundary at ~50 km depth corresponding to the Moho.

Control points #2–4 are from the ABKT receiver function model, the Ashkabad Test Site (Altyyev *et al.*, 1988) and the Kopet Dag–Aral Sea N–S DSS profile (Yegorkin & Matushkin, 1970). The top of the granitic layer beneath ABKT (#2) coincides with the increase in velocity from 3.5–5.25 km s^{-1}; the top of the basaltic layer with the increase in velocity from 6.4 to 6.9 km s^{-1} and the Moho to the transition to velocities greater than 8 km s^{-1} at ~45 km depth. Altyyev *et al.*(1988) investigated the structure beneath the Ashkabad Test Site (#3) using seismic reflection techniques and estimated the velocity contrasts across reflecting horizons by matching amplitudes. They identified three prominent boundaries: the top of the granitic layer (the 4.0 to 5.8-6.1 km s^{-1} horizon) at 5-7 km depth, the top of the basaltic layer (the increase from 6.7 to 7.1 km s^{-1}) between 19-22 km depth, and the Moho at ~45 km depth.

The deeper portion of the velocity structure for #4 is constrained by the Kopet Dag–Aral Sea DSS model of Yegorkin & Matushkin (1970) and the near-surface velocity structure from the velocity model from DSS profiles N3 and N7 of Radzhabov & Agranovsky (1960). The crustal structure beneath the Kopet Dag–Aral Sea profile is similar to that beneath the Dushak–NE profile; however, the deep structures toward the south end of this model dip toward the Kopet Dag Mountains. Profiles N3 and N7 consist of a series of shallow penetrating (5–7 km) refraction and reflection surveys conducted within the foreland basin just north of the Kopet Dag (Radzhabov & Agranovsky, 1960). The top of the granitic layer occurs as the velocity steps from 4.6 to 6.45 km s^{-1} at 3.5-5.5 km/depth, and the step in velocity from 6.85 to 8.1 km s^{-1} projected from the southern end of the Kopet Dag–Aral Sea DSS model at ~45 km depth defined the Moho.

The velocity structure at #5 is derived from the central portion of the Okarem–Darvaz profile. Kurbanov & Rzhanitsyn's (1982) crustal model from these data show a transition from thicker continental crust beneath the Kara Kum Desert to anomalously thin crust beneath the West Turkmenian Lowlands near the coast of the Caspian Sea. This crustal thinning occurs primarily as a decrease in thickness of the granitic layer from northeast to southwest with some compensating increase in thickness of the sedimentary layer. Kurbanov & Rzhanitsyn's model indicates the top of the granitic layer is at 5-7 km depth, the top of the basaltic layer is at ~25 km depth, and the Moho is at ~35 km depth.

3.2 South Caspian Basin

Control points #6–8 constrain the crustal structure across the eastern margin of the south Caspian basin. The velocity increase from 4.6 to 5.8 $km\,s^{-1}$ at 9 km depth beneath KAT (#6) (Fig. 2) defines the top of the granitic layer, from 5.8 to 6.7 $km\,s^{-1}$ the top of the basaltic layer at 26 km depth, and the Moho at ~33 km depth.

The southern portion of the crustal model from the Atrek–Saggyz profile (Rezanov & Chamo, 1969) constrains the velocity structure at #7. Along the southern end of the profile the crust is 30–33 km thick but thickens dramatically at ~39°N to ~50 km thick beneath the West Turkmenian Depression(Fig. 1). North of this Depression both the granitic and basaltic crustal layers exist. Beneath the West Turkmenian Lowlands there is a velocity increase from 4.4–4.8 $km\,s^{-1}$ to 5.6–6.0 $km\,s^{-1}$ at ~12 km depth which marks the top of the granitic layer. Rezanov & Chamo (1969) show a 4–5 km thick granitic layer beneath the West Turkmenian Lowlands which pinches out to the southwest beneath the south Caspian basin. The top of the basaltic layer coincides with the 6.2 to 6.6 $km\,s^{-1}$ velocity increase at 15–17 km depth. Rezanov & Chamo (1969) place the Moho at 30–33 $km\,s^{-1}$ depth but the sub–Moho material has the unusually high P_n velocity of 8.5±0.1 $km\,s^{-1}$. They also include results from several shorter DSS profiles and show a Moho contour map which aids in constraining the Moho depth across the transition from the West Turkmenian Lowlands to the south Caspian basin.

The western portion of the Okarem–Darvaz profile (Kurbanov & Rzhanitsyn, 1982) clearly shows the thinning of the granitic layer beneath the West Turkmenian Lowlands(#8). The sediment thickness contour map of Neprochnov *et al.* (1970) shows a 15 km thick sedimentary layer beneath the West Turkmenian Lowlands which lies directly on the basaltic layer; the 30 km Moho depth is from the crustal thickness contour map of Rezanov & Chamo (1969). The Ogurtchin–Sarykamysh model of Shikalibeily & Grigoriants (1980) shows that the top of the basaltic layer is overlain by ~12 km of sediments and the Moho is at at 28–30 km depth (#9). No velocities are given in the southwest part of this profile. Neprochnov *et al.* (1970) show a 15 km thick sedimentary layer in about the same location.

The marine DSS profiles across the central Caspian Sea (Aksenovich *et al.*, 1962; Gal'perin *et al.*, 1962) show the fundamental difference in crustal structure between the northern and southern Caspian basin. In the northern Caspian (B – Fig. 3), the crust has a

2–3 km thick sedimentary layer, a 10 km thick granitic layer and a 15-20 km thick basaltic layer. The granitic layer pinches out just south of the Apshceron-Balkan Sill, and further south the crust consists of a 15-25 km thick sedimentary layer that directly overlies a basaltic basement. The overall crustal thickness increases from 40-45 km at B to 50 km beneath the Apshceron–Balkhan Sill and then decreases again to 34–35 km at A (Fig. 3). DSS profile–9 (#10), profile–6 (#11), profile–11 (#12), and profile–1/2 and cross section A–B (#13) from Aksenovich et al., (1962) and Gal'perin et al. (1962) constrain the thickness of the sedimentary and basaltic layers across the northern portion of the south Caspian basin. In some cases these profiles do not constrain the Moho depth. Profile–9 shows that the base of the sedimentary layer is between 13–15 km depth and Neprochnov et al. (1970) show a $\sim$15 km thick sedimentary layer in about the same location. Profile–6 shows an increase in velocity from 4.5 to 6.8 km s^{-1} at 18–19 km depth and the Moho at 30 km depth; Neprochnov et al. (1970) show a $\sim$20 km thick sedimentary layer in about the same location. Profile–1/2 and cross section A–B show that the base of the sedimentary layer (V$_p$ 3.0–4.8 km s^{-1}) is at $\sim$18 km depth and directly overlies a basaltic layer (V$_p$ 6.6–6.8 km s^{-1}). The Moho is at 34–35 km depth and the P$_n$ velocity is 8.0 km s^{-1}. The LNK receiver function crustal model (#14) (Fig. 2) has low velocity (3.0 km s^{-1}) sediments at the near surface which lies directly on a high-velocity basement (V$_p$ 6.4–7.1 km s^{-1}).

3.3 Azerbaijan

DSS profiles A1–A4 constrain the crustal structure of the Kura Depression (#15, #16) west of the south Caspian basin in southeastern Azerbaijan (Shekinskii et al., 1967). The step in velocity from 3.9–4.9 km s^{-1} to 5.7–6.1 km s^{-1} near the intersection of A4 and A3 (#15) defines the top of the granitic layer, the step in velocity from 5.9–6.3 km s^{-1} to 6.8 km s^{-1} at 14 km depth defines the top of the basaltic layer, and the Moho is at $\sim$45 km depth. Further west beneath A3 (#16) the top of the granitic layer is marked by the increase in velocity from 5.3 to 6.3 km s^{-1} at $\sim$8 km depth, the step in velocity from 6.7 to 7.1 km s^{-1} marks the top of the basaltic layer, and the Moho is at 49–50 km depth.

The Black Sea–Caspian Sea cross-section of Khalilov et al. (1987) constrains the west end of the cross-section at 46°E (#17). They primarily used data from a DSS profile extending from the Black Sea to the Caspian Sea to derive this model but also used other geophysical

constrains. Their model shows the top of the granitic layer (V_p 6.2 km s^{-1}) at 7–8 km depth, the top of the basaltic layer (V_p 7.1 km s^{-1}) at ~15 km depth, and the top of the upper mantle (V_p 8.0 km s^{-1}) at ~56 km depth. At the east end of this DSS model, the granitic layer pinches out at approximately the coastline of the Caspian Sea.

4 DISCUSSION

Teleseismic receiver function modelling and a synthesis of published DSS results constrain a crustal cross–section across the south Caspian basin and the adjacent areas of southern Azerbaijan and southern Turkmenia. Beneath the Kura Depression in southeast Azerbaijan the crustal thickness varies from 45 to 60 km. The sedimentary layer is 5 to 7 km thick, the underlying crystalline upper crust is only 5 to 7 km thick, but the lower crust varies from ~45 km thick in the western part of the Kura Depression to ~30 km thick in southeastern Azerbaijan. Beneath the south Caspian basin the upper granitic crust is extremely thin or disappears entirely. Sedimentary deposits are as much as 20 km thick beneath the western part of the basin but somewhat thinner beneath the eastern part of the basin. The depth to the top of the lower crust beneath the basin is not significantly different from that observed beneath southeast Azerbaijan. The 30–33 km Moho depth in the central part of the basin is determined entirely from DSS results and this is perhaps the most important but least well-constrained aspect of the crustal cross–section. The Moho has a broad arch–like structure whose western boundary is a relatively narrow zone to the west of LNK across which the crust thins rapidly. To the east of the Caspian the crust gradually increases in thickness beneath the west Turkmenian lowlands. This form of structure results from the opposing sides of the south Caspian basin being foreland basins which are overthrust in opposite directions. In the east beneath the Kopet Dag Mountains, the crust is 45 to 50 km thick and resembles a typical continental crustal velocity profile. The sedimentary layer is ~3 km thick, the upper crust is ~18 km thick, and the lower crust is ~25 km thick. The top of the lower crust is significantly deeper beneath western Turkmenia than beneath either southeastern Azerbaijan or the south Caspian basin.

The goal of this study is to determine if the south Caspian basin is floored by continental or oceanic crust. Normally, oceanic and continental crust are easily distinguishable. The earliest marine refraction surveys determined that normal oceanic crust is thinner than

continental crust and has a remarkably uniform structure. More recent petrological studies show that the composition of normal oceanic crust is consistent with a mid–ocean ridge basalt composition. Compilations of seismic studies (eg., Raitt, 1963; Shor *et al.,* 1970; Christensen & Salisbury, 1975; White *et al.,* 1992) show that the igneous oceanic crust consists of two layers. The upper layer, ~1.5 km thick and with a velocity between about 5.0 and 5.2 km s^{-1} is probably extrusive basaltic lavas and dikes formed at the spreading centers. The lower layer, which is about 5 km thick and has a velocity between 6.7 and 6.8 km s^{-1} , probably consists of intrusive gabbro and may be a relic of a magma chamber beneath a spreading ridge. A few regions possess anomalously thick (15–25 km) oceanic crust such as the Ontong–Java (Furumoto *et al.,* 1976) and Kerguelin Plateaus (Recq *et al.,* 1990); however, these regions are thought to have been affected by mantle plumes (White *et al.,* 1992). Little is known of the crustal structure of marginal seas. Continental crust is much more variable in both thickness and composition resulting from the long time period and diverse processes by which it has formed. The upper continental crust has a composition similar to granodiorite, and the lower continental crust is thought to consist of granulite facies rocks with an average composition approaching that of a primitive basalt (Rudnick & Fountain, 1995).

The fundamental problem in resolving the nature of the crystalline crust of the south Caspian basin is that it is not possible to uniquely associate a seismic velocity with a specific rock type. Fig. 4 compares laboratory velocity measurements made at high pressure and temperature (Volarovich *et al.,* 1980) with the P–wave velocity models beneath ABKT and LNK. Volarovich *et al.* (1980) use a geotherm for the central part of Turkmenia to infer rock types from the Kopet Dag–Aral Sea DSS cross–section (Fig. 3). The rock types comprising the upper crustal "granitic" layer may include granite, granite–gneiss and granodiorite. The "basaltic" layer in the lower crust beneath ABKT may comprise gabbros and amphibolites (Fig. 4). The equivalent layer beneath LNK is 0.3 km s^{-1} faster, suggesting a more mafic composition. Birch (1960) shows that anorthosite and several other high–grade metamorphic rock types have velocities in the same range as those of gabbro and amphibolites given by Volarovich *et al.,* (1980). Christensen & Fountain (1975) show that granulite facies metamorphic rocks at pressures of 4–10 kbar have P–wave velocities between 6.5–7.5 km s^{-1} which span the range of velocities of the "basaltic" layer in the ABKT and LNK models. Thus at this time, one cannot assign a unique rock type to the seismic velocities of the "basaltic"

layer at either ABKT or LNK.

The south Caspian basin behaves as a relatively rigid aseismic block surrounded by actively deforming zones (Jackson & McKenzie, 1984; Priestley et al., 1994). This anomalous behavior of the basin within the Alpine–Himalayan orogenic belt suggests a fundamental compositional difference between the south Caspian basin crust and the crust of the surrounding region. The south Caspian crustal model shown in Fig. 3 does not distinguish between the two competing hypotheses that the "basaltic" layer is lower continental crust or oceanic crust. The crystalline crust beneath the basin is significantly thinner than the lower crustal layer beneath southeastern Azerbaijan and somewhat thinner than the lower crustal layer beneath southern Turkmenia, but appears to be substantially thicker than normal oceanic crust.

The ability of the lithosphere to resist tectonic deformation is derived primarily from the strength of the lithospheric mantle layer. The strength of this material, which is probably peridotite, varies with temperature. The limited data from the south Caspian basin shows the heat flow is 30–60 mWm^{-2} (Cermák & Rybach, 1979) which is not significantly different from much of the surrounding region. In addition, the high sedimentation rate in this region since the Pliocene has most likely depressed the surface heat flow by 20–40% (Kutas et al., 1979; Cermák & Rybach, 1979; Lubimova, 1980). At a given temperature, continental crustal rocks which range in composition from granites to basalts, are weaker than peridotite (Sonder & England, 1986). In the oceanic lithosphere the peridotite layer of the upper mantle is at a much shallower depth than in the continental lithosphere, and as a result is presumably cooler and much stronger. Hence, the resistance of the south Caspian basin crust to tectonic deformation probably results from the shallow depth to the Moho beneath the basin and not necessarily from its oceanic crustal composition. A similar resistance to tectonic deformation might arise if the crystalline crust of the south Caspian basin were heavily intruded, stretched, and thinned continental crust.

From P-wave velocities alone, it is not possible to distinguish between lower continental and oceanic crust. Poisson's ratio is a more powerful compositional discriminant than P-wave velocity alone (Zandt & Ammon, 1995; Christensen, 1996). We are now reanalyzing the older seismic refraction seismograms from the south Caspian basin and surface wave propagation across the basin. We expect that the combined results of these studies will improve the estimate of the Moho depth beneath the basin and the combined measurement

13

of P– and S–wave velocities will result in greater discriminating power for the composition of the crystalline crust of the south Caspian basin.

ACKNOWLEDGEMENTS

References

Aksenovich, G.I., Aronov, L.E., Gagelganz, A.A., Gal'perin, E.I., Zaionchkovsky, Y., Kosminskaya, I.P., & Krakshina, R.M., 1962. Deep Seismic Sounding in the Central Part of the Caspian Sea, *Akademizdat*, Moscow, 151 pp.

Altyyev, D., Bezrodkov, V.A., Doblikina, N.A., Kakabayev, B., Kul'Dzhanov, A.K., Lykov, V.I., Potapova, O.V., & Preobrazhensky, V.B., 1988. Seismic studies at Ashkhabad test site 1978-1983, *Izv. Earth Phys.*, **24**, 121-132.

Ammon, C.J., 1991. The isolation of receiver effects from teleseismic P waveforms, *Bull. seism. Soc. Am.*, **81**, 2504-2510.

Ammon, C.J., Randall, G.E., & Zandt, G., 1990. On the resolution and non–uniqueness of receiver function inversions, *J. geophys. Res.*, **95**, 15303-15318.

Berberian, M., 1976. An explanatory note on the first seismotectonic map of Iran; a seismotectonic review of the country, in, *Contribution to the seismotectonics of Iran (Part II)*, Geological Survey of Iran, Report No. 39, 7-141.

Berberian, M., & King, G.C.P., 1981. Towards a paleogeography and tectonic evolution of Iran, *Can. J. of Earth Sci.*, **18**, 210-265.

Berberian, M., 1983. The Southern Caspian: A compressional depression floored by a trapped, modified oceanic crust, *Can. J. Earth Sci.*, **20**, 163-183.

Birch, F., 1960. The velocity of compressional waves in rocks to 10 kilobars; Part 1. *J. geophys. Res.*, **65**, 1083-1102.

Bulin, N.K., 1978. New ideas on crust structure (from seismic data), *Internat. Geology Rev.*, **20**, p 887-889.

Cassidy, J.F., 1992. Numerical experiments in broadband receiver function analysis, *Bull. seism. Soc. Am.*, **82**, 1453-1474.

Cermák, V. & Rybach, 1979. *Terrestrial Heat Flow in Europe*, Springer–Verlag Press.

Christensen, N.I., & Fountain, D.M., 1975. Constitution of the lower continental crust based on experimental studies of seismic velocities in granulite, *Geol. Soc. Am. Bull.*, **86**, 227-236.

Christensen, N.I., & Salisbury, M.H., 1975. Structure and composition of the lower oceanic crust, Rev. geophys. **13**, 57-86.

Christensen, N.I., 1996. Poisson's ratio and crustal seismology, *J. geophys. Res.*, **101**, 3139-

3156.

DeMets, C., Gordon, R.G., Agrus, D.F., & Stein, S., 1990. Current plate motions, *Geophys. J. Int.*, **101**, 425–478.

Furumoto, A.S., Webb, J.P., Odegard, M.E., & Hussong, D.M., 1976. Seismic studies on the Ontong–Java plateau, 1970, *Tectonophysics*, **34**, 71–90.

Gal'perin, Y., Kosminskaya, I., & Krakshina, P., 1962. Main characteristics of deep waves recorded during deep seismic sounding in central part of Caspian sea. In: *Deep Seismic Sounding of the Earth's crust in the U.S.S.R.*, Acad. Sci. USSR, Moscow.

Hearn, M.H. & Ni, J.F., 1994. P_n velocities beneath continental collision zones: the Turkish–Iranian Plateau, *Geophys. J. Int.*, **117**, 273–283.

Jackson, J.A., & McKenzie, D., 1984. Active tectonics of the Alpine–Himalayan Belt between western Turkey and Pakistan, *Geophys. J. R. astr. Soc.*, **77**, 185–264.

Jackson, J.A., Haines, J.,& Holt, W., 1995. The accommodation of Arabia–Eurasia plate convergence in Iran, *J. geophys. Res.*, **88**, 15205-15219.

Jestin, F., Huchon, P., & Gaulier, J.M., 1994. The Somalia Plate and the East African Rift System: present–day kinematics, *Geophys. J. Int.*, **116**, 637–654.

Kadinsky–Cade, K., Barazangi, M., Oliver, J., & Isacks, B., 1981. Lateral variations of high frequency seismic wave propagation at regional distances across the Turkish and Iranian Plateaus, *J. geophys. Res.*, **86**, 9377–9396.

Khalilov, E.N., Mekhtiyev, SH.F., & Khain, V.YE., 1987. Some Geophysical Data Confirming the Collisional Origin of the Greater Caucasus, *Geotectonics*, **21**, 132–136.

Knopoff, L, Schwab, F., Kausel, E., 1973. Interpretation of L_g, *Geophys. J. R. astr. Soc.*, **33**, 387–404.

Kurbanov, M.K., & Rzhanitsyn, V.A., 1982. Structure of the Crust in West Turkmenistan from Geological and Geophysical Data, *Geotectonics*, **16**, 389–396.

Kutas, R.I., Lubimova, E.A., & Smirnov, Ya.B., 1979. Heat Flow studies in the European part of the Soviet Union. In: *Terrestrial Heat Flow in Europe* (Eds., V. Cermák & L. Rybach), Springer–Verlag, 301–308.

Langston, C.A., 1977. The effect of planer dipping structure on source and receiver responses for constant ray parameter, *Bull. seism. Soc. Am.*, **67**, 713–724.

Langston, C.A., 1979. Structure under Mount Rainier, Washington, inferred from teleseismic body waves, *J. geophys. Res.*, **84**, 4749–4762.

Lubimova, E.A., 1980. Heat flow, epeirogeny and seismicity for the East European Plate. In: *Earth Rheology Isostasy and Eustasy* (Ed. N.A. Moauer), J. Wiley and Sons.

Mangino, S.G., 1997. Eurasian crust and upper mantle structure, Ph.D. dissertation, 245pp, University of Cambridge Library.

McKenzie, D.P., 1972. Active tectonics of the Mediterranean region, *Geophys. J. R. astr. Soc.*, **30**, 109–185.

Mindeli, P.S., Neprochnov, Yu.P., & Pataraya, E.I., 1965. Definition of the area without granitic layer in the Black Sea basin on DSS data and seismology, *Izv. Earth Phys.*, **12**, 7–15.

Molnar P. & Oliver, J., 1969. Lateral variation of attenuation in the upper mantle and discontinuities in the lithosphere, *J. geophys. Res.*, **74**, 2648–2682.

Neprochnov, Yu.P., 1968. Structure of the Earth's crust of epi–continental seas: Caspian, Black and Mediterranean, *Can. J. Earth Sci.*, **5**, 1037–1043.

Neprochnov, Yu.P., Kosminskaya, I.P., & Malovitsky, YA.P., 1970. Structure of the crust and upper mantle of the Black and Caspian Seas, *Tectonophysics*, **10**, 517–538.

Owens, T.J., Zandt, G., & Taylor, S.R., 1984. Seismic evidence for an ancient crustal rift beneath the Cumberland Plateau, Tennessee: A detailed analysis of broadband teleseismic P waveforms, *J. geophys. Res.*, **89**, 7783–7795.

Press, F., & Ewing, M., 1952. Two slow surface waves across North America, *Bull. seism. Soc. Am.*, **42**, 219–228.

Philip, H., Cisternas, A., Gvishian, A., & Gorshkov, A., 1989. The Caucasus: an actual example of the initial stages of continental collision, *Tectonophysics*, **161**, 1–21.

Priestley, K., Baker, C., & Jackson, J., 1994. Implications of earthquake focal mechanism data for the tectonics of the south Caspian basin and surrounding regions, *Geophys. J. Int.*, **118**, 111–141.

Priestley, K., Schultz, C., & Patton, H., 1996. Anomalous surface wave propagation across the south Caspian basin and the blockage of regional seismic phases, *Seism. Res. Lett.*, **67**, 50.

Radzhabov, M.M. &. Agranovsky, L.E, 1960. Determination of depths and relief of an interface by means of single transverse travel time curves of refracted waves, *Izv. Earth Phys.*, **6**, 562–570.

Raitt, R.W., 1963. The crustal rocks, in *The Sea*, vol. 3, edited by M.N. Hill, 85–102,

Wiley–Intersciences, New York.

Recq, M., Brefort, D., Malod, J., & Veinante, J.-L., 1990. The Kerguelin Isles (southern Indian Ocean): results on deep structure from refraction profiles, *Tectonophysics, 182*, 227–248.

Rezanov, I.A. & Chamo, S.S., 1969. Reasons for absence of a granitic layer in basins of the South Caspian and Black Sea type, *Can. J. Earth Sci.*, **6**, 671–678.

Rudnick, R.L., & Fountain, D.M., 1995. Nature and composition of the continental crust: a lower crustal perspective, *Rev. geophys.*, **33**, 267–309.

Ryaboy, V., 1969. Structure of the Earth's crust in the central regions of Turkmenia according to deep seismic sounding data. In: *Proceedings of the Eighth Assembly of the European Seismological Commission*, (Ed. E. Bisztricsany), 216–221, Akad. Kido, Budapest, Hungary.

Savarensky, E.F. & Valdner, N.G., 1960. L_g and R_g waves from earthquakes of the area of the Black Sea and some consideration about their origin, *Seismic Investigation Geofiz. Com. U.S.S.R.*, Akademizdat, 4, 55–77.

Shekinskii, E., Radzhabov, M., Tumikyan, G., Levi, V., & Riger, R., 1967. Ivz. Akad. Nauk. Azerbaijan CCP Ser. Nauk. Zemli, **5**, 41–50.

Shikalibeily, E.Sh. & Grigoriants, B.V., 1980. Principal features of the crustal structure of the south Caspian basin and the conditions of its formation, *Tectonophysics*, **69**, 113–121.

Shor, G.G., Menard, H.W., & Raitt, R.S., 1970. Structure of the Pacific Basin, in *The Sea*, vol. 4, Part II, edited by A.E. Maxwell, 3–27, Wiley–Intersciences, New York.

Şengör, A.M.C., 1990. A new model for the late Palaeozoic–Mesozoic tectonic evolution of Iran and implications for Oman, in *The Geology and Tectonics of the Oman Region*, Robertson, A.H.F., Searle, M.P, & Ries, A.C., Geological Society of London Special Publication No 49, 797–831.

Sonder, L.J., & England, P., 1986. Vertical averages of rheology of the continental lithosphere: relation to thin sheet parameters, *Earth Plt. Sci. Lttr.*, **77**, 81–90.

Tchalenko, J.S., 1975. Seismicity and structure of the Kopet Dagh, Iran, (USSR), *Phil. Trans. Roy. Soc. Lond.*, **278**, 1–25.

Volarovich, M.P., Volynets, L.N., & Levshin, A.L., 1980. Composition of the Earth's crust and the upper mantle from DSS data in central Turkmenia and laboratory measurements for high thermodynamic parameters, *Izv. Earth Phys.*, **16**, 441–446.

White, R.S., McKenzie, D., & O'Nions, K., 1992. Oceanic crustal thickness from seismic measurements and rare Earth element inversions, *J. geophys. Res.*, **97**, 19683–19715.

Yegorkin, A.V. & Matushkin, B.A., 1970. Crustal structure of the Caucasus and Western Central Asia based on geophysical sounding data, *Internat. Geol. Rev.*, **12**, 281–290.

Zandt, G., & Ammon, C.J., 1995. Continental crust composition constrained by measurements of crustal Poisson's ratio, *Nature*, **374**, 152–154.

Zonenshain, L.P. & Le Pichon, X., 1986. Deep basins of the Black Sea and Caspian Sea as remnants of Mesozoic back–arc basins, *Tectonophysics*, **123**, 181–211.

Zveryev, S.M., & Kosminskaya, I.P., 1978. DSS Method–Progress and Perspectives, *Izv. Earth Phys.*, 735–743.

Figure Captions

Figure 1. Topographic map of the south Caspian basin and surrounding region. Elevation varies from ~30m below sea level in the Caspian Sea to over 2 km above sea level in the adjacent mountains. The contour interval is 1000 m; solid triangles denote the Caspian Seismograph Network stations used in this study. In Turkmenia the stations used are located at Krasnovodsk (KRF), Nebit Dag (NBD), and Kizyl Atrek (KAT). The only station in Azerbaijan used in this study is located at Lenkoran (LNK). The IRIS station Alibek (ABKT), Turkmenia is shown as a solid square. The West Turkmenian depression is denoted by the 45 km Moho depth contour from Rezanov & Chamo (1969).

Figure 2. Summary of the receiver function modeling results (V_p in km s^{-1}) for the four Caspian stations and IRIS station ABKT.

Figure 3. Cross-section of the crust and uppermost mantle (lower panel) beneath the region denoted by the box in the upper panel. Three principal crustal layers are characterized by their P–wave velocities: sediment and consolidated sediment ($Vp < 4.8$ km s^{-1} – tan), "granitic" (Vp between 4.8–6.4 km s^{-1} – red), "basaltic" (Vp between 6.4–7.4 km s^{-1} – green), and upper mantle ($Vp \geq 8.0$ km s^{-1} – gray). Control points numbered 1–17 correspond to the following DSS (open arrows) and receiver function results (solid arrows): (1) Dushak–NE (Yegorkin & Matushkin 1970), (2) IRIS station ABKT, (3) ATS (Altyyev *et al.*, 1988), (4) Kopet Dag–Aral Sea (Yegorkin & Matushkin 1970), (5) Okarem–Darvaz (Kurbanov & Rzhanitsyn 1982), (6) Station KAT, (7) Atrek–Sagyz (Rezanov & Chamo 1969), (8) Okarem–Darvaz (Kurbanov & Rzhanitsyn 1982), (9) Ogurtchin–Sarykamysh (Shikalibeily & Grigoriants 1980), {(10) 9, (11) 6, (12) 11, (13) 1, A–B (Aksenovich *et al.*, 1962; Gal'perin *et al.*, 1962)}, (14) Station LNK, {(15) A4, (16) A3 (Shekinskii *et al.*, 1967)}, and (17) Black Sea–Caspian Sea (Khalilov *et al.* 1987).

Figure 4. High pressure–temperature laboratory velocity measurements of rock types from Volarovich *et al.* (1980) compared to the receiver function models for stations ABKT and LNK.

FIGURE 1

FIGURE 2

22

46° 50° 54° 58° 62°

44°

Aral Sea

Caspian Sea

42°

Kara Bogaz Gol

Atrek-Sagyz

Azerbaijan

Kopet Dag - Aral Sea

Turkmenistan

40° Black Sea - Caspian Sea A1 KRF

A2 A3 A4 A 3 9 NBD Krasnovodsk - Hindu Kush

5 8 B 2 4

38° Ogurtchin - Sarykamysh Okarem - Darvaz ATS N7 Dushak - NE

1 11 6 LNK KAT ABKT N3

100 km

36°

Iran

FIGURE 3

W 0 0 E

15 15

30 30

45 45

60 60

17 16 14 13 12 11 10 9 8 7 6 5 4 3 2 1
15

Sediments   Granitic   Basaltic   Upper-Mantle

23

FIGURE 4

Appendix A

Teleseismic receiver function analysis is now a well–established seismological technique (*see* Langston, 1979; Owens *et al.*, 1984; Ammon *et al.*, 1990; Cassidy, 1992) and in this discussion we describe only the details of receiver function analysis which are pertinent to determining the velocity models shown in Fig. 3. We have determined true amplitude radial and tangential receiver functions by computing the spectral ratio of the radial or tangential spectrum and the vertical component spectrum (Langston, 1979; Ammon, 1991) for the events listed in Table A1. Deconvolutions were computed for water fill values ranging from 0.1 to 0.0001 and smoothed with a Gaussian value of 1.0. These values were selected using a qualitative assessment of deconvolution stability, noise levels, and a polarization analysis as a function of frequency (Mangino, 1997). This Gaussian value passes frequencies up to ∼0.4 Hz, resulting in reduced resolution of the crustal velocity features. However, these low frequency receiver functions can resolve the main crustal features for comparison with the DSS models. We stacked those receiver functions within a small range of backazimuth and epicentral distance whose averaging functions resembled a narrow Gaussian pulse to give a mean estimate of the radial and tangential receiver functions. The variance of the stacked receiver functions at each time point was calculated, and from this, ±1 standard deviation bounds were determined. These bounds were used to evaluate how well a particular part of the waveform is constrained.

1–D velocity models were then determined using the time–domain linearized inversion procedure of Ammon *et al.* (1990). Starting models were developed from velocity models of nearby DSS profiles. Models were parameterized as stacks of horizontal layers to a depth of 60 km with the deeper layers 2 km thick and the upper few layers 1 km thick. The inversion produces a range of vel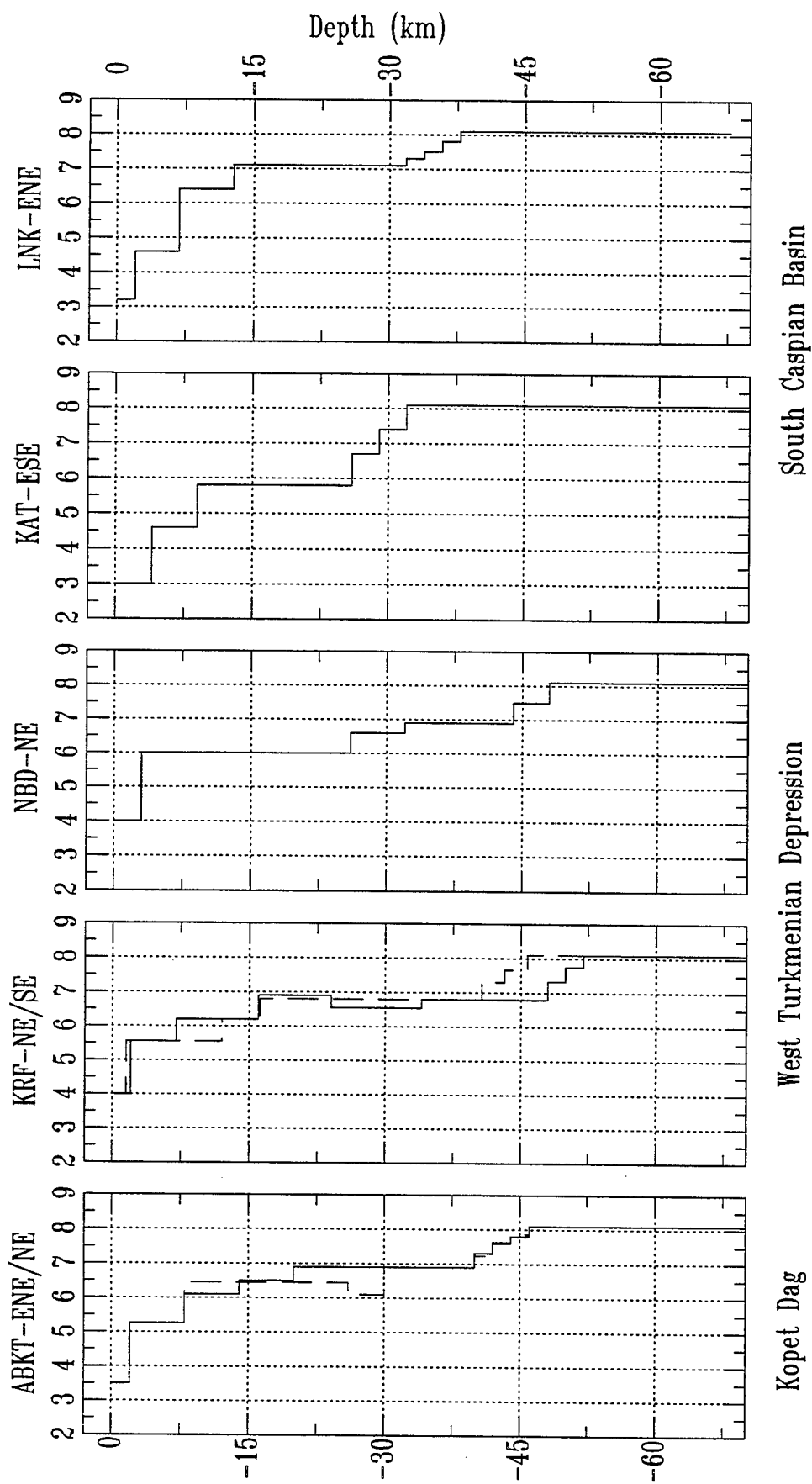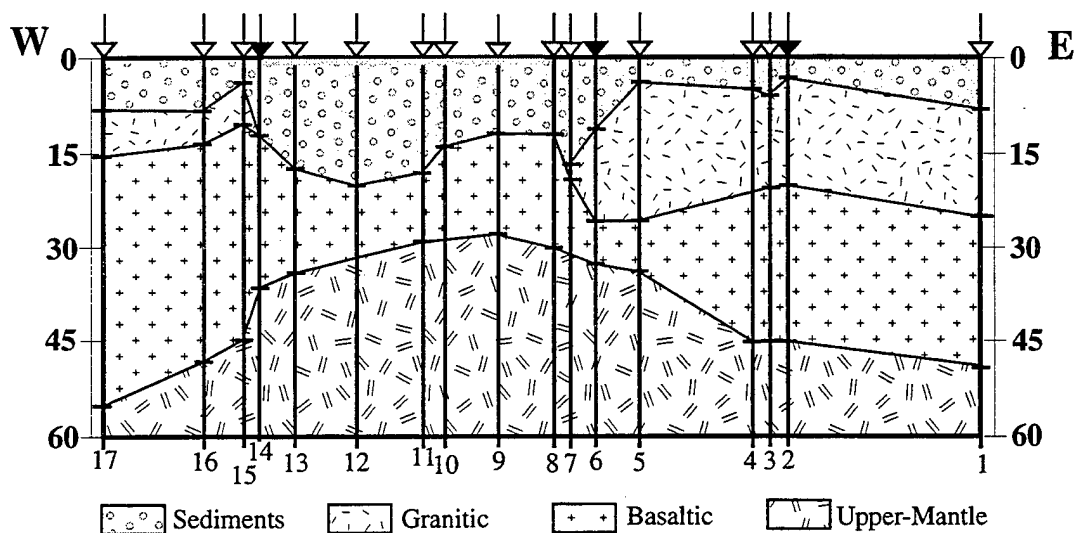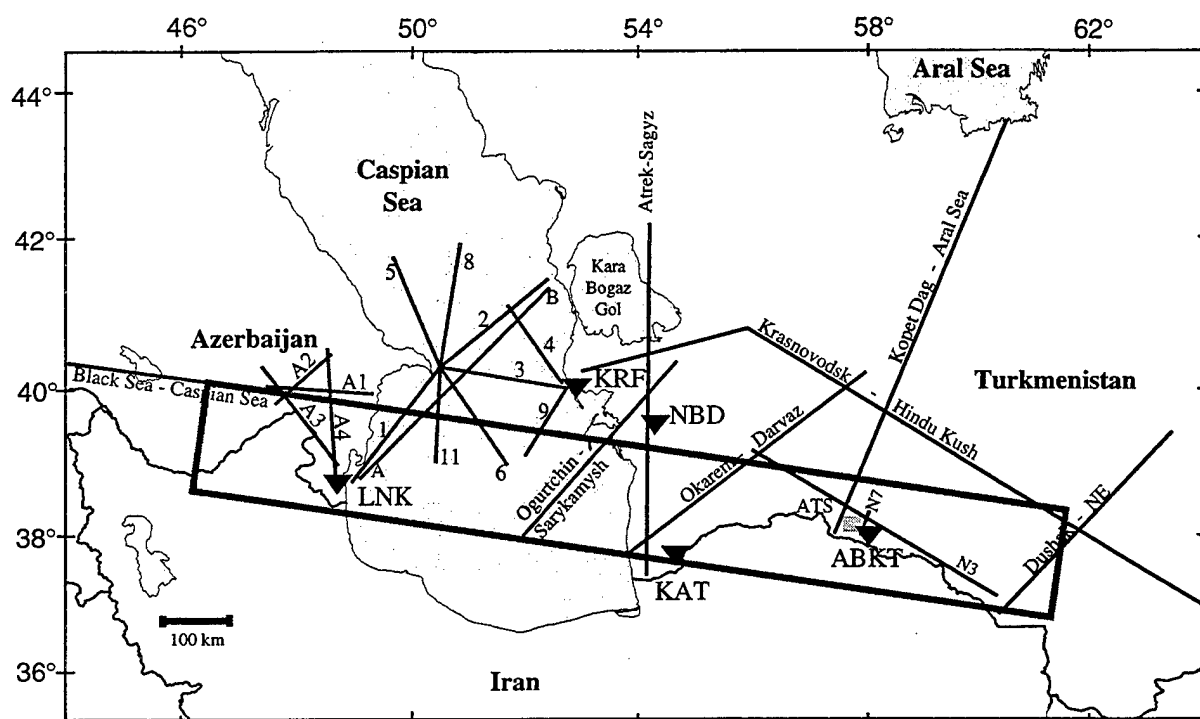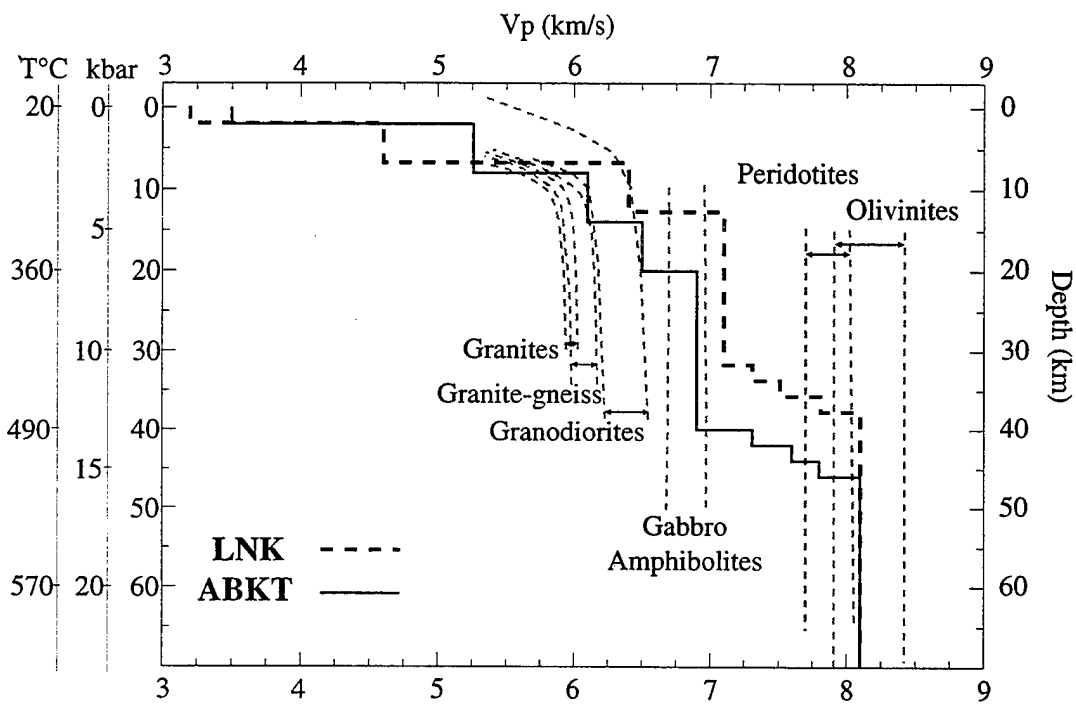ocity models whose synthetic receiver functions fit the observed receiver function bounds to varying degrees. We simplified the velocity model by first averaging the acceptable inversion models, then collecting adjacent layers of similar velocities into single layers to form a "coarse" velocity model. We then used forward modelling to test these simplified models to determine how well their various features were constrained by arrivals in the observed receiver functions. The upper mantle P–wave velocity was fixed at 8.1 km s^{-1} in the forward calculations because receiver functions are relatively insensitive to this parameter. All sites exhibit clear indications of a departure from laterally homogeneous structures. Cases where this lateral heterogeneity appeared to result from planar dipping interfaces were investigated by forward modelling the radial and tangential receiver functions using the ray tracing procedure of Langston (1977).

In the following discussion we first describe the receiver function analysis for KRF and then give a more abbreviated summary of the receiver function analysis for the other stations.

A1.1 Krasnovodsk (KRF)

25

KRF (Fig. 1 and A1) is located on the eastern coast of the Caspian Sea along a band of seismicity extending from the Kopet Dag in the east to the Apshceron–Balkhan Sill in the central Caspian Sea. Although mapped faults are sparse (Fig. A1), the region has experienced high levels of seismicity. Fig. A2 shows the KRF stacked radial and tangential receiver functions for three backazimuths. The KRF–NE and KRF–SE receiver functions have good signal–to–noise ratio and moderate amplitude tangential components. The KRF–W receiver function shows higher noise levels and larger tangential amplitudes compared to the KRF–NE or KRF–SE receiver functions. The complications of the KRF–W stack are probably due to the lower number and smaller magnitude of the events used and to the more complex crustal structure to the west of KRF in the vicinity of the Apshceron–Balkhan Sill. We have used only the KRF–NE and KRF–SE receiver functions in determining the structure beneath KRF.

The results of the KRF–NE and KRF–SE receiver function inversions are shown in Fig. A3. The average and simplified inversion model for KRF–NE is shown in Fig. A4a. The simplified KRF–NE model has a velocity step from 4.0 to 5.5 $km\,s^{-1}$ at 2 km depth, several layers forming a positive gradient to 22 km depth, a low velocity zone (LVZ) from 22 to 32 km depth, and a gradational Moho from 48 to 52 km depth. The synthetic receiver function computed for this model is similar to those of the inversion models except for the small positive phase arriving between the direct P and the Ps phases, an arrival which is a multiple generated at the 7 km depth boundary. We can significantly reduce the amplitude of this multiple phase by decreasing the amplitude contrast at 7 km depth with a 1 km thick gradational layer; however, we do not consider this feature essential in matching the significant arrivals in the data and therefore it is not included in the final model.

The results of the forward modelling tests for the KRF–NE receiver function are shown in Fig. A4b − f. Fig. A4b shows that including a 2 km thick 4.0 $km\,s^{-1}$ sedimentary layer results in ~0.2 s improvement in the arrival time fit of the synthetic and observed direct radial P–wave compared to synthetics for a model without this structure. Fig. A4c compares the KRF–NE receiver function to synthetic receiver functions computed for crustal models with and without a LVZ between 22–32 km depth. Both models produce synthetic receiver functions which approximately fit the main features of the KRF–NE receiver function. However, inclusion of the LVZ improves both the arrival time and amplitude fit of the 9 s arrival and results in a broad positive arrival between 12–16 s, which better fits this part of the observed waveform. Replacing the crustal structure above the Moho transition by a single layer with a velocity 6.4 $km\,s^{-1}$ (Fig. A4d) results in a synthetic receiver function in which the PpP_ms and PpS_ms are late compared to the observed arrivals. Including the interface at 16 km depth results in an improved fit to the 7 and 9 s arrivals due to the PpP_is and PpS_is phases, respectively. The observed arrivals between 9 and 16 s are not present in the synthetic of the model without this interface. Fig. A4e compares synthetic receiver functions for a first–order

discontinuity Moho at 50 km depth and a second–order discontinuity Moho between 48 and 52 km depth. The gradational Moho gives a better fit of the amplitude, arrival time, and pulse width of the PpP_ms and PpS_ms arrivals compared to those generated by a first–order discontinuity.

Results for similar tests of the KRF–SE inversion model (Fig. A4f) show that the crustal model for KRF–SE resembles the KRF–NE model except that the mid–crust LVZ is absent and the Moho transition is shallower (40 to 46 km depth). However, the KRF–SE tangential receiver function (Fig. A2) has significantly larger amplitudes relative to the radial than does the KRF–NE tangential in the period 9–16 s after the direct P–wave, suggesting greater amplitude off–azimuth arrivals for the southeast backazimuth.

Modeling of the KRF receiver functions has shown that to the east of KRF the crust consists of a 2 km thick V_p 4.0 km s^{-1} sedimentary layer below which V_p increases to 5.55 km s^{-1} followed by a gradual increase to 6.9 km s^{-1} at 16 km depth. To the northeast of KRF there is evidence for a mid–crustal LVZ which may exist to the southeast of KRF but may not be resolved due to higher noise levels in the KRF–SE receiver function. The crust–mantle transition is gradational over a 4 km depth range, but for the northeast azimuth the Moho is at 52 km depth while for the southeast azimuth it is at 46 km depth. Models for both azimuths are tabulated in Table A2.

A1.3 Nebit Dag (NBD)

NBD is located along the northeastern margin of the west Turkmenian lowlands, (Fig. 1 and A1) approximately 90 km southeast of KRF on the inferred extension of the Main Fault and directly south of the Khrebet Bol'shoy Balkan, a low group of folded hills separated from the main Kopet Dag range. Fig. A5 shows NBD receiver functions for four backazimuths. The NBD–NE receiver function was inverted and the average and simplified inversion models are shown in Fig. A6. Below the 3 km thick low velocity surface layer there is an uniform upper crustal section with a V_p of 6.0 km s^{-1} which extends to a depth of 26 km. Below this there is a gradual increase in velocity until upper mantle velocities are reached at 48 km depth. The direct P–wave of the radial receiver functions (Fig. A5) has an average delay of ~0.3 s, indicating about a 3 km thick sedimentary layer. Increasing the depth to the mid–crustal discontinuity to 32 km degrades the fit of the synthetic to the observed receiver function slightly. Because of this and the fact that nearby DSS models have a mid–crustal discontinuity at about 25 km depth, this interface was left at 26 km depth in the final NBD model. Replacing the gradational Moho with a first–order discontinuity primarily affects the PpP_ms and PpS_ms arrivals between 18–25 s but given the large tangential amplitudes at this time, either model could fit the data equally well. Table A3 gives the details of the NBD model.

A1.3 Alibek (ABKT)

ABKT is located ~300 km east of the south Caspian basin along the northern front of the Kopet Dag Mountains (Fig. 1), a range consisting of sub-parallel NW–SE trending faults and folds in the vicinity of ABKT that are truncated to the north by the Main Fault (Fig. A1) (Tchalenko 1975). The Kopet Dag has an abrupt northeast topographic front associated with a number of right–lateral strike–slip earthquakes (Tchalenko, 1975; Priestley *et al.*, 1994). Elsewhere in the Kopet Dag south of ABKT there is thrust faulting and regional folding consistent with the north motion of the Iranian plate.

Fig. A7 shows the ABKT radial and tangential receiver functions for four backazimuths. The ABKT–NE receiver function has the smallest amplitude tangential of the four azimuths and was inverted for a 1–D crustal model. For comparison we also inverted the ABKT–ENE radial receiver function. The average ABKT–NE receiver function inversion model is shown in Fig. A8a along with the simplified inversion model. Removing the LVZ (Fig. A8b) eliminates the arrival in the synthetic corresponding to the prominent positive arrival at ~13 s. This arrival cannot be matched by altering the model so that the LVZ becomes a mid-crustal interface which also preserves the crustal travel time (Fig. A8c). We have conducted similar forward modelling tests of the other three ABKT receiver functions (Mangino, 1997) and despite the larger tangential amplitudes, find no evidence in these for a mid–crustal LVZ. The final result for the ABKT–ENE receiver function is shown in (Fig. A8d). For this reason we have included models with and without the LVZ for ABKT (Fig. 3). Table A4 gives the details of the ABKT models.

We examined the nature of the azimuthal variation in the receiver functions by comparing 2–D synthetic receiver functions for models which were the same as the 1–D model but with some dipping interfaces. ABKT is on the northern slope of the Kopet Dag Mountains, which are being thrust southwards over the foreland depression of the Kara Kum; the general dip of the sediments and the Moho beneath the Kara Kum is then likely to be southwest towards the Kopet Dag. We computed synthetic receiver functions for a southward dipping layer beneath ABKT but found that these matched neither the azimuthal variation of the waveforms nor the observed P–wave polarization pattern (Mangino, 1997). Fig. A9 shows the results for the model whose synthetic receiver functions best fit the observed receiver functions. This model is the same as the final 1–D ABKT model in Fig. A8a, but the two shallow interfaces at 1.8 and 3.8 km depth strike N335°E and dip 15° to the northeast. Multiple combinations of planar dipping interfaces were examined, but the waveforms after the first 2–3 s could not be fit satisfactorily. This shallow (~1 km depth) dipping element, while strongly affecting the ABKT receiver functions, is probably a minor structural feature associated with the Kopet Dag range front and its prominent effect in the receiver functions results from the strong velocity contrast between the sediments and basement. It is not surprising that any

hypothesised deeper SW dipping structure beneath the Kopet Dag margin is not observed since the velocity contrast associated with this structure is likely to be much less than the contrast between the sediments and basement.

A1.4 Kizyl Atrek (KAT)

KAT is located along the southeastern margin of the West Turkmenian lowlands (Fig. A1) just east of the Caspian Sea in a region of the Kopet Dag where the faults and folds trend NE–SW and merge into the Alborz Mountains. Fig. A10 shows the KAT radial and tangential receiver functions. Except for the KAT–ESE receiver function, the tangential amplitude equals or exceeds the radial amplitude, implying a laterally heterogeneous receiver structure. There is no clear pattern in the receiver functions with azimuth. The direct radial P–wave arrival is delayed 0.5 – 1.0 s (Fig. A10), suggesting a thick accumulation of low velocity sediment. The delay pattern implies that the thickness of the sedimentary layer is greater both northeast and west of KAT than to the southwest, consistent with the location of KAT on the southeastern edge of the basin (Fig. 1 and A1).

The KAT–ESE receiver function has the smallest tangential amplitude component and this receiver function was inverted. The average and simplified inversion models are shown in Fig. A11a. The main features of the first 7–8 s of the KAT–ESE receiver function can be fit by the synthetic receiver functions computed for a simplified version of the average inversion model consisting of two low velocity surface layers, a uniform 5.9 km s^{-1} layer between 10 and 27 km depth, and a gradational crust–mantle transition between 27 and 32 km depth. Increasing the number of layers in the sedimentary section (Fig. A11b) gives an improved fit to the waveform between 7–15 s, but it also significantly reduces the amplitude of the 3–4 s arrival. Forward modelling shows that most of the differences in the first several seconds of the four KAT radial receiver functions are due to variations in the velocity structure of the sedimentary layer which lead to variations in the constructive/destructive interference pattern between the near–surface multiples. Tests of the crust–mantle transition structure show that a sharp Moho results in a multiple peaked lower amplitude PpP$_m$s arrival compared to the three–step model. A model with a more gradational Moho fits the observations better, but because of the large amplitude tangential arrivals at this time, the nature of the Moho is not well resolved. The KAT crustal model is tabulated in Table A5.

A1.6 Lenkoran (LNK)

LNK is located in southeastern Azerbaijan between the Talesh Mountains and the southwest Caspian Sea (Fig. 1 and A1). From earthquake focal mechanism studies Berberian (1983), Jackson & McKenzie (1984), and Priestley et al. (1994) have shown that the Talesh Mountains are being thrust from the west over the southwest Caspian Sea. Fig. A12 shows the

LNK radial and tangential receiver functions for backazimuths ranging from 65° to 117°. A stack of the 65° and 76° backazimuth receiver functions was inverted; a second stack consisting of the 96°, 97° and 103° backazimuth receiver functions was also inverted for comparison.

The average and simplified inversion models are shown in Fig. A13a. Fig. A13b shows a synthetic radial receiver function computed from an overly simplified two–layer crust over a half–space model. The synthetic receiver function fits the arrival times and polarities of the secondary arrivals for the first 14–16 s, but the amplitude is clearly overestimated. These large amplitudes are due mainly to multiple phases generated at the 4.0 km s^{-1} discontinuity at 5 km depth. A step in velocity at 35 km depth generates relatively lower amplitude Ps, PpP$_m$s and PpS$_m$s phases that arrive at 4.5 s, ∼15 s and ∼17 s respectively. Fig. A13b demonstrates that the arrival times and polarities of the most significant arrivals on the LNK radial receiver function can be fit using just two velocity discontinuities: a shallow discontinuity inferred to be the sediment–basement contact and a deeper discontinuity inferred to be the Moho.

The final 1–D model for LNK (Fig. A13a) was obtained by retaining the two near–surface velocity discontinuities, which dramatically improves the synthetic fit for two reasons. First, the change in velocity from the mid–crust to the near surface is distributed over three discontinuities rather than a single large discontinuity, thus generating lower amplitude P–to–S phases. Second, most of the multiple phases interfere destructively with each other. This modification also reduces the amplitude of the higher order multiples that arrive after ∼16 s. A test of the crust–mantle transition showed that it was not possible to distinguish between a first– and second–order discontinuity Moho. The LNK crustal model is tabulated in Table A6.

The Talesh Mountains are being thrust from the west over the southwest Caspian Sea. All of the receiver functions in Fig. A12 show a delayed first arrival consistent with the thick sediments to the east of LNK. The 50° azimuthal span of the receiver functions in Fig. A11 shows a regular variation in the initial amplitude of the tangential component. In considering the tectonics, one would expect the structures offshore to dip W towards the Talesh Mountains. Synthetic receiver functions for a deeper westward dipping interface match neither the azimuthal variation in the receiver functions nor P–wave polarization measurements (Mangino, 1997). The results for the dipping layer model whose receiver functions best fit the observed receiver functions are shown in Fig. A14. This model has a N350°E striking, 15° northeast dipping interface at 3 km depth. The strike is controlled by the reversal in tangential first motion polarity between 65° and 97° backazimuth, and the 15° dip angle and the velocity contrast across the dipping interface control the amplitude of the tangential waveforms. Since the velocity contrasts in the LNK model are large (1–1.5 km s^{-1}), the 15° dip results in large amplitude tangential waveforms. The depth to the dipping interface and the average velocity above this interface control the timing of the negative tangential

arrival observed at ~2 s. Although the first several seconds are reasonably well matched, the synthetics poorly fit the LNK waveforms after ~6 s. Additional dipping interfaces were introduced at greater depths, but there was no significant improvement in the resulting synthetic waveform fit. This northeastward dipping structure probably approximates a more complex three–dimensional shallow structure associated with the Talesh Mountains – Caspian Sea transition. Like the ABKT case, the velocity contrast across the presumed, deeper westward dipping structure is likely to be too small, compared to the near–surface sediment – basement interface, to have much effect on the receiver function.

TABLE A1. CASPIAN RECEIVER FUNCTION SOURCE PARAMETERS

Event No.	Date (m/d/y)	Origin Time	Latitude (N°)	Longitude (E°)	m_b	Depth (km)	stack name (station–backazimuth)
1	05/25/93	23:16:43	55.021	-160.513	6.2	37	NBD–NNE
2	05/29/93	06:50:13	19.072	-26.476	5.9	12	KRF–W, NBD–SE
3	05/30/93	17:08:53	1.546	127.207	6.0	81	LNK–96, NBD–E
4	06/08/93	13:03:36	51.218	157.829	6.4	71	LNK–E, NBD–NE, ABKT–NE
5	07/12/93	13:17:11	42.851	139.197	6.6	17	ABKT–NE, KRF–NE
6	08/07/93	00:00:37	26.585	125.612	6.0	155	ABKT–ENE, LNK–76
7	09/01/93	00:41:23	31.712	141.611	5.4	45	NBD–NE
8	09/20/93	10:17:42	0.750	-29.354	5.8	10	KRF–W
9	10/11/93	15:54:21	32.020	137.832	6.4	351	ABKT–NE, KRF–NE, KAT–NE, LNK–65
10	12/09/93	04:32:19	0.486	125.995	6.5	15	ABKT–ESE, KRF–SE, KAT–ESE, LNK–97
11	01/19/94	01:53:34	-3.176	135.970	6.1	23	ABKT–ESE, KAT–ESE, LNK–94
12	03/06/94	08:01:43	-21.556	-113.701	5.6	10	LNK–117
13	05/11/94	08:18:15	-2.008	99.770	6.0	21	ABKT–SE
14	06/05/94	01:09:30	24.511	121.905	6.1	11	ABKT–ENE
15	07/13/94	11:45:23	-7.532	127.770	6.5	159	ABKT–ESE, KRF–SE, LNK–103
16	07/21/94	18:36:31	42.340	132.865	6.5	471	KRF–NE, KAT–NE
17	10/04/94	13:22:55	43.773	147.321	7.3	14	KRF–NE
18	10/15/94	05:10:00	45.749	149.167	6.4	117	KRF–NE
19	10/31/94	11:48:13	3.019	96.192	5.7	29	KAT–SE, ABKT–SE
20	11/15/94	20:18:11	-5.589	110.186	6.2	561	KRF–SE
21	03/31/95	14:01:40	38.150	135.058	6.0	365	ABKT–NE, KRF–NE
22	04/17/95	23:28:08	45.904	151.288	6.1	34	ABKT–NE
23	04/20/95	08:45:10	6.288	126.828	6.2	85	KAT–ESE, KRF–SE
24	04/21/95	00:09:56	11.999	125.699	6.1	33	ABKT–ESE, KAT–ESE, ABKT–ENE
25	04/28/95	16:30:00	44.058	148.055	6.6	29	KAT–NE, KRF–NE
26	05/04/95	02:18:51	1.857	128.488	6.0	55	ABKT–ESE
27	05/05/95	03:53:47	12.622	125.314	6.2	33	ABKT–ENE
28	05/18/95	00:06:26	-0.950	-21.985	6.2	10	KAT–W
29	07/12/95	18:38:49	12.316	125.037	5.8	33	KRF–SE
30	07/26/95	23:42:02	2.562	127.692	5.9	66	KRF–SE

Table A2 – KRF receiver function model parameters

KRF–NE			KRF–SE	
Vp (km s^{-1})	Thickness (km)		Vp (km s^{-1})	Thickness (km)
4.00	2.0		4.00	1.5
5.55	5.0		5.50	10.5
6.20	9.0		6.20	4.2
6.90	8.0		6.80	24.5
6.55	10.0		7.31	2.5
6.80	14.0		7.67	2.5
7.35	2.0		8.10	∞
7.75	2.0			
8.10	∞			

Table A3 – NBD–NE model parameters

Vp $(\text{km s}^{-1}$	Thickness (km)
4.00	3.0
6.00	23.0
6.60	6.0
6.90	12.0
7.50	4.0
8.10	∞

Table A4 – ABKT–ENE model parameters

Vp (km s^{-1})	Thickness (km)
3.50	1.8
5.25	6.0
6.10	6.0
6.50	6.0
6.90	20.0
7.30	2.0
7.60	2.0
7.80	2.0
8.10	∞

Table A5 – KAT–ESE model parameters

Vp (km s^{-1})	Thickness (km)
3.00	4.0
4.60	5.0
5.80	17.0
6.70	3.0
7.40	3.0
8.10	∞

Table A6 – LNK–ENE model parameters

Vp (km s^{-1})	Thickness (km)
3.20	2.0
4.60	4.8
6.40	6.0
7.10	22.0
8.10	∞

Appendix A Figure Captions

Figure A1. Fault map of the region surrounding the south Caspian basin taken from Berberian (1976). The Caspian seismic stations used in this study are denoted by the solid triangles and the IRIS station at Ashkabad is denoted by the solid square. The lines emanating from each station symbol denote the azimuth for which a receiver function was determined. The azimuth of the receiver function is denoted at the end of each line segment.

Figure A2. KRF radial (left) and tangential (right) receiver functions. The dotted lines are the $\pm 1\sigma$ bounds computed from the variance of the stack. To the left of each receiver function pair is the stack name, the number of events in the stack, the mean backazimuth, the mean ray parameter, and the water level parameter for the deconvolution. The vertical line denotes the zero time of the direct vertical arrival. The KRF–NE radial receiver function consists of high amplitude arrivals at 7 s, 9 s and 18–25 s which may be the Ps (a), PpP_ms (b), and PpS_ms (c) phases generated at the Moho. The 9 s (d) negative arrival complicates this straightforward interpretation and is evidence for a second prominent velocity discontinuity in the crust beneath KRF. The KRF–SE radial receiver function has large amplitude arrivals at approximately 5 s and between 15–26 s. These arrivals may be the Ps, PpP_ms and PpS_ms phases but unlike the KRF–NE receiver function, the prominent 9 s (d) negative arrival is absent. The KRF–SE tangential amplitude between 7–15 s exceeds the radial amplitude at the same time period and these arrivals are evidence of a more laterally heterogeneous structure to the southeast of KRF. The KRF–W receiver function is much more complicated than either the KRF–NE or KRF–SE receiver functions.

Figure A3. KRV–NE (a) and KRV–SE (b) inversion results. The inversion velocity models are shown on the right as solid lines and the range of starting models is indicated by the dotted lines. The span of starting models covers a large enough range of velocities to include most possible rock types found in the crust and upper mantle. The inversion model synthetic receiver functions (solid line) are compared on the right to the $\pm 1\sigma$ bounds (dotted lines) of the radial receiver function (top left) and the mean radial (solid line) and tangential (dashed line) receiver functions are compared at the bottom left. The KRF–NE inversion results have a relatively narrow range of models. Arrivals (a), (b), and (c) (Fig.A2) are fit with the P–to–S phases generated from the positive gradients between 16–20 km depth and a deeper interface gradient at 48–52 km depth. The negative velocity gradient between 20–30 km depth generates the negative arrival (d) and the subsequent positive arrivals between (d) and (b). The KRF–SE inversion results show a greater range of possible velocity models. The three main arrivals are fit with P–to–S phases generated from the strong positive gradients between 15 and 20 km depth and between 45

and 50 km depth. All of the KRF–SE inversion models have a negative velocity gradient between 30 and 40 km depth, moving the associated phases closer in time to the Moho multiples.

Figure A4. (a) Comparison of the KRF–NE average inversion (dotted line) and simplified inversion velocity model (solid line) on the right and the comparison of the synthetic radial receiver function (solid line) for the simplified velocity model with the observed receiver function bounds (dotted lines) on the left. The phases corresponding to the inter–crustal (i) and Moho (m) are identified above the receiver function. (b) Comparison of the observed delay of the KRF–NE direct radial P–wave (dotted lines), that for a model with a 2 km thick sedimentary layer (solid line), and that with no sedimentary layer (dashed line). Test of the effects (c) of a mid–crustal low velocity zone (solid line) and a uniform velocity midcrust (dashed line), (d) of a mid–crustal discontinuity (solid line) and a no discontinuity (dashed line), and (e) of a second– (solid line) and first–order (dashed line) crust–mantle transition. (f) Results for simplifying and forward modeling the KRF–SE inversion model.

Figure A5. NBD radial (left) and tangential (right) receiver functions. The format of this figure is the same as Fig. A2. Only the NBD–NE receiver function consists of more than one event. The NBD–E and NBD–ESE receiver functions have a poor signal–to–noise level and the tangential amplitude equals or exceeds the radial amplitude for at least the first 20 s. The pre–signal noise and tangential amplitudes are lower for the NBD–NNE and NBD–NE receiver functions. The phases labeled (a), (b) and (c) on the NBD–NE radial receiver functions may be the Ps, PpP_ms and PpS_ms arrivals respectively, generated at the Moho. These arrivals on NBD–NE correspond to large amplitude phases in the NBD–NNE receiver function. The (d) phases in the NBD–NNE and NBD–NE tangential receiver functions at approximately 12 s indicate an off–azimuth arrival. The amplitude of this arrival is smaller in the NBD–NE stack than in the single event NBD–NNE receiver function.

Figure A6. Simplification and forward modeling results of the NBD–NE velocity model; testing of the midcrustal interface showed that this could be as deep as 32 km and still adequately fit the data. However we have left the midcrustal interface at 26 km depth in agreement with the midcrustal interface seen in nearby DSS studies. Testing of the Moho showed the data could not distinguish between a first– and second– order discontinuity.

Figure A7. ABKT radial (left) and tangential (right) receiver functions. The format of this figure is the same as for Fig. A2. One of the most striking features of the ABKT receiver functions is the variation of the tangential first motion. The ABKT–NE tangential receiver function has the lowest first motion amplitude as well as a relatively low overall

amplitude compared to the radial. The ABKT–ENE, ABKT–ESE and ABKT–SE tangential receiver functions have a positive first motion followed by a negative pulse that increases in amplitude with increasing backazimuth. The apparent delay of the direct radial arrival with respect to the vertical arrival varies from 0.7 s for the ABKT–NE receiver function to 0.2 s for the ABKT–SE receiver function which is consistent with thick sediments to the north beneath the Kara Kum foreland depression and thinner sediments in the uplifted Kopet Dag.

Figure A8. Simplification and forward modeling test of the ABKT–NE velocity model: (a) average inversion model (dotted line), simplified average model (dashed line), and final model (solid model) of this azimuth, (b) effect with (solid line) and without (dashed line) a mid–crustal low velocity zone, (c) effect with (solid line) and without (dashed line) a mid–crustal discontinuity, and (d) Forward modeling test of the ABKT–ENE velocity model for the effect of a first– and second–order crust–mantle transition.

Figure A9. Comparison of the ABKT observed (solid line) and calculated receiver functions (dotted lines) *vs* azimuth on the left for the dipping interface model shown on the right.

Figure A10. KAT radial (left) and tangential (right) receiver functions. The format of this figure is the same as Fig. A2. All the radial receiver functions show a delayed direct P–wave arrival, a variable amplitude second arrival (a), a prominent negative arrival at 8–10 s, a positive arrival with a peak near 15 s (b) and a negative arrival between 18–22 s (c). The prominent phase closely following the direct arrival is probably a multiple generated within the thick laterally heterogeneous sedimentary layer. There is a delay of the KAT direct radial P–wave of 0.5 s for KAT–SE to 1.0 s for KAT–W and KAT–NE which corresponds to thick sediments beneath the Turkmenian Lowlands west and north of KAT and thinner sediments in the mountainous region southeast of KAT.

Figure A11. Simplification and forward modeling test of the KAT–ESE velocity model: (a) average inversion model (dotted line), simplified average model (dashed line), and final model (solid model), and (b) effect of a near surface gradient.

Figure A12. LNK single event radial (left) and tangential (right) receiver functions *vs* azimuth. To the left of each receiver function pair is the backazimuth, ray parameter for the event, and water fill parameter used in the deconvolution. The radial receiver functions have common features during the first ∼15 s, consisting of a delayed direct P–wave arrival, a prominent 4.0–4.5 s positive arrival, a broad negative arrival between 8–11 s and a positive arrival between 12–15 s. The tangential receiver functions show a systematic variation with backazimuth. Except for the arrival between 9–11 s, the amplitude of the 65° backazimuth tangential receiver function is small relative to the radial receiver function amplitude. For backazimuths greater than 96°, the tangential receiver function

amplitude is about equal to the radial amplitude during the first 12–15 s, and is greater after this time. The azimuthal coverage is small but the pattern of the tangential receiver function first arrival is suggestive of that generated by a northeast dipping interface. The direct radial P–wave arrival is delayed on average by 0.9 s, implying the presence of a thick accumulation of low velocity sediment consistent with that observed in the Caspian Sea east of LNK (~10 km thick – Neprochnov, 1970). We interpret the 4.0–4.5 s arrival common to all backazimuths as a Ps phase generated at the Moho. However, the presence of a thick sedimentary section suggests that this arrival may also be affected by a multiple generated at the sediment – basement interface.

Figure A13. Simplification and forward modeling test of the LNK–NE velocity model: (a) average inversion model (dotted line),simplified average model (solid model), and (b) receiver functions for an overly simplified two–layer crust.

Figure A14. Comparison of the LNK receiver functions (solid line) *vs* azimuth (denoted by the number on the left) and calculated receiver functions (dotted lines) on the left for the dipping interface model shown on the right.
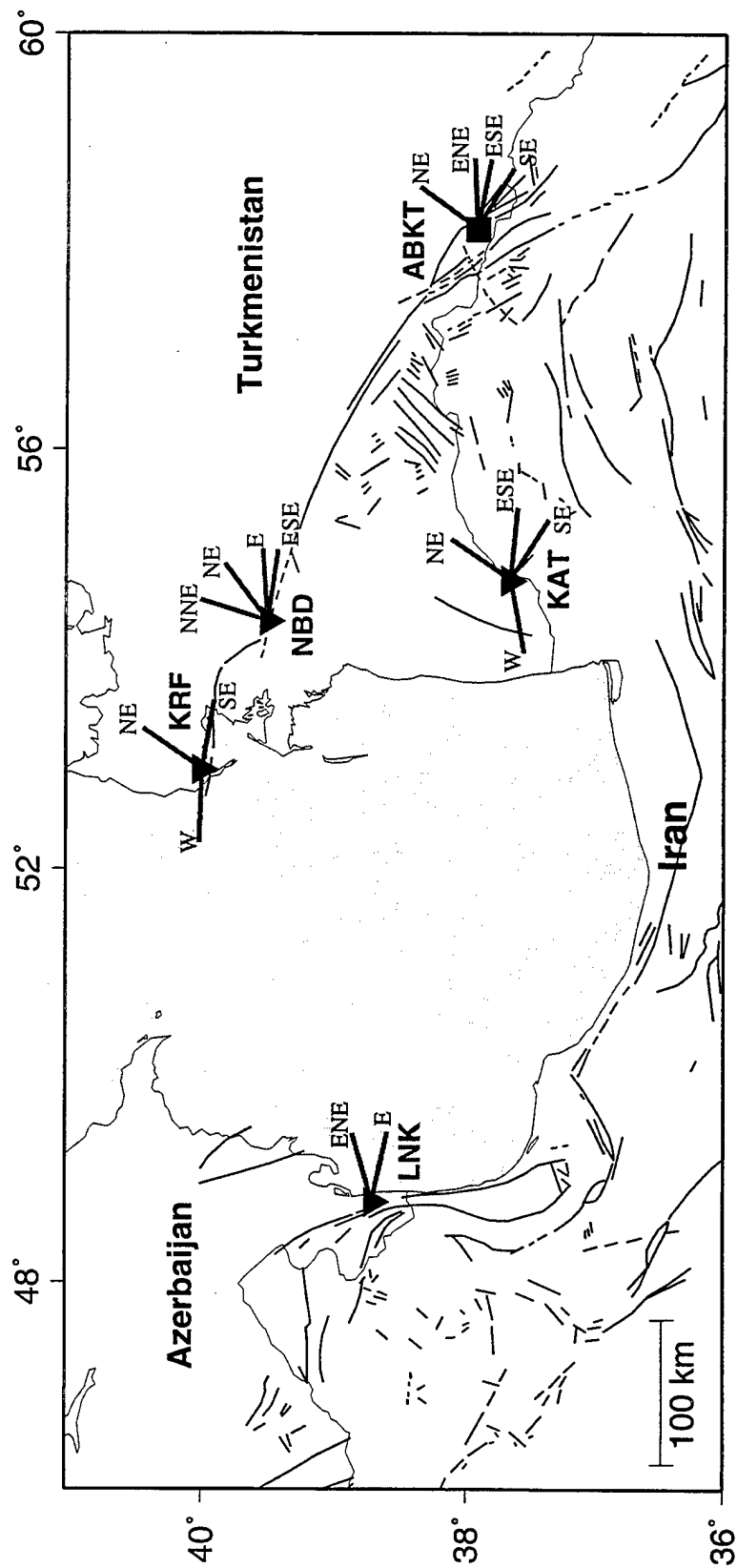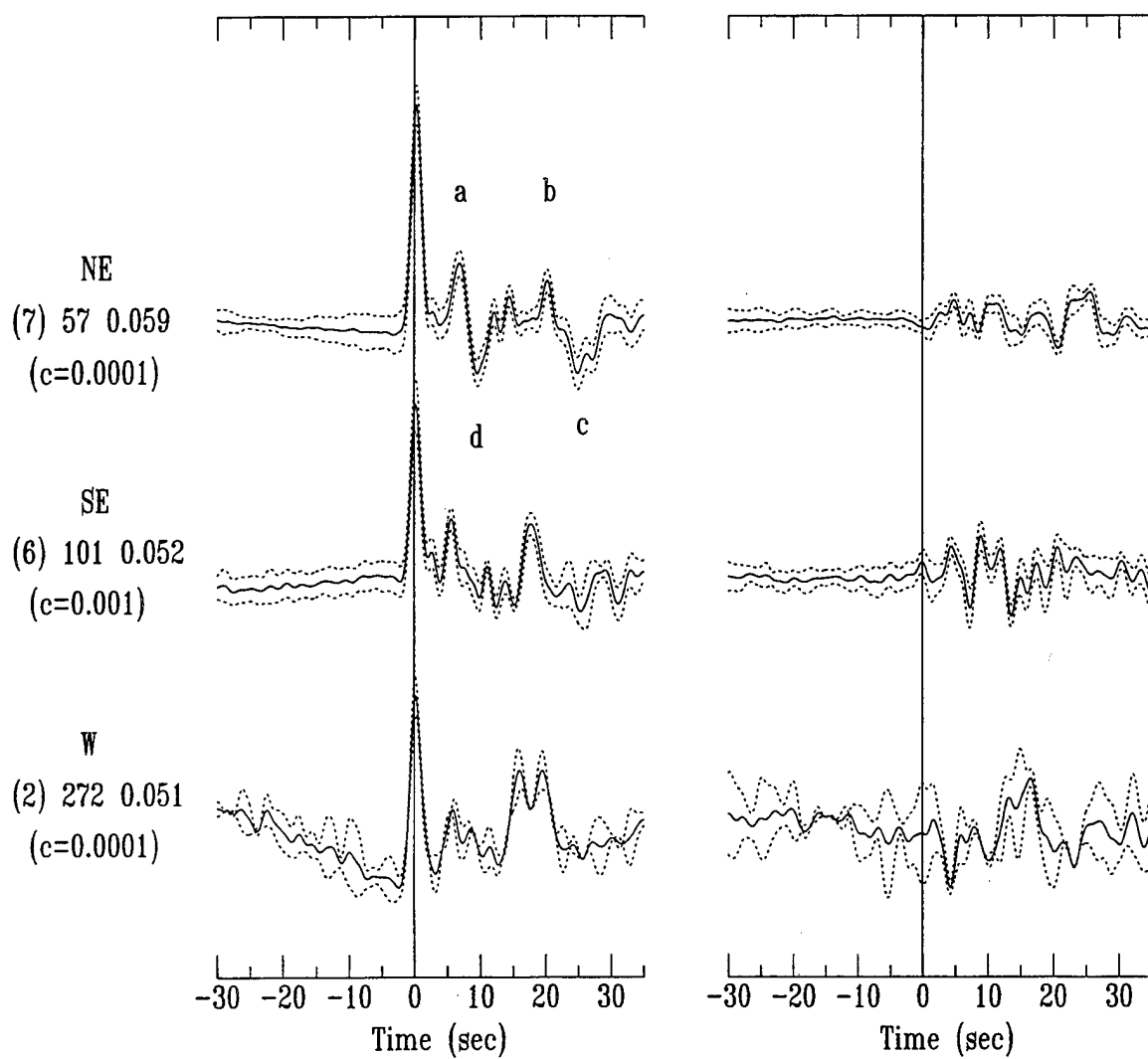
FIGURE A1

FIGURE A2
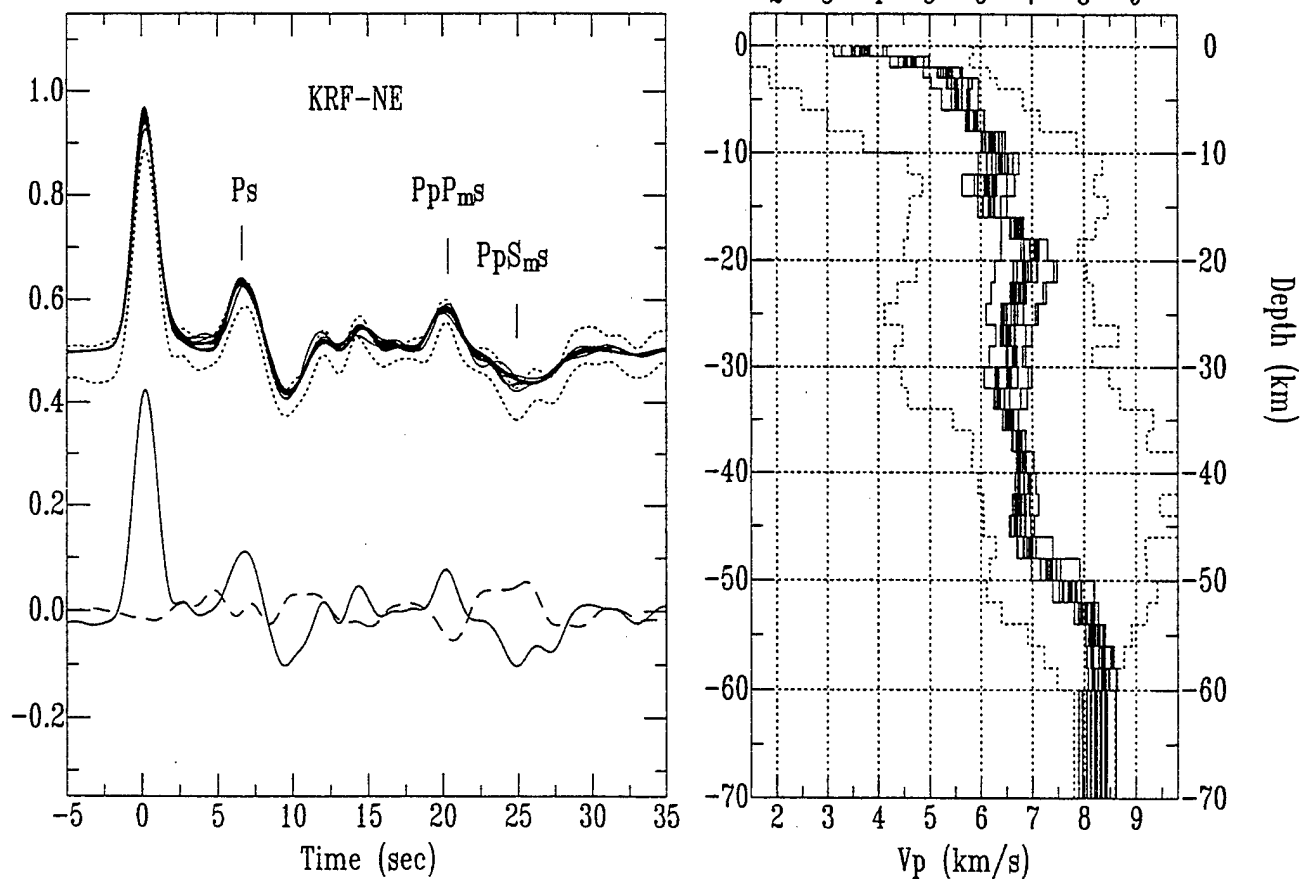
FIGURE 3A

FIGURE 3B

40
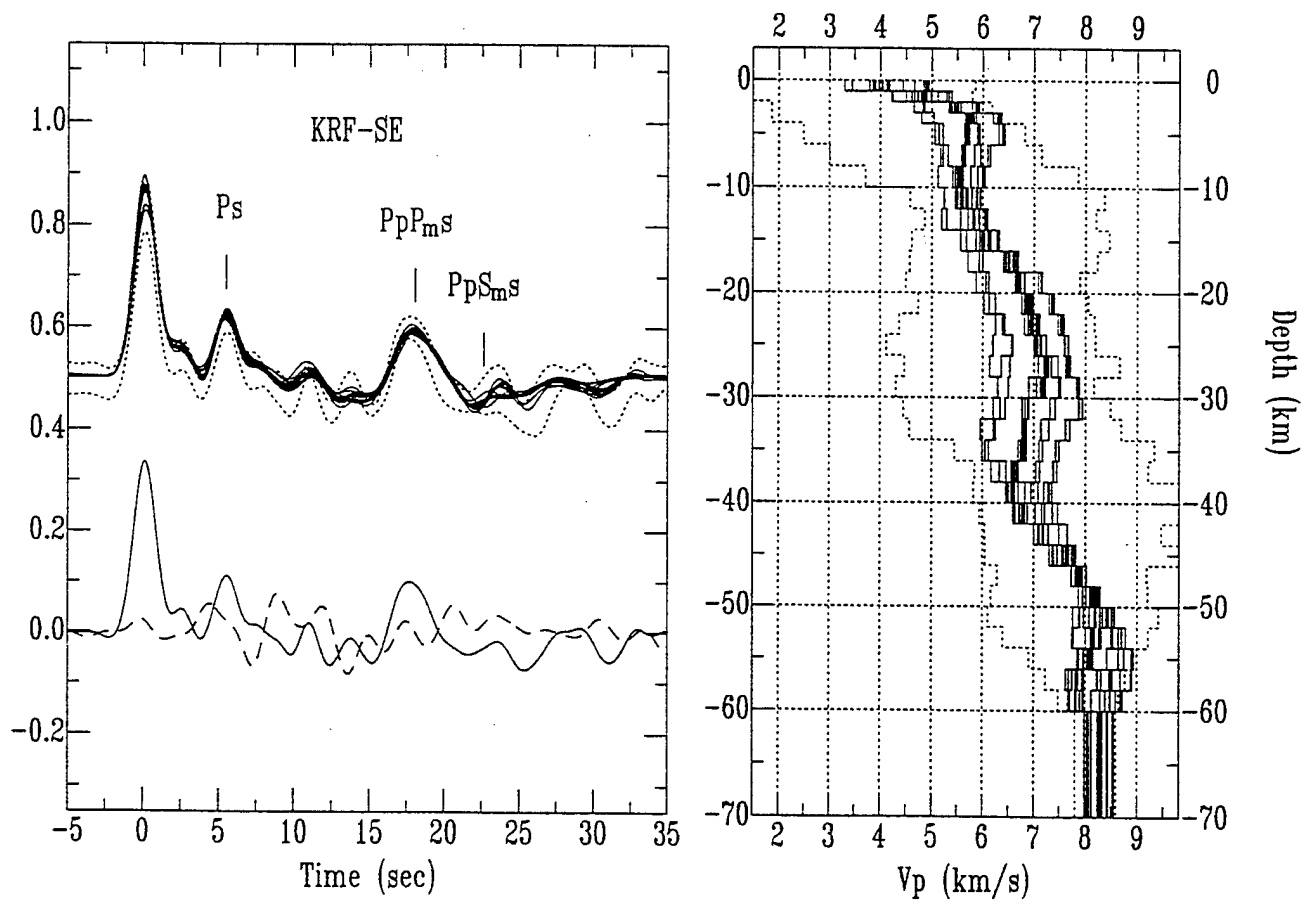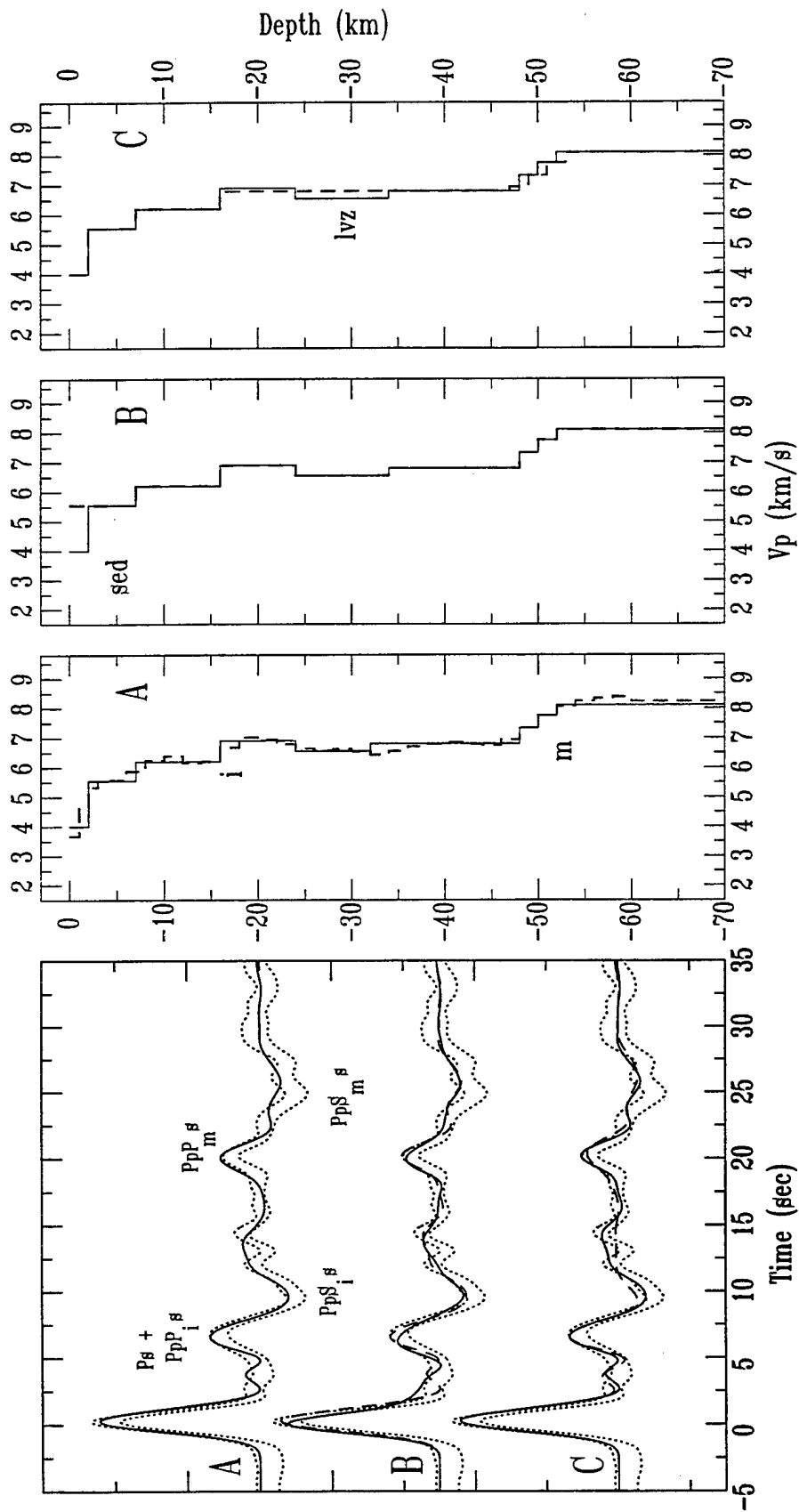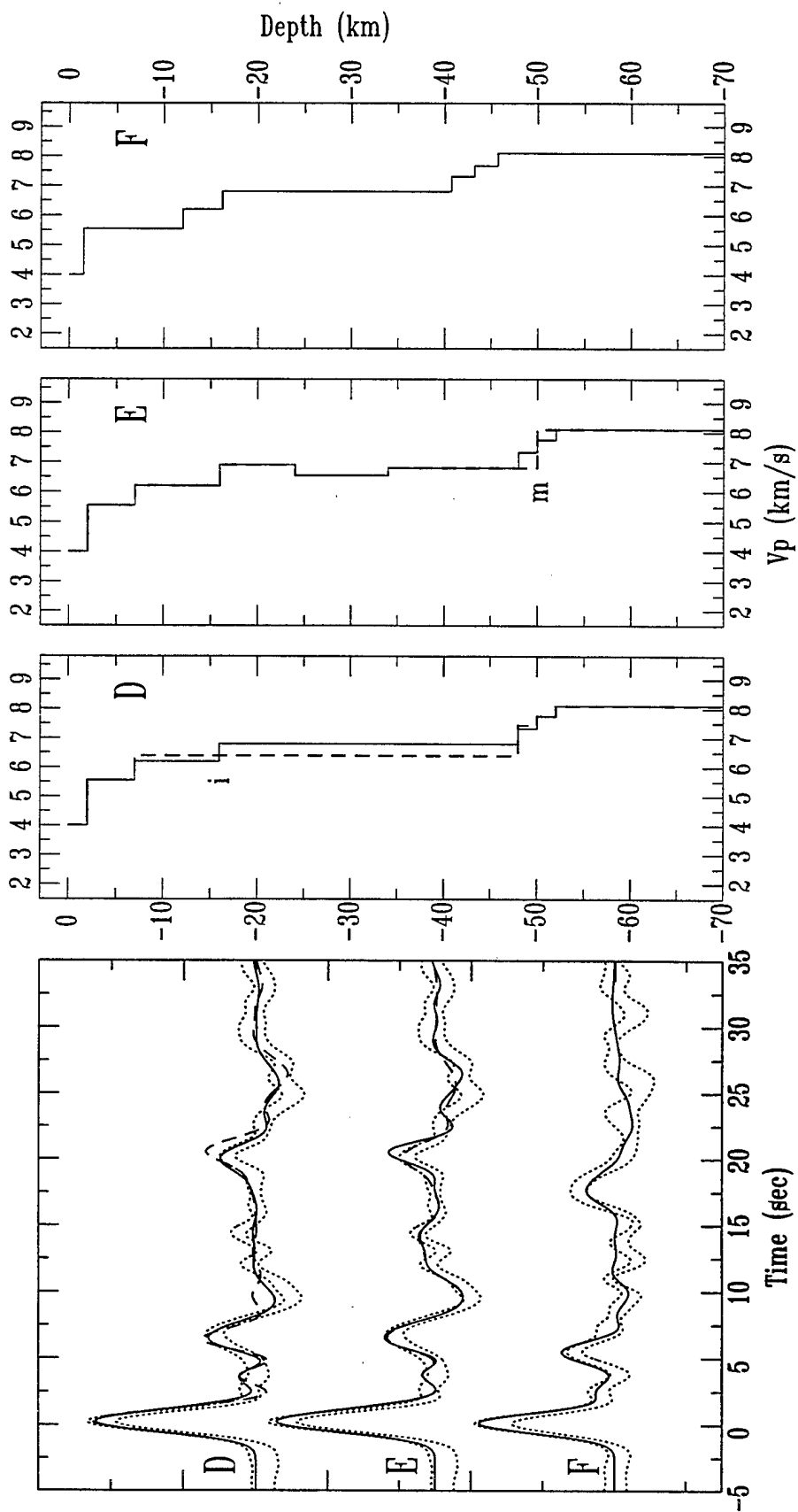
FIGURE A4(a)

FIGURE A4(b)
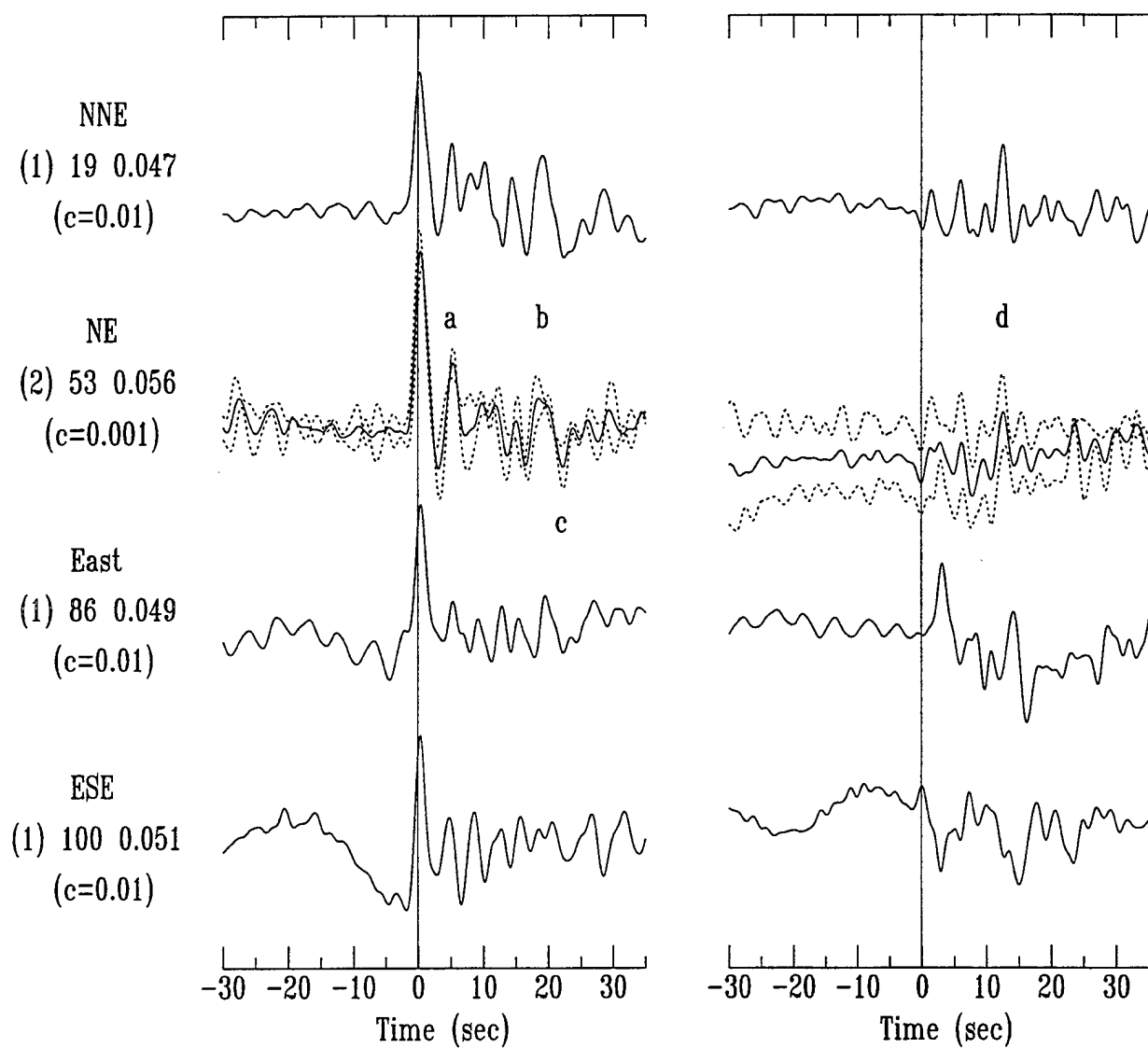
FIGURE A5

FIGURE A6

44

NE

(5) 56 0.059

(c=0.0001)

ENE

(4) 88 0.061

(c=0.0001)

ESE

(4) 103 0.051

(c=0.0001)

SE

(2) 126 0.067

(c=0.0001)

Time (sec)

Time (sec)

FIGURE A7

45

FIGURE A8(a)

FIGURE A8(b)

46

FIGURE A9

NE
(3) 56 0.058
(c=0.01)

ESE
(4) 97 0.061
(c=0.01)

SE
(1) 122 0.051
(c=0.01)

West
(1) 261 0.048
(c=0.01)

a

b

c

-30 -20 -10 0 10 20 30
Time (sec)

-30 -20 -10 0 10 20 30
Time (sec)

FIGURE A10

48

FIGURE A11

BAZ	p	c
65	0.054	0.10
76	0.058	0.01
94	0.042	0.01
96	0.048	0.01
97	0.048	0.01
103	0.044	0.01
117	0.057	0.01

Time (sec)

Time (sec)
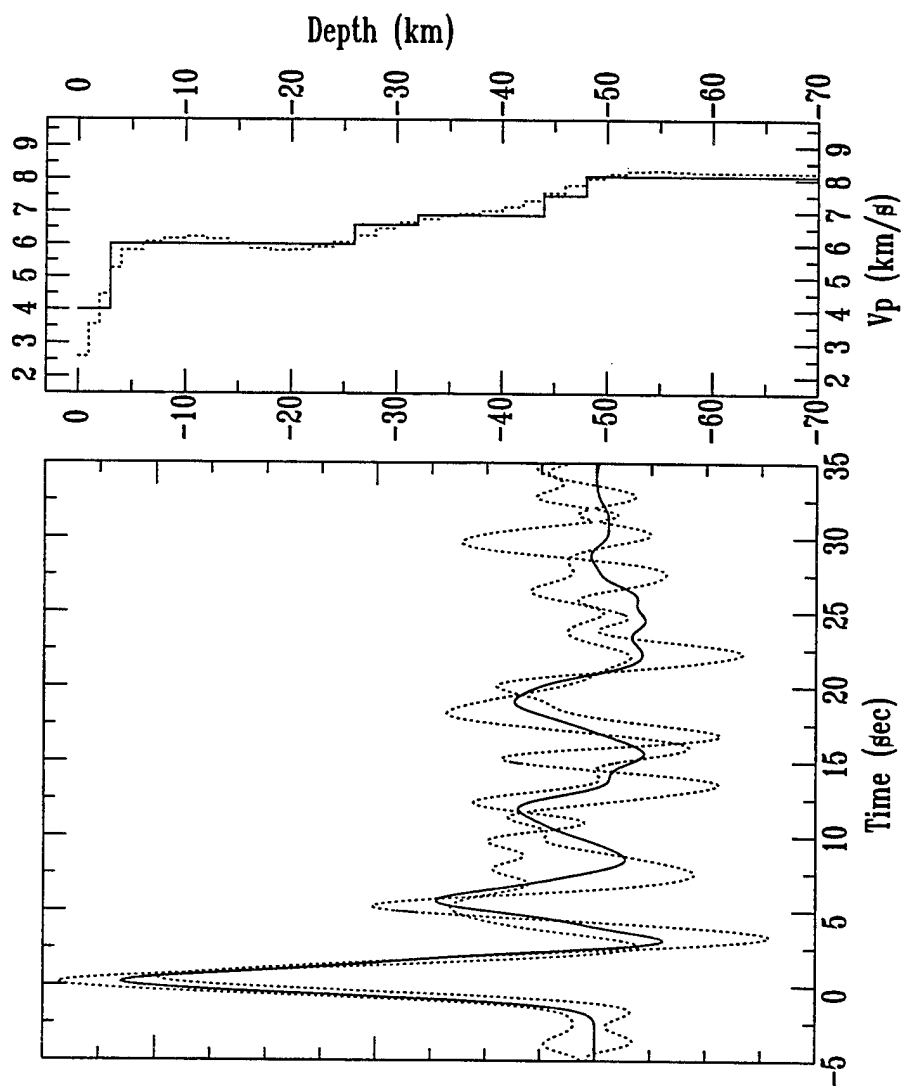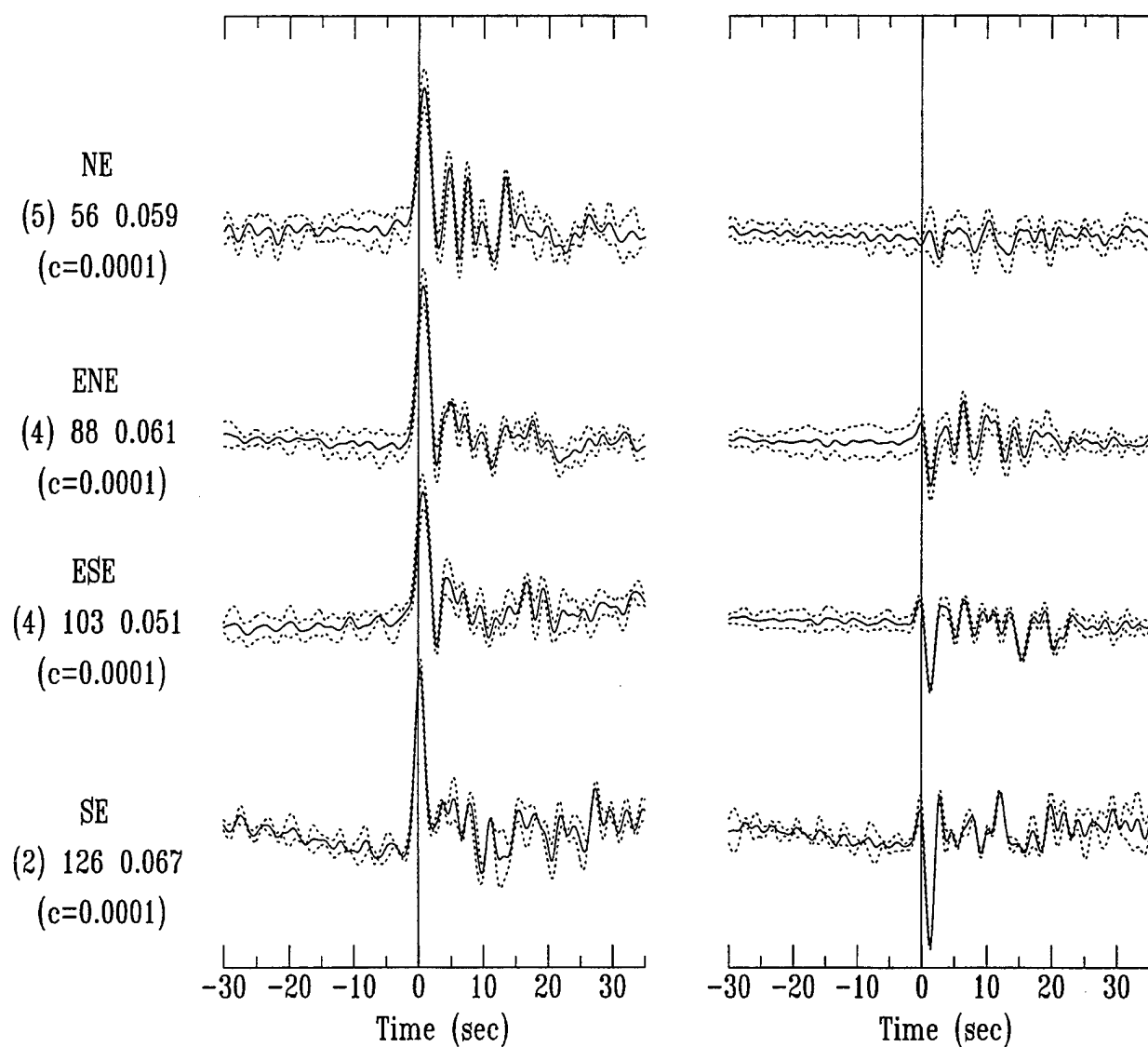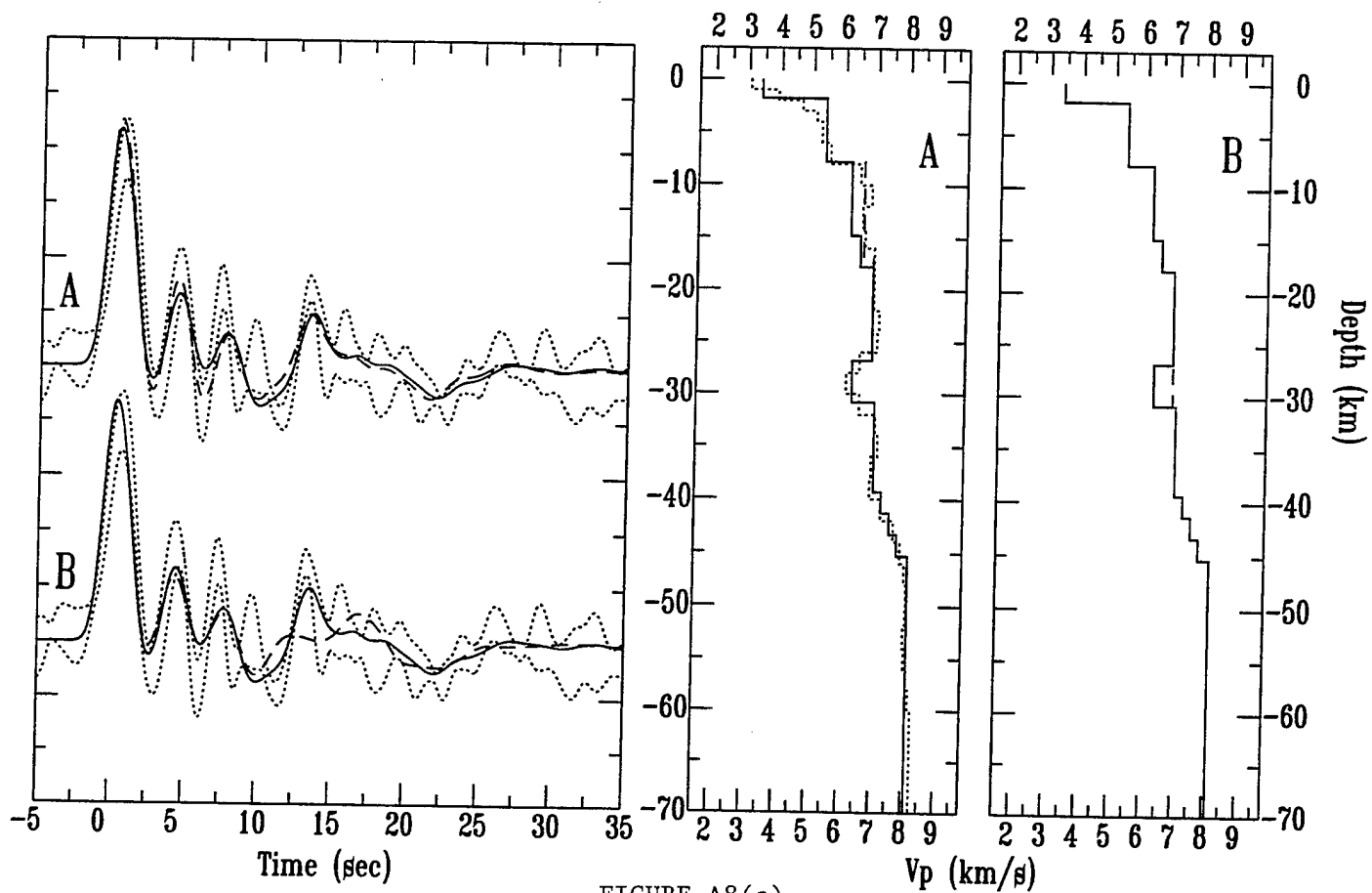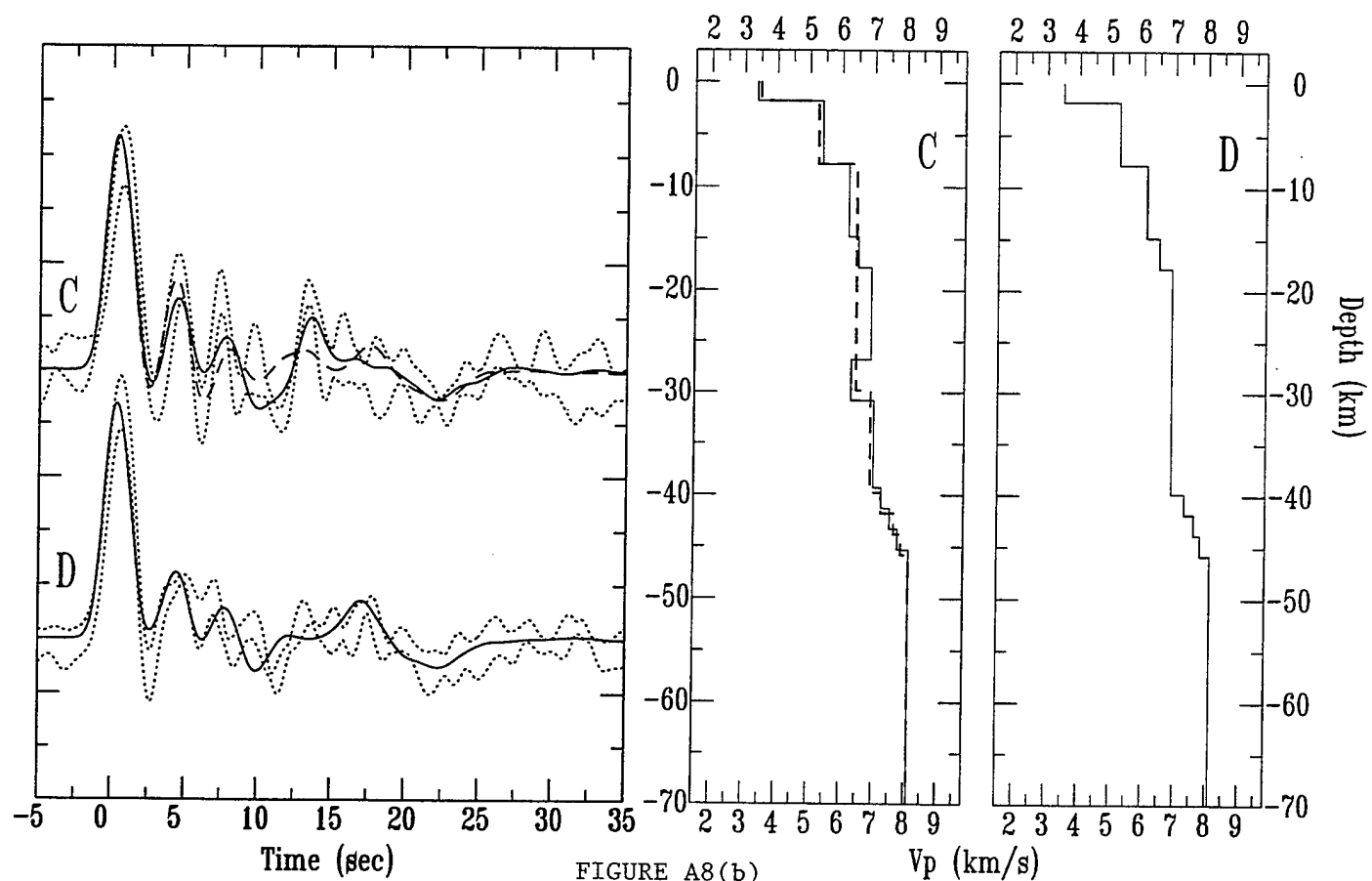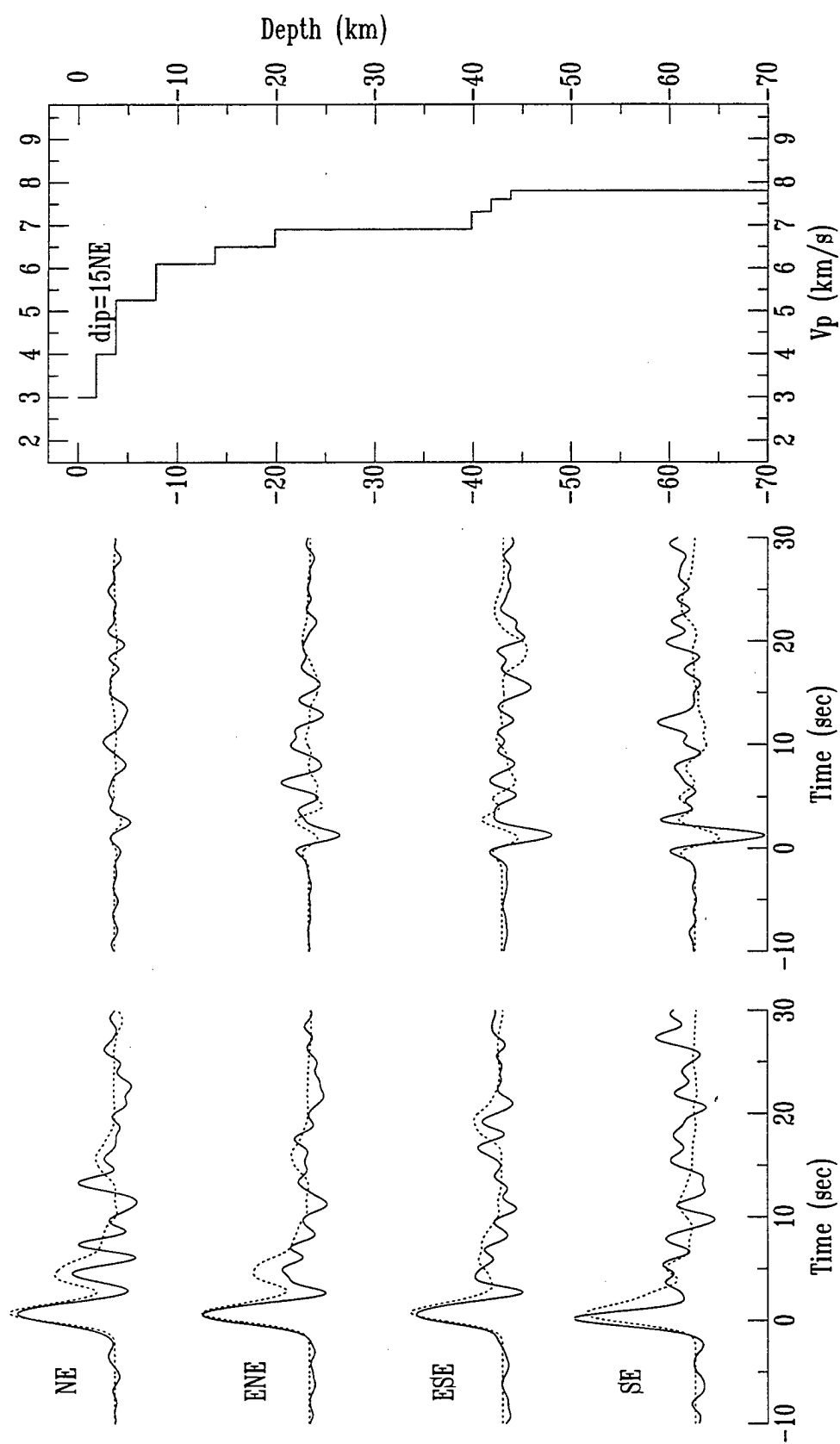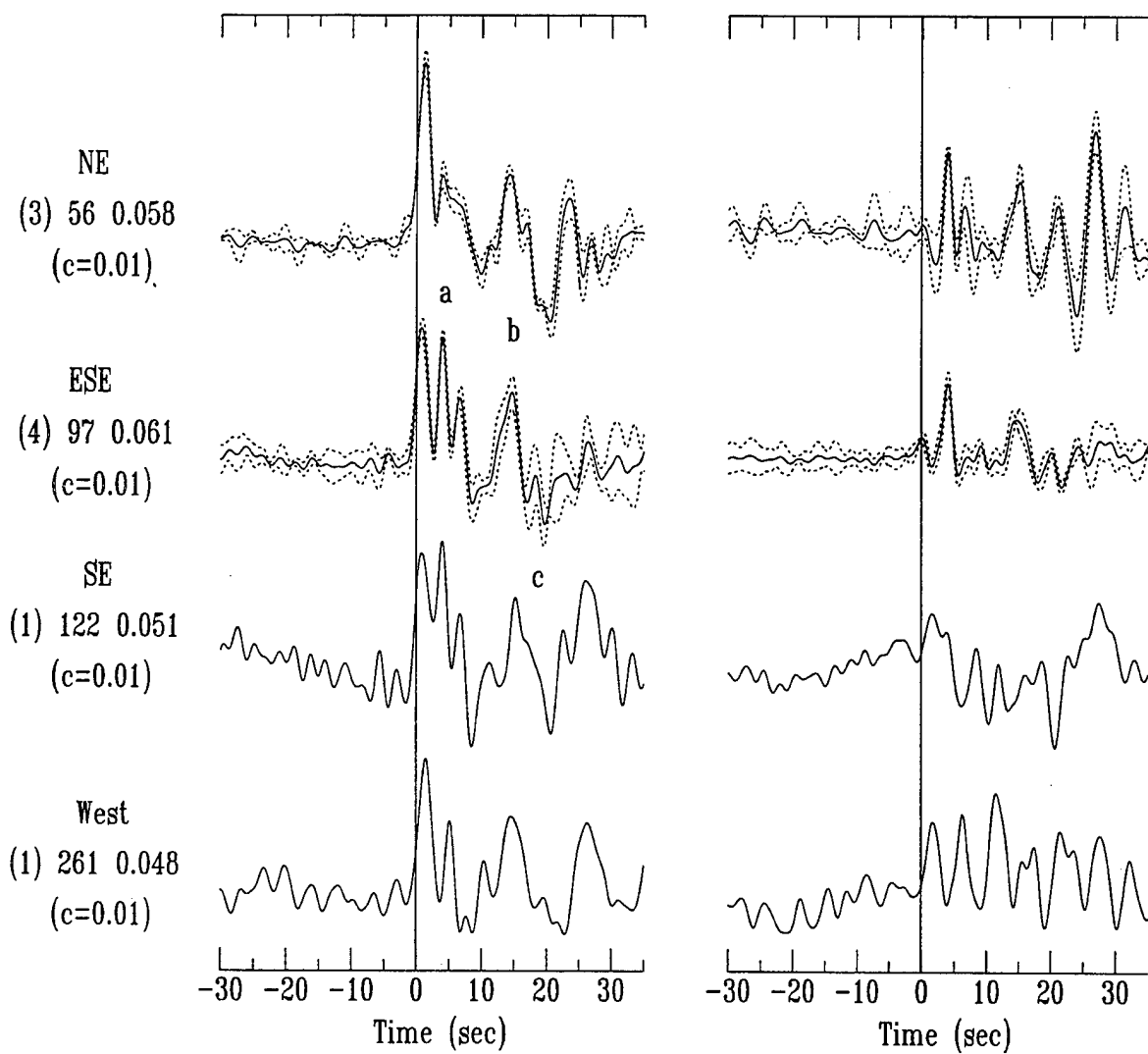
FIGURE A12

FIGURE A13

51
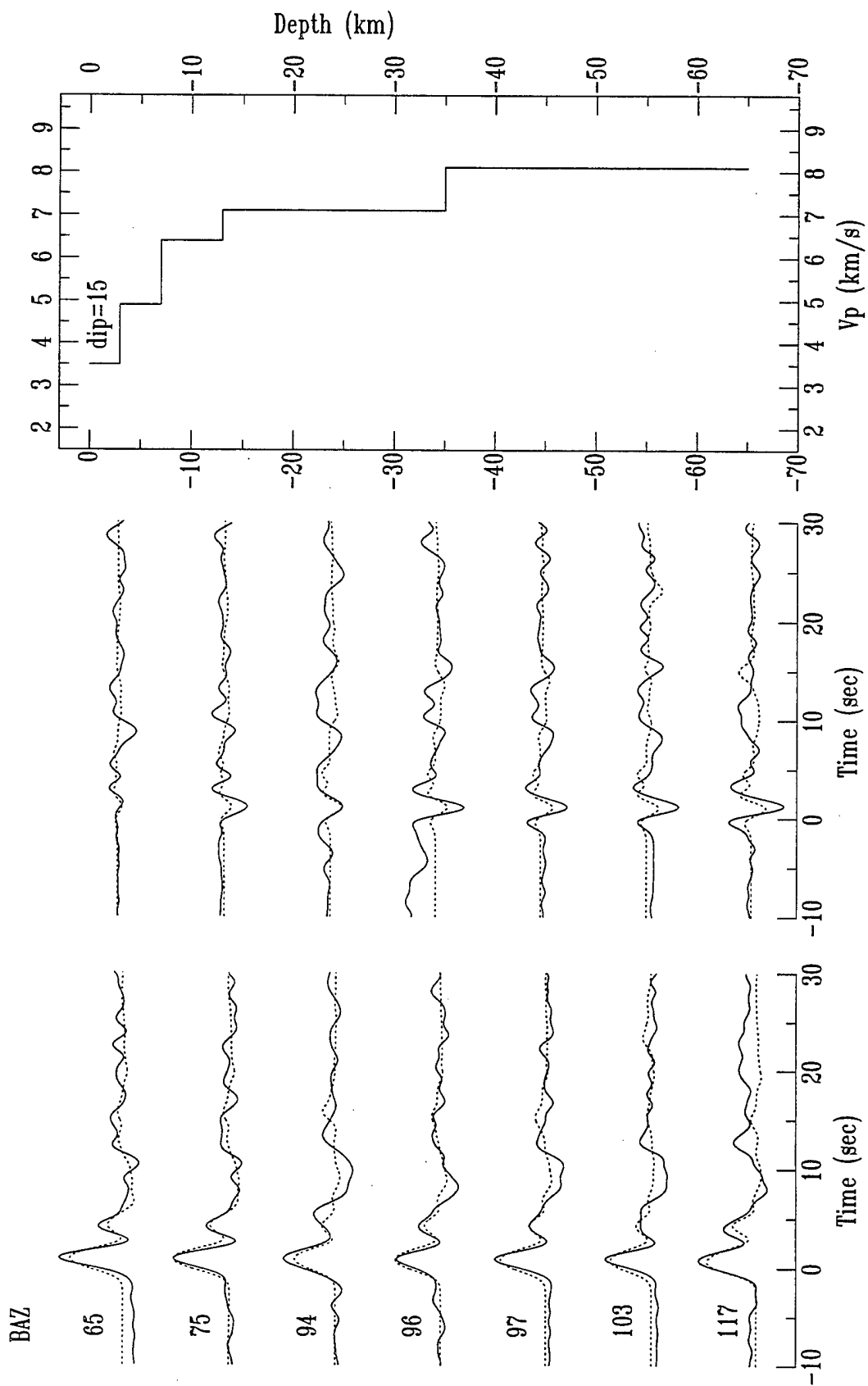
FIGURE A14

The Caspian Seismograph Network

S. Mangino[1], M. Roshkov[2], V. Kiseleivich[2], B. Karryev[3], T. Ashirov[3],
A. Gasanov[4], S. Agamirzoev[4], J. McKenzie[1], J. Cipar[5] and K. Priestley[1]

[1]Bullard Laboratory, University of Cambridge, Cambridge, U.K., [2]SYNAPSE Science
Center, Moscow, Russia, [3]Turkminia Acadamy of Science, Ashkabad, Turkmenia,
[4]GEOSEISM, Baku, Azerbaijan, [5]Phillips Laboratory, Hanscome AFB, Ma., U.S.A.

Introduction

This report covers the installation, operation, and calibration of the Caspian seismic network.

Network Operation and Instrumentation

For both logistical and security reasons, each Caspian Seismic Network (CSN) station was installed at an existing seismic station of the Scientific and Information Bureau of the Turkmenistan Academy of Science or Geoseism in Azerbaijan. The stations are permanently occupied by a station–keeper and family which therefore contribute to the noise generated at each site. The locations of the stations are shown in Figure 1 and the installation parameters are given in Table 1. The five initial stations installed during May and June, 1993 were located at Krasnovodsk (KRF), Nebit Dag (NBD), Kizyl Atrek (KAT), Lenkoran (LNK) and Baku (BAK). In December, 1993, a station was insta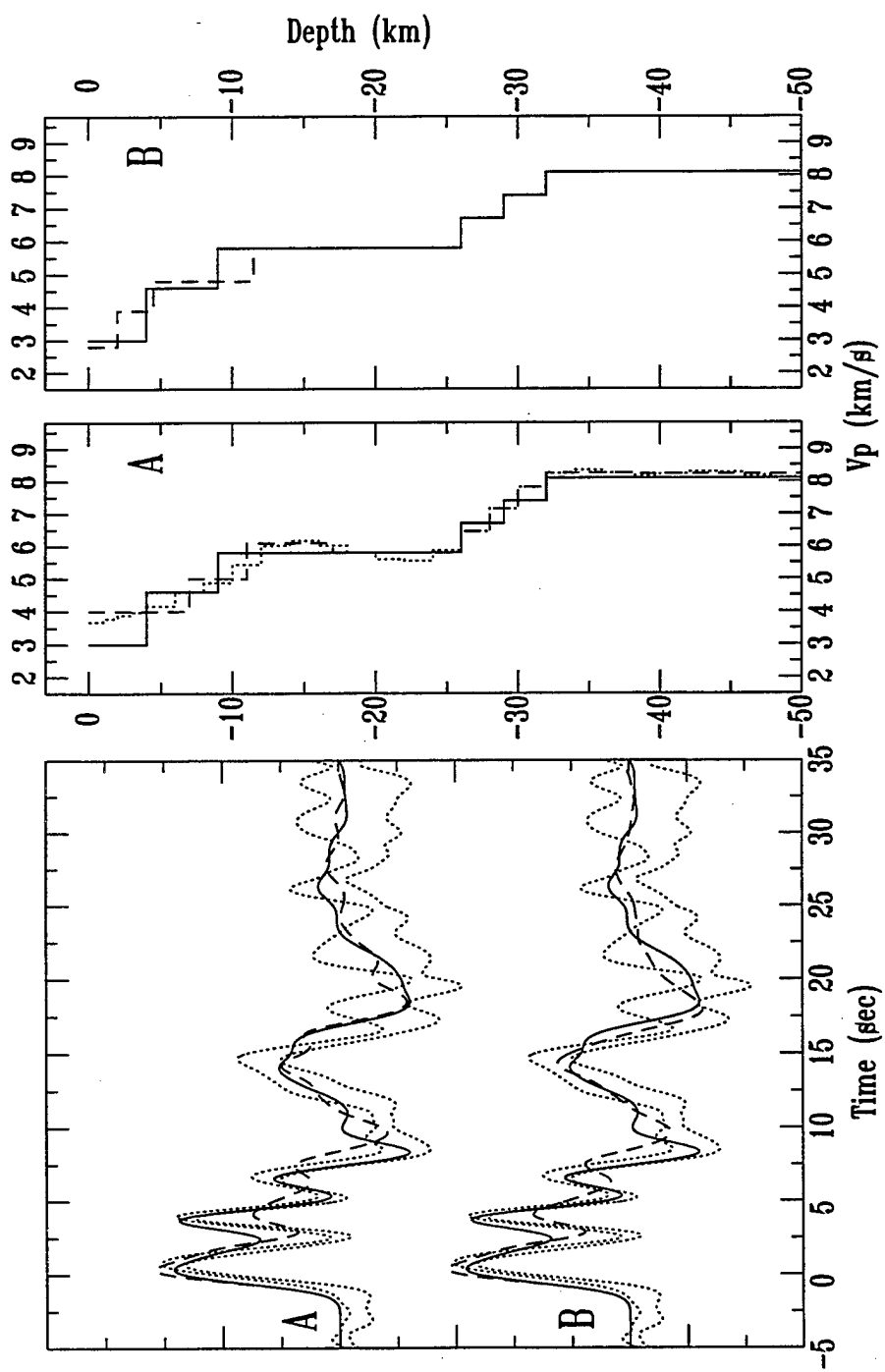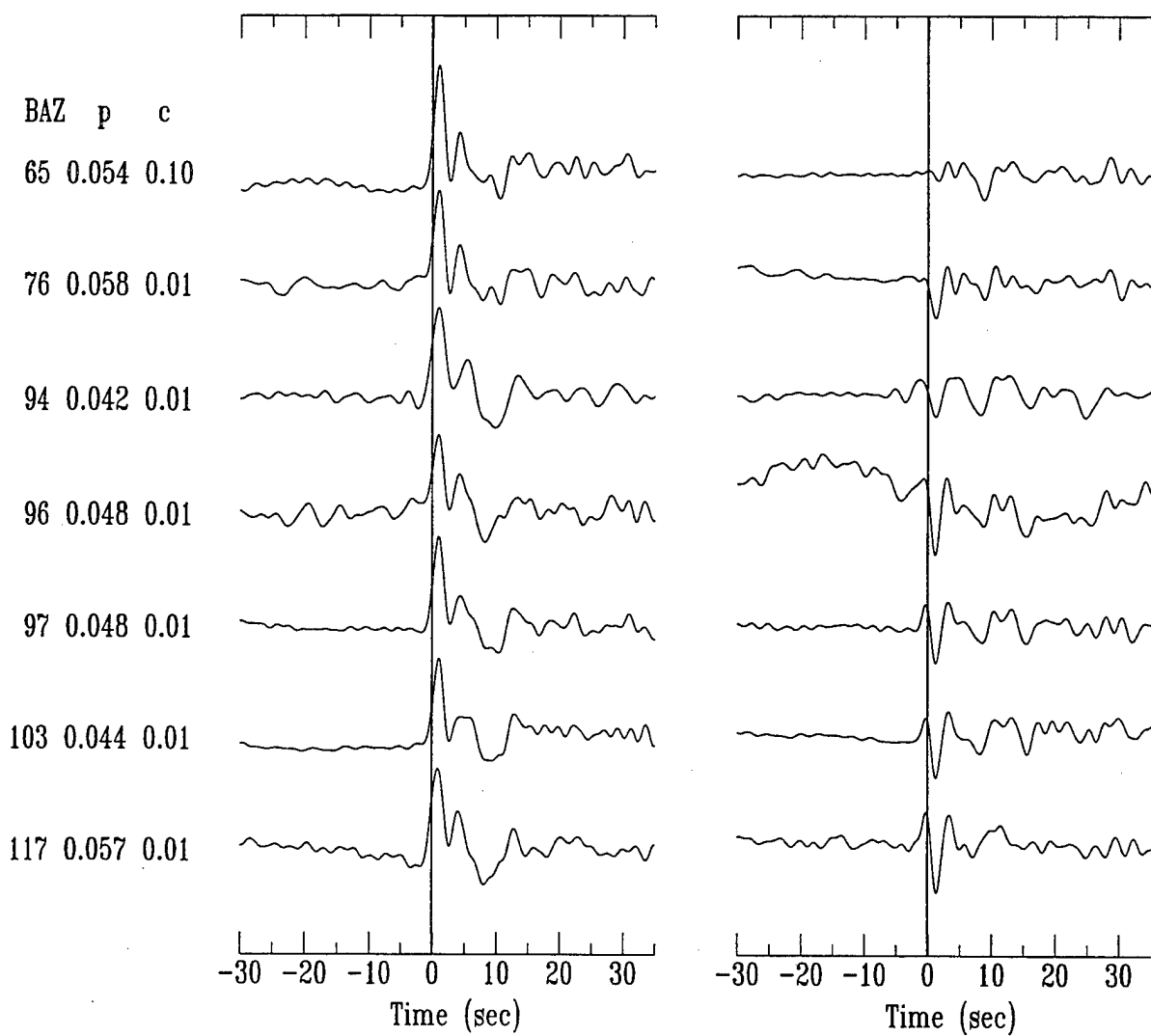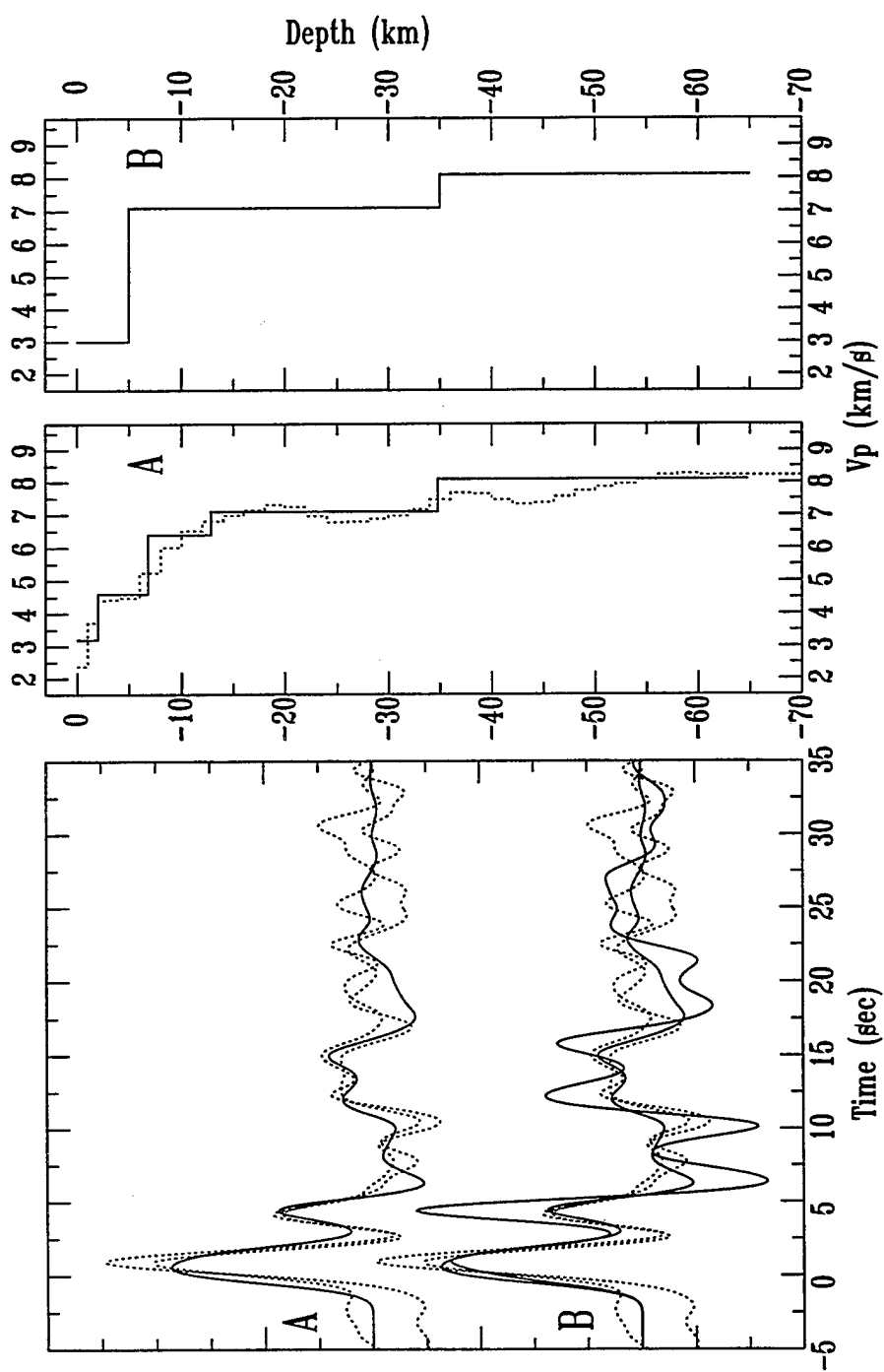lled at Dana Tag (DTA). In June, 1994 the seismic equipment from BAK was moved to Shemaha (SHE); LNK and SHE were closed in March, 1995.

Station locations in Table 1 were determined using a Magellan hand–held GPS receiver. KRF and DTA had GPS clocks that recorded both time and position information. The average of 151 GPS positions recorded by the GPS clock at KRF is within 42 m of the position obtained from the hand–held receiver. The average of 113 positions at DTA is within 82 m of the Magellan position. Based on these measurements, a conservative estimate of the station location error is of the order of 100 m.

The instrumentation at each station consisted of a Refraction Technology 72a–02 16–bit data logger with an external hard disk, Omega or GPS timing, and either a Guralp CMG–3T broadband (BB) feedback seismometer or a set of Teledyne Geotech SL–210/220 long period (15s free period) (LP) pendulum seismometers. To correct for drift of the BB seismometers, a re–centering device was also installed which issued centering commands to the CMG–3T. The LP seismometers were manually re–centered by the station operators; however, there are a number of time periods when the LP seismometers drifted to end–stops. All stations

were operated using local mains power and were equipped with battery backup for external power failure. Unfortunately, long power outages of up to several weeks' duration were a frequent occurrence especially in Azerbaijan and the batteries were insufficient to operate the station during these times.

The seismometers were installed on concrete piers inside an insulated enclosure and inside concrete vaults in a sub–basement of the station house (KRF, NBD, KAT, LNK, SHE, KAR) or in a surface vault adjacent to the station house (DTA, BAK). Data logger channels 1, 2 and 3 record the vertical, north–south and east–west components of ground motion, respectively. A positive signal corresponds to ground motion up for the vertical, and ground motion in the azimuth stipulated in Table 1 for the horizontal component. The horizontal components were aligned to magnetic north using a Brunton compass. Component azimuths in Table 1 include the correction from magnetic to geographic north. Declination corrections were taken from U.S. Defense Mapping Agency maps of the Caspian region. However from an analysis of teleseismic P–wave backazimuth anomalies, Mangino (1997) determined that the horizontal components at KRF were misaligned by approximately 17°. The corrected orientations of the KRF north–south and east–west components relative to geographic north are N201.8°E and N291.8°E, respectively.

During most of the lifetime of the network, the data loggers were programmed to record one data stream consisting of three components of ground motion in continuous, one–hour record blocks at a sample rate of 10 samples/sec (sps). At some stations the sample rate was temporarily set to 5 sps, and at station DTA, a second 50 sps triggered data stream was used for a limited time to record regional events. Table 2 lists the time periods when a given station's sample rate differed from the standard rate of 10 sps. At approximately two month intervals, each site was visited and the data transferred from disk to either Exabyte or DAT tape and returned to the SYNAPSE Science Center/IRIS Moscow Data Center where the data was inspected; duplicate copies were then made and sent to Cambridge. Instruments at each station were calibrated with a step function during each station visit. A more complete calibration using a pseudo–random binary input (Berger et al., 1979) and a sinusoidal input was made annually. Analysis of the step calibrations indicates that the seismograph characteristics did not deviate significantly during the deployment. Figure 2 compares the frequency response curves for the CMG–3T and SL210/220 sensors used in the CSN with the response of the STS–1 at the IRIS seismic station ABKT about 300 km to the east of the Caspian Sea.

Throughout the duration of this experiment, several changes were made to the network configuration. In October, 1993 the BB seismometer at KAT was returned to England to repair a faulty mass–locking mechanism. At that time the BB seismometer initially installed at NBD was permanently moved to KAT. In December, 1993 the repaired BB seismometer was installed at DTA and a set of LP seismometers was installed at NBD. BAK proved to

have very high ground noise and extremely unreliable power, and as a consequence, was closed in June 1994. The BAK equipment was re-installed at SHE, and although several Omega clock errors occurred and thus the timing at SHE is unreliable, the waveform data is still usable. The unstable political climate in Azerbaijan caused by the war with Armenia and the war in nearby Chechnya made servicing of the Azerbaijan stations difficult throughout the experiment and forced us to close LNK and SHE in March, 1995.

Calibration

CSN stations were calibrated with a step function (+0.3 volts BB, +2.0 volts LP) during station visits. We also calibrated each station in June, 1994 with a sinusoidal input and a pseudo-random binary input (+0.3 volts BB, +2.5 volts LP). Calibrations were made using an external voltage source applied to the seismometer calibration circuit.

Sensitivity

Sinusoidal calibrations were used to determine the sensitivity of each seismometer. Figure 2 shows the sinusoidal calibration output signal recorded by BB station KRF (channels 1-3), as well as the input calibration signal (channel 4). The input acceleration is obtained by dividing the input calibration current by the seismometer coil constant:

$$input\ acceleration = \frac{input\ current}{coil\ constant}\ \left(\frac{m}{s^2}\right).$$

Calibration coil constants for the BB seismometers are listed in Table 3; the nominal value of 0.0125 $A/m/s^2$ specified by Teledyne Geotech was used for each LP seismometer. The input velocity is computed from the input acceleration by dividing by the angular frequency of the input sinusoid:

$$input\ velocity = \frac{input\ acceleration}{angular\ frequency}\ \left(\frac{m}{s}\right).$$

The sensitivity for each channel is obtained by dividing the peak-to-peak sinusoidal output voltage by the input velocity. The peak-to-peak amplitude is measured in the time window unaffected by the longer period response to the onset of the calibration input. Sensitivity for a single channel is expressed as:

$$sensitivity = \frac{peak-to-peak\ Volts}{input\ velocity}\ \left(\frac{V}{m/s}\right).$$

Table 4 provides the sensitivities for each CSN seismometer and were determined using the above procedure. Comparison between these results and those provided by Guralp Systems are within 3.3% on average. The measured sensitivities of the LP seismometers are less than the 90-93 V/m/s specified by Teledyne Geotech. Until more precise LP calibration coil constants are obtained, the LP values represent best estimates of the sensitivity.

Variation of the sensitivity over time

We examined the possibility of variation in the sensitivity with time by comparing the peak amplitudes of the step calibrations performed during each routine station visit to the sensitivities determined by sinusoidal calibration. Individual peak amplitude measurements were made from the step calibrations after windowing the pulses for each channel for a given calibration day. Typically, a series of step calibrations was made over a 10–15 minute period during each routine station visit, and these individual measurements were averaged. Figure 3 shows the peak amplitude step calibration observations verses time for stations KRF and LNK. Tables 5–6 give the average peak amplitudes for each station. The KRF peak amplitudes are relatively constant over time, while at LNK, the east–west component shows some variability compared to the other two channels. LNK was often found to be not operational upon arrival for a routine station visit. LNK down–time was always due to local power failure, and some of these variations could be an artifact of system power–up and seismometer mass re–centering, rather than actual changes in the sensitivity. The averaged value of all step calibrations for each component is considered more reliable than any individual measurement. Sinusoidal calibration sensitivities are compared to the averaged peak amplitudes of the step calibrations by computing the ratio between the vertical and horizontal components:

$$\frac{S(Z)}{S(N)} \equiv \frac{A(Z)C(Z)}{A(N)C(N)} \quad \text{and} \quad \frac{S(N)}{S(E)} \equiv \frac{A(N)C(N)}{A(E)C(E)}.$$

where S represents the sinusoidal calibration sensitivity, A is the average peak amplitude, C is the calibration coil constant, and Z, N and E correspond to channels 1, 2 and 3, respectively. We find that the ratios between the sinusoidal and the BB step calibrations differ by approximately 1.3% and conclude that the BB relative sensitivity estimates are consistent over time. The ratios between the LP sinusoidal and step calibrations differ by approximately 7% for SHE, 6% for BAK and 35% for NBD. The source of the variation between estimates at NBD is not known. Except for NBD, the LP sensitivities determined by sinusoidal calibration are also consistent with the sensitivity estimates obtained from the step calibrations.

Transfer Functions

Figure 4 shows the BB and LP amplitude versus frequency response curves computed from a pole–zero model for each type of seismometer. The BB model was obtained from the CMG–3T manual provided by Guralp Systems, and the LP model was determined analytically by considering the response of a mass on a spring. These curves show that the feedback seismometers have a nearly flat amplitude response in velocity over a wide frequency range, while the response of the LP seismometer is peaked over a relatively smaller range. Figure 5 shows an example of a synthetic fit between a typical BB step response and the synthetic step response using the pole–zero model provided by Guralp Systems. Figure 6 shows individual

LP synthetic fits to the data. Tables 7-8 provide the pole–zero models used in Figure 5 and Figure 6. In both figures, the synthetic fits match the observed step response, indicating that the corresponding pole–zero models approximate the response of the seismometer.

Random Binary Calibration

To verify the instrument response, a pole–zero model was also determined for each seismometer using a pseudo–random binary input (PSRB) calibration signal. Figure 7 shows an example of a short section of the PSRB calibrating signal. The advantage of using a PSRB input is that it has a flat power spectrum (up to a pre–defined cut–off frequency) distributed over a wide range of frequencies. In practice, the input PSRB signal was recorded on channel 4 and the seismometer output was recorded on channels 1–3 for $\sim$1 hour at 1000sps. The PSRB signal consists of constant amplitude boxcar functions with a variable width. The width of each individual step function is a random function of a pre–set time interval "τ", and the PSRB period was set so that the first spectral hole occurs at a frequency higher than that of the dominant poles of the LP and BB seismometers.

Transfer functions from the PSRB calibration signal are determined numerically from the cross spectrum between the PSRB input "i" and the output "o" (Berger et al., 1979). To limit the effects of noise, the coherent output response (Z_{obs}) is expressed as:

$$Z_{obs} = \frac{io^*}{ii^*},$$

where the $*$ denotes complex conjugation. The cross–spectra between the input and output are expressed as:

$$\gamma = \frac{(io^*)\ (oi^*)}{(ii^*)\ (oo^*)}.$$

In the above expression, γ is frequency dependent and can also be thought of as the covariance between two complex rational functions normalized by the variance of both functions. The transfer function is estimated from the cross–spectra by an iterative optimization using Powell's method. The misfit χ that is minimized is proportional to the difference between Z_{obs} and the prior estimate of the response (Z_{calc}), and is expressed as:

$$\chi = \left[\frac{1}{1.1 - \gamma}\right]^2 [log(\omega + \delta\omega) - log(\omega)]^2 \, [log\,(|\,Z_{obs}|\,) - log\,(|\,Z_{calc}|\,)]^2 \,,$$

where $\delta\omega$ is the frequency step between points in the Fourier transform. In this equation there are three terms enclosed by square brackets. If γ in the first term is unity, the energy is coherent and this observation will be weighted greater than if γ is less than one. The second term weights the lower frequencies more than the higher frequencies the same way that a log–log plot does. The third term is proportional to the relative difference between the two amplitudes at each frequency point rather than the absolute difference. This scheme weights amplitudes in the same way as a log–log plot. Figure 8 shows a sample of the

first few minutes of a typical PSRB output signal, the predicted output signal obtained by convolving the input (channel four) by the PSRB derived pole zero model and the predicted output signal obtained by convolving the input by the model given in Table 8. There is no significant difference in the fits to the data. This was found to be the case for all BB seismometers and the model given in Table 7 can be used for all CSN BB stations. This was not found to be the case for the LP seismometers. The PSRB derived pole–zero models for the LP seismometers are given in Table 9.

Reference

Berger J., D. Agnew, R. Parker & W. Farrell, 1979. Seismic system calibration: 2 Cross–spectral calibration using random binary signals, *Bull. Seism. Soc. Am.*, **69**, 271–288.

Mangino, S.G., 1997. Eurasian crust and upper mantle structure, *Ph.D. Thesis*, University of Cambridge, England.

Station code	Latitude Longitude Elevation	Azimuth N-S E-W	DAS No. Clock Sensor	Notes
KRF	40.0063° N 52.9575° E +4 m	N184.8°E N274.8°E	580 GPS CMG-3T	Installed 5/93 CMG-357. The sensors are located in a sub-basement vault that overlies bedrock, ~3 km west of the Caspian Sea along the edge of the Krasnovodsk Plateau, Turkmenistan.
NBD	39.5077° N 54.3872° E +18 m	N4.6°E N94.6°E	458 Ω CMG-3T/ LP	Installed 5/93 CMG-360; 12/93-present: LPZ=186 LPN=50, LPE=48; The sensors are located in a sub-basement vault that overlies unconsolidated sand and clay in the West Turkmenian Lowlands.
KAT	37.6697° N 54.7766° E +84 m	N4.1°E N94.1°E	454 Ω CMG-3T	Installed 5/93 CMG-363; 12/93-present CMG-360 The sensors are located in a sub-basement vault that overlies alluvium in the West Turkmenian Lowlands, ~20 km north of the Alborz Mountains.
LNK	38.7100° N 48.7788° E -2 m	N4.4°E N94.4°E	450 Ω CMG-3T	Installed 6/93 CMG-362. The sensors are located in a surface vault near the foothills of the Talesh Mtns.,~10 km west of the Caspian Sea, Azerbaijan.
BAK	40.5813° N 49.9869° E -27 m	N4.8°E N94.8°E	456 Ω LP	Installed 5/93 LPZ=77 (ch2), LPN=43, LPE= 39 (ch3). From 93281: LPZ=(ch1) and LPN=(ch2). Removed 6/94; Surface vault over unconsolidated sands and clay, ~1 km west of Caspian Sea on the Apsheron Peninsula, Azerbaijan.
DTA	39.0755° N 55.1663° E +319 m	N4.5°E N94.5°E	582 GPS CMG-3T	Installed 12/93 CMG-363; The sensors are located in surface vault that overlies silt stone and shale in the Kopet Dag Mtns., Turkmenistan.
SHE	40.6433° N 48.6394° E +829 m	N184.8°E N274.8°E	456 Ω LP	Installed 6/94: LPZ=77, LPN=43, LPE=39. Operational until 1/95; Sensors located in surface vault that overlies carbonates in the Caucasus Mtns. Azerbaijan.
ABKT	37.9304° N 58.1189° E +678 m	N0°E N90°E	IRIS GPS STS-1	Operated and installed by IRIS 4/93; The sensors are located in a tunnel within carbonates and silt-stone in the Kopet Dag Mtns., Turkmenistan.
KAR	38.4375°N 56.2709°E +304 m	N184.3°E N274.3°E	456 Ω CMG-3T	Installed 6/95 CMG-362; The sensors are located in a subsurface vault in the Kopet Dag Mtns., Turkmenistan.

Table 1: CSN station locations and instrument parameters.

| Station | On | Off | Sample |
code	m/d/yr	m/d/yr	rate
BAK	07/02/93 — 07/05/93		5
BAK	09/18/93 — 10/01/93		5
DTA	10/05/94 — 10/30/94		50
NBD	12/14/93 — 06/20/94		5
LNK	06/03/93 — 08/09/93		5
LNK	09/07/93 — 09/28/93		5

Table 2: Time periods when CSN station sample rates differed from the standard 10 sps. At DTA a sample rate of 50 sps was only used in trigger mode on data stream 2.

Sensor	Vertical	North–South	East–West
357	0.0310	0.0350	0.0377
360	0.0318	0.0362	0.0366
362	0.03495	0.03329	0.03497
363	0.0318	0.03719	0.03456

Table 3: Calibration coil constants for the BB seismometers specified in units of $A/m/s^2$.

Sensor	Vertical	North–South	East–West
BB 357	1930.21	2212.85	2362.26
BB 360	1946.49	1980.18	1839.03
BB 362	1995.14	2325.08	2288.29
BB 363	1935.86	1958.09	1939.22
LP SHE	47.58	61.75	67.83
LP NBD	20.64	38.87	62.97
LP BAK	55.34	62.30	65.77

Table 4: CSN sensor sensitivities in units of V/m/s determined from the sinusoidal calibration.

Station, sensor	Vertical	North–South	East–West
KRF 357	2.7825	2.7887	2.7851
NBD 360	2.8283	2.8175	2.8019
KAT 363	2.7795	2.3695	2.5288
KAT 360	2.7673	2.7507	2.7282
LNK 362	2.4876	2.6890	2.3937
DTA 363	2.6671	2.2919	2.4516
KAR 362	2.4141	2.5854	2.3454

Table 5: Average peak amplitudes of the BB step calibrations up to October 1995.

Station, date	Vertical	North–South	East–West
NBD 93348	0.01948	0.02260	0.02564
NBD 94171	0.01884	0.02009	0.02547
NBD 94232	—	0.02223	—
NBD 94340	—	0.02166	0.02491
NBD 95148	0.02217	0.02164	0.02551
BAK 93280	0.01742	0.01966	0.02077
BAK 93281	0.02108	0.02658	0.02775
SHE 94178	0.01884	0.02621	0.02751
SHE 94224	0.01817	0.02658	0.03115
SHE 94295	—	0.02695	0.03124

Table 6: LP sensor step calibration peak amplitudes up to October 1995. The NBD calibrations for 94171 are scaled assuming a linear relationship from a 2.5 V input to a 2.0 V input. The dashed line indicates that the calibrations were unusable.

	Real	Imaginary
Z	0.0	0.0
	0.0	0.0
	945.6201	0.0
P	−0.4442215E–01	±0.4442215E–01
	−5.057968E+02	±1.935223E+02
C	−310.1713	

Table 7: CMG–3T (BB) sensor poles (P) and zeros (Z) model. The constant (C) is normalised at 1.0 Hz and the units are in radians/sec.

61

	Real, Imaginary	Real, Imaginary	Real, Imaginary
	BAK Vertical	BAK North–South	BAK East–West
Z	0.0 0.0	0.0 0.0	0.0 0.0
P	−0.2100 ±0.3500	−0.2900 ±0.33550	−0.2450 ±0.3300
C	6.20707561	6.2787901	6.27546443
	NBD Vertical	NBD North–South	NBD East–West
Z	0.0 0.0	0.0 0.0	0.0 0.0
P	−0.3100 ±0.3490	−0.2290 ±0.4990	−0.2380 ±0.3620
C	6.2790946	6.2518829	6.2714319
	SHE Vertical	SHE North–South	SHE East–West
Z	0.0 0.0	0.0 0.0	0.0 0.0
P	−0.2400 ±0.3800	−0.3020 ±0.3320	−0.2440 ±0.3138
C	6.2694428	6.2802442	6.2770360

Table 8: SL210–220 (LP) sensor poles (P) and zeros (Z) models estimated from the step calibrations. The constant (C) is normalised at 1.0 Hz and the units are in radians/sec.

	Real, Imaginary	Real, Imaginary	Real, Imaginary
	BAK Vertical	BAK North-South	BAK East-West
Z	0.0 0.0	0.0 0.0	0.0 0.0
P	-0.2252958 ±0.3422979	-0.2956192 ±0.3250473	-0.2523122 ±0.3603323
C	6.2726688	6.2803577	6.2727244
	NBD Vertical	NBD North-South	NBD East-West
Z	0.0 0.0	0.0 0.0	0.0 0.0
P	-0.3920840 ±0.5465154	-0.2268839 ±0.6666290	-0.2080997 ±0.3595312
C	6.2604924	6.2208417	6.2695550
	SHE Vertical	SHE North-South	SHE East-West
Z	0.0 0.0	0.0 0.0	0.0 0.0
P	-0.3359690 ±0.3859690	-0.2924684 ±0.3148742	-0.2510040 ±0.2927102
C	6.2775812	6.2810929	6.2796247

Table 9: SL210–220 (LP) sensor poles (P) and zeros (Z) models estimated from the PSRB calibration. The constant (C) is normalised to 1.0 Hz and the units are in radians/sec.
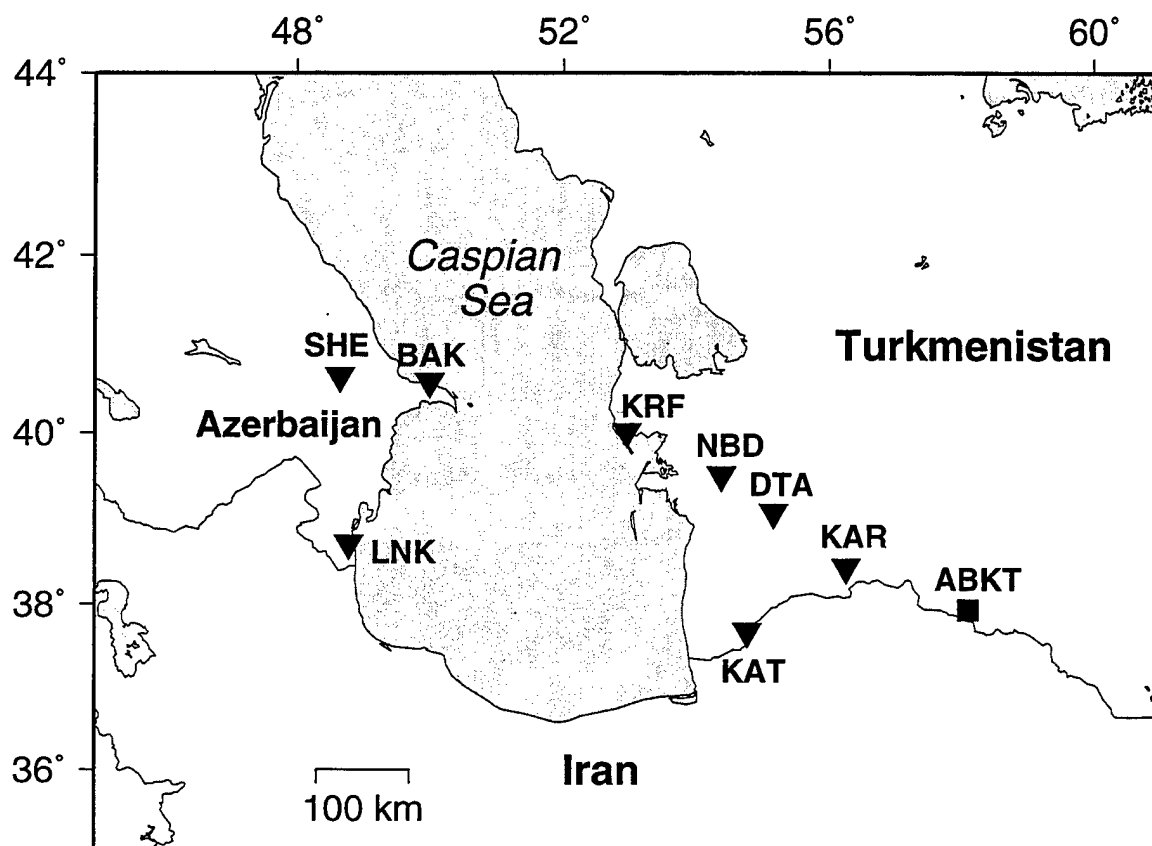
Figure 1: Location map of the Caspian Seismograph Network (solid triangles). In Turkmenistan the stations were located near Krasnovodsk (**KRF**), Nebit Dag (**NBD**), Kizyl Atrek (**KAT**), Dana Tag (**DTA**) and Kala Kara (**KAR**). In Azerbaijan the stations were located near Lenkoran (**LNK**), Baku (**BAK**) and Shemaha (**SHE**). Also shown is the IRIS station (**ABKT**) Alibek, Turkmenistan.
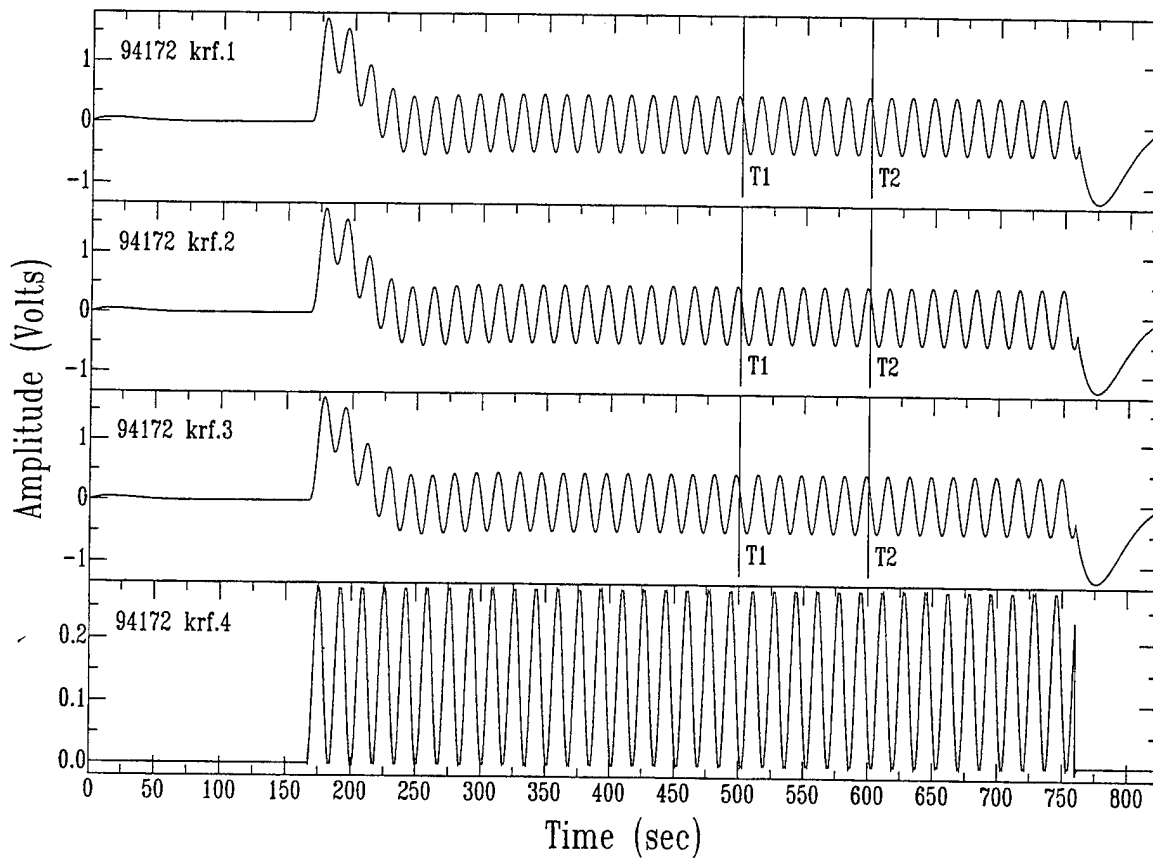
Figure 2: Sinusoidal calibration output (channels 1–3) and the input signal (channel 4) recorded by BB station KRF. Peak-to-peak amplitude is measured between $t1$ and $t2$.
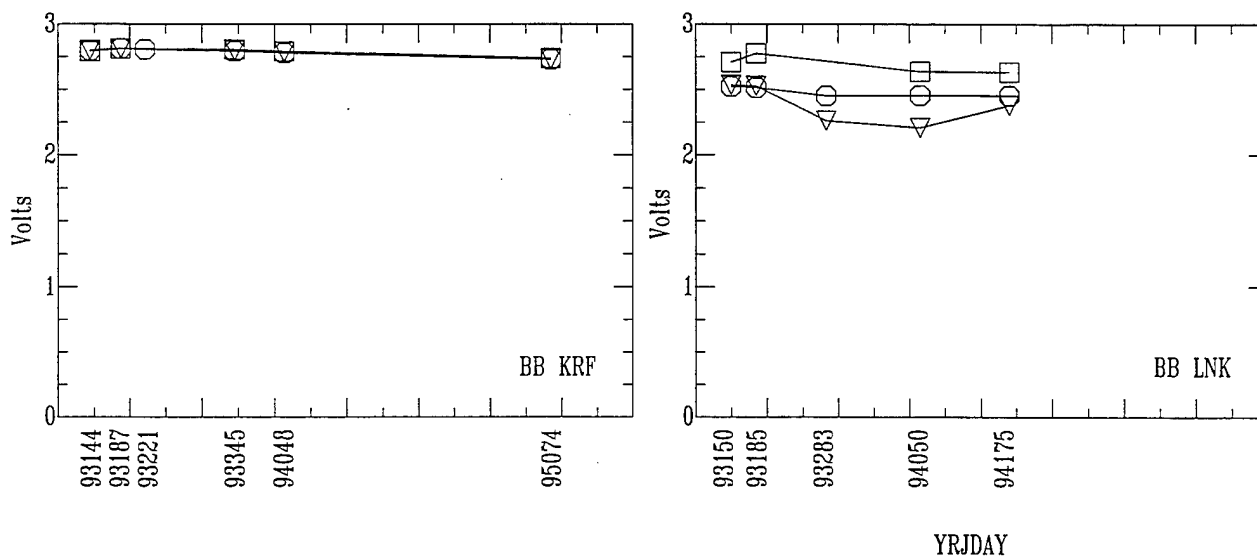
Figure 3: Observed peak amplitudes of the step calibration over time for BB stations KRF (left) and LNK (right). Open circles, squares and triangles represent the vertical, north–south and east–west components of each station, respectively The time axis are specified by year and Julian day (i.e. 93144 corresponds to year 1993, Julian day 144).

64
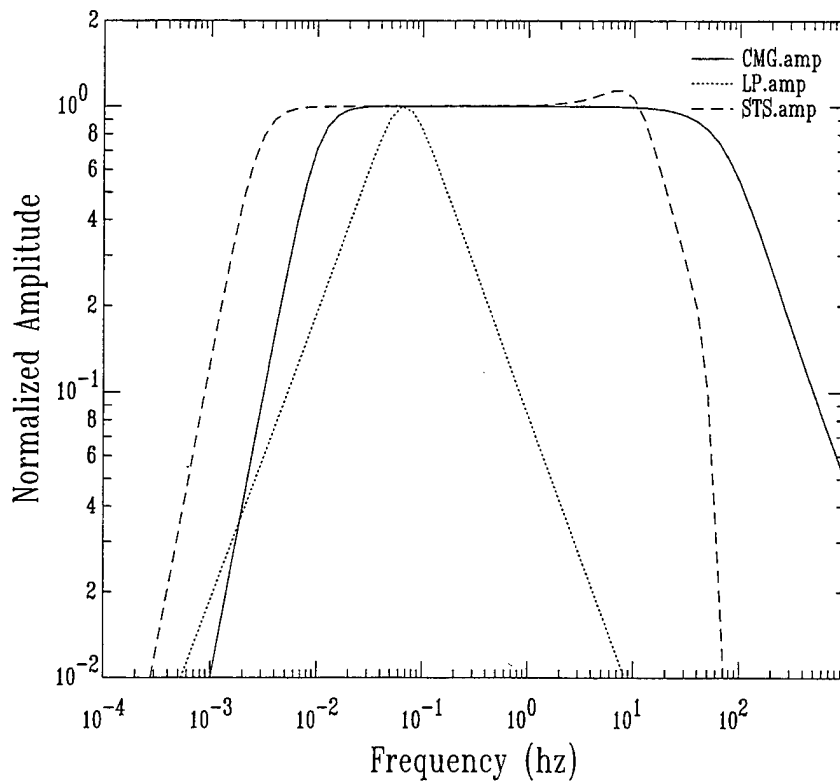
Figure 4: Amplitude versus frequency response curves for the CSN stations equipped with either Guralp CMG–3T broadband sensors (CMG.amp) or Teledyne Geotech SL210–220 long period sensors (LP.amp). The response curve of the nearby IRIS station ABKT equipped with with Streckeisen STS–1 sensors (STS.amp) is also shown for comparison.
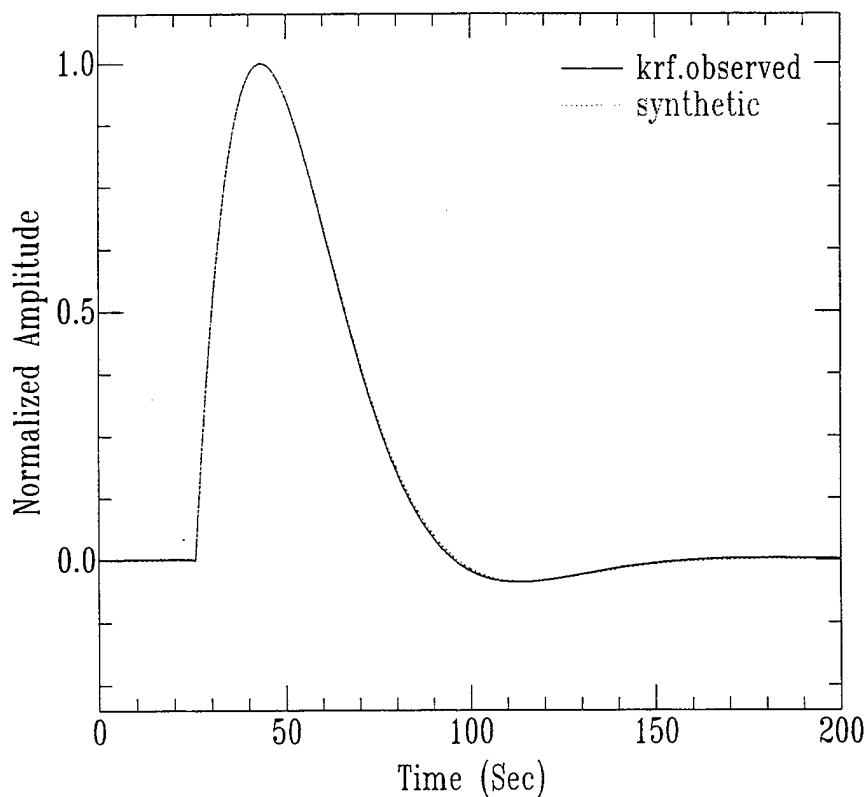
Figure 5: Synthetic BB step response compared to an observed step calibration response of BB station KRF.

65
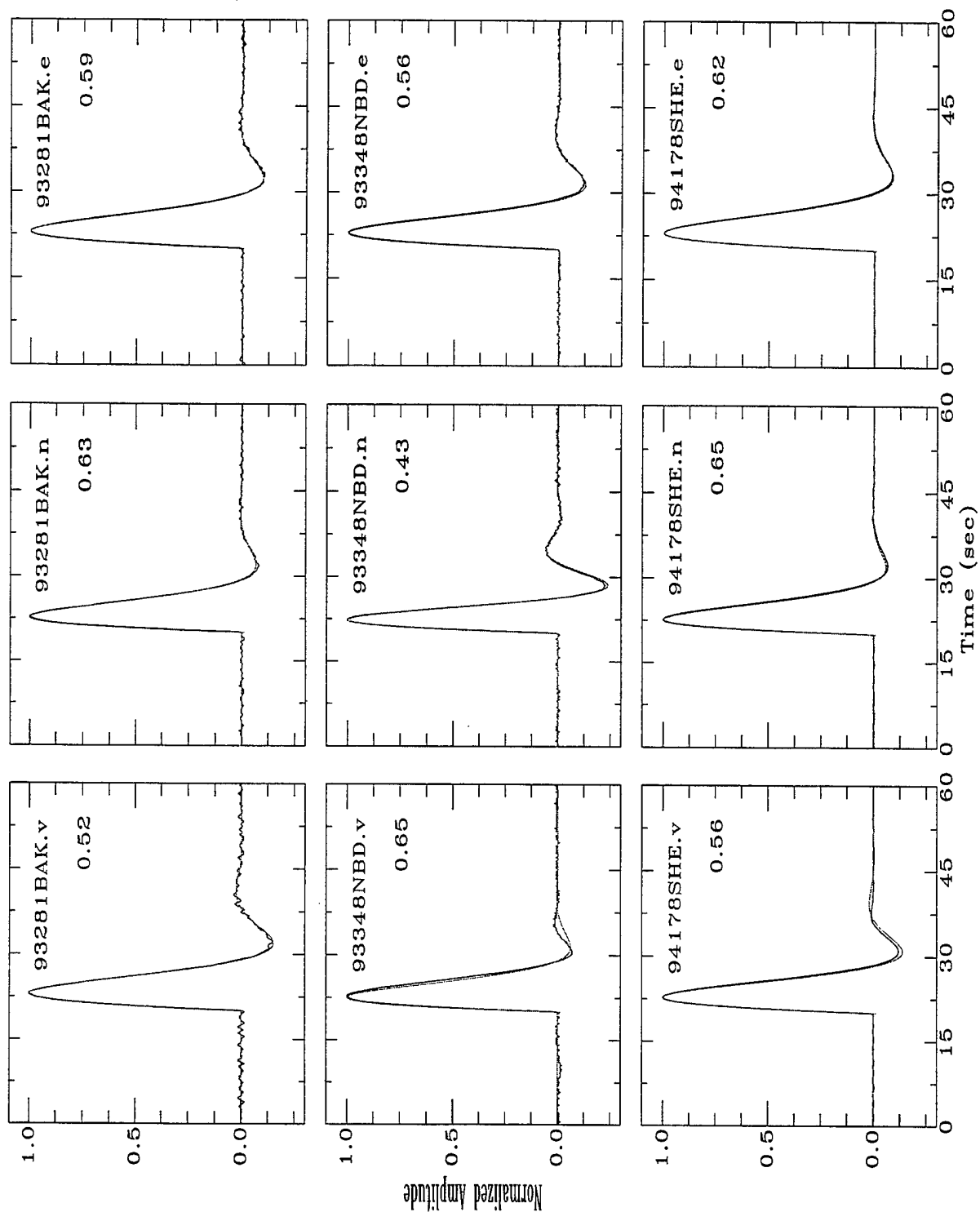
Figure 6: LP observed and synthetic (red) step calibration responses using the pole–zero models given in Table 8. Each filename is specified by year, Julian day, station name and component. Sensor damping is given beneath each filename.

66
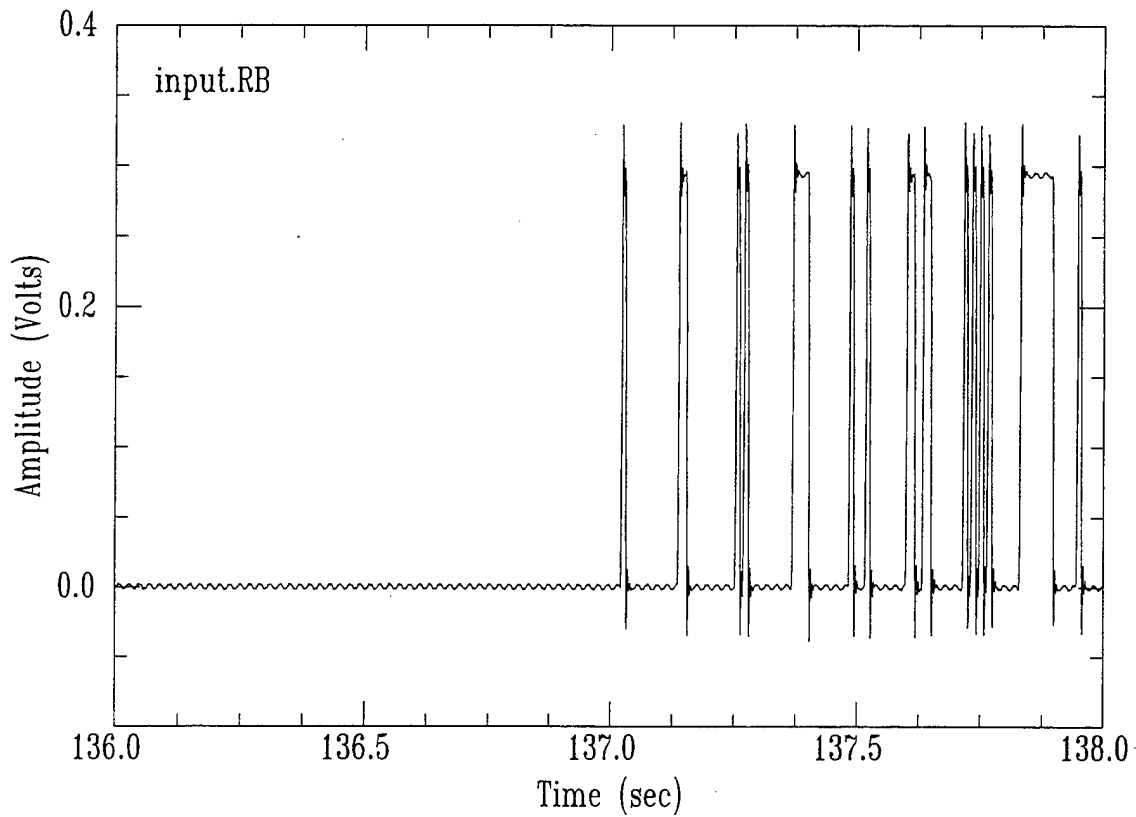
Figure 7: Sample input PSRB calibration signal.
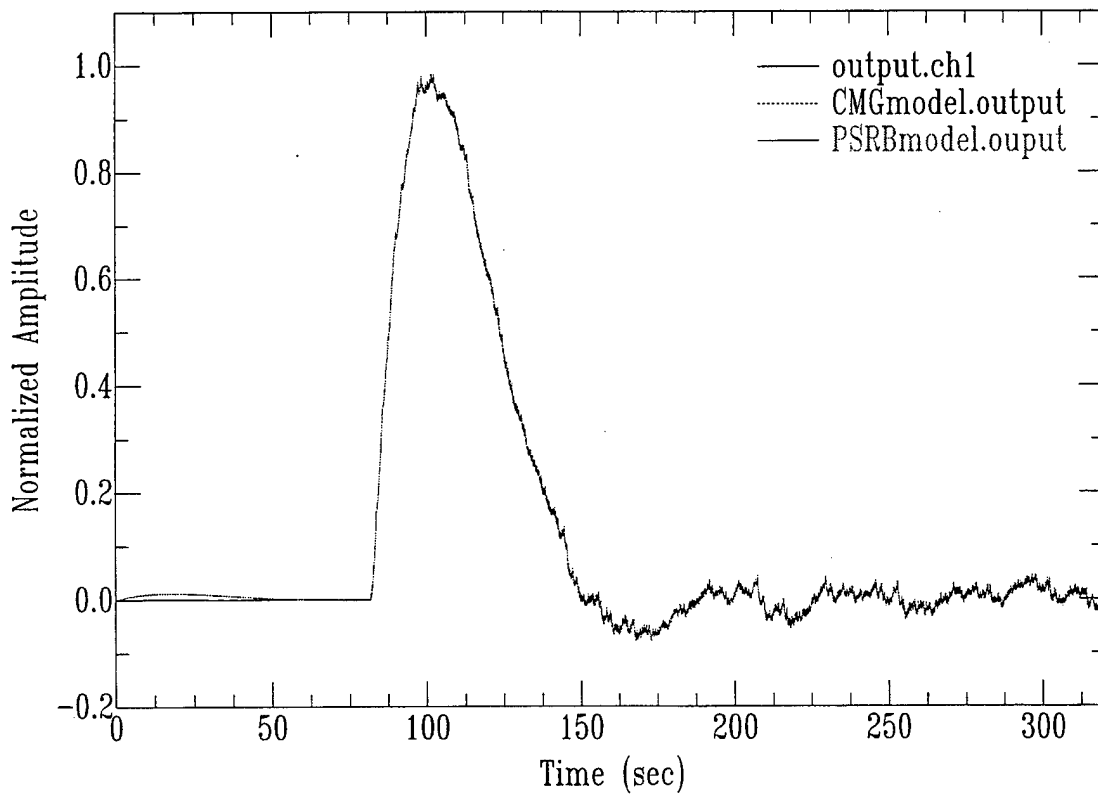
Figure 8: The first few minutes of a PSRB output signal recorded by BB sensor 363 compared to synthetic output obtained by convolving the pole–zero model obtained from the random binary calibration analysis (PSRBmodel.output). Also shown is the synthetic output obtained by convolving the pole–zero model given in Table 7 (CMGmodel.output).

67

Modeling anomalous surface–wave propagation across the Southern Caspian Basin

Keith Priestley, Howard Patton, and Craig Schultz

Abstract

The crust of the south Caspian basin consists of 15–25 km of low velocity, highly attenuating sediment overlying high velocity crystalline crust. The Moho depth beneath the basin is about 30 km as compared to about 50 km in the surrounding region. Preliminary modeling of the phase velocity curves shows that the thick sediments in the south Caspian basin are also underlain by a 30–35 km thick crystalline crust and not by typical oceanic crust. This analysis also suggests that if the effect of the over-pressuring of the sediments is to reduce Poissons' ratio, the over–pressured sediments observed to ∼5 km do not persist to great depths. It has been known since the 1960's that the south Caspian basin blocks the regional phase Lg. Intermediate frequency (0.02–0.04 Hz) fundamental–mode Rayleigh waves propagating across the basin are also severely attenuated, but the low frequency surface waves are largely unaffected. This attenuation is observed along both east–to–west and west–to–east great circle paths across the basin, and therefore it cannot be related to a seismograph site effect. We have modeled the response of surface waves in an idealized rendition of the south Caspian basin model using a hybrid normal–mode/2–D finite difference approach. To gain insight into the features of the basin which cause the anomalous surface wave propagation, we have varied parameters of the basin model and computed synthetic record sections to compare with the observed seismograms. We varied the amount of mantle upwarp, the shape of the boundaries, the thickness and shear wave Q of the sediments and mantle, and the depth of the water layer. Of these parameters, the intermediate frequency surface waves are most severely affected by the sediment thickness and shear wave attenuation. Fundamental mode Rayleigh wave phase velocities measured for paths crossing the basin are extremely low.

Introduction

The crust and upper mantle structure of the south Caspian Basin is enigmatic. Early Soviet studies (Gal'perin *et al*, 1962; Neprochnov *et al*, 1968; Rezanov and Chamo, 1969; Neprochnov *et al*, 1970; Yegorkin and Matushkin, 1970) show that the crust of the basin consists of two layers: a thick sedimentary section (15–25 km) with low P–wave velocity (3.5–4.0 km/s) overlying a 12–18 km thick basaltic lower crust. Mangino and Priestley (1998) analyzed receiver functions from teleseismic events recorded on four broadband seismographs of the Caspian Seismic Network (CSN) located on the periphery of the basin (Fig. 1) to determine the crustal structure beneath these sites and compared these models with the crustal structure beneath the IRIS seismograph station at ABKT. This study showed that the crust in Turkmenia along the trend of the Apshceron–Balkhan Sill — Kopet Dag Mountains (Fig. 1 – KRF, NBD, and ABKT) is 50 km thick. In the southwestern part of the Caspian basin (LNK – Fig. 1) the 33 km thick crust consists of a 13 km thick sedimentary section lying on a high velocity ($V_p \sim 7.1$ km s^{-1}) lower crustal section. In the southeastern part of the basin (KAT – Fig. 1) the crust is 30 km thick and consists of a 10 km thick sedimentary section overlying a 20 km thick low velocity ($V_p \sim 5.8$ km s^{-1}) crystalline crust. Mangino and Priestley (1998) combined the receiver function models with simplified velocity models from the previous Russian Deep Seismic Sounding (DSS) results to form a $\sim$1800 km long ESE–WNW trending crustal cross–section across the Kura Depression, the south Caspian basin and the Kopet Dag Mountains (Fig. 1). The most significant features of this crustal model are the 20 km variation in thickness of Cenozoic sedimentary basin deposits, the absence of a "granitic" ($V_p \sim 5.8$–6.5 km s^{-1}) crustal layer in the central part of the south Caspian basin, and 20 km of crustal thinning beneath the central part of the basin. The Moho beneath the south Caspian basin has a broad arch–like structure whose western boundary is a relatively narrow zone across which the crust thins rapidly ($\sim$20 km thinning over a 100 km zone) and whose eastern boundary has a more gradual change in crustal thickness ($\sim$20 km thinning over a 400 km zone).

Early Soviet studies showed that the regional seismic phase L$_g$ was blocked for propagation paths across the south Caspian basin (Savarensky and Valdner, 1960; Mindeli *et*

al 1965). L_g is sensitive to changes in crustal structure along its propagation path and is absent in seismograms after propagating across ∼150 km of oceanic crust (Press & Ewing, 1952). Other studies have shown the conversion of oceanic S_n to continental L_g (Shurbet, 1964, 1975; Isacks & Stephens, 1975; Seber et al, 1993) or the conversion of continental L_g to oceanic S_n (Shapiro et al, 1996) at the continent–ocean boundary. Kadinsky–Cade et al. (1981) demonstrate that L_g is blocked for paths crossing the south Caspian Basin while propagating efficiently in the surrounding region. On the other hand, S_n propagates efficiently for paths across the south Caspian but inefficiently in the region south and west of the basin. This is clearly demonstrated by the seismograms in Figure 2 for an earthquake near KRF (Fig. 1) on the eastern shoreline of the central Caspian Sea. The crust in the vicinity of the epicenter is about 50 km thick (Mangino and Priestley, 1998). The *Preliminary Determination of Epicenter* depth for the event is 40 km but because focal depths in this area are not well constrained, it is not clear whether the event is in the crust or mantle. Jackson and Priestley (unpublished work) have used waveform modeling to constrain the depth at 45 km, placing it in the crust. The seismogram at LNK on the southwestern coastline shows an impulsive S_n phase but little energy in the L_g group velocity window. The crust between KRF and ABKT has nearly a uniform thickness of 50 km. The seismogram at ABKT shows an S_n and L_g phase typical of that seen on stable continental paths. The seismogram at KAT near the southeastern coastline is anomalous, with a clear S_n phase which is followed by a high amplitude long duration coda.

In this report we examine surface wave propagation across the south Caspian basin. We show that the fundamental mode Rayleigh wave phase velocities are extremely low and that intermediate frequency fundamental mode surface waves propagating across the south Caspian Basin are severely attenuated. We examine the effect of the south Caspian basin structure on the propagation of surface waves by computing finite difference synthetic surface wave seismograms for an idealized rendition of the south Caspian basin crustal model shown in Figure 1. We then vary the crustal and upper mantle parameters of the idealized model and recompute the synthetic seismograms to examine which of these parameters most influence the surface wave propagation across the basin.

Surface wave observations

We have determined interstation phase velocity dispersion curves from teleseismic surface wave trains for the paths KRF–LNK, LNK–KAT, and KAT–KRF (Fig. 1). The phase velocity measurements were made using the constrained least–squares method of Gomberg *et al* (1988) in which the phase velocity measurement is considered as a linear filter estimation problem. If $S_1(\omega)$ is the Fourier transform of the Rayleigh wave seismogram at station 1, then $S_2(\omega)$, the transformed seismogram at station 2 after propagating the distance, Δr, along a great circle path between the stations, is given by

$$S_2(\omega) = F(\omega)S_1(\omega)$$

where ω is the angular frequency. The Earth filter $F(\omega)$ may be written

$$F(\omega) = e^{-\gamma(\omega)\Delta r}e^{ik(\omega)\Delta r} = A(\omega)e^{i\phi(\omega)} \tag{1}$$

where $k(\omega)$ is the wavenumber, $A(\omega)$ describes the amplitude decay, and the phase velocity, $C(\omega)$, is determined from the phase term

$$k(\omega)\Delta r = \frac{\omega}{c(\omega)}\,\Delta r = \phi(\omega)$$

A number of seismogram pairs can be used simultaneously to estimate the phase velocity by taking the least-squares solution. The shape of the phase velocity curve can be constrained by limiting the final group velocity to be within some specified range of the starting model group velocity. The phase term is computed by solving for a correction vector to an initial "assumed" earth model. The data are weighted in the least–squares solution by a weight matrix consisting of a subjective weight factor, which depends on the relative quality of each pair of recordings and on the squared coherence of the data.

The amplitude of high frequency (>0.04 Hz) surface waves for distant earthquakes is small and correlation of these for propagation paths across the south Caspian basin is difficult. In order to extend the dispersion curves to higher frequencies we use the method of Brune, *et al* (1960) to determine the phase velocity from events occurring within and on the boundary of the basin. The phase velocity curve may be obtained for a dispersed wave train provided

71

the initial phase is known. We have chosen the initial phase so that the phase velocities at the lowest frequencies in the single station determination will match the phase velocities of the highest frequencies determined by the interstation method; we then extended the curve to higher frequency, assuming that initial phase is not a function of frequency. Any variation of initial phase as a function of frequency introduces only a small error in phase velocity since the frequency used is high. Poor epicenter location may cause some error in the high frequency part of these data. The uncertainty in the value of phase velocity at any given frequency estimated from this data is probably about 0.03 km/sec.

Figure 3 compares the fundamental mode Rayleigh wave phase velocity dispersion curve for the south Caspian basin with phase velocity curves measured in two other regions of thick sediments, the Bengal Fan in the northern Indian Ocean (Brune and Singh, 1986) and the Barents Sea (Levshin and Berteussen, 1979; Chan and Mitchell, 1985). The sediments in the northern Bay of Bengal are ~22 km thick (Brune *et al*, 1992), similar to the sediment thickness in the south Caspian basin. The Barents Sea is underlain by 10–25 km of sediment lying on a 15-32 km thick crust. This comparison suggests that the thickness of the crystalline crust beneath the sediments in the south Caspian basin is more likely "continental–like" than normal "oceanic–like" crust.

The amplitudes of intermediate frequency surface wave are severely attenuated by propagation across the south Caspian basin. In many cases the recordings on the near side of the basin show well dispersed surface waveforms; however, recordings on the far side of the basin are deficient in intermediate frequency (0.033 – 0.10 Hz) surface waves. There are several instances where the stations LNK and KAT lie along the same great circle path for an earthquake and the anomalous effect of propagation across the basin is particularly clear. Examples of this are shown in Figure 4. The top pair of seismograms in this figure show broadband vertical component seismograms, the middle pair show the waveforms high–passed at 22 mHz, and the bottom pair show the waveforms low–passed at 22 mHz. All waveforms are plotted on the same time scale and each of the pairs are plotted on the same amplitude scale. In each case the upper seismogram of each pair is the input to the basin and the lower is the output. This shows that there is a well–developed surface wave train for the waveform entering the basin, but the intermediate frequency surface waves are

greatly reduced in amplitude in the surface wave train emerging from the far side of the basin only 450 km away. The low frequency surface waves are not significantly affected. Since this effect is observed for both eastward and westward propagating surface waves across the south Caspian basin, the erosion of the intermediate frequency surface waves is not likely to result from a site or instrumental effect.

Surface wave propagation across an idealized south Caspian basin structure

The anomalous surface wave propagation across the south Caspian basin could possibly result from a number of features of the basin. To isolate the features responsible for the anomalous surface wave propagation, we have computed 2–D finite difference seismograms for an idealized model of the south Caspian basin and the surrounding region. We then perturbed features of the 2–D basin model to see how these affect the surface wave propagation. This procedure shows the effect of 2–D structure on the waveform; however, the crustal structure in the south Caspian region shows large 3–D variations, and 3–D propagation effects which are not modeled in our finite difference calculations, likely have a significant effect on the observed waveforms.

The idealized south Caspian basin model used in the finite difference computation is shown in Figure 5 and the parameters of the model are tabulated in Table 1. The background velocity model consists of a one–layer crust over a mantle half–space. The background model is 900 km wide by 450 km deep and is gridded at a 1.05–km interval in both distance and depth. The basin lies between 381 km and 761 km from the left edge of the grid. The basin crustal model consists of a 2.625–km thick water layer, a 14.375–km thick sedimentary layer, and a 16–km thick high velocity lower crustal layer. This simple model emulates the main features of the south Caspian crustal model shown in Figure 1 and is the reference model in the comparisons discussed below. The inputs at the left edge of the finite difference grid are the stresses and displacements as a function of depth for a fundamental mode Rayleigh wave generated by a 12 km deep explosion source located 2000 km away. These were generated by a normal–mode synthetic seismogram code. Although all of the events observed are earthquakes, we have used an explosion source to eliminate potential ambiguities resulting

73

from the source radiation pattern. Receivers are placed at 50 km intervals across the model and are located on the solid surface, i.e., in those models with a water layer, the receivers are placed at the water–solid interface. The seismograms are computed with 20000 0.075 s time steps.

Figure 6 shows the vertical component synthetic seismograms at a 50 km interval spacing across the reference model in two pass bands: < 0.020 Hz (left) and > 0.033 Hz (right). All seismograms in a record section are plotted at the same amplitude scale, but the two record sections have different scales. The basin effect on the wave train is most pronounced on the high frequency waves, but the basin structure effects are also apparent for the low frequency waves. The high frequency wave train shows an increased amplitude after entering the basin which results from the impedance mismatch across the basin boundary. Small amplitude converted body waves propagate into the basin and small amplitude converted body waves and reflected surface waves propagate back towards the left edge of the model (The amplitudes of these waves are too small to be seen at the amplitude scale used in Figure 6). The duration of the surface wave train increases during propagation across the basin due to the increased dispersion resulting from the thick, low velocity sediments; this is shown more clearly in Figure 7 discussed below. High frequency surface waves reverberate in the basin at large travel times. The intermediate frequency surface wave amplitudes on the right side of the figure are reduced after the wave train passes out of the basin and enters the more rigid material on the right side of the basin. The highest frequency components in the low frequency pass band are also amplified upon entering the basin as well as reflected back towards the left edge of the model. Surface waves of these frequencies are affected by the increased dispersion across the basin and are attenuated on passing out of the basin. The lowest frequency component shows little effect of the basin structure.

To isolate the features which most contributed to the anomalous surface wave propagation, we next perturbed the basin model velocity and attenuation structure in a number of ways and compared synthetic seismograms computed for these models with those computed for the reference model. Most of the structural features of the basin such as the thickness of the crystalline crust beneath the basin, degree of mantle upwarp beneath the basin, shape of the basin boundaries, *etc*, had little effect on the synthetic seismograms compared

to the seismograms of the reference model. The features which significantly influence the surface waveforms are the sediment thickness and the attenuation structure of the basin, and these are shown in Figure 7. This figure compares high– and lowpassed finite difference seismograms at distance 350 and 800 km from the left–hand edge of the model. All of the seismograms in each passband are plotted at the same amplitude scale but the amplitude scale for the two passbands is different. The light trace is the synthetic seismogram computed for the reference model (Fig. 5); the dark trace is the synthetic seismogram computed after altering one of the parameters. Figure 8 makes the same comparison but in the frequency domain. The pair of traces at middle left labeled BASIN INPUT are the highpass and low-pass seismograms at 350 km near to the left edge of the basin. The pairs of seismograms above, to the right, and below the input seismograms are the the seismograms at 850 km after emerging from the basin.

The seismogram pair labeled NO BASIN demonstrate the increased dispersion of the basin structure, primarily the thick, low velocity sediments. The highpassed seismogram is extended in time, but only the highest frequency components of the lowpassed seismogram are affected by the basin structure. Increasing the sediment thickness from 14.4 to 22.4 km has a small additional dispersion effect on the highpassed seismogram, but the thicker sediments have a increased effect on the lowpass seismogram. Decreasing the Q_β in the sediments from 50 to 10 reduces the amplitude of the highpass waveform by more than a factor of 2 but has only a small effect on the lowpass waveform. Increasing the attenuation in the mantle beneath the basin does not significantly lower the lowpass waveform amplitudes.

The two pairs of seismogram labeled SLOPING SIDES and EXTENDED BASIN show effects of the configuration of the basin boundaries. The basin model with sloping boundaries has a basin transition from the surrounding model which extends over a 45 km distance rather than the abrupt boundaries of the reference model. This gradational basin boundary has little effect on the synthetic seismogram. The basin model labeled EXTENDED BASIN has a two–step basin boundary with the sediments extending to a depth of 10 km beneath the stations and the same depth as the reference model in the interior of the basin. In this model the observation points are effectively within the basin and are more in agreement with the receiver function analysis (Mangino and Priestley, 1998). These seismograms show an

enhancement of the highpass waveform but there is little effect on the lowpass waveform. This shows up in the spectral ratio as a spectral resonance peak at about 0.04 HZ. Halving the sediment thickness increases the frequency of this peak slightly, but it primarily reduces the amplitude of the spectral peak.

Figure 9 compares the observed fundamental mode Rayleigh wave spectral ratio between stations LNK and KAT and the phase velocity dispersion for the south Caspian basin (Fig. 3) with the spectral ratios and phase velocity dispersion for the various finite difference models. The dispersion curves are included only for reference since the finite difference models are oversimplified in terms of the velocity structure. The KAT–LNK spectral ratio is near one at 0.01 Hz. Between about 0.017 and 0.033 Hz the spectral amplitude decays by more than a factor of three. At frequencies higher than 0.033 Hz the spectral ratio increases with a peak near 0.05 Hz. The upper panel of Figure 9 shows that increasing the sediment thickness to 22.4 km or decreasing the sediment Q to 10 attenuates the high frequency surface waves but does not produce the attenuation in the 0.02 to 0.03 Hz band seen in the data. Increasing the attenuation in the mantle beneath the basin (Fig. 9 – lower panel) reduces the low frequency amplitudes but not to the extent observed in the data. The data show a large amplitude peak between 0.04 and 0.05 Hz. Extending the basin sediments beneath the observation points in the finite difference model causes a lower amplitude, lower frequency resonance peak. No variations of the south Caspian basin model (Fig. 5) reduced the energy in the 0.02 to 0.03 Hz band in the synthetic seismograms to the degree seen in the KAT–LNK seismograms.

Discussion and Conclusions

The south Caspian is an actively subsiding basin with extremely high rates of Cenozoic sedimentation, in some places as high as 1,300 m/my. Figure 1 shows that the basin contains an enormous thickness of sediments, as much as 25 km in the deepest parts. Borehole data in the Caspian Sea south of Baku show that to at least 5 km depth these sediments consist of both sand and shale beds that have pore–fluid pressure substantially in excess of hydrostatic fluid pressure (Bredehoeft et al, 1988). This high pore–fluid pressure is the likely cause of the large number of mud volcanos found along the coast and on the bed of the south Caspian

76

Sea.

The thick sediments have a pronounced effect on the propagation of surface waves. Intermediate frequency ($>$ 22 mHz) surface waves are severely affected in propagating across the south Caspian basin whereas low frequency ($<$ 22 mHz) surface waves show little effect of the basin structure. We have used a hybrid normal mode–finite difference program and a simplified model of the south Caspian basin to study which of the basin features cause the anomalous effect on the surface wave propagation. Variations in the velocity of the crystalline crust of the basin and in the mantle upwarp beneath the basin result in a small part of the surface wave energy being converted into body waves and being lost, but on the whole these features have little effect on the intermediate frequency surface waves. The thick, highly attenuating sediments do have a significant effect on the surface waveform. This results from (1) the increased high frequency dispersion which gives an apparent decrease in amplitude by stretching the waveform out in time and (2) the high attenuation of the sediments which has a large effect on the high frequency surface waves but little effect on the low frequency surface waves.

The 2–D finite difference modeling has reproduced a number of trends in the data but not the details. There are strong 3–D variations in the crustal structure in the region of the south Caspian basin. The Talesh mountains form the western boundary, the Alborz mountains constitute the southern boundary, and the Kopet Dag and Alborz mountains form the eastern boundary. The Apshceron–Balkhan sill, a seismically active shallow ridge separating the northern and south Caspian, makes up the northern boundary of the basin. The station LNK lies between the Talesh Mountains and the southwest Caspian coast and on about 10 km of sediment. Station KAT is in the west Turkmenian lowlands east of the south Caspian basin located in a large sedimentary basin considered to be structurally part of the south Caspian basin. The effects of the complex structure are apparent in the data. Surface wave polarization measurements of the backazimuth *vs.* frequency show that the low frequency ($<$ 0.033 Hz) Rayleigh waves arrive near the theoretical source–receiver great circle azimuth, whereas there is considerable scatter in the azimuth of approach of the higher frequency surface waves. This result suggest that 3–D effects could be important for amplitudes at high frequency.

Acknowledgements:

References

Bredehoeft, J.D, R.D. Djevanshir, and K.R. Belitz (1988). Lateral fluid flow in a compacting sand–shale sequence: south Caspian basin, *Am. Assoc. Petroleum Geologists Bull.*, **72**, 416–424.

Brune, J., J. Nafe, and J. Oliver (1960). A simplified method for the analysis and synthesis of dispersed wave trains, *J. geophys. Res.*, **65**, 287–304.

Brune, J., and D.D. Singh (1986). Continent–like crustal thickness beneath the Bay of Bengal sediments, *Bull. seism. Soc. Am.*, **76**, 191–203.

Brune, J., J. Curry, L. Dorman, and R. Raitt (1992). A proposed super–thick sedimentary basin, *Geophys. Res. Letts.*, **19**, 565–568.

Chan, W.W., and B.J. Mitchell (1985). Surface wave dispersion, crustal structure, and sediment thickness variations across the Barents shelf, *Geophys. J. R. astr. Soc.*, **80**, 329–344.

Gal'perin, Y., I. Kosminskaya, and P. Krakshina (1962). Main characteristics of deep waves recorded during deep seismic sounding in central part of Caspian sea. In: *Deep Seismic Sounding of the Earth's crust in the U.S.S.R.*, Acad. Sci. USSR, Moscow.

Gomberg, J.S., K.F. Priestley, T.G. Masters, and J.N. Brune (1988). The structure of the crust and upper mantle of northern Mexico, *Geophys. J.*, **94**, 1–20.

Isacks, B., and C. Stephens (1975). Conversion of S_n to L_g at a continental margin, *Bull. seism. Soc. Am.*, **65**, 235-244.

Kadinsky–Cade, K., M. Barazangi, J. Oliver, and B. Isacks (1981). Lateral variations of high frequency seismic wave propagation at regional distances across the Turkish and Iranian Plateaus, *J. geophys. Res.*, **86**, 9377–9396.

Levshin, A. and K.-A. Berteussen (1979). Anomalous propagation of surface waves in the Barents Sea as inferred from NORSAR recordings, *Geophys. J. R. astr. Soc.*, **56**, 97–118.

Mangino, S. and K. Priestley (1998). The crustal structure of the southern Caspian region, *Geophys. J. Int.*, in press.

Mindeli, P.S., Yu.P. Neprochnov, and E.I. Pataraya (1965). Definition of the area without granitic layer in the Black Sea basin on DSS data and seismology, *Izv. Earth Phys.*, **12**, 7–15.

Neprochnov, Yu.P., (1968). Structure of the Earth's crust of epi–continental seas: Caspian, Black and Mediterranean, *Can. J. Earth Sci.*, **5**, 1037–1043.

Neprochnov, Yu.P., I.P. Kosminskaya, and YA.P. Malovitsky (1970). Structure of the crust and upper mantle of the Black and Caspian Seas, *Tectonophys.*, **10**, 517–538.

Press, F., and M. Ewing (1952). Two slow surface waves across North America, *Bull. seism. Soc. Am.*, **42**, 219–228.

Rezanov, I.A., and S.S. Chamo (1969). Reasons for absence of a granitic layer in basins of the South Caspian and Black Sea type, *Can. J. Earth Sci.*, **6**, 671–678.

Savarensky, E.F., and N.G. Valdner (1960). L_g and R_g waves from earthquakes of the area of the Black Sea and some consideration about their origin, *Seismic Investigation Geofiz. Com. U.S.S.R.*, Akademizdat, 4, 55–77.

Seber, D, M. Barazangi, B.A. Tadili, M. Ramdani, A. Ibenbrahim, D.B. Sari, and S.O.E. Alami (1993). S_n to S_g conversion and focusing along the Atlantic margin, Morocco: Implications for earthquake hazards evaluation, *Geophys. Res. Letts.*, **20**, 1503–1506.

Shapiro, N., N. Bethoux, M. Campillo, and A. Paul (1996). Regional seismic phases across the Ligurian Sea: L_g blockage and oceanic propagation, *Phys. Earth planet. Int.*, **93**, 257–268.

Shurbet, D.H., (1964). The high–frequency S phase and the structure of the upper mantle, *J. geophys. Res.*, **69**, 2065–2070.

Shurbet, D.H., (1975). Conversion of S_n at a continental margin, *Bull. seism. Soc. Am.*, **65**, 327–329.

Yegorkin, A.V. and B.A. Matushkin (1970). Crustal structure of the Caucasus and Western Central Asia based on geophysical sounding data, *Internat. Geol. Rev.*, **12**, 281–290.

Table 1

Model	Thickness (km)	V_p km s^{-1}	V_s km s^{-1}	ρ gm cm^{-3}	Q_p	Q_s
Background Model	38.0	6.40	3.70	2.82	∞	∞
	450.5	8.13	4.70	3.37	∞	∞
Basin Model	2.625	1.51	0.00	1.00	∞	∞
	14.375	3.46	2.00	1.88	100	50
	16.000	7.44	4.30	3.15	1000	500

Figure Captions

Figure 1. The upper part of this figure shows a location map of the south Caspian region. The solid inverted triangles denote CSN stations used in the receiver function study of Mangino and Priestley (1998); the solid black lines denote the location of DSS profiles used by Mangino and Priestley (1998) to construct the crustal velocity model for the south Caspian region shown in the lower part of the figure. The crustal cross–section corresponds approximately to the region of the box on the map. The three crustal and single mantle layers are characterized by their P–wave velocities: sediment and consolidated sediment ($V_p < 4.8$ km s^{-1}), "granitic" (V_p between 4.8–6.4 km s^{-1}), and "basaltic" (V_p between 6.4–7.4 km s^{-1}); upper mantle are $V_p \geq 8.0$ km s^{-1}. In this study we have measured fundamental mode Rayleigh wave phase velocities between the station pairs KAT–KRF, KRF–LNK, and LNK–KAT.

Figure 2. Regional seismograms of an earthquake occurring near KRF (Fig. 1) and recorded at stations LNK, KAT, and ABKT. The inset map shows the propagation paths to each of the CSN seismographs. Double arrows indicate the times of the L_g window corresponding to group velocities of 3.6 and 3.2 km/s.

Figure 3. Comparison of the fundamental mode Rayleigh wave phase velocity curve measured for the south Caspian basin with curves measured in two other regions of anomalously thick sediments.

Figure 4. Example of the anomalous effect of the south Caspian basin structure on the propagation of intermediate frequency surface waves. The Jan. 25, 1994 earthquake is propagating from west–to–east on the same great circle path as that between LNK and KAT: the LNK seismogram is the basin input and the KAT seismogram is the basin output. The upper pair of seismograms are the broadband records, the middle pair are the highpassed records, and the bottom pair are the lowpassed records. Each pair of seismograms is plotted with the same amplitude scale, but the amplitude scales differ for each pair. The July 13, 1994 earthquake is propagating from east–to–west along the same great circle path as that between KAT and LNK: the KAT seismogram is the basin input and the LNK seismogram is the basin output.

Figure 5. Simplified model of the south Caspian basin used in the finite difference calcula-

tions. The parameters of the model used in the finite difference calculation are given in Table 1. This model is called teh reference model in the text.

Figure 6. Lowpass and highpass record sections of the finite difference seismograms computed for the reference model shown in Figure 5. Arrows indicate the basin boundaries. The seismograms are plotted at a 50 km interval across the model.

Figure 7. Comparison of basin input and output finite difference synthetic seismograms for six perturbations of the reference model (Figure 5) structure. In each comparison the light background seismogram is the synthetic computed for the reference model and the darker seismogram is computed for the perturbed model. The upper seismogram of each pair is the highpass (>0.033 Hz) filtered record and the lower seismogram is the lowpass (<0.02 Hz) filtered record. The input seismogram is at 350 km distance across the model and the output seismogram is at 800 km distance across the model.

Figure 8. Comparison of the spectral ratios computed for the seismograms in Figure 7 with the spectral ratio for the reference model (unlabled dark line).

Figure 9. Comparison of the same spectral ratios (left panels) shown in Figure 8 with the average spectral ratio measured between LNK and KAT (dark line). On the right are shown the fundamental mode phase velocity for the various finite difference models compared to the observed phase velocity.

FIGURE 1

ABKT (483 km)

3.6 – 3.2 Group
Velocity Window

July 1, 1994 -- 10:12:41.2

40.22°N 53.39°E 41 km m_b 5.6

Pn

Sn

KAT (309 km)

Pn

Sn

LNK (431 km)

Pn

Sn

ABKT

KAT

LNK

0   100   200

Seconds
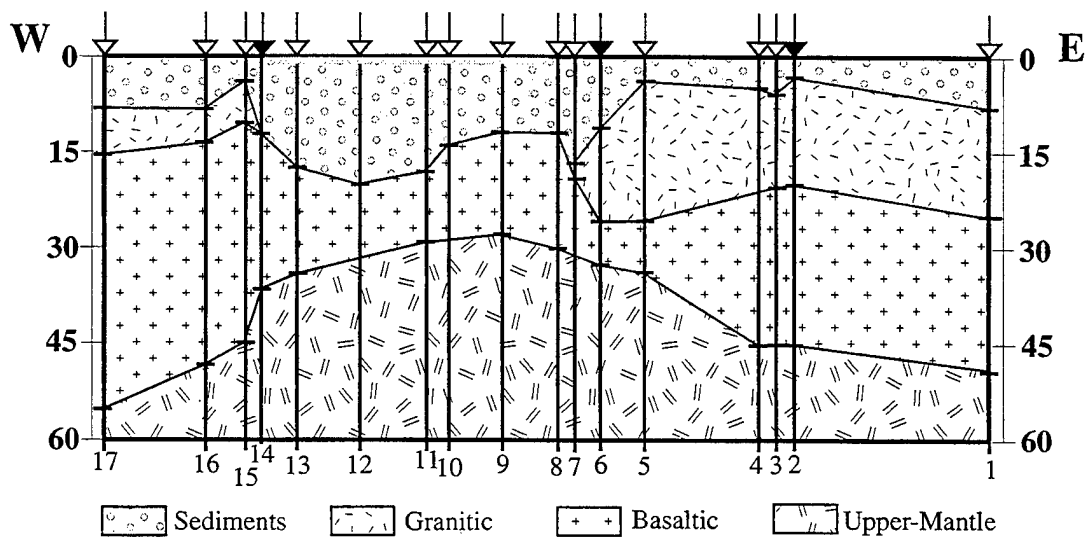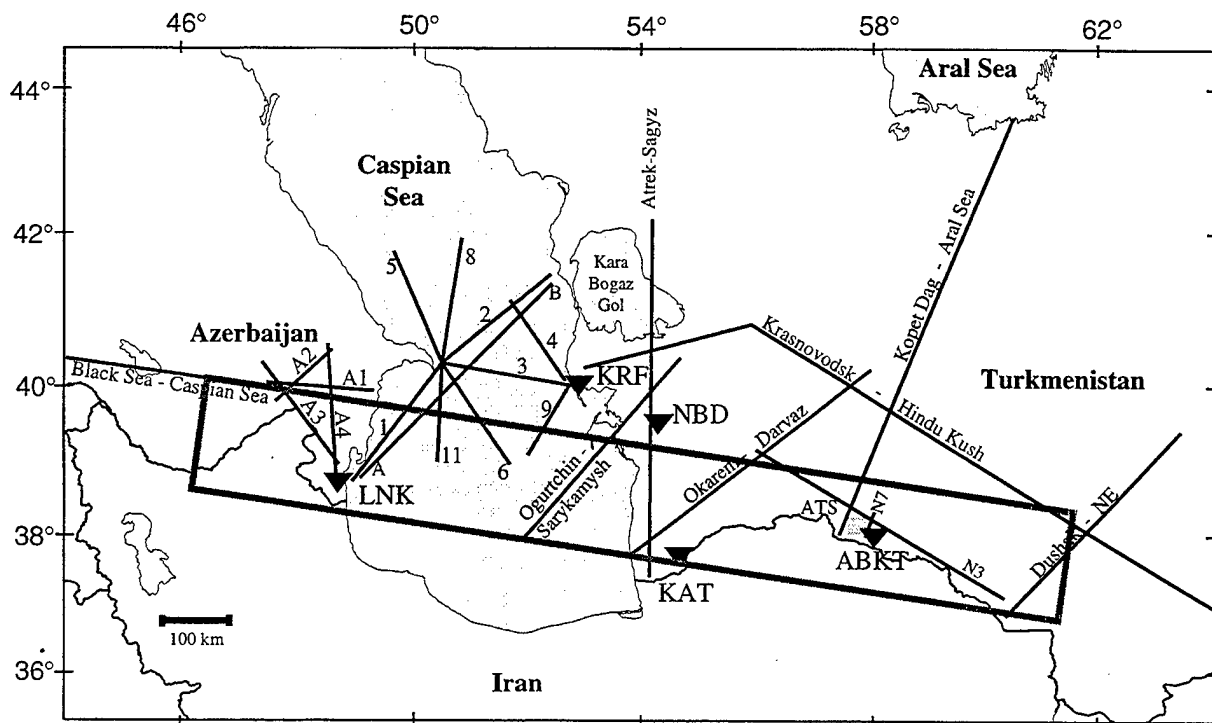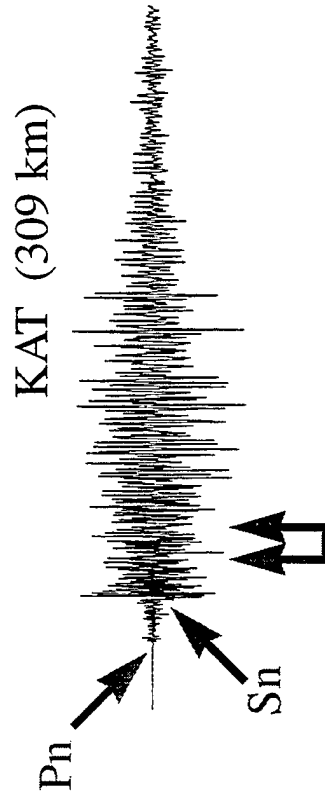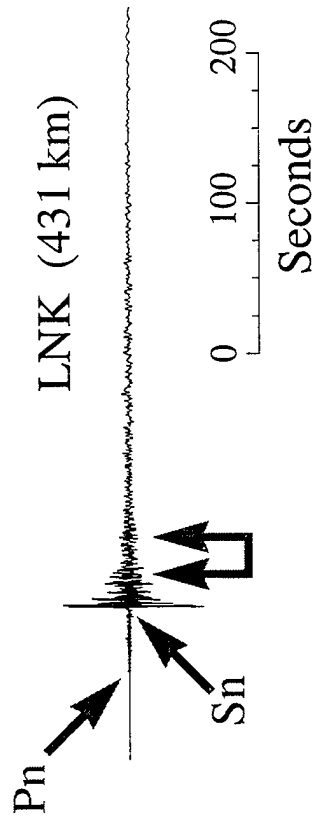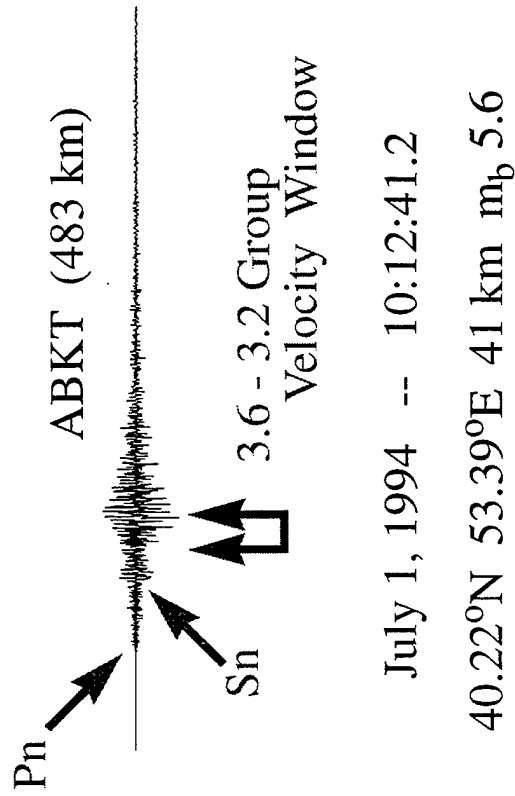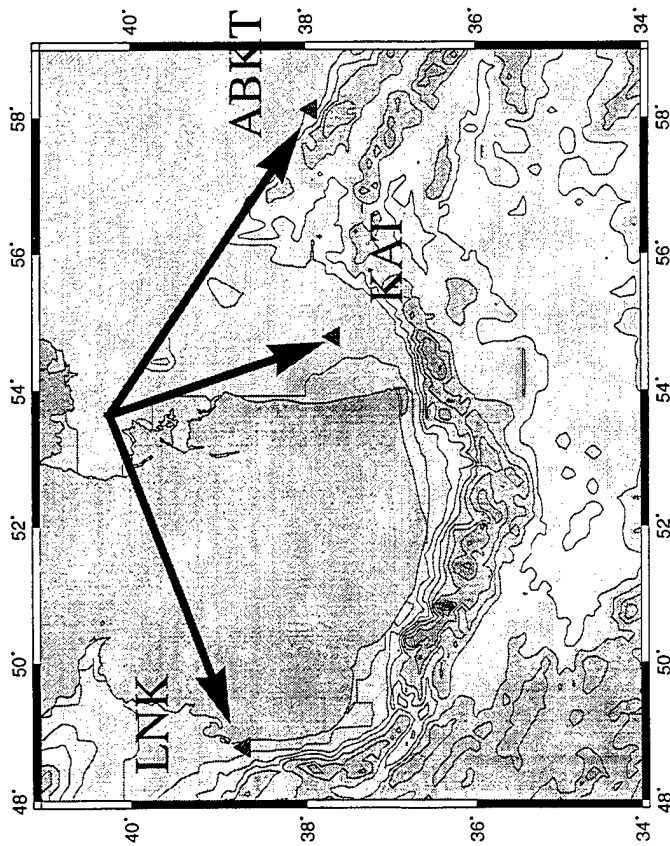
FIGURE 2

Fundamental Mode Rayleigh Wave Dispersion

Phase Velocity (km/sec)

Period (sec)

South Caspian Basin
East Barent Sea
Bay of Bengal

FIGURE 3

86

FIGURE 4

Simplified South Caspian Basin Model

FIGURE 5

FIGURE 6

NO BASIN

INCREASED SEDIMENT THICKNESS

BASIN INPUT   100 sec

INCREASED SEDIMENT ATTENUATION

INCREASED MANTLE ATTENUATION

EXTENDED BASIN

SLOPING SIDES

FIGURE 7

90

FIGURE 8

91
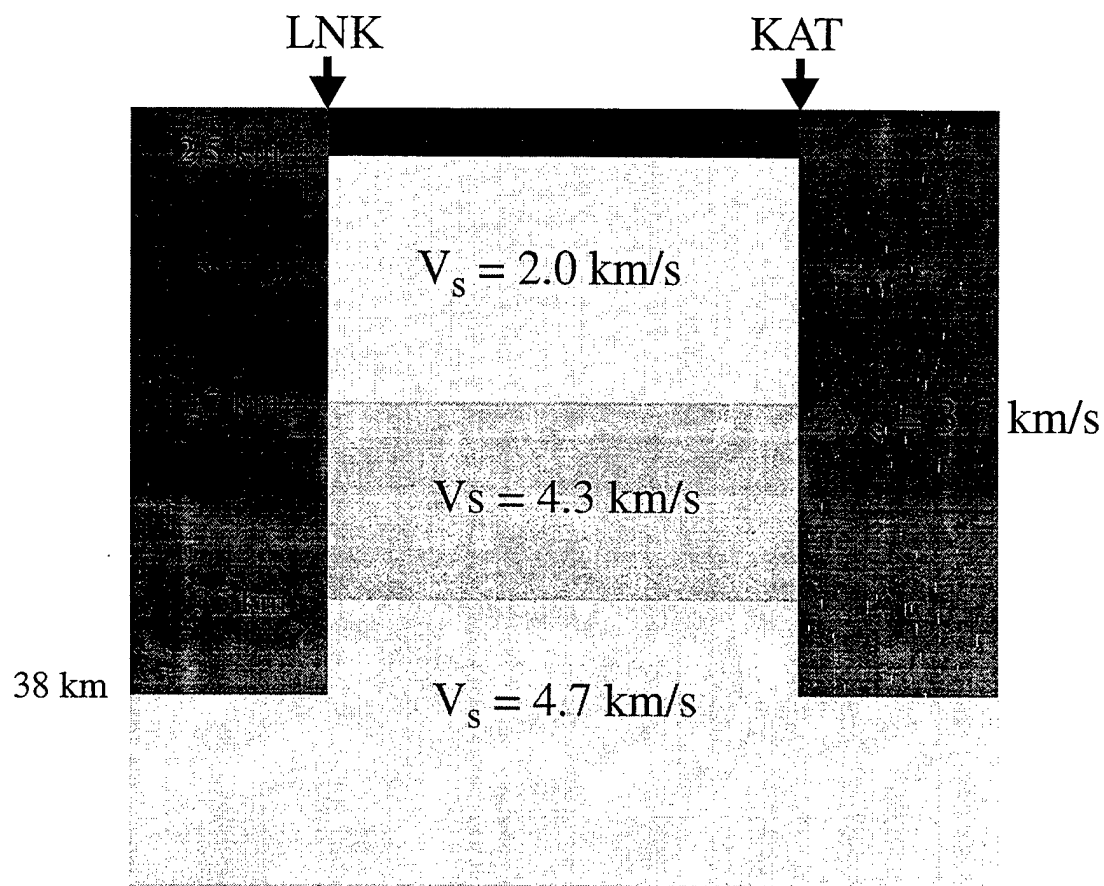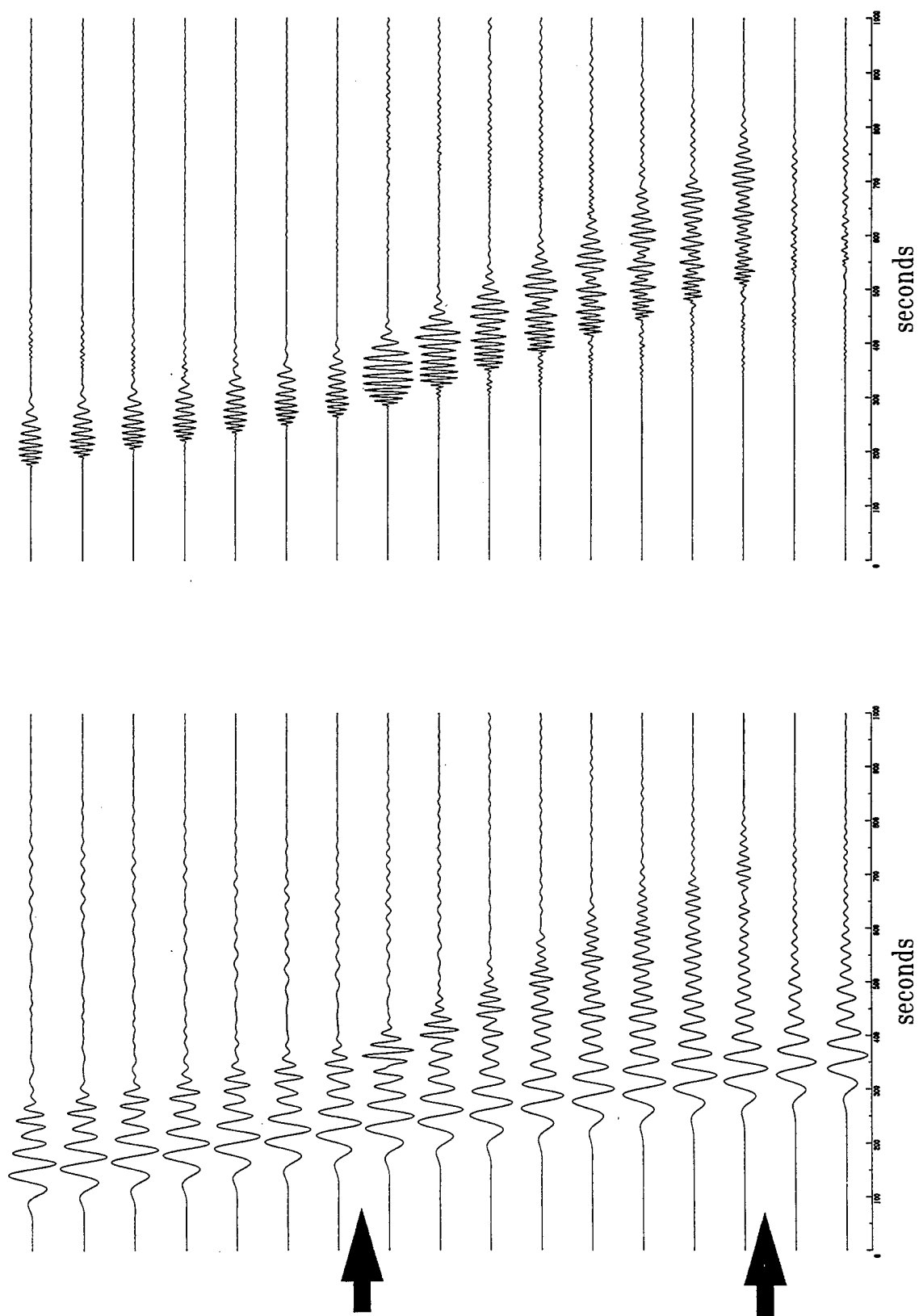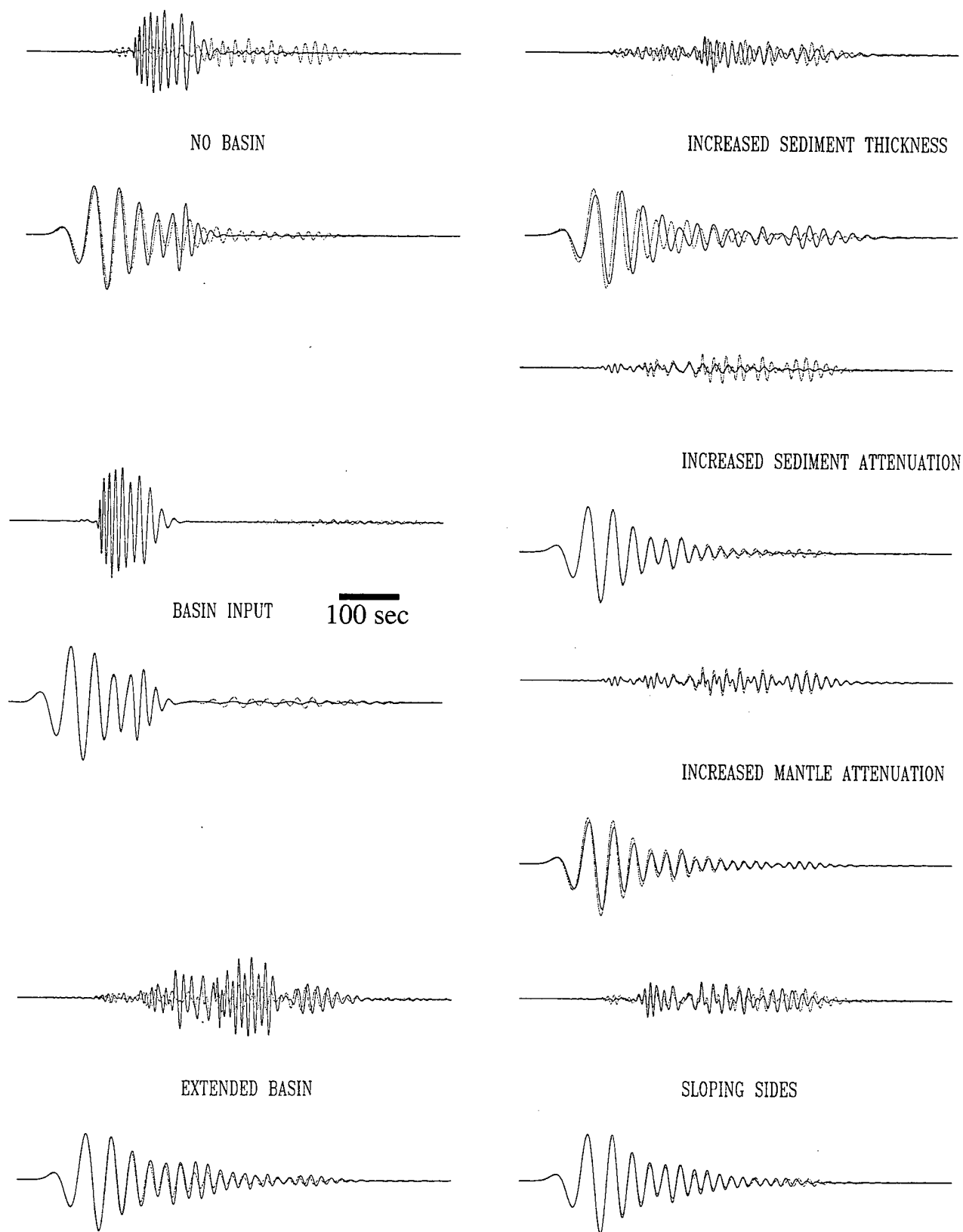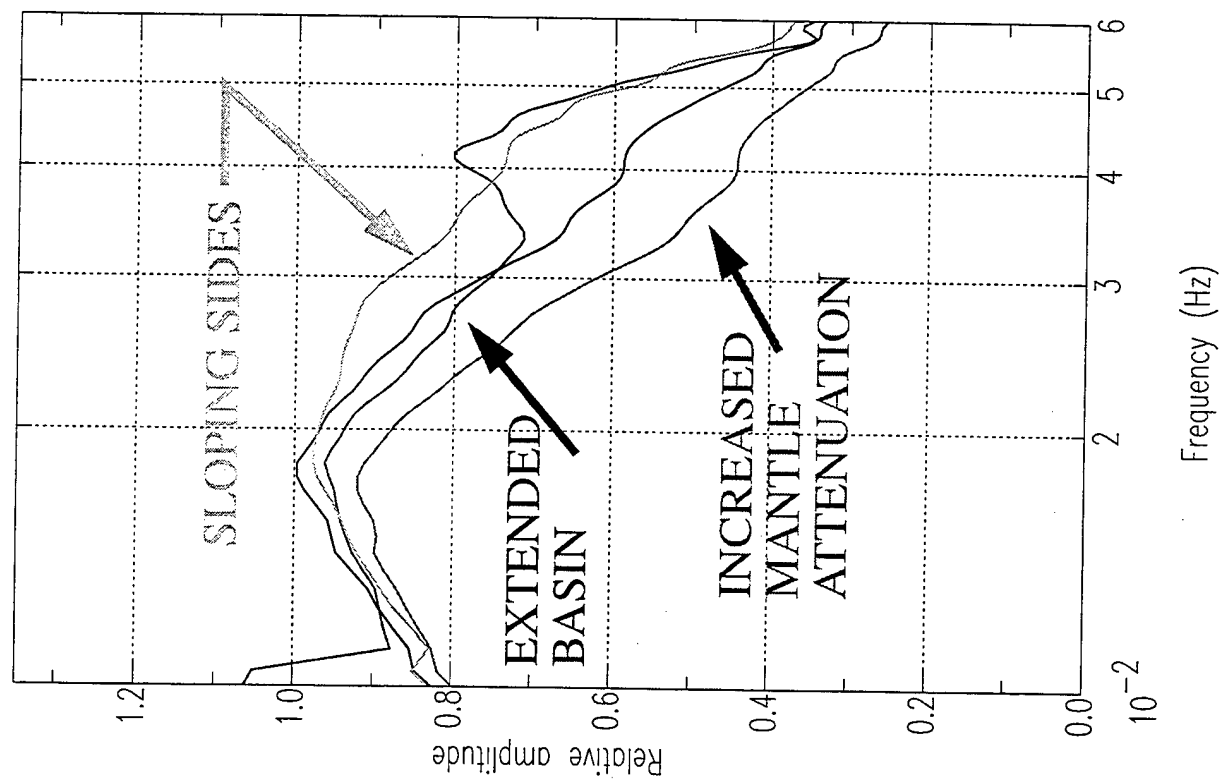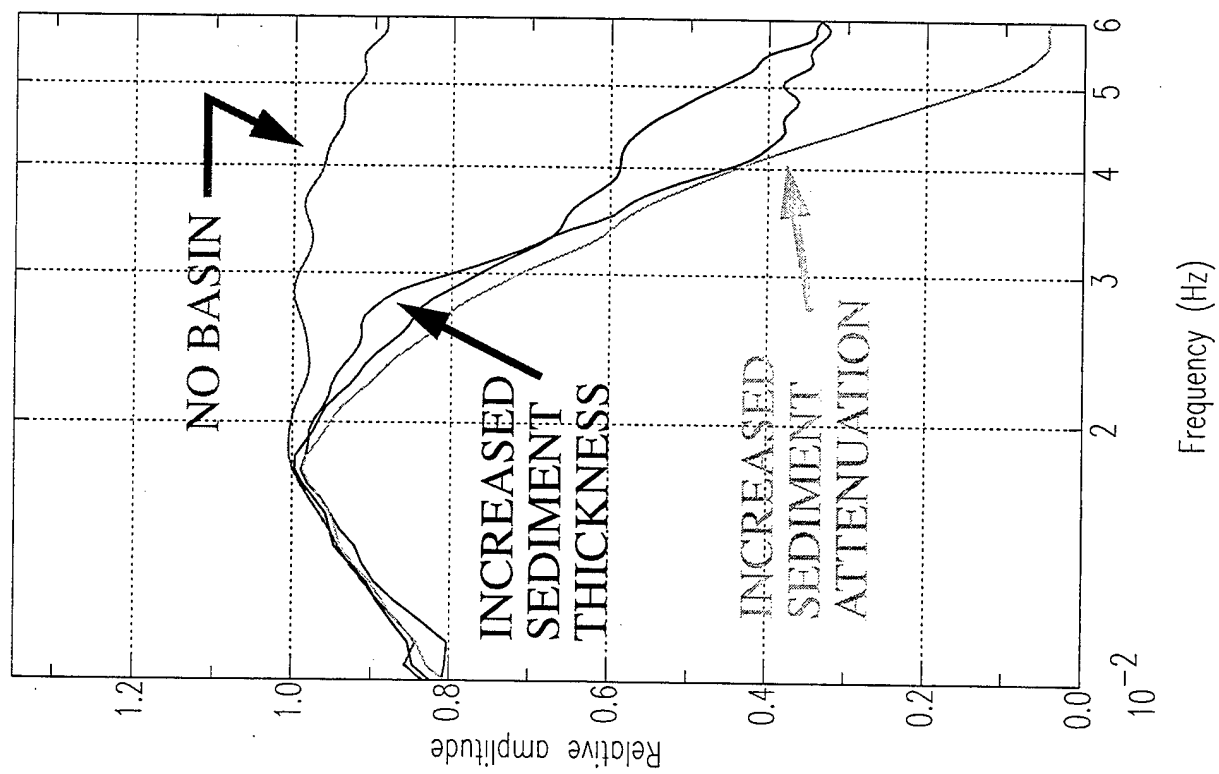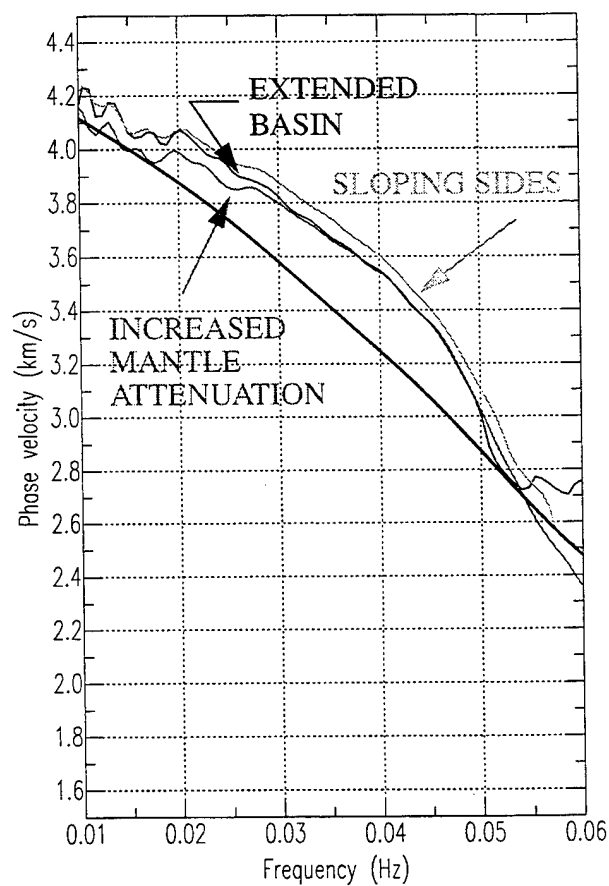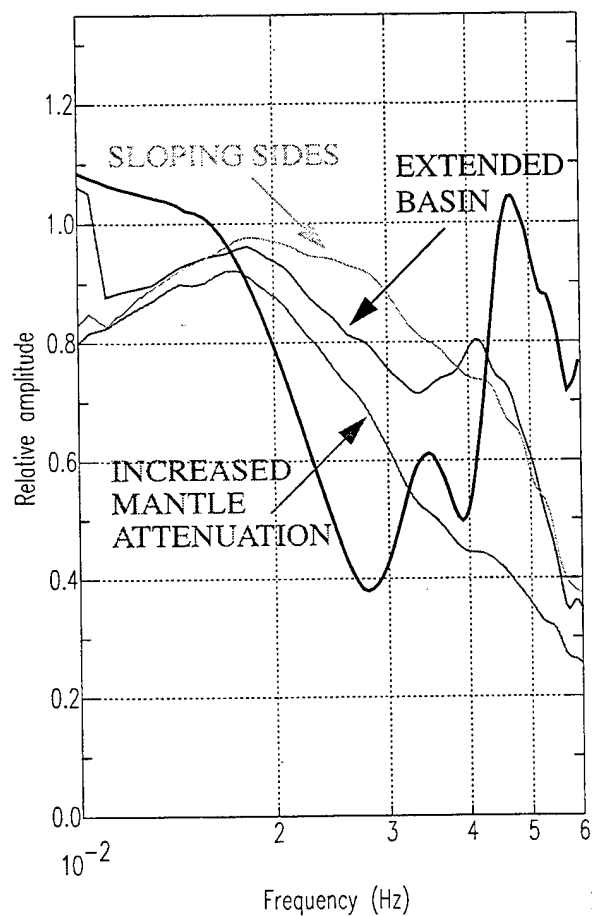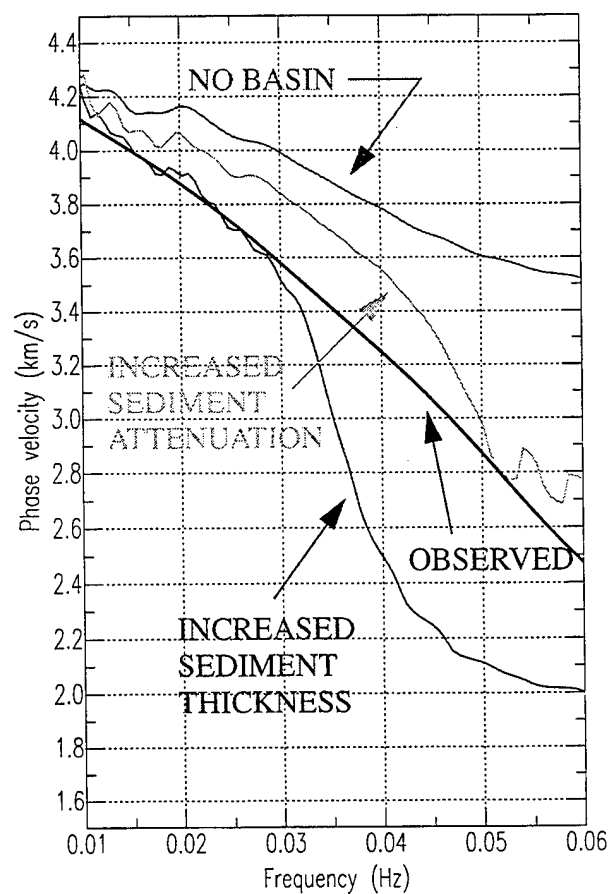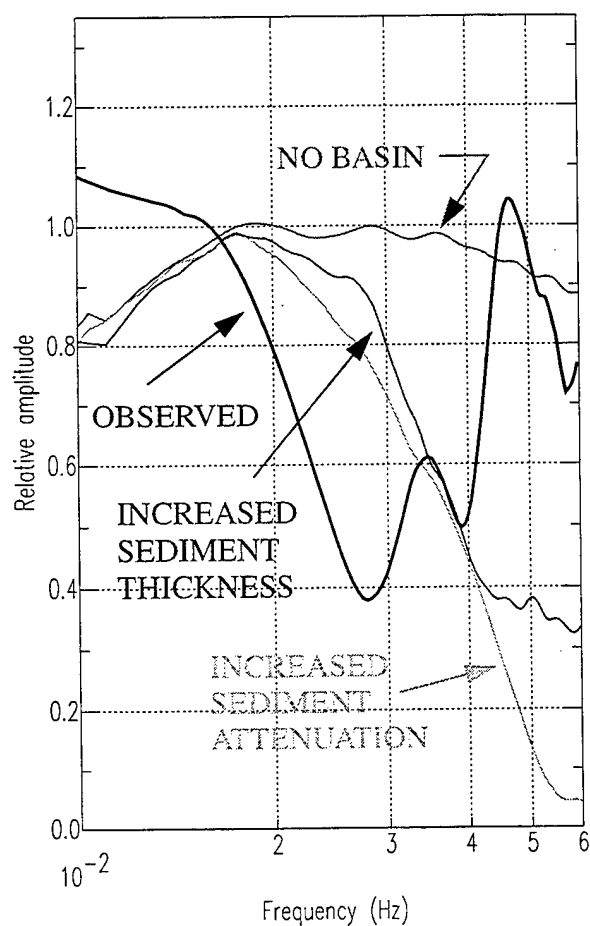
FIGURE 9

CENTRAL SIBERIA UPPER MANTLE CROSS–SECTION FROM DEEP SEISMIC SOUNDING EXPLOSIONS

J. CIPAR Earth Sciences Division, Phillips Laboratory,

Hanscom Air Force Base, MA 01730, USA

K. PRIESTLEY Bullard Laboratories, Dept. of Earth Sciences

Madingley Rise, Madingley Road, Cambridge CB30EZ, UK

Abstract

We describe a quasi–two dimensional velocity profile for the upper mantle beneath the Siberian Platform based on observations of the 2600–km long Deep Seismic Sounding profile RIFT. The analyses combine forward travel–time modeling and waveform matching using reflectivity synthetic seismograms. The sub–Moho velocity gradients are weak. A high gradient zone exists between 180 and 250–km depth which we identify with the Lehmann discontinuity. This feature is deepest in the north (235 km) beneath the northern part of the Siberian Platform and shallowest in the south (180 km) beneath the Siberian Platform/Baikal Rift transition zone. The velocity structure is complex above the Lehmann discontinuity; below it is less well constrained but the structure appears to be less complex. The transition zone consists of two discontinuities; a 35 km broad zone between 400 and 435 km depth where the velocity increases from 8.64 to 9.40 $km\,s^{-1}$ and a narrower zone between 655 and 659 km depth where the velocity increases from 10.20 to 10.58 $km\,s^{-1}$. There is no evidence of a transition zone discontinuity near 520 km depth beneath the Siberian Platform.
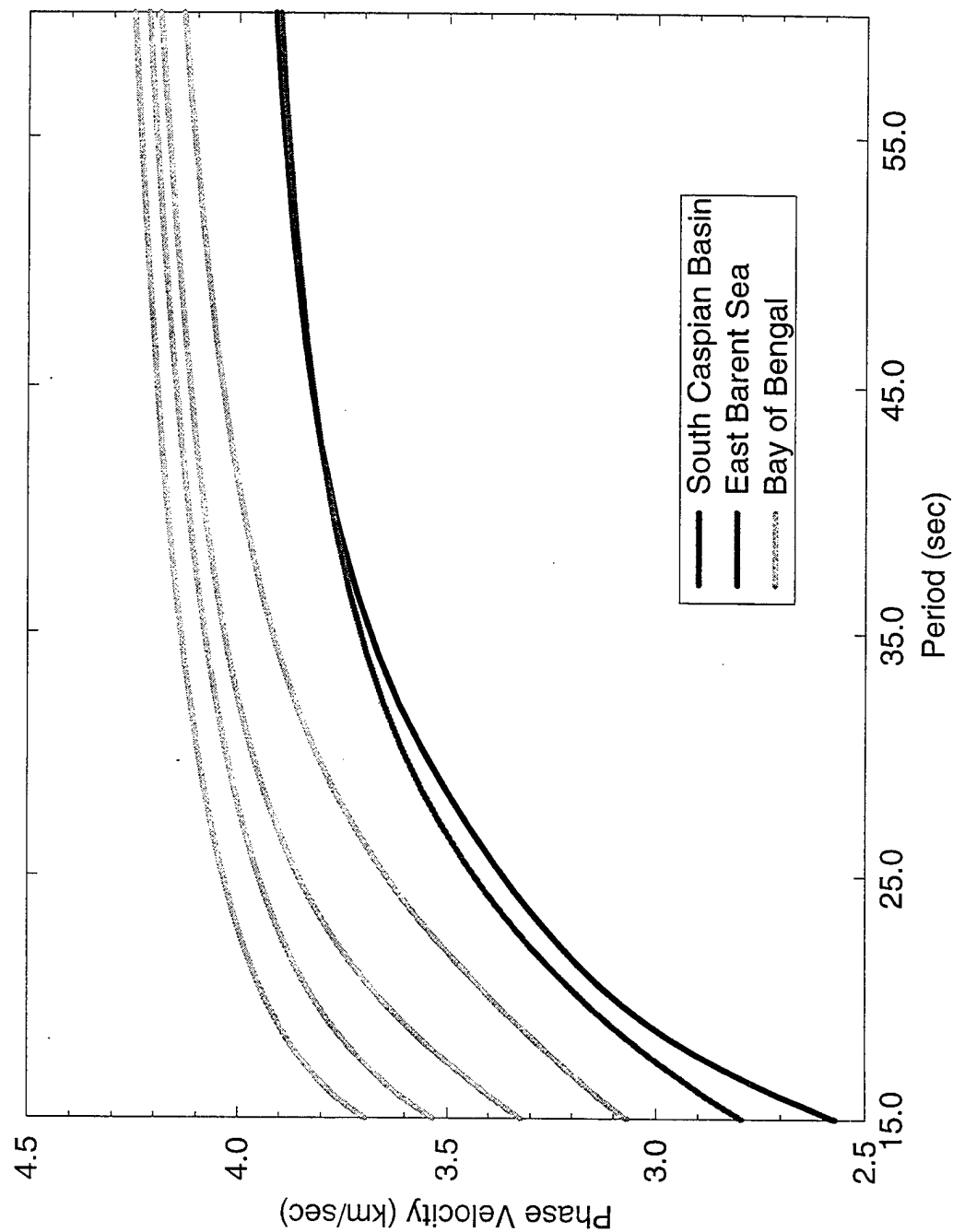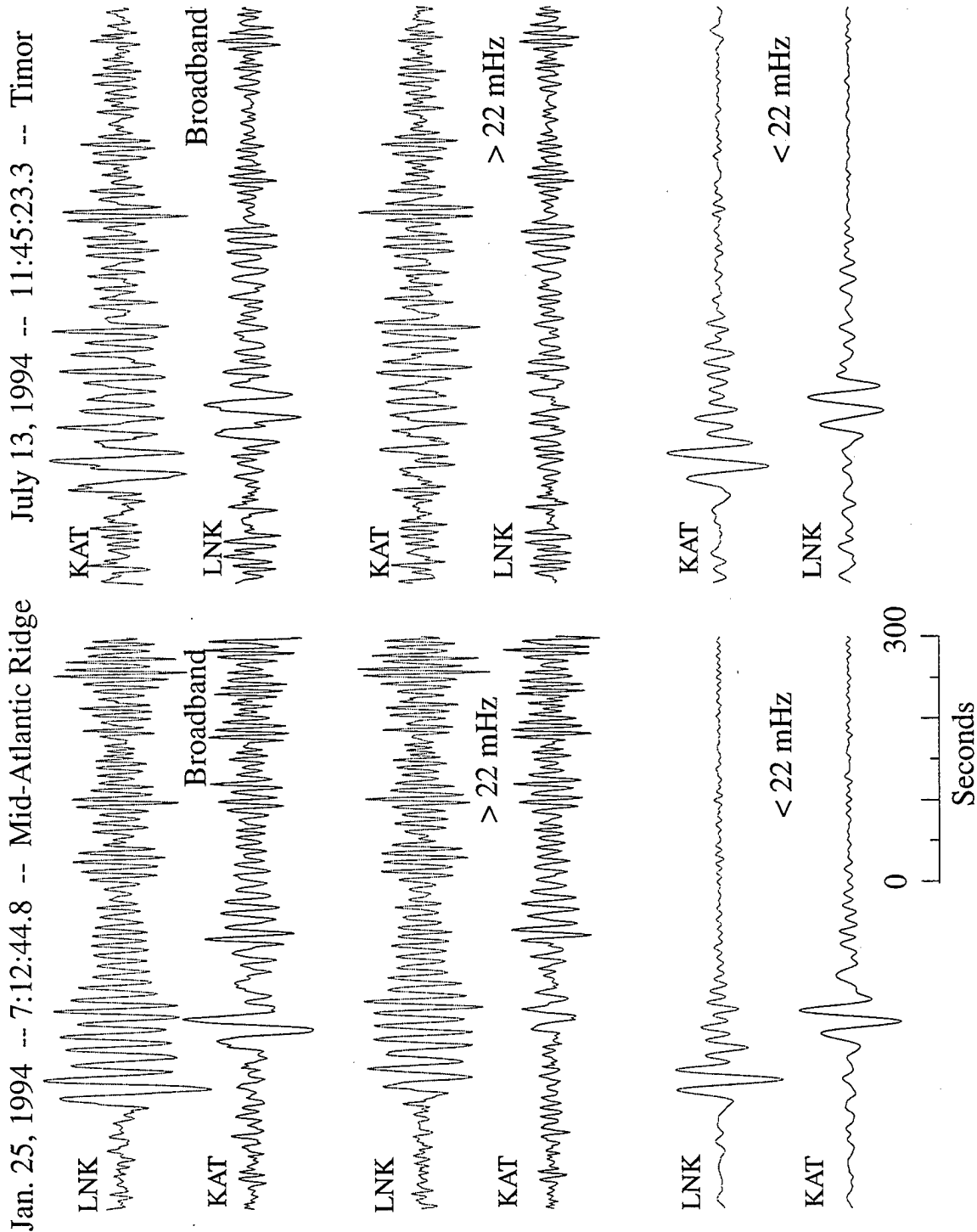
1 Introduction

In the mid–1950's Soviet seismologists initiated an extensive active seismic exploration program of the Eurasian crust and upper mantle. These Deep Seismic Sounding (DSS) profiles employed a dense set of recordings; many used peaceful nuclear explosions (PNE's) as seismic sources for recordings to long distances (up to about 4500 km) and chemical explosions for recordings at shorter distances (up to about 750 km) [1]. While the restricted bandwidth of the recording instruments used in this program is a limitation, these long range profiles

are the only data available for imaging upper mantle and transition zone structures using controlled source seismology. This has an advantage over passive seismic observations using earthquakes since the timing and location of the explosions are precisely known, the source radiation is better known, and the wave field is normally much more densely sampled.

Studies of the data from several of these long DSS profiles have now been published [2], [3], [4], [5], [6], [7]. In this report we summarize the P–wave velocity structure beneath the Siberian Platform derived from the DSS profile RIFT. We have discussed details of the analyses elsewhere [5], [7], [8].

2 Modeling of the RIFT Profile data

The 1982 RIFT profile extends 2600 km across the Archaean–Proterozoic Siberian Platform from the Yamal Peninsula in NW Norilsk to the Mongolian border SE of Lake Baikal (Fig. 1). Seismic data were recorded from three nuclear explosions and thirty–four chemical explosions [5]. The northernmost nuclear shot (SP245 – Fig. 1.) is located within the West Siberian rift (latitude 69.206°N, longitude 81.647°E). Data for this shot were recorded to more than 2400 km distance to the SE and 165 km to the NW. The central nuclear shot point (SP173 – Fig. 1) is located within the Tunguska Basin (latitude 64.313°N, longitude 97.834°E), approximately 700 km SE of SP245. Recordings from this shot extend 560 km NW, reversing a section of the profile from SP245 and 1700 km SE across the Baikal rift. The southernmost nuclear shot point (SP035 – Fig. 1) is located 250 km NW of Lake Baikal (latitude 53.810°N, longitude 104.130°E). Seismograms from this shot extend 325 km to the SE across the Baikal rift and nearly 2200 km to the NW, reversing both SP245 and SP173. Instrumental problems resulted in a significant data gap for SP035 but this was partly filled in by the large, nearby chemical shot, SP036.

An examination of the record sections (Fig. 2) indicates marked lateral variations in the velocity structure beneath the profile. The approach we used was to model each section of the data independently using forward modeling of the travel times combined with reflectivity synthetic [9] calculations to check relative amplitudes. We use the Priestley *et al* [7] central Siberia model (Model T) as the starting model for analyzing the observations for shot points

SP173 and SP035. The resulting 1–D models were then combined, creating a quasi–2–D cross–section. The reason for proceeding in this manner was that even though the profiles are "reversed," there is little overlapping ray coverage at depth. To make the cross–section we have placed the structure in our quasi–2–D model near the turning point of the ray. This shows where along the profile the rays sample and hence approximately where the model is actually constrained.

Model T of Priestley *et al* [7] from the SP245–SE data contains second–order discontinuities near 120 km, 235 km, 410 km, and 660 km depth. The Moho velocity is 8.25 km s^{-1}, below which there is a weak gradient to 117 km depth. The velocity increases from 8.30 to 8.51 km s^{-1} over the depth interval 117 to 123 km, below which there is a sharp negative gradient between 136 and 145 km depth. The weak gradient below the Moho is required to match the weak first arrivals in the 300 to 1500 km distance range (Fig. 2a). The velocity increase at 117 km depth produces the large amplitude second arrival first seen at about 750 km distance. The negative gradient below 136 km depth is required to diminish the amplitude of the first arrival at about 1300 km distance. There is a second velocity jump from 8.62 to 8.78 km s^{-1} over the interval 233 to 235 km depth which produces the large secondary arrival first observed at about 1250 km distance.

The transition zone in Model T consists of discontinuities near 410 and 660 km depth. The 410–km discontinuity consists of a broad gradient zone extending from 400 to 435 km depth over which the velocity increases from 8.64 to 9.40 km s^{-1}. The strong reflection from the lower discontinuity is best modeled as a velocity increase from 10.20 to 10.58 km s^{-1} over the depth range 655 to 659 km. The velocity gradient below the 410–km discontinuity is well constrained by a set of strong arrivals. Similar arrivals cannot be seen from the 660–km discontinuity, indicating a weak gradient below 660 km. There is no evidence for a transition zone discontinuity near 520–km depth in the SP245 data.

The SP173–SE record section (Fig. 2b) exhibits a prominent crustal phase with an apparent velocity of 6.0 to 6.5 km s^{-1} from the source to approximately 700 km. The low–amplitude P_n phase becomes the first arrival at about 190 km range and extends as an identifiable phase to about 600 km range. A strong second arrival becomes prominent at about 400 km, becoming the first arrival around 600 km range after the extinction of P_n. At

about 900 km range, the apparent velocity of the first arrival increases from 8.1–8.3 km s^{-1} to 8.6–8.8 km s^{-1}. Note that the first arrival branch beyond 900 km range is not a straight line, but is composed of a series of curved segments, or "scallops." Beyond about 1500 km range, the first arrivals are delayed by 2 to 3 seconds compared to first arrivals at closer ranges.

The SP173–SE data suggests that the upper mantle has a structure consisting of thin high–velocity layers embedded in lower velocity material. The P$_n$ phase consists of arrivals from a thin layer of 8.05 km s^{-1} material extending from the Moho at 40 km to 46 km depth, underlain by a 12–km thick layer of 8.33–8.35 km s^{-1} material. The cutoff of P$_n$ at about 600 km range indicates an abrupt decrease in velocity below 58 km depth. Our model (Model Tand 120 km depth. The prominent set of arrivals in the 790 to 1150 km distance range results from the velocity increase between 120 and 140 km depth. The forward branch is terminated at about 1000 km distance by an abrupt decrease in velocity to 8.30 km s^{-1} at 140 km depth. A similar type structure consisting of a moderate positive velocity gradient (160–184 km depth), thin high gradient zone (184 to 185 km depth), and a low, positive gradient (185 to 200 km) terminated by a thick low–velocity, low–gradient zone is repeated. This structure accounts for the observed increase in apparent velocity at about 900–km range. Beyond about 1200 km this branch is the first arrival. A similar structure is observed in the SP245 profile at a slightly greater depth of 233 km.

SP035/SP036–NW (Fig. 2c) arrivals from the uppermost mantle do not exhibit the strong scalloping prominent in record sections for the other shots. The increase in apparent velocity at about 900 km range is accounted for in our model (Model J1–NW) by a moderate velocity gradient between 75 and 90 km depth and with a broad zone of low or slightly negative velocity gradient to 180 km depth. The velocity in this depth range is 8.33–8.34 km s^{-1}. The low–gradient zone ends in a 10–km thick zone of moderate gradient from 180 to 190 km depth where the velocity increases from 8.31 to 8.74 km s^{-1}. The velocity increases from 8.74 km s^{-1} at 190 km depth to 8.78 km s^{-1} at 208 km depth. This forward branch is terminated by an abrupt decrease in velocity at 208 km depth. This structure lies at nearly the same depth as similar structures observed in the record sections for SP173 and SP245.

The SP035–NW data extends to sufficient range to record arrivals from the 410 discontinuity; however, the seismograms in this range exhibit what appears to be strongly scattered

arrivals. Bandpass filtering (0.2–1.25 Hz) improves the transition zone signal somewhat, but the SP035 waveforms do not allow the detailed interpretation that was possible for the SP245 waveforms. Nevertheless, applying the SP245–SE model to the SP035–NW seismograms results in a reasonable fit between the calculated and observed travel times and a fair correspondence between synthetic and observed seismograms. The observations show high amplitude arrivals from the 410 discontinuity to a range of 1620 km at 15 s reduced time. This arrival does not exist at closer ranges. The synthetics seismograms predict a similar falloff in amplitude at these ranges.

Fig. 3 shows the 1–D velocity–depth profiles for each shot point. We also indicate where these 1–D values plot approximately in two dimensions along the profile. The dark rectangles in Fig. 3 represent the position of zones of high velocity gradient that produce prominent arrivals on the record section. Data from both SP245 and SP035 constrain the 410 discontinuity but the moderate gradient between the 410 and 660 discontinuities and the 660 discontinuity are constrained only by the SP245 data.

The 2–D cross–section is perhaps more interesting for the region above the transition zone since the three shot points provide some overlapping coverage at these depths. One of the most prominent features of the record sections is the change in moveout of the travel time curve at about 1200 km distance. We model this observed feature as a rapid jump in P–wave velocity in the depth range 180 to 240 km. Above these depths, P–wave velocities are on the order of 8.2–8.5 km s^{-1}. Within the zone, P–wave velocities jump to as much as 8.8 km s^{-1}. The zone of high velocities appears to be thin layers approximately 40 to 45–km thick, below which consist of P–wave velocities drop to values around 8.6 km s^{-1}. This zone of high velocity or high velocity gradient exists in all three profiles and we identify it as the Lehmann (L) discontinuity [10], [11]. The L–discontinuity appears to be somewhat deeper (210–253 km) under the Siberian platform as observed on the SP245 record section but is about 40–km shallower on the SE part of the profile toward the Baikal rift zone (SP173 and SP035 observations).

Each shot point reveals considerable structure in the upper mantle between the M– and L–discontinuities. Because of the distance between shot points, correlation of zones of high velocity gradient between profiles is problematic. The observations may be revealing a thin,

97

highly variable, yet continuous structure at depths of 70 to 120 km in this region of Siberia. Alternatively, the arrivals could be caused by a thin, discontinuous lens of high–velocity material embedded in lower velocity mantle.

3 Discussion and Conclusions

Analyses of the seismograms from the RIFT profile indicate a prominent velocity discontinuity at 180 to 235–km depth which we identify with the L–discontinuity. Our model for the L–discontinuity consists of a thin zone of high velocity gradient sandwiched between thick zones of much lower velocity gradient. The L–discontinuity decreases from 235–km depth beneath the Siberian Platform to 180–km depth beneath the boundary of the Siberian Platform and the tectonically active zone containing the Baikal rift. Other structures similar to the L–discontinuity, thin zones of high–velocity gradient, are present in the uppermost mantle at various depths below the Moho. Our observations are too sparse to ascertain whether these are continuous features or a thin lens of high velocity/high gradient material embedded in the mantle. The increasing depth of the L–discontinuity beneath the shield agrees with the anisotropy models for the L–discontinuity [12], [13], [14].

The width of the 410 discontinuity is controlled by the near distance to which the critical reflection is observed (1580 km for SP245 and 1620 km for SP035 – Fig. 2a,c). However, the significant difference in the nature of the SP245 and SP035 phases returning from the 410 discontinuity suggests there are important lateral differences in the fine scale properties of this boundary but it is not clear at this point what these differences are. Ryberg *et al.* [16] also noted differences in the transition zone phase from the northern and southern shots on the QUARTZ profile.

Neves *et al,* [15] inverted the same seismograms from SP245 using a non–linear inversion scheme employing a genetic algorithm for optimization and the WKBJ method to compute the synthetic seismograms. They showed that the 410 discontinuity beneath the Siberian Platform was indeed broad but could be better modeled as a two–stage gradient structure with velocities increasing from 8.70 to 9.25 $km\,s^{-1}$ over a depth range of 400 to 415 km and from 9.25 to 9.60 $km\,s^{-1}$ over a depth range of 415 to 435 km. Following the suggestion

of Vidale and Benz [17] Mechie *et al* [6] modeled the 410 discontinuity as a first–order discontinuity at 420 km depths beneath the QUARTZ DSS profile which is located about 1200 km west of the RIFT profile. However, there are no clear indications of precritical reflections at near distance ranges in the QUARTZ profile data and the observed phases from the 410 could have been matched from structures with a $\sim$20 km thick gradient zone for the 410 discontinuity [18]. Vinnik and Ryaboy [19] found the 410 discontinuity to have a 20 km width beneath the East European Platform, whereas Egorkin *et al.* [4] show a first–order 410 discontinuity beneath the RUBIN and METEOR profiles in Siberia. However, it is not certain that the RUBIN and METEOR travel–time data require a first–order 410 discontinuity. In the analysis of the RIFT profile travel–time data Cipar *et al.* [5] modeled the 410 as a first–order discontinuity; however, amplitude modeling [7] required it to be a high gradient zone and this may also be the case for the 410–discontinuity beneath the RUBIN and METEOR profiles.

In this study, we examine P–wave observations from three nuclear explosions recorded along the RIFT profile across the Siberia Platform. A 1–D model is derived independently for each shot point and combined in a quasi–2–D cross–section (Fig. 3). This model shows considerable complexity in the structure above about 250–km depth. The Soviet Deep Seismic Sounding program provides a unique and irreplaceable data set for the study of the structure of the Earth's crust and upper mantle in Eurasia. The combination of high signal–to–noise nuclear sources and long–range recordings reveal structural details which cannot be observed on other extant data sets.

Acknowledgements

References

[1] Benz, H M., Unger, J.D., Leith, W.S., Mooney, W.D., Solodilov, L., Egorkin, A.V., and Ryaboy, V.Z. (1992) Deep Seismic Sounding in Northern Eurasia, *EoS*, **Vol. 73**, pp. 297–300.

[2] Yegorkin, A.V. & Pavlenkova, N.I. (1981) Studies of Mantle Structure of U.S.S.R. Territory on Long-range Seismic Profiles, *Phys. Earth planet. Inter.*, **Vol. 25**, pp. 12–26.

[3] Pavlenkova, N.I., and Yegorkin, A.V. (1983) Upper Mantle Heterogeneity in the Northern Part of Eurasia, *Phys. Earth planet. Int.*, **Vol. 33**, pp. 180–193.

[4] Egorkin, A.V., Zuganov, S.K., Pavlenkova, N.A., and Chernyshev, N.M. (1987) Results of lithospheric studies from long–range profiles in Siberia, in *Seismic Studies of the Continental Lithosphere*, eds Asano, S., and Mooney, W.D., *Tectonophysics*, **Vol. 140**, pp. 29–47.

[5] Cipar, J., Priestley, K., Egorkin, A., and Pavlenkova, N. (1993) The Yamal Peninsula–Lake Baikal Deep Seismic Sounding Profile, *Geophys. Res. Lett.*, **Vol. 20**, pp. 1631–1634.

[6] Mechie, J., Egorkin, A.V., Fuchs, K., Ryberg, T., Solodilov, L., & Wenzel, F. (1993) P-wave mantle velocity structure beneath northern Eurasia from long-range recordings along the profile Quartz, *Phys. Earth planet. Inter.*, **Vol. 79**, pp. 269–286.

[7] Priestley, K., Cipar, J., Egorkin, A., and Pavlenkova, N. (1994) Upper–mantle velocity structure beneath the Siberian platform, *Geophys. J. Int.*, **Vol. 118**, pp. 369–378.

[8] Cipar, J., and Priestley, K. (1997) Two–dimensional upper mantle velocity structure beneath the Siberian Platform from the RIFT profile data, in preparation for submission to *Geophys. J. Int.*.

[9] Fuchs, K., and Muller, G. (1971) Computations of synthetic seismograms with the reflectivity method and comparison to observations, *Geophys. J. R. astr. Soc.*, **Vol. 23**, pp. 417–433.

[10] Lehmann, I. (1959) Velocities of longitudinal waves in the upper parts of the Earth's mantle, *Ann. Geophys.*, **Vol. 15**, pp. 93–118.

[11] Anderson, D.L. (1979) The Deep Structure of Continents, *J. Geophys. Res.*, **Vol. 84**, pp. 7555–7560.

[12] Leven, J.H., Jackson, I., and Ringwood, A.E. (1981) Upper mantle seismic anisotropy and lithospheric decoupling, *Nature*, **Vol. 289**, pp. 234–239.

[13] Karato, S. (1992) On the Lehmann discontinuity, *Geophys. Res. Lett.*, **Vol. 19**, pp. 2255–2258.

[14] Gaherty, J., and Jordan, T. (1995) Lehmann Discontinuity as the Base of an Anisotropic Layer Beneath Continents, *Science*,**Vol. 268**, pp. 1468–1471.

[15] Neves, F.A., Singh, S.C., and Priestley, K. (1996) Velocity structure of upper–mantle transition zones beneath central Eurasia from seismic inversion using genetic algorithms, *Geophys. J. Int.*, **Vol. 125**, pp. 869–878.

[16] Ryberg, T., Wenzel, F., Mechie, J., Egorkin, A., Fuchs, C., and Solodilov, L. (1996) Two-dimensional velocity structure beneath northern Eurasia derived from super long–range seismic profile quartz, *Bull. Seism. Soc. Am.*, **Vol. 86**, pp. 857–867.

[17] Vidale, J.E., and Benz, H.M. (1992) Upper–mantle seismic discontinuities and the thermal structure of subduction zones, *Nature*, **Vol. 356**, pp. 678–683.

[18] Mechie, J., personal communications, 1995, 1997.

[19] Vinnik, L.P., and Ryaboy, V.Z. (1981) Deep structure of the East European Platform according to seismic data, *Phys. Earth planet. Inter.*, **Vol. 25**, pp. 27–37.

FIGURE CAPTIONS

Figure 1. Simplified tectonic map of Central Asia. The "RIFT" profile is marked by the heavy solid line and large solid dots denote the locations of the three nuclear explosions detonated along the profile.

Figure 2. (a) Record section of data from SP245 plotted with travel–times from Model T (upper panel) and synthetic seismograms for this model (lower panel) along with the travel–time curves for reference. (b) Record section of data from SP173 plotted with travel–times from Model T5–SE (upper panel) and synthetic seismograms for these models along with the travel–time curves (lower panel). (c) Record section of data from SP035 and SP036 plotted with travel–times from Model J1–NW (upper panel) and synthetic seismograms for this model along with the travel–time curves (lower panel).

Figure 3. Cross–section showing the derived 1–D velocity–depth function for each shot point (solid lines) and the approximate location along the profile where the structure is sampled. The density of the shading of the denotes the nature of the velocity gradient.

FIGURE 1

Travel Time - Distance/8.2 (sec)

SP245 Observed Data

Distance (km)

BP filter @ 0.2-1.25 Hz

Trace Normalized

Travel Time - Distance/8.2 (sec)

Synthetics - Model T
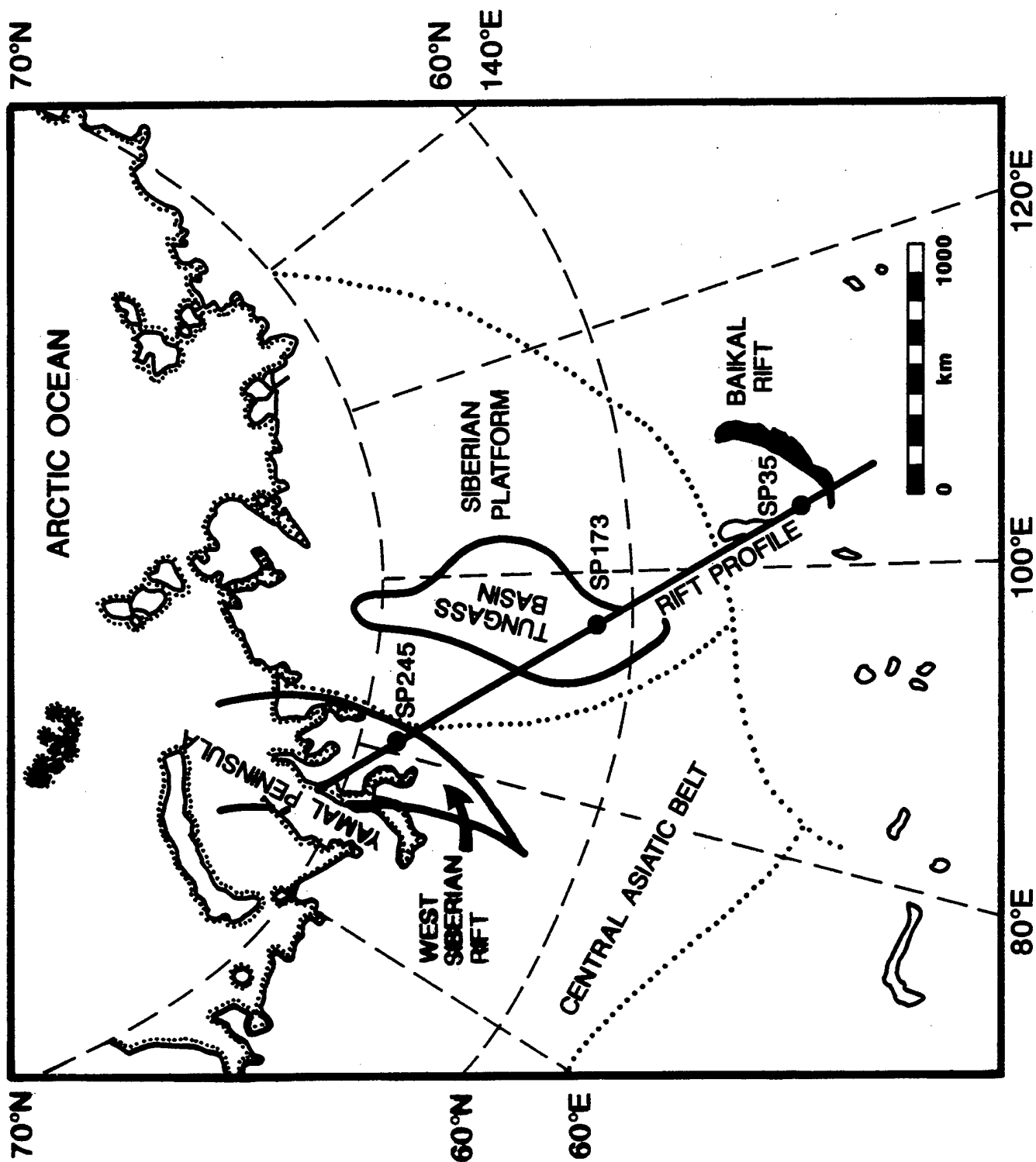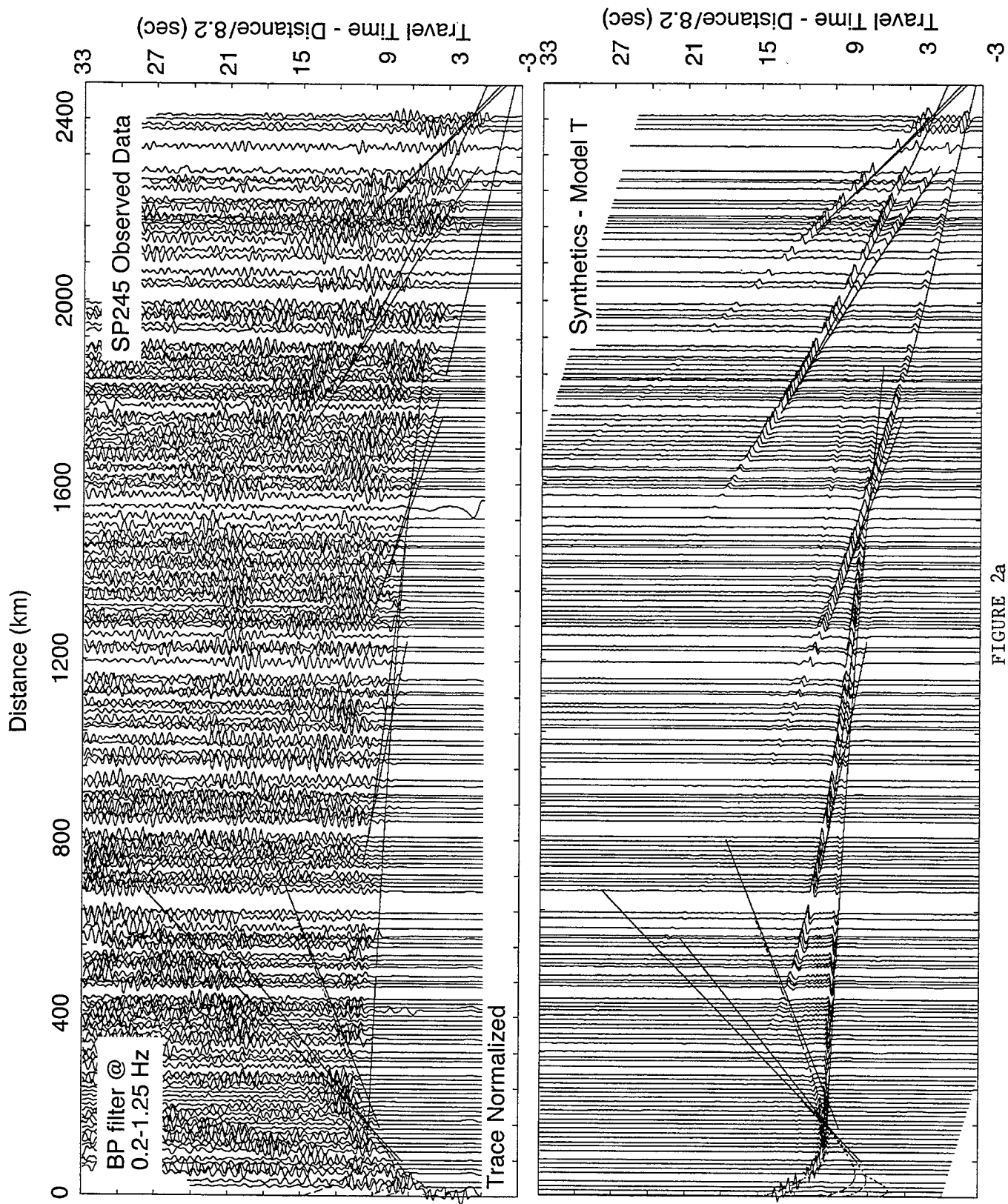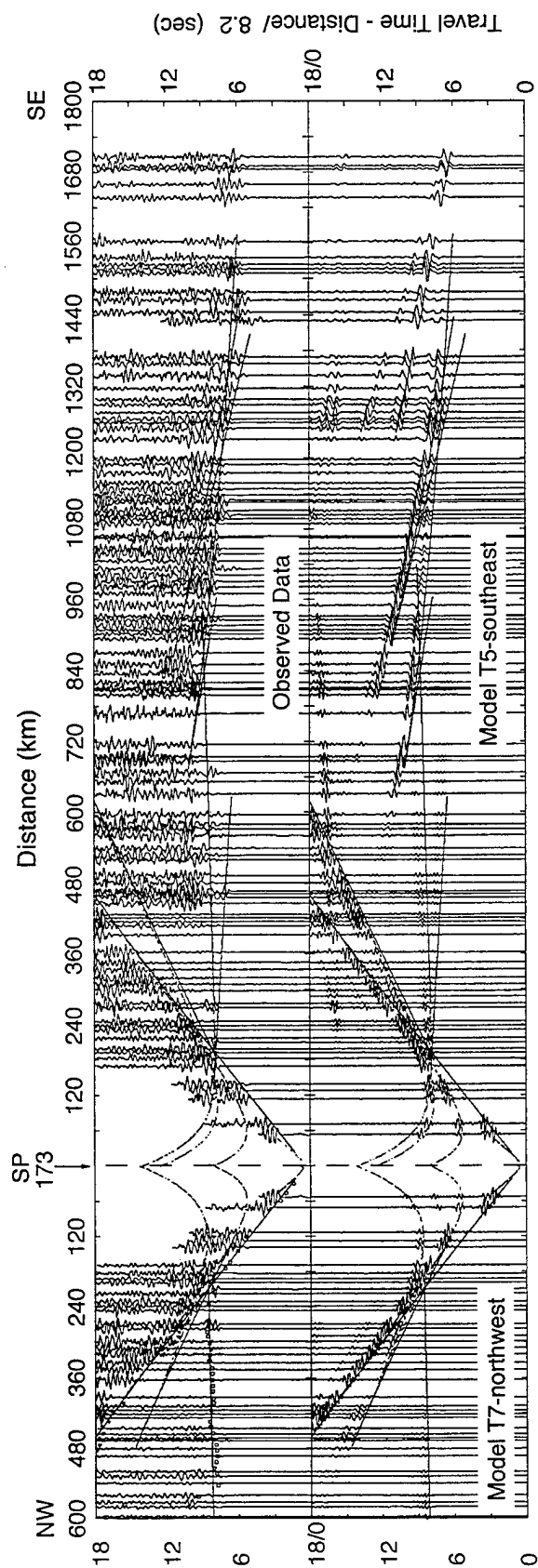
FIGURE 2a

DSS Rift Profile - Shot Point 173

FIGURE 2b
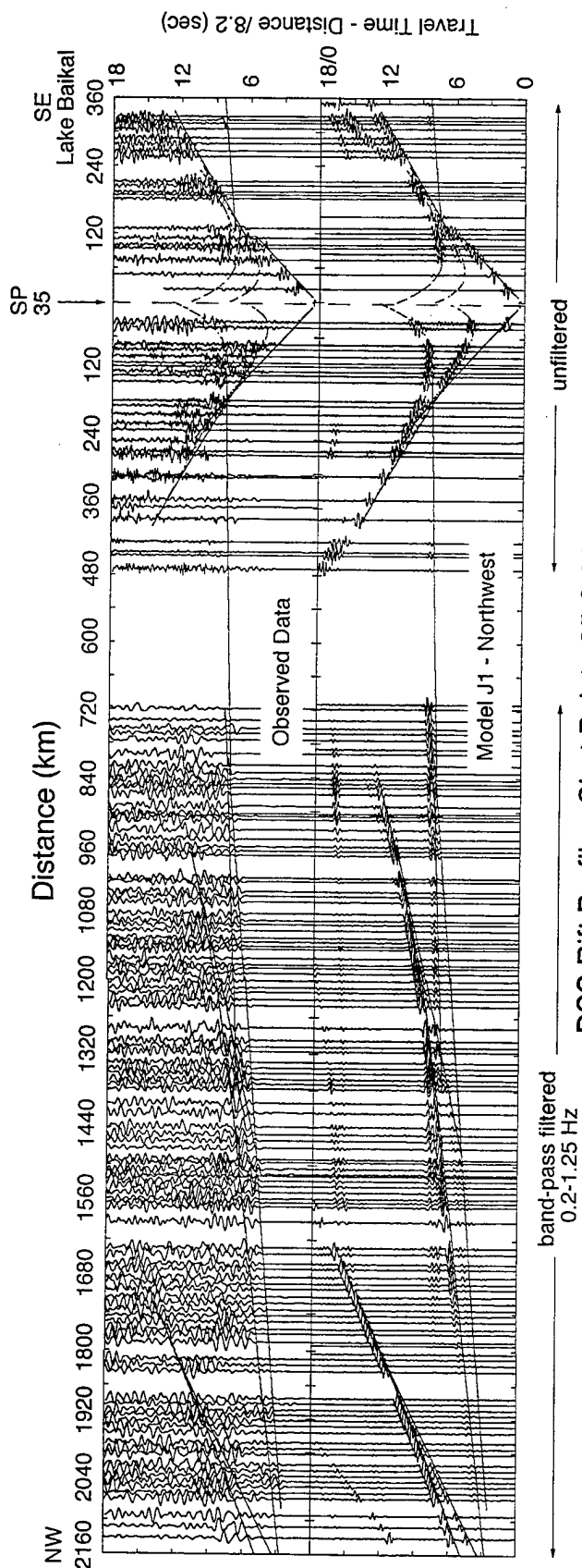
DSS Rift Profile - Shot Points 35 & 36

FIGURE 2c

105

FIGURE 3

106
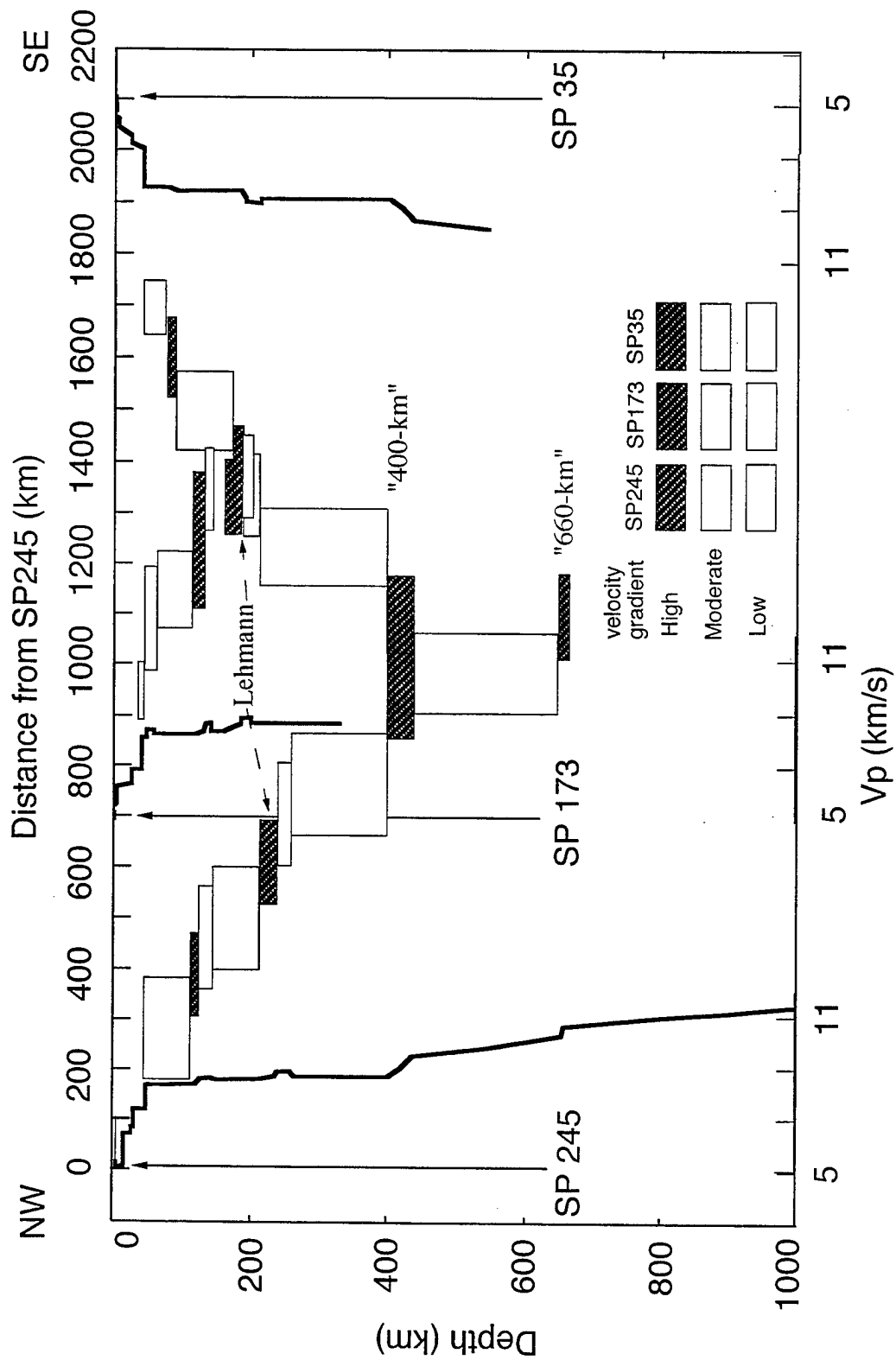
The receiver structure beneath the China Digital Seismograph Network stations

S. Mangino[1], K. Priestley

University of Cambridge, Bullard Laboratories

J. Ebel

Boston College, Weston Observatory

Abstract   Six new models of the crust and upper mantle velocity structure beneath the China Digital Seismograph are obtained by waveform modeling broadband teleseismic P–wave receiver functions. The models are based on several years' worth of high–quality broadband receiver functions from a broad range of azimuths. Surface geological observations were also used to constrain the models for these stations. The average crustal velocity beneath the CDSN stations is ~6.4 km s^{-1} and the crustal thicknesses are: MDJ, 36 km; BJI, 40 km; HIA, 39–40 km; KMI, 50 km; LZH, 58 km. The crust and uppermost mantle beneath HIA, MDJ, BJI, KMI and LZH are characterized by relatively simple horizontally layered structure, while at WMQ a dipping near-surface structure best fits the data.

Introduction

China is a composite of several tectonic blocks delineated by suture zones and mountain belts (Figure 1). The four largest tectonic units are the Sino–Korean Platform, the Yangtze Platform, the Tibetan Plateau and the Tarim Basin. The Tarim Basin and the Sino–Korean Platform are believed to have formed the "nucleus" of paleo-China, on to which the other land masses accreated during the Phanerozoic, but the relative timing of emplacement, the number of terrains and their boundaries are debated (*see* Gilder *et al.*, 1990; Hsu *et al.*, 1990; Zhao *et al.*, 1990; Huang and Opdyke, 1991; Shangyou, 1991; Metcalfe, 1996; Packham, 1996). The eastern half of China is affected by circum–Pacific tectonics and back arc extension associated with the convergence between the Philippine and Australian Plates and the Eurasian Plate. The tectonics of western China are dominated by the collision of the Indian and Eurasian Plates resulting in the uplift of the Tibetan Plateau. The earthquakes within the N–S trending seismogenic belt between ~100–107°E are thought to result from the northeastward displacement of Tibet (Avouac and Tapponnier, 1993).

---

[1] Now at: Center for Monitoring Research, Arlington VA, USA

There have been a number of studies concerned with the crustal structure of China, primarily by seismic refraction. In this study we examine the crustal structure beneath six stations of the Chinese Digital Seismic Network and compare the crustal structure using this method with published estimates of crustal structure in China.

Data and Analysis

The Chinese Digital Seismic Network (CDSN) stations (Figure 1, Table 1) consist of a three-component Streckeisen STS–1 seismometer recorded on 16 bit data loggers designed by the U.S. Geological Survey Albuquerque Seismological Laboratory. The broadband channels are digitized at 20 sps and have a flat velocity response between 0.05–5.0 Hz (Peterson and Kexin, 1987). The CDSN seismograms used in this study were selected by searching the 1987–1994 *Preliminary Determination of Epicenter* bulletins for $m_b \geq 5.7$ earthquakes in the epicentral distance range 30°–90°. The waveforms were obtained from either the Incorporated Research Institutions for Seismology Data Management Center or Harvard University.

The use of receiver functions to determine crustal structure beneath a three-component broadband seismograph is now a well–established technique (*see* Langston, 1979; Owens *et al.*, 1984; Ammon *et al.*, 1990). We compute true amplitude receiver functions (Langston, 1979; Ammon, 1991) and lowpass filtered these at 0.4 Hz. Those receiver functions whose averaging functions (Cassidy, 1992) resembling a narrow Gaussian pulse and which clustered in backazimuth and epicentral distance were stacked and the ±1 standard deviation (σ) bounds calculated. These bounds were used to evaluate how well particular phases of the waveform are determined. Tables 2 and 3 list the events comprising the stacks for each station. Horizontally layered crustal velocity models were determined using the inversion routine of Ammon *et al.* (1990). We simplified the velocity model by averaging the acceptable inversion models and collecting adjacent layers of similar velocities into single layers to form a more "coarse" velocity model. We then used forward modeling to test the significant features of these simplified models to estimate how well they were constrained by arrivals in the data. The receiver function for station WMQ shows indications of planar dipping interfaces. For this reason we did not invert the WMQ receiver function but used the ray tracing routine of Langston (1977) to forward model these data. Starting models were constructed from published studies of crustal structure in the vicinity of the CDSN stations. Acceptable models were taken as those physically realistic velocity models whose

synthetic receiver function lay within or close to the $\pm 1\sigma$ bounds of the most significant observed P–to–S phases.

Receiver Structure beneath the CDSN stations

Hailar (HIA). HIA is located on the Hulun-Buir Plateau in northeastern China (Figure 1). Rocks exposed at the surface are predominantly granites with some basalts (Peng, 1986). The crustal thickness beneath the Hulun–Buir Plateau has been estimated to be 38–40 km thick in controlled source experiments (Yuan *et al.*, 1986), ~45 km thick from surface wave analysis (Rui *et al.*, 1981), and 40 km thick from regional P and PP waveform modeling (Beckers *et al.*,1994).

HIA receiver functions (Fig. 2) each consisting of a stack of several events were determined for four azimuths. All have a large amplitude positive arrival at ~4 s (Ps). This is followed in the SE receiver function by a prominent positive arrival at 13–15 s (PpP_ms) and a negative arrival at 17–19 s ($PpS_ms + PsP_ms$). The SE tangential receiver function has the lowest amplitude; the NE tangential receiver function has a large amplitude arrivals between 7–12s, and the NW tangential receiver function has large amplitudes during the first 10 s.

The four radial receiver functions were inverted for a one–dimensional model using a starting model derived from the crustal models of Rui *et al.* (1981) and Beckers *et al.* (1994). All of the inversion models (Fig. 3) have a high velocity near–surface layer between 3–6 km depth, a thin low velocity layer between about 6–10 km depth, and a gradational Moho between 38–42 km depth. The velocity in the mid–crust (about 10–30 km depth) varies between the models, but the velocity discontinuities are relatively small and the average velocities are similar. For example, between 12–30 km depth, the NE models have a 9 km thick ~5.9 km/s layer that overlies a 9 km thick ~6.35 km/s layer, while the SE models have a 9 km thick ~6.35 km/s layer that overlies a 9 km thick ~5.9 km/s layer. These small variations are probably not significant.

The inversion models were simplified and the main model features tested using forward modeling. The upper mantle velocity was fixed at 8.0 km/s in the forward modeling since receiver functions are relatively insensitive to this parameter. A greater emphasis was placed on fitting the HIA-SE $\pm\sigma$ bounds since the receiver function from this azimuth had the lowest tangential amplitudes. Two forward models were examined (Fig. 4). Model A is a simplified model from the average of all the HIA inversion results; Model B has all of the same features except for the shallow, thin (3 km thick), low velocity (V_p 5.8 km/s) layer in Model A. A comparison of the synthetics with the observed data shows that the most

significant velocity discontinuity beneath HIA is the Moho. Model A synthetics yield a marginally better fit to the negative motion at 2–3 s and to the peak amplitude of the 4 s Ps Moho phase. The motion at 2–3 s is fit with reverse polarity Ps and PpP$_h$s arrivals generated at the top of the low velocity layer, and the peak amplitude of the 4 s Ps Moho phase is augmented by the simultaneous arrival of the PpS$_h$s phase. Both models have an 8 km thick positive gradient (6.3 km/s to 8.0 km/s) between 32–40 km depth, the base of which defines the crust mantle boundary. The presence of the gradational Moho provides a broader and lower amplitude PpP$_m$s and and also provides PpS$_m$s phases that fit the data better than do the synthetics generated from a single–step Moho model.

Mudanjiang (MDJ). MDJ is situated in the Laoye–Ling Mountains in northeastern China (Figure 1). There are two known and several inferred faults present near the station (Haomin *et al.*, 1989). Published estimates of crustal thickness in this region vary over a large range. The crustal thickness in the vicinity of MDJ has been determined to be 42–43 km thick from surface wave modeling (Rui *et al.*, 1981), 34–36 km thick from modeling gravity data (Yuan *et al.*, 1986; Zhilong *et al.*, 1986), and 27 km thick from regional P and PP waveform modeling (Beckers *et al.*, 1994).

MDJ receiver functions for four azimuths are shown in Figure 5. The NE and NW receiver functions consist of single events and the SE and SW receiver functions are stacks of several events each. The SE and SW waveforms are very similar in that the radial receiver functions have a low amplitude positive arrival at 4 s and a larger amplitude positive arrival at 15 s. Except for the impulsive first arrival, the SE and SW tangential receiver functions have low amplitudes. The NE and NW radial receiver functions both have a large amplitude positive arrival at 4 s but following this the waveforms are considerably different. The NE radial receiver function has a large negative arrival between 4 and 8s but this occurs at the same time as a large arrival in the tangential receiver function. The NW radial receiver function has a broad, positive arrival between 14 and 15s, followed by a lower amplitude negative arrival between 17 and 18s. The NW tangential amplitude is moderately high throughout the whole interval where the crustal conversions and reverberations are expected.

All four MDJ receiver functions were inverted for a one–dimensional crustal model and the results are shown in Figure 6. We have greater confidence in the SE and SW crustal models since these models are derived from receiver function stacks. All four models indicate that the crust is 36–42 km thick beneath MDJ. The large amplitude negative arrival at 7–8 s in the NE receiver function requires

a converted phase generated in the mid–crustal low velocity. The SE and SW models differ most at the near surface. Between 0–6 km depth, the layer velocities oscillate from 5–6.2 km/s in the SE models, while the SW models show a positive velocity gradient from 5 to 6 km/s. Between 12 and 35 km depth both the SE and SW models have a nearly constant velocity. The NW models have a positive gradient at the near surface, a negative gradient between 5 and 33 km depth, and a positive gradient below 33 km that reaches upper mantle velocity below 42 km depth.

The MDJ forward modeling tests of the simplified inversion model are shown in Figure 7; the parameters of the final model are tabulated in Table 4. Models A, B and C were derived from the average inversion result of the SE, SW and NW receiver functions, respectively. The main difference between the SE, SW and NW radial receiver functions result from differences in the near–surface velocity structure. Model A has a velocity step at 6 km depth (h) while Model B has a similar step at 3 km depth. The P–to–S phases generated at this interface control the first few seconds of motion in the radial receiver functions. The negative amplitude PpS_hs phase in model A destructively interferes with the 4–5 s Ps / Moho phase. Decreasing the depth to the interface h shifts the PpS_hs arrival to 2–3 s, which matches the negative motion at this time in the NW receiver function. The Ps Moho arrival is larger in the NW data than in the SE and SW receiver functions because the PpS_hs near–surface multiple arrives earlier.

The synthetics generated from Model B have a broader PpP_ms phase which better matches the NW receiver function than do the synthetics generated from model A, but the waveform after this time is not well matched by either model. A comparison of the NW models and Model A suggests that the crust thickens toward the northwest beneath MDJ. This variation is consistent with the previous estimates of crustal thickness in this region (Yuan et al., 1986).

Beijing (BJI). BJI is situated on the northwestern margin of the North China Basin (Figure 1), which consists of several NNE and EW trending basement graben structures overlain by recent fluvial and lacustrine sediment (Zhao and Windley, 1990; Allen et al., 1996). Hellinger et al. (1985) examined the development of the basin using the extension model of McKenzie (1978) and found its evolution involving rapid lithospheric stretching and crustal thinning followed by thermal subsidence. Allen et al. (1996) suggest that at present the North China Basin is in a post-rift phase of lithospheric cooling and thermal subsidence. Chen and Nabelek (1988) suggest that the North China Basin is a "pull–apart" basin between sub-parallel NNE trending strike–slip faults (Tanlu Fault Zone).

Four BJI receiver functions, each consisting of a stack of several events, were determined (Figure 8). The NW radial receiver function has three large amplitude arrivals: positive arrivals at 5–6 s (Ps) and 16–17 s (PpS_mS), and a negative arrival at 17–19 s (PpP_mS). The Ps arrival in the NW receiver function correlates with arrivals in the other three radial receiver functions; however, the multiple phases in the NW receiver function are difficult to identify in the other receiver function. The four tangential receiver functions have moderate amplitudes. These azimuthal variations in the receiver functions may be due to scattering of P-wave energy within the graben structures east of BJI, but may also indicate a laterally heterogeneous receiver structure which cannot be described in terms of a one-dimensional crustal model.

The crustal structure in the vicinity of BJI is better constrained than in most areas of China. Shaoquan *et al.* (1981) used recordings of explosions on the Beijing regional seismograph network and determined that the crust is 37 km thick, the P_n velocity varies between 7.9–8.1 km/s, and the Moho dips 2° NW beneath BJI. Shedlock and Roecker (1987) estimate a 35 km thick crust and an upper mantle P-wave velocity of 8.0 km/s from travel time residuals of regional and teleseismic earthquakes. East of BJI, near the epicenter of the 1978 Tangshan earthquake, Shedlock and Roecker (1987) infer a low velocity zone (V_p 5.8 km/s) between 20 and 35 km depth and an upper mantle velocity of 7.9 km/s. Changquan and Shixu (1986) also find evidence for a mid–crustal low velocity zone beneath the Cangzhou–NW seismic profile near Tangshan. South of BJI, the Cangzhou–NW refraction results (Wucheng *et al.*, 1989) indicate a complex crustal structure. From the surface and 4 to 7 km depth there are several graben structures filled with 3.0–4.6 km/s sediment that overly a 5.5 km/s basement. There is a broad low velocity zone in the mid–crust (V_p ~5.85 km/s) centered near 18 to 20 km depth, and a 5 to 7 km thick gradational Moho reaching an upper mantle velocity of 8.0 km/s between 42 and 44 km depth. One refraction profile passes within ~25 km of BJI (Xuezhong and Jiaru, 1989) and is oriented approximately parallel to the azimuths of the BJI–NW and SE stacked data. The crustal model from these data do not show a mid–crustal low velocity zone, nor do they resolve the velocity structure of the crust shallower than 8 km.

Figure 9 shows the inversion results for the four BJI receiver functions. The NW crustal models all have a strong positive gradient from the surface to 5–7 km depth, a weak positive gradient between about 7 and 36 km depth, and gradational crust–mantle transition with velocities increasing from 6.6–7.0 km/s to 7.8–8.0 km/s between 36–42 km depth. The BJI–NE, SE and SSE inversion results have similar velocity–depth profiles, indicating a low velocity zone near

~30 km depth. Although a mid–crustal low velocity layer has been identified across the North China Basin by other workers, the azimuthal variation in the NE, SE and SSE receiver functions in this study suggests that the differences between the NW model and the NE, SE and SSE models may be the result of fitting off–azimuth arrivals with P–to–S phases generated at horizontal interfaces.

The results of the forward modeling test of the BJI inversion models are shown in Figure 10. In the forward modeling the P_n velocity was fixed at 8.0 km/s. Figure 10 compares synthetic receiver functions for four simple crustal models with the observed receiver function. Model A has a uniform velocity between 5 and 38 km depth and a gradational Moho between 38 and 42 km depth, Model A1 is identical to Model A except that the Moho is a first order discontinuity, Model B has the same uniform crustal velocity but a first order discontinuity Moho at 39 km depth, and Model C has a uniform velocity upper crust of 6.4 km/s to 25 km depth, an uniform velocity lower crust of 6.7km/s below 25 km depth, and a gradational Moho between 38 and 42 km depth (Figure 10). Models C follows the averaged inversion result more closely than Models A and B. The synthetic receiver function from Models B significantly overestimates the amplitude of the PpP_ms arrival. The velocity contrast across the mid–crustal interface i produces an increased amplitudes of the PpP_is and PpS_is phases which better match the observed waveform.

Kunming (KMI). KMI is situated to the southeast of the Tibetan Plateau in central China (Figure 1). The most significant tectonic features in the vicinity of the station are several north–south trending strike–slip faults with over 100 km of surface rupture (Kechang *et al.*, 1989). The near–surface rocks in the region are mostly Paleozoic and Triassic carbonates, which have been eroded to form a karst landform (Peng, 1986). Two crustal refraction studies have been conducted in this region. West of KMI, beneath the Jiangchuan–Eryuan profile, the crustal thickness increases from ~45 km near Jiangchuan to ~50 km near Eryuan, and the P_n velocity 8.0±0.1 km/s (Kan *et al.*, 1986). East of Eryuan they identify two prominent intra–crustal boundaries: a velocity increase from 6.0 to 6.4 km/s at ~15 km depth, and a velocity increase from 6.4 to 6.85 km/s at ~35 km depth. The results of the Malong–Simao seismic survey (Qizhong *et al.*, 1985) indicate that southwest of Malong, the crust is 43 to 45 km thick with an average velocity of ~6.3 km/s and an upper mantle velocity of 8.15 to 8.20 km/s.

KMI receiver function stacks have been determined for three azimuths (Figure 11). There is a large amplitude positive arrival at 5 s on each radial receiver function, but after about 7 s the waveforms are different. The NE tangential receiver

function has an impulsive first motion followed by a second, large amplitude arrival between 12–20 s. The amplitude of the SE tangential receiver function is the lowest of all three back azimuths, and the amplitude of the NW tangential compared to the corresponding motion on the radial receiver function is also low. These azimuthal variations indicate a laterally heterogeneous receiver structure. The 5 s phase on the radial receiver functions may be the Moho Ps phase, but the corresponding multiples generated at the same depth boundary are not clearly identified.

Figure 12 shows the KMI–NE, SE and NW inversion result. The inversion model from the NE receiver function is poorly constrained, probably due to attempting to fit the off azimuth arrivals between about 10–20 s. At the near surface and at 20 km depth the velocity in the SE varies by $\sim$1.5 km/s although the corresponding synthetic receiver functions are very similar. It is difficult to estimate the significance of the features in either of these models in terms of a one-dimensional structure given the level of the off–azimuth arrivals in the data. The NW result has a much lower tangential component and a relatively well–defined structure: a step in velocity at 12 km depth, a second interface at 33 km depth and a crust mantle boundary between 48 and 51 km depth. These features are similar to the previously identified intra–crustal discontinuities in the seismic refraction results to the east in Eryuan.

Figure 13 (top) shows the KMI–NW forward modeling result. The upper mantle velocity was fixed at 8.15 km/s, based on the average P_n velocity near Malong (Qizhong $et\ al.$, 1985) and the P_n velocity east of Eryuan (Kan $et\ al.$, 1986). A comparison between Model A and the averaged inversion result shows that most of the fine–scale crustal structure of the inversion models can be removed without significantly increasing the misfit between the synthetic and observed receiver functions. Table 6 gives the parameters of KMI Model A. The thickness and average velocity of the upper crustal layer, as well as the velocity contrast across $i1$, controls the shape of the first 6 to 7 s of the waveform. The Ps phase generated at $i1$ fits the low amplitude positive arrival at 2 s, and the $PpP_{i1}s$ and $PpS_{i1}s$ phases interfere with the Ps Moho phase to yield a single pulse at $\sim$5 s. This is demonstrated by comparing the synthetic computed from Model B, which has a single 6.1 km/s upper and mid-crustal layer, to the data (Figure 13 bottom). Model B's synthetic has a broad, twin peaked arrival between 4 and 6 s which does not fit the data. The most significant phases from interface i2 are $PpP_{i2}s$ and $PpS_{i2}s$ multiples that fit the waveform between 13 s and 17.5 s. The $PpP_m s$ and $PpS_m s$ phases arrive at $\sim$20 s and 25 s, respectively. At KMI the crust is $\sim$50 km thick, the average velocity is $\sim$6.45 km/s and the Moho beneath KMI

is best fit with a sharp discontinuity. These results indicate that the crust and upper mantle structure east of Eryuan are very similar to the crust and upper mantle northwest of KMI.

Lanzhou (LZH). LZH is located in central China near the northeastern boundary of the Tibetan Plateau (Figure 1). The most significant tectonic feature in the vicinity of LZH is the Haiyuan Fault. Gaudemer *et al.* (1995) suggest that the net motion across this left-lateral strike-slip fault is consistent with the northeastward motion of Tibet relative to Eurasia. There are significant differences in the previous estimates of crustal thickness (51–68 km) and upper mantle velocity (V_p 8.0 ±0.2 km/s) in the region of LZH. Jinchang and Zengyi (1989) and Liang and Li (1991) propose that the crust is ~51–53 km thick and the upper mantle P–wave velocity is ~7.9 km/s. Yuan *et al.* (1986) show a 52–54 km thick crust with a SW dipping Moho. In contrast, Zhao and Xie (1993) obtained a crustal thickness of 68±5 km and an ~8.0–8.1 km/s upper mantle velocity from P_n travel time tomography. The preferred model of Zhao and Frohlich (1996) indicates that the crust is 63–64 km thick beneath LZH with an upper mantle velocity of 7.8 km/s.

Figure 14 shows the LZH receiver functions for four backazimuths. The NE, SE and W receiver functions each consist of stacks of several events while the S back azimuth is a single event receiver function. All of the radial components have a large amplitude positive arrival between 6 to 7 s, but after this time correlation between the phases is poor. If the 6 to 7 s arrival on the radial receiver functions is the Ps phase generated at the Moho, then the positive arrival at ~22 s in the NE, SE and S receiver functions is the PpP_ms multiple. The W tangential receiver function exceeds the amplitude of the W radial; the SE tangential receiver function has large amplitude arrival at 7–14 s; the level of the tangential energy is moderate in the NE and S tangential receiver functions over the time span in which the crustal conversions and reverberations are expected.

Since the amplitude of what we infer to be the Moho phases rises above the level of the tangential arrivals on the NE, SE and S receiver functions, these arrivals were inverted for one–dimensional crustal models (Figure 15). The NE and SE models contain a single family of models, while the S result has two families of models with synthetic receiver functions that fit the data without a significant difference in waveform misfit. All the models predict a 55 to 60 km thick crust beneath the station, but there are differences between the models for each back azimuth. For example, the SE and S models have a strong positive gradient at the near surface while the NE model has relatively higher and constant velocities.

115

The NE model has a 0.5 to 0.7 km/s step in velocity at 15 km depth; the SE model has relatively constant velocities and a low velocity layer, and the S model also has a low velocity layer. Given the amplitude levels on the tangential receiver functions, these differences are probably not significant.

These results were combined into a single model and simplified for further investigation by forward modeling (Figures 16). During the forward modeling tests the upper mantle was fixed at 8.0 km/s. These tests showed that the LZH radial receiver functions can be fit with P-to-S phases generated by two features: a low velocity near–surface layer that overlies a higher velocity basement, and a gradational Moho. The near–surface layer is required to fit the large amplitude negative arrival at 2.5 s as well as the arrivals between this and the Ps Moho phase at 6 to 7 s. This low velocity near–surface layer is consistent with the surface loess deposits on which the station is sited (Peterson and Kexin, 1987). These tests also show that a gradational Moho gives a better fit to the data than does a first–order discontinuity. The LZH forward modeling tests have demonstrated that the presence of a low velocity near–surface layer dominates the first few seconds of the radial receiver functions. The total crustal thickness is ~58 km with an average velocity of ~6.4 km/s, and the Moho is best fit with a 6 km thick transition zone.

Figure 17 compares the synthetic radial component receiver function computed from the preferred LZH model given by Zhao and Frohlich (1996) to the NE, SE and S data. The synthetics generated from this model yield a poor fit to the LZH data. Zhao and Frohlich (1996) estimate that the average velocity of the upper 43 km of crust beneath LZH is 5.42 km/s and 5.88 km/s for the entire crust. These values are unusually low compared to the average crustal velocities of 6.25–6.30 km/s in the vicinity of LZH reported by Mooney (written communication). A starting model for the inversion procedure was determined based on forward modeling.

Urumqi (WMQ). WMQ is situated on the northern flank of the Tien Shan Mountains in northwestern China (Figure 1)which consist of several sub–parallel, roughly east–west trending ranges that extend for ~2500 km across central Eurasia. Near WMQ the north–south dimension is ~150 km. North of WMQ is the Junggar Basin, a roughly triangular shaped intra–continental sedimentary basin (Figure 1) with dimensions ~320 km NS and ~700 km EW. Previous estimates of the crustal thickness in this region range from 46 km (Gao and Richards, 1994) to 52 km (Beckers *et al.*, 1994).

Figure 18 shows the WMQ radial and tangential receiver functions. The waveforms are different for each back azimuth and the relative amplitude of tangential

to radial at WMQ is the highest of all the CDSN stations. The direct P–wave arrival on the NE radial receiver function has a relatively broad pulse, the direct P–wave arrival on the SE radial receiver function has a relatively narrow pulse, and the SW and NW arrivals have pulse widths that are intermediate between these two extremes. The peak amplitude arrival time of the direct P–wave on the NW radial receiver function is delayed by ~1.0 s compared to the other three stacks. With the exception of the SE receiver function, the amplitudes of the NE, SW and NW tangential waveforms are larger than the corresponding radial arrivals. These observations indicate a laterally heterogeneous receiver structure. The polarity of the first arrival on the tangential receiver functions reverses between the SE and SW data, and reverses again between the NW and NE data. Because of the large variation in the four WMQ radial receiver functions and the large amplitude in the tangential receiver functions, inverting the data for a one–dimensional structure is not justifiable. Instead we have examined the WMQ receiver structure using forward modeling by perturbing the crustal model of Gao and Richards (1994, 1995).

Figure 19 shows a suite of 23 WMQ radial and tangential receiver functions. The first arrival on the tangential receiver functions alternates from positive to negative between 140° and 163° back azimuth, and from negative to positive between 295° and 15° back azimuth; there is also a significant time delay of the direct radial P–wave between about 245° and 030° back azimuth. Simple polarity reversals in tangential receiver functions such as these occur when there is a plane–dipping, high contrast interface beneath the site (Langston, 1977a). The reversal in the tangential polarity between event at 31° and 57° indicates a northwest dipping interface with a strike between N230°E and N253°E. Gao and Richards (1995) have also note the presence of a dipping interface beneath WMQ. Figure 20 shows that the delay of the peak amplitude arrival times of the direct P–wave on the radial receiver functions has a maximum of between 270° and 030°. Owens and Crosson (1988) show that such an azimuthal variation can result from a dipping interface between a lower velocity surface layer and a higher velocity basement. This interpretation for the WMQ receiver function is consistent with the northward dip of the sediment–basement contact at the southern boundary of the Junggar Basin (Xiling and Guojun, 1989; Hongze, 1992) but is different from that of Gao and Richards (1995) who analyzed P–wave polarization data at WMQ and suggest that the dipping interface beneath WMQ is the Moho.

Figure 21 compares synthetic receiver functions computed for the model of Gao and Richards (1994; 1995) with the observations. Model A is their crustal model but with a gradational Moho which has no dip; Model B is the same crustal

model with a first–order discontinuous Moho which strikes N240°E and dips 30°. The synthetics for neither model match the arrival time delays and the pulse width variations on the radial receiver functions or the large amplitude tangential waveforms.

We have determined a crustal model for WMQ by starting with the crustal model of Gao and Richards (1994; 1995) from Figure 21, assuming a shallow dipping interface as suggested by Figure 20, and modeling the data by trial–and–error forward modeling. The range in strike of the dipping interface was constrained by the polarity variations in Figure 19 and the magnitude of the dip was constrained by the tangential P–wave amplitude. During the forward modeling, an improvement to the synthetic waveform fit for one back azimuth sometimes resulted in the degradation to the fit in a different back azimuth. These trade–off effects suggest that the actual structure is three-dimensional. Because of the large tangential to radial amplitude, only the first few seconds of the WMQ receiver functions can be confidently modeled with a planar dipping layered structure.

Figure 21 shows the WMQ forward modeling result, and Figure 22 shows the fit of the delay of the synthetic direct P–wave arrival to the observations. Model D has two interfaces at 4 and 8 km depth dipping 18° to the northwest. Below ∼12 km depth the velocity structure is similar to that of Gao and Richards (1994, 1995). The parameters of this crustal model are tabulated in Table 7. The upper crust of this model is consistent with the shallow seismic prospecting results across the southern margin of the Junggar Basin to the west of WMQ (Xiling and Guojun, 1989; Hongze, 1992; Avouac et al., 1993). These show that the thickness of Mesozoic and Tertiary aged sedimentary rocks increase rapidly from 0.0 km to more than 12 km thick along the southern margin of the Junggar Basin. At the southern edge of the basin the sediment–basement contact has a 10°–20° dip northwards toward the basin center, and the basement shows several down–stepping normal faults.

The receiver function analysis of the WMQ data revealed the presence of a NW dipping structure in the upper 4 to 8 km beneath the station. Below ∼12 km depth, the velocity model of Gao and Richards (1994, 1995) matches the data well. This analysis has shown that the azimuthal variations of the WMQ receiver functions are primarily due to the near–surface structural differences between the Junggar Basin and the Tien Shan Mountains.

Discussion

The crustal velocity structure beneath six CDSN stations has been determined

by inverse and forward modeling of stacked and single event teleseismic receiver functions (Figure 23). The phases modeled in this study were the Ps , *PpPs* and *PpSs* phases generated at the two highest impedance interfaces, the Moho, and the interface between the low velocity near–surface layer and the crystalline basement. These are the best constrained features of the crustal models. CDSN models beneath HIA, MDJ, BJI, KMI, and LZH are characterized by relatively simple horizontally layered structure, while at WMQ, a dipping layered model was required to fit the data. A gradational Moho exists beneath HIA and KMI. The crustal thicknesses are: MDJ, 36 km; BJI, 40 km; HIA, 39-40 km; KMI, 50 km; LZH, 58 km and WMQ, 46 km, these Moho depths generally agree with the Moho depth map (Figure 24) of Yuan *et al*, 1986.

The crustal models in Figure 23 are consistent with some published estimates of crustal structure near to the CDSN stations, but not others. Zhao and Frohlich (1996) determined a 63–64 km thick crust with an unusually low average velocity of ~5.8 km/s beneath LZH from the inversion of a single receiver function. We find the crust beneath LZH to be 58 km thick crust and with an average velocity of ~6.4 km/s. It is not clear how Zhao and Frohlich (1996) estimate the effects of lateral variations in structure in the vicinity of LZH. It is noteworthy that our receiver function model for LZH is similar to the first iteration result discussed in Zhao and Frohlich (1996), which has a single 56 km thick 6.6 km/s layer representing the crust.

We find that except for the location of the dipping interface, our WMQ receiver functions are well fit by the crustal model of Gao and Richards (1994, 1995). We place the dipping interface in the upper crust and where it forms part of the Tien Shan – Junggar transition; Gao and Richards (1994, 1995) locate the dipping interface at the Moho. The one-dimensional model of Gao and Richards (1994) was developed by modeling regional waveforms from an explosion at a Chinese nuclear test site located approximately 240 km south of WMQ. This model represents the average structure along the travel path rather than the structure beneath the station. Gao and Richards (1995) suggest that a dipping Moho is present beneath WMQ, based on P–wave polarization anomalies. In the determination of this result, these authors limited the source of their polarization anomalies to be within a 15 km thick layer centered at Moho depth (46 km) and they fixed the P–wave velocity above and below our layer. The results of our study have shown that a near–surface dipping structure fits the observed data better than a dipping Moho at WMQ. Our results are also consistent with the laterally heterogeneous near surface geology of the Junggar Basin.

References

Allen, M.B., D.I.M. Macdonald, Z. Xun, S.J. Vincent & C. Brouet-Menzies, 1996. Early Cenozoic two-phase rifting and Late Cenozoic thermal subsidence and inversion of the Bohai Basin, northern China, (manuscript).

Ammon, C.J., 1991. The isolation of receiver effects from teleseismic P waveforms, *Bull. seism. Soc. Am.*, **81**, 2504–2510.

Ammon, C.J., G.E. Randall & G. Zandt, 1990. On the resolution and non-uniqueness of receiver function inversions, *J. geophys. Res.*, **95**, 15303–15318.

Avouac, J.P., & P. Tapponnier, 1993. Kinematic model of active deformation in central Asia, *Geophys. Res. Lett.*, **20**, 858–898.

Avouac, J.P., P. Tapponnier, M. Bai, H. You & G. Wang, 1993. Active thrusting and folding along the northern Tienshan and late Cenozoic rotation of the Tarim relative to Dzungaria and Kazakhstan, *J. geophys. Res.*, **98**, 6755–6804.

Bäth, M. & R. Steffanson, 1966. $S–P$ conversions from the base of the crust, *Ann. Geophys.*, **19**, 119–130.

Beckers, J., S.Y., Schwartz & T. Lay, 1994. The velocity structure of the crust and upper mantle under China from broadband P and PP waveform analysis, *Geophys. J. Int.*, **119**, 574–594.

Birch, F., 1960. The velocity of compressional waves in rocks to 10 kilobars; Part 1. *J. geophys. Res.*, **65**, 1083–1102.

Burchfiel, B.C., P. Zhang, W. Yipeng, Z. Weiqi, S. Fangmin, D. Qidong, P. Molnar & L. Royden, 1991. Geology of the Haiyuan Fault zone, Ningxia–Hui autonomous region, China, and its relation to the evolution of the northeastern margin of the Tibetan Plateau, *Tectonics*, **10**, 1091–1110.

Burdick, L.J. & C.A. Langston, 1977. Modelling crustal structure through the use of converted phases in teleseismic body wave forms, *Bull. seism. Soc. Am.*, **67**, 677–691.

Cassidy, J.F., 1992. Numerical experiments in broadband receiver function analysis, *Bull. seism. Soc. Am.*, **82**, 1453–1474.

Changquan, L. & J. Shixu, 1986. Structural property of the crust and upper mantle in the Tangshan Earthquake Region, *Acta Seismologica Sinica*, **8**, 1–22.

Chen, W.P. & J. Nabelek, 1988. Seismogenic strike-slip faulting and the development of the north China Basin, *Tectonics*, **7**, 975–989.

Fangqiu, H. H. Jun, B. Meixiang, C. Songtao, Z. Dianying & L. Jingyuan, 1989. Seismotectonics of Xinjiang Uygur Autonomous Region, In: *Lithospheric Dynamics Atlas of China*, (Ed. M. Xingyuan) China Cartographic Publishing House, Beijing.

Gao, L. & P. Richards, 1994. Studies of earthquakes on and near the Lop Nor, China, Nuclear test site, In: *Proceedings of the 16th Annual Seismic Research Symposium*, 106–112. PL-TR-94-2217, ADA284667

Gao, L. & P. Richards, 1995. Lower crustal and upper-most mantle structure beneath station WMQ, China by using teleseismic P wave polarisation signals, In: *Proceedings of the 17th Annual Seismic Research Symposium*, 209–217. PL–TR–95–2108, ADA310037

Gaudemer, Y., P. Tapponnier, B. Meyer, G. Peltzer, G. Shunmin, C. Zhitai, D. Huagung & I. Cifuentes, 1995. Partitioning of crustal slip between linked, active faults in eastern Qilian Shan, and evidence for a major seismic gap, the "Tianzhu gap", on the western Haiyuan Fault, Gansu (China), *Geophys. J. Int.*, **120**, 599–645.

Gilder, S.A., G.R. Keller, M. Luo & P.C. Goodell, 1990. Timing and spatial distribution of rifting in China, *Tectonophysics*, **197**, 225–243.

Haomin, X., G. Deming & Y. Qingkai, 1989. Seismotectonics of Heilongjiang Province, In: *Lithospheric Dynamics Atlas of China*, (Ed. M. Xingyuan) China Cartographic Publishing House, Beijing.

Hellinger, S., K. Shedlock, J. Sclater & H. Ye, 1985. The Cenozoic evolution of the north China Basin, *Tectonics*, **4**, 343–358.

Holt, W.E. & T.C. Wallace, 1990. Crustal thickness and upper mantle velocities in the Tibetan plateau region from the inversion of regional P_{nl} waveforms: evidence for a thick upper mantle lid beneath southern Tibet, *J. geophys. Res.*, **95**, 12499–12525.

Hongze, H., 1992. A review of seismic prospecting in the Junggar Basin, In: *Bulletin of Chinese Geophysical Society Volume 2: Geophysical Case Histories in China*, (Eds., M. Ersheng & F. Weicui), Beijing, 238–246.

Huang, K. & N.D. Opdyke, 1991. Paleo-magnetism of Jurassic rocks from the southwestern Sichuan and the timing of the closure of the Qinling Suture, *Tectonophysics*, **200**, 299–316.

Huang, S. & J. Wang, 1991. On variations of heat flow and P_n velocity — A case study from the continental area of China, *J. Geodynamics*, **13**, 13–28.

Hsu, K.J., L. Jiliang, C. Haihong, W. Qingchen, S. Shu & A.M.C. Sengor, 1990. Tectonics of south China: Key to understanding West Pacific geology, *Tectonophysics*, **183**, 9–39.

Jinchang, Z. & W. Zengyi, 1989. Seismotectonics of Gansu Province, In: *Lithospheric Dynamics Atlas of China*, (Ed. M. Xingyuan) China Cartographic Publishing House, Beijing.

Kan, R., H. Hu, R. Zheng, W. Mooney & T. McEvilly, 1986. Crustal Structure of Yunnan Province, People's Republic of China, from seismic refraction profiles, *Science*, **234**, 433–437.

Kechang, L., C. Guangshu, H. Xueying & H. Niwang, 1989. Seismotectonics of Yunnan Province, In: *Lithospheric Dynamics Atlas of China*, (Ed. M. Xingyuan) China Cartographic Publishing House, Beijing.

Langston, C.A., 1977a. The effect of planer dipping structure on source and receiver responses for constant ray parameter, *Bull. seism. Soc. Am.*, **67**, 713–724.

Langston, C.A., 1977b. Corvallis, Oregon crustal and upper mantle receiver structure from teleseismic P and S waves, *Bull. seism. Soc. Am.*, **67**, 1029–1050.

Langston, C.A., 1979. Structure under Mount Rainier, Washington, inferred from teleseismic body waves, *J. geophys. Res.*, **84**, 4749–4762.

Lee, J.J. & C.A. Langston 1983. Wave propagation in a three-dimensional circular basin, *Bull. seism. Soc. Am.*, **73**, 1637–1653.

Liang, G. & W. Li, 1991. The characteristics of deep structure of the north segment of the North-South Seismic Belt, *Acta Seismologica Sinica*, **4**, 259–273.

Metcalfe, I., 1996. Pre-Cretaceous evolution of SE Asian terranes, In: *Tectonic Evolution of Southeast Asia*, (Eds., R. Hall & D. Blundell), Geological Society of London special publication No. 106, Geological Society Publishing House, London.

Owens, T.J., G. Zandt & S.R. Taylor, 1984. Seismic evidence for an ancient crustal rift beneath the Cumberland Plateau, Tennessee: A detailed analysis of broadband teleseismic *P* waveforms, *J. geophys. Res.*, **89**, 7783–7795.

Owens, T.J. & R.S. Crosson, 1988. Shallow structure effects on broadband teleseismic *P* waveforms, *Bull. seism. Soc. Am.*, **78**, 96–108.

Packham, G., 1996. Cenozoic SE Asia: reconstructing its aggregation and re-organisation, In: *Tectonic Evolution of Southeast Asia*, (Eds., R. Hall & D. Blundell), Geological Society of London special publication No. 106, Geological Society Publishing House, London.

Peng, C.S., 1986. Atlas of Geo–Science analysis of land-sat imagery in China, Science Press, Beijing, 132 pp.

Peterson J. & Q. Kexin, 1987. *The China Digital Seismograph Network*, In: A joint report by the Institute of Geophysics, State Seismological Bureau and the Albuquerque Seismological Laboratory, US Geological Survey, Beijing, China.

Qizhong, Y., Z. Guoqing, K. Rongju & H. Hongxiang, 1985. The crust structure of Simao to Malong Profile, Yunnan Province, China, *J. seismol. Res.*, **8**, 249–273.

Rui, F., Z. Jieshou, D. Yunyu, C. Guoying, H. Zhenqin, Y. Shubin, Z. Hainan & S. Kezhong, 1981. Crustal structure in China from surface waves, *Acta Seismologica Sinica*, **3**, 335–350.

Shaoquan, Z., L. Chuzhen & A. Changqiang, 1981. A Preliminary study of the form of the Moho discontinuity in the Beijing area, *Acta. Seismologica Sinica*, **3**, 370–383.

Shangyou, N., 1991. Paleo-climate and paleo-magnetic constraints on the Paleozoic reconstructions of south China, north China and Tarim, *Tectonophysics*, **196**, 279–308.

Shedlock, K.M. & S.W. Roecker, 1987. Elastic wave velocity structure of the crust and upper mantle beneath the north China Basin, *J. geophys. Res.*, **92**, 9327–9350.

Wang, Y. & Z. Zhang, (1980). *Loess in China*, Shaaxi People's Art Publishing House, Beijing, China.

Wucheng, S., L. Changquan, Z. Zhiping, Z. Li, S. Songyan & Z. Xiankang, 1989. Velocity structure of the crust and upper mantle in northern part of north China, In: *Lithospheric Dynamics Atlas of China*, (Ed. M. Xingyuan) China Cartographic Publishing House, Beijing.

Xiling, P., & Z. Guojun, 1989. Tectonic features of the Junggar Basin and their relationship with oil and gas distribution, In: *Sedimentary Basins of the World, 1: Chinese Sedimentary Basins*, Ed. X. Zhu, Elsevier Science Publishers B.V., Amsterdam, The Netherlands, 17–31.

Xuezhong, S. & Z. Jiaru, 1989. Structure of the lithosphere in northern part of north China, In: *Lithospheric Dynamics Atlas of China*, (Ed. M. Xingyuan) China Cartographic Publishing House, Beijing.

Xuecheng, Y., 1996. Atlas of Geophysics in China, Geological Publishing House, Beijing, 168 pp.

Xuezhong, S. & J. Zhang, 1989. Structure of the lithosphere in northern part of north China, In: *Lithospheric Dynamics Atlas of China*, (Ed. M. Xingyuan) China Cartographic Publishing House, Beijing.

Yuan, X., S. Wang, L. Li & J. Zhu, 1986. A geophysical investigation of the deep structure in China. In: *Reflection Seismology: A Global Perspective*, Geodynamic Series, **13**, American Geophysical Union, 151–160.

Zhang, Z.M., J.G. Liou & R.G. Coleman, 1984. An outline of the plate tectonics of China, *Geol. soc. Am. Bull.*, **5**, 295–312.

Zhao, L.P. & J. Xie, 1993. Lateral variations of the compressional velocity structure beneath the Tibetan Plateau from P_n travel time inversion, *Geophys. J. Int.*, **115**, 1070–1084.

Zhao, X., R.S. Coe, Y. Zhou, H. Wu & J. Wang, 1990. New paleomagnetic results from northern China: collision and suturing with Siberia and Kazakhstan, *Tectonophysics* **181**, 43–81.

Zhao, Z,Y. & B.F. Windley, 1990. Cenozoic tectonic extension and inversion of the Jizhong Basin, Hebi, northern China, *Tectonophysics*, **185**, 83–89.

Zhao, L.S. & C. Frohlich, 1996. Teleseismic body waveforms and receiver structures beneath seismic stations, *Geophys. J. Int.*, **124**, 525–540.

Zhihong, S., L. Zhanpo & Y. Xiuhua, 1989. Crustal thickness by gravity inversion, In: *Lithospheric Dynamics Atlas of China*, (Ed. M. Xingyuan) China Cartographic Publishing House, Beijing.

Table 1. CDSN station coordinates

Station name	Station code	Latitude (°)	Longitude (°)	Elevation m
Beijing	BJI	40.0403	116.1750	43
Hailar	HIA	49.2667	119.7417	610
Kunming	KMI	25.1233	102.7400	1952
Lanzhou	LZH	36.0867	103.8444	1560
Mudanjiang	MDJ	44.6164	129.5919	250
Urumqi	WMQ	43.8211	87.6950	970

Table 2. CDSN event source parameters

Event No.	Date (m/d/y)	Origin Time	Latitude (°)	Longitude (°)	m_b	Depth (km)
1	02/10/87	00:59:28	−19.489	−177.456	6.2	395
2	02/11/87	07:56:12	−15.834	167.355	5.9	24
3	03/21/87	10:41:35	52.056	−177.547	6.0	64
4	05/05/87	15:40:47	36.480	70.673	5.8	202
5	06/17/87	01:32:53	−5.777	130.791	6.6	67
6	06/21/87	05:46:10	54.211	−162.601	6.2	34
7	10/12/87	13:57:04	−7.288	157.371	6.3	25
8	11/17/87	08:46:53	58.586	−143.270	6.6	10
9	12/04/87	19:51:35	−5.777	154.555	5.9	145
10	02/07/88	18:15:05	50.785	173.465	6.2	33
11	02/16/88	04:22:36	51.564	175.041	5.9	33
12	03/06/88	22:35:38	56.953	−143.032	6.8	10
13	03/25/88	19:36:46	62.154	−124.182	6.1	10
14	04/03/88	01:33:05	49.917	78.945	6.1	0
15	04/25/88	10:10:33	−7.791	158.255	6.1	44
16	05/30/88	21:11:11	−7.501	128.325	6.5	86
17	06/05/88	18:22:48	−15.397	167.578	6.0	110
18	07/02/88	10:01:28	−14.278	167.180	5.9	177
19	07/05/88	20:32:07	−5.964	148.780	6.0	53
20	07/23/88	15:17:08	−6.526	152.779	6.7	17
21	07/25/88	06:46:06	−6.081	133.667	6.5	28
22	07/27/88	21:55:09	−13.112	167.051	5.9	172
23	08/06/88	06:26:55	−7.136	151.057	5.9	25
24	12/07/88	07:41:24	40.987	44.185	6.2	5
25	01/10/89	05:55:01	−3.162	130.556	5.9	47
26	02/04/89	22:10:38	−4.625	153.066	6.1	52
27	03/10/89	21:49:45	−13.702	34.420	6.2	30
28	03/11/89	05:05:00	−17.766	−174.761	6.4	230
29	06/26/89	10:38:39	39.112	−28.242	5.7	11
30	07/14/89	20:42:40	−8.081	125.129	6.4	10
31	07/31/89	17:07:27	−8.048	121.384	6.3	14
32	08/20/89	11:16:56	11.766	41.942	5.8	12
33	08/21/89	01:09:06	11.874	41.870	6.3	16
34	09/04/89	13:14:58	55.543	−156.835	6.5	11
35	09/16/89	02:05:08	40.337	51.534	6.4	55
36	09/17/89	00:53:39	40.203	51.749	6.1	34
37	09/25/89	14:17:47	−20.355	169.277	6.1	34
38	10/07/89	15:48:29	51.314	−179.028	6.1	20
39	04/26/90	12:08:29	−22.015	−179.470	6.0	587
40	05/01/90	16:12:21	58.840	−156.858	6.1	211
41	05/30/90	10:40:06	45.841	26.668	6.7	89
42	05/31/90	00:17:47	45.811	26.769	6.1	88
43	07/27/90	12:37:59	−15.355	167.464	6.4	126
44	08/12/90	21:25:22	−19.435	169.132	6.3	140
45	09/28/90	19:44:47	−13.559	167.079	6.0	176
46	11/06/90	18:45:52	28.251	55.426	6.2	11

Table 2 (continued)

Event No.	Date (m/d/y)	Origin Time	Latitude (°)	Longitude (°)	m_b	Depth (km)
47	12/28/90	22:32:17	−14.875	66.777	6.0	17
48	12/30/90	19:14:18	−5.097	150.967	6.6	179
49	01/05/91	14:57:11	23.478	95.983	6.3	20
50	02/21/91	02:35:34	58.427	−175.450	6.2	20
51	04/29/91	09:12:47	42.453	43.673	6.2	17
52	05/21/91	11:00:19	−7.517	126.539	6.2	18
53	05/30/91	13:26:40	54.567	−161.61	6.3	28
54	06/07/91	11:51:25	−7.204	122.533	6.2	536
55	06/15/91	00:59:20	42.461	44.009	6.1	9
56	06/20/91	05:18:52	1.196	122.787	6.2	31
57	07/02/91	05:14:30	−1.068	99.843	5.8	54
58	08/08/91	18:19:20	57.589	−142.846	6.3	14
59	09/03/91	08:44:48	33.649	138.778	5.9	27
60	09/28/91	20:26:56	−5.184	150.959	5.8	28
61	09/30/91	00:21:46	−20.878	−178.591	6.3	566
62	10/12/91	16:26:24	−13.742	166.673	5.9	44
63	03/04/92	03:49:54	−3.008	147.882	6.0	19
64	03/13/92	17:18:39	39.710	39.605	6.2	27
65	04/03/92	03:19:51	−5.696	151.164	5.8	27
66	04/24/92	07:07:23	27.550	66.065	5.9	25
67	05/12/92	18:05:42	−16.524	−172.367	6.4	15
68	05/15/92	07:05:05	−6.075	147.572	6.2	58
69	05/17/92	09:49:19	7.239	126.645	6.2	33
70	06/15/92	02:48:56	24.027	95.932	5.8	17
71	08/07/92	18:19:20	57.589	−142.846	6.3	14
72	09/26/92	22:15:57	1.289	129.118	5.9	28
73	10/23/92	13:04:40	−5.352	152.616	5.8	31
74	10/23/92	23:19:45	42.589	45.104	6.1	16
75	11/04/92	18:13:13	−14.238	167.641	6.1	14
76	01/20/93	17:31:15	−7.205	128.566	6.2	33
77	03/01/93	01:39:27	−3.744	138.536	6.1	89
78	04/16/93	14:08:38	−17.778	−178.864	6.0	565
79	05/11/93	18:26:51	7.219	126.570	6.1	59
70	05/13/93	11:59:49	55.177	−160.458	6.4	32
81	05/30/93	14:12:20	−3.674	142.703	5.9	6
82	06/12/93	18:26:42	−4.375	135.118	5.8	10
83	07/12/93	13:17:11	42.851	139.197	6.6	17
84	07/24/93	20:24:50	−13.060	167.06	5.8	194
85	08/04/93	11:31:18	−1.629	99.615	5.9	32
86	08/09/93	12:42:48	36.379	70.868	6.2	215
87	08/29/93	09:57:54	−7.005	129.560	5.8	147
88	09/06/93	03:56:00	−4.641	153.231	6.2	49
89	10/11/93	15:54:21	32.020	137.832	6.4	351
90	10/13/93	02:06:00	−5.889	146.020	6.4	25
91	11/13/93	01:18:04	51.934	158.647	6.5	34
92	12/09/93	04:32:19	0.486	125.995	6.5	15

Table 2. (continued)

Event No.	Date (m/d/y)	Origin Time	Latitude (°)	Longitude (°)	m_b	Depth (km)
93	12/09/93	11:38:27	0.425	125.890	6.3	16
94	12/20/93	13:56:14	−6.876	131.34	6.4	8
95	01/19/94	01:53:34	−3.176	135.970	6.1	23
96	01/21/94	02:24:29	1.015	127.733	6.2	20
97	02/11/94	21:17:31	−18.773	169.169	6.4	206
98	02/12/94	17:58:23	−20.553	169.631	6.4	28
99	02/23/94	08:02:04	30.853	60.596	6.1	6
100	02/24/94	00:11:12	30.775	60.495	6.1	10
101	02/26/94	02:31:11	30.897	60.549	5.8	9
102	03/09/94	23:28:06	−18.039	−178.413	6.6	563
103	03/31/94	22:40:52	−22.057	−179.533	6.1	580
104	07/09/94	01:53:34	−3.176	135.970	6.1	23
105	07/13/94	11:45:23	−7.532	127.770	6.5	159
106	07/21/94	18:36:31	42.340	132.865	6.5	471

Table 3. Event for CDSN station receiver function stacks

Stack name	Event Nos.
BJI–NE	8, 12, 34, 40, 53
BJI–SE	17, 37, 43, 44, 45, 98
BJI–SSE	21, 25, 30, 95, 96
BJI–NW	42, 46, 64
HIA–NE	12, 71, 13
HIA–SE1	63, 77, 81
HIA–SE2	7, 15, 20, 23, 60, 73
HIA–SE3	17, 18, 43, 45, 62, 75
HIA–SE4	61, 67, 102, 103
HIA–SW	4, 49, 70
HIA–NW	24, 36, 51, 55, 64
KMI–NE	3, 10, 34, 50, 59, 64, 106
KMI–SE1	9, 26, 48, 65, 68
KMI–SE2	2, 17, 37, 43, 44, 45, 75, 97
KMI–SE3	1, 28, 39, 78, 103
KMI–NW	35, 36, 51, 66, 99, 101
LZH–NE	8, 11, 12, 34, 38, 40
LZH–SE	5, 54, 72, 79, 82, 94, 105
LZH–S	85
LZH–W	46, 99, 100, 101
MDJ–NE	71
MDJ–SE	37, 62, 63, 84, 88, 90
MDJ–SW	31, 52, 69, 76, 79, 92, 93
MDJ–NW	86
WMQ–NE	6, 12, 34, 40, 80
WMQ–SE	16, 30, 31, 52, 56, 58, 82, 87, 92, 93, 96
WMQ–SW	24, 74
WMQ–NW	32, 33

Table 4. HIA model parameters

Vp (km/s)	Model A thickness (km)	Model B thickness (km)
6.30	6.0	0.0
5.80	3.0	0.0
6.30	23.0	32.0
6.75	2.0	2.0
7.25	3.0	3.0
7.60	3.0	3.0
8.00	∞	∞

Table 5. MDJ model parameters

Vp (km/s)	A Thickness (km)	B Thickness (km)	C Thickness (km)
5.50	6.0	3.0	3.0
6.60	31.0	34.0	36.0
7.40	—	4.0	—
8.00	∞	∞	∞

Table 6. BJI–NW model parameters

Vp (km/s)	Model C thickness (km)
3.80	1.5
4.60	1.5
5.55	1.5
6.20	21.0
6.60	14.5
8.00	∞

Table 7. LZH model parameters

Vp (km/s)	Model A thickness (km)
4.00	2.4–2.6
6.40	49.0
6.90	3.0
7.65	3.0
8.00	∞

Table 8. KMI–NW model parameters

Vp (km/s)	Model A thickness (km)
5.75	12.0
6.30	21.0
7.20	17.0
8.15	∞

Table 9. WMQ model parameters

Vp (km/s)	thickness (km)	strike (km)	dip (°)
4.00	4.2	240	18.0
5.10[†]	4.0	240	18.0
6.10 [†]	4.5	0.0	0.0
6.18	2.5	0.0	0.0
6.21	2.5	0.0	0.0
6.25	2.5	0.0	0.0
6.31	2.5	0.0	0.0
6.37	2.5	0.0	0.0
6.43	2.5	0.0	0.0
6.50	2.5	0.0	0.0
6.56	2.5	0.0	0.0
6.61	2.5	0.0	0.0
6.68	2.5	0.0	0.0
6.75	2.5	0.0	0.0
6.90	2.5	0.0	0.0
7.05	1.0	0.0	0.0
7.35	1.0	0.0	0.0
7.70	1.0	0.0	0.0
8.00	∞	0.0	0.0

[†] The top interface of this layer dips 18° northwest

Figure Captions

Figure 1. Tectonic structure sketch of China. The outlines of the tectonic provinces are from Hsu *et al.* (1990). The CDSN stations are shown as inverted triangles. Table 1 lists the coordinates of each station.

Figure 2. HIA radial (left) and tangential (right) component receiver functions. The dotted lines are $\pm 1\sigma$ bounds computed from the variance of the stack. At the left of each trace pair are the stack name, the number of events comprising the stack (in parentheses), the mean back azimuth and ray parameter. The relative amplitude is preserved between all data.

Figure 3. Synthetic radial component receiver functions computed from each inversion solution model are compared to the $\pm 1\sigma$ bounds of the HIA–NE, SE, SW and NW data (dotted lines). The range of starting models is also shown.

Figure 4. (a) A comparison of synthetic receiver functions (solid lines) to the $\pm 1\sigma$ bounds of the HIA–NE, SE, SW and NW data (dotted lines) computed from Model A (top row) and Model B (bottom row). (b) The dotted line is the average of all inversion models.

Figure 5. MDJ radial (left) and tangential (right) receiver functions. The figure format is the same as in Figure 2.

Figure 6. Synthetic radial component receiver functions computed from each inversion solution model are compared to the $\pm 1\sigma$ bounds of the SE, SW stacked data and to the NE and NW single event receiver functions (dotted lines). The range of starting models is also shown with the corresponding solution models.

Figure 7. A comparison of the synthetic radial receiver functions computed from the MDJ northern and southern models to the data (solid line). Also shown are the averaged inversion results (dotted line).

Figure 8. BJI radial (left) and tangential (right) receiver functions. The figure format is the same as in Figure 2.

Figure 9. BJI–NW inversion result and the NE, SE and SSE receiver functions. The format is the same as in Figure 3.

Figure 10. BJI–NW forward modelling tests of the possible Moho structures (top) and a similar test with the inclusion of a mid-crustal discontinuity (bottom).

Figure 11. KMI radial (left) and tangential (right) receiver functions. The format format is the same as in Figure 2.

Figure 12. KMI–NE, SE and NW inversion result. The format is the same as in Figure 3.

Figure 13. KMI–NW forward modelling result.

Figure 14. LZH radial (left) and tangential (right) receiver functions. The plotting format is the same as in Figure 2.

Figure 15. LZH–NE and SE inversion result. The format is the same as in Figure 3.

Figure 16. LZH–NE, SE and S forward modelling result.

Figure 17. A comparison of synthetic radial component receiver functions (solid lines) computed from the LZH model given by Zhao & Frohlich (1996) to the $\pm1\sigma$ bounds of the NE and SE stacked radial receiver functions and to the S single event radial receiver function (dotted lines).

Figure 18. WMQ radial (left) and tangential (right) receiver functions. The plotting format is the same as in Figure 2.

Figure 19. WMQ radial (left) and tangential (right) receiver functions. At the left of each trace pair are the event number (see Table 5.2) and back azimuth. All radial receiver functions are plotted at the same scale, and all tangential receiver functions are plotted at the same scale, but the scale is not the same between both components. The +/- and -/+ symbols indicate first–motion polarity reversals on the tangential receiver functions.

Figure 20. Peak amplitude time delay versus event back azimuth of the first pulse on the radial receiver function. The largest delays occur for travel paths through the down–dip direction.

Figure 21. WMQ dipping layered modelling result. Model D has two northwest dipping interfaces at 4 and 8 km depth that strike N240°E and have an 18° dip. The velocity structure below this depth is parameterised using horizontal layers based on the results of Gao & Richards (1994)

Figure 22. A comparison between the observed direct P wave arrival time delays (dark) on the WMQ radial receiver functions shown in Figure 19 and synthetic delays (light) obtained from synthetic radial component receiver functions predicted from Model D using the same parameters as that of the data. The predicted time delays were measured from synthetic radial component receiver functions computed using the same ray parameter, incident P–wave azimuth and Gaussian filter as that of the data. The synthetics were computed using the same mean ray parameter, incident P–wave azimuth of approach and Gaussian filter as that of the data.

Figure 23. Receiver function modeling results (Vp in km/s) for the CDSN stations.

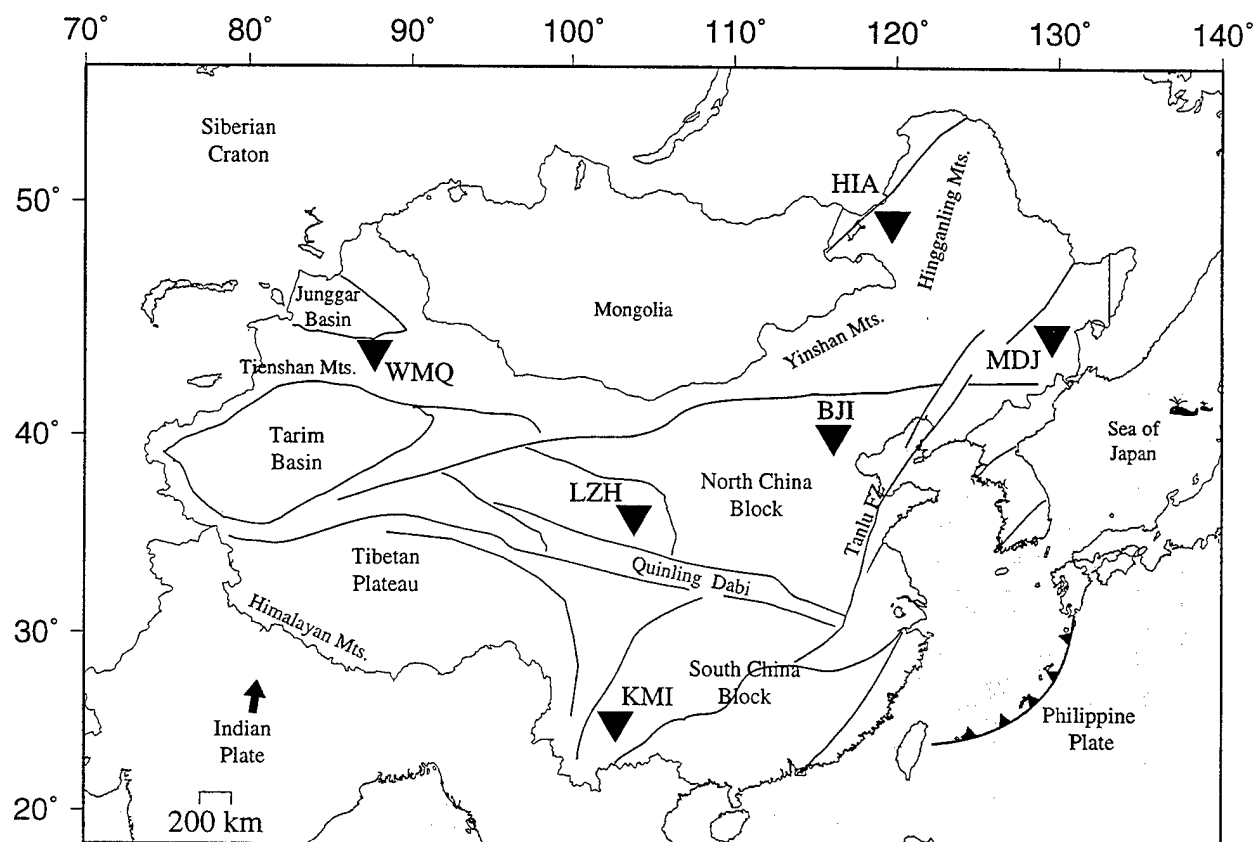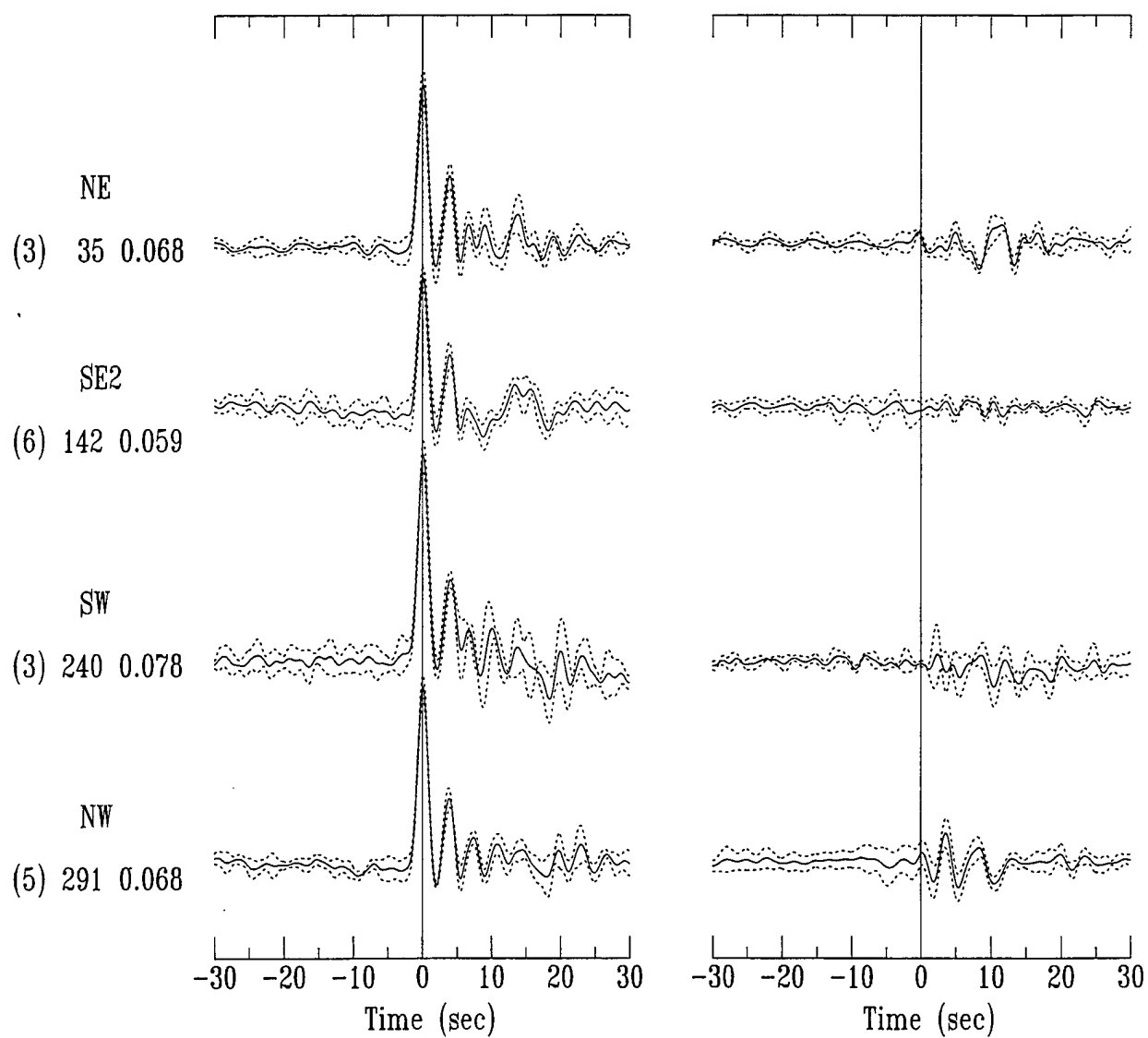Figure 24. Contour map of Moho depth (in kilometres) across China, from Yuan et al. (1986).
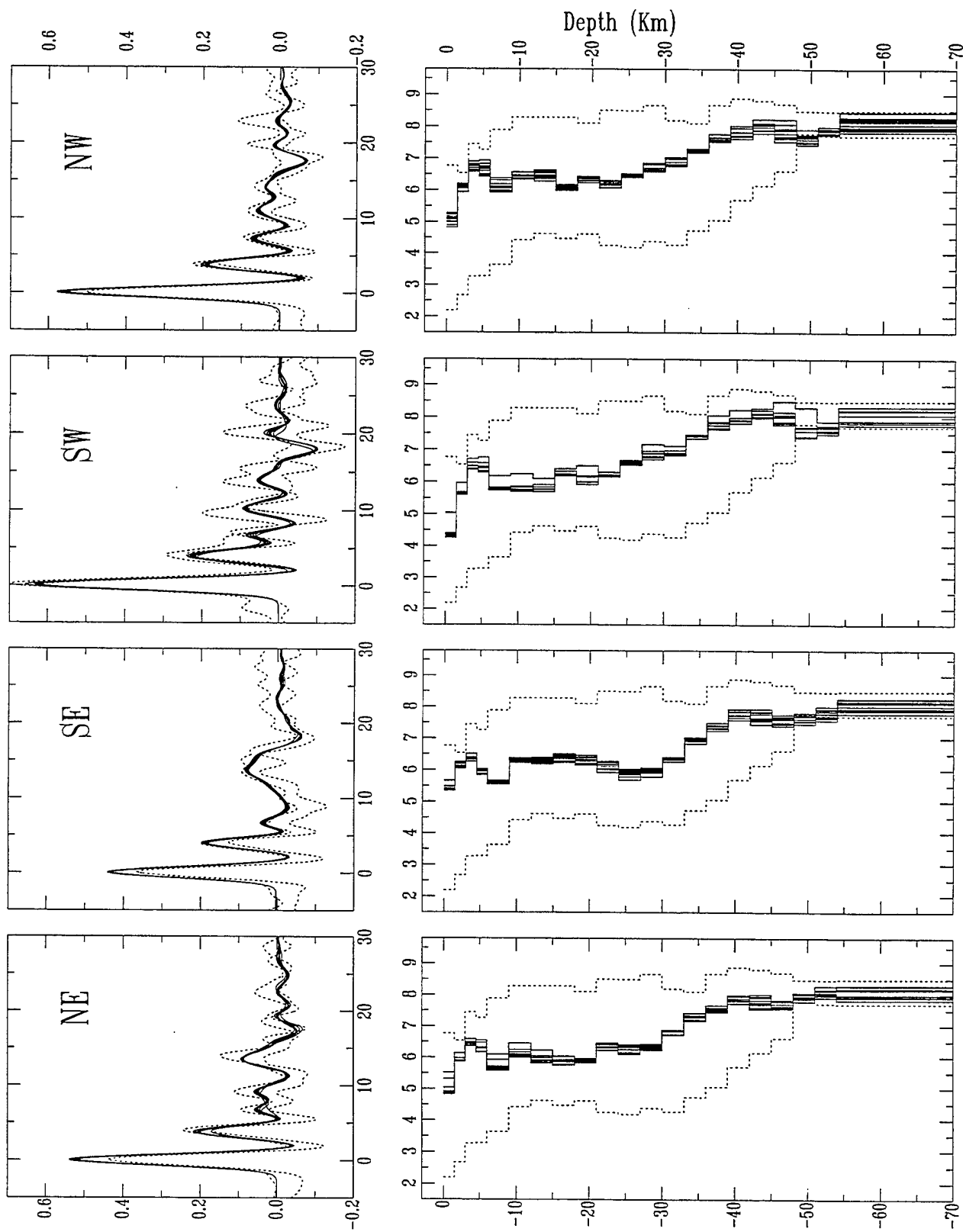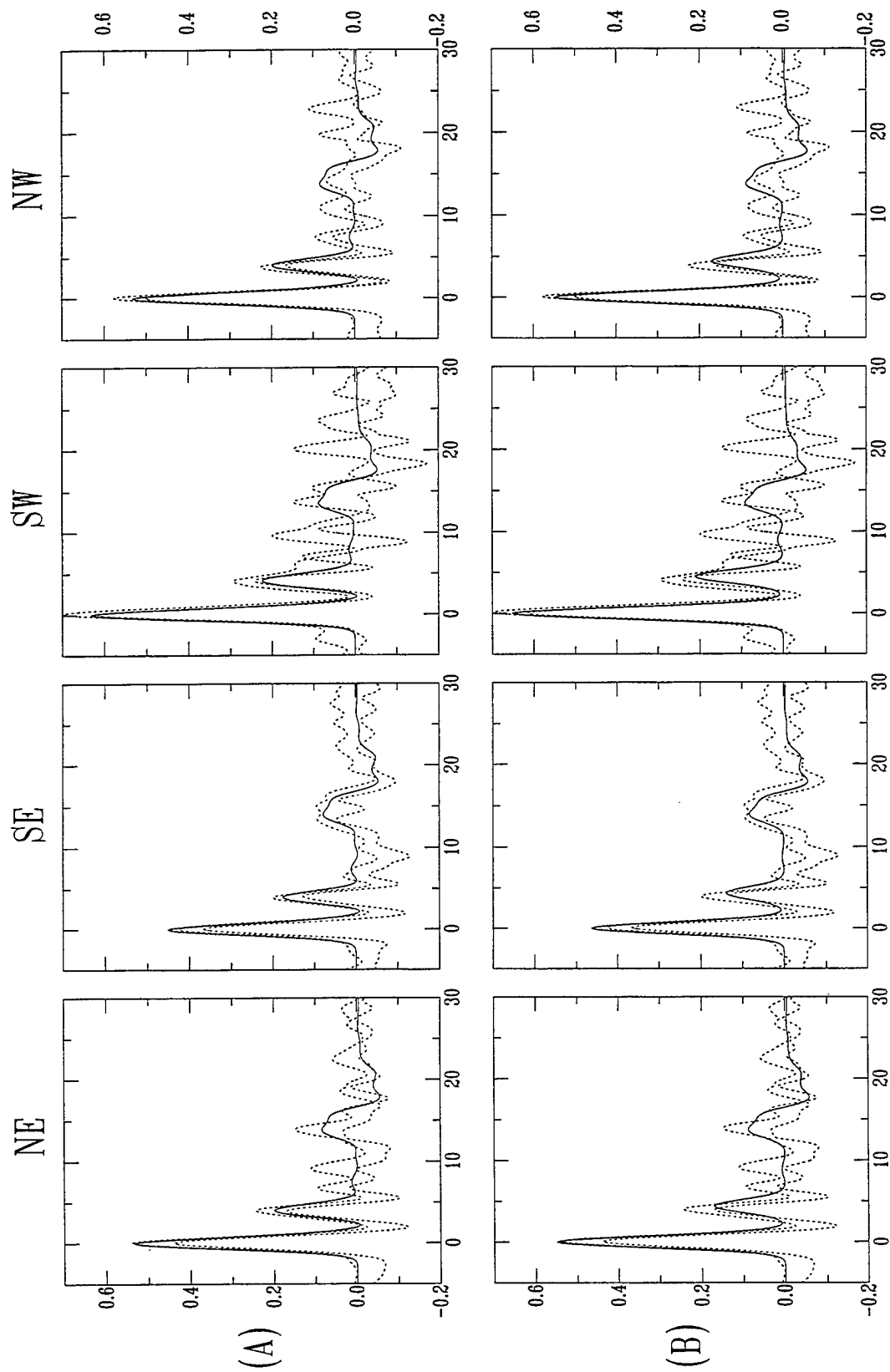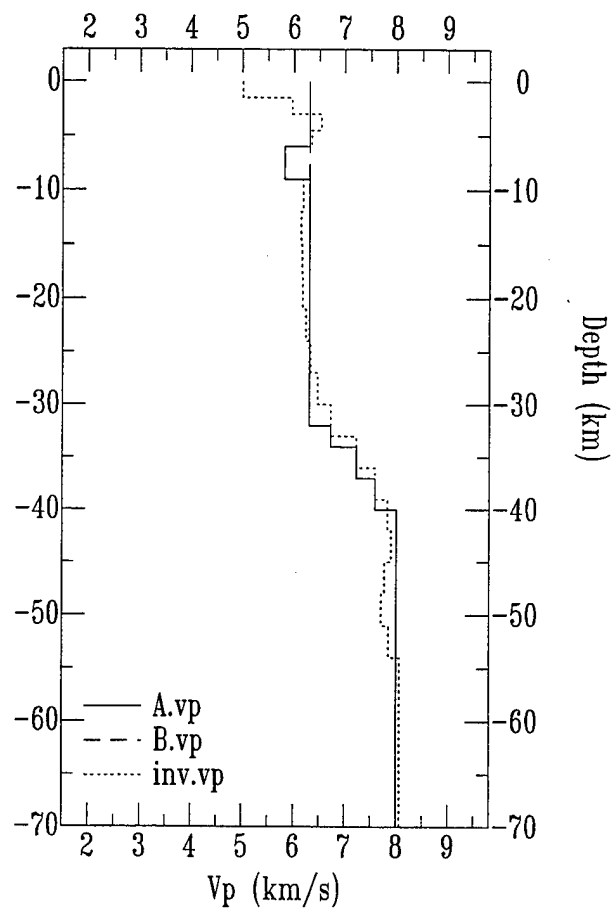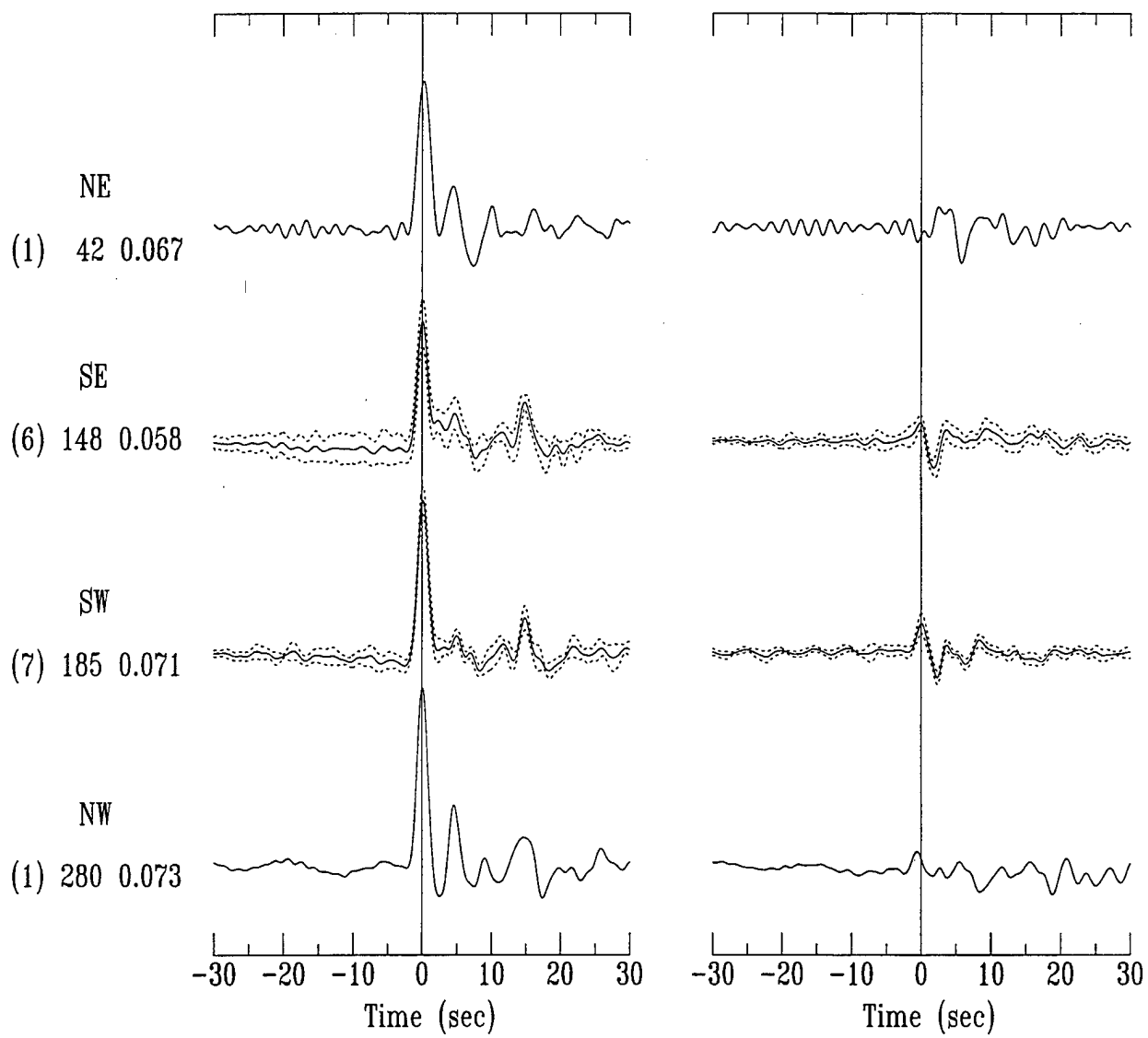
FIGURE 1

FIGURE 2

FIGURE 3
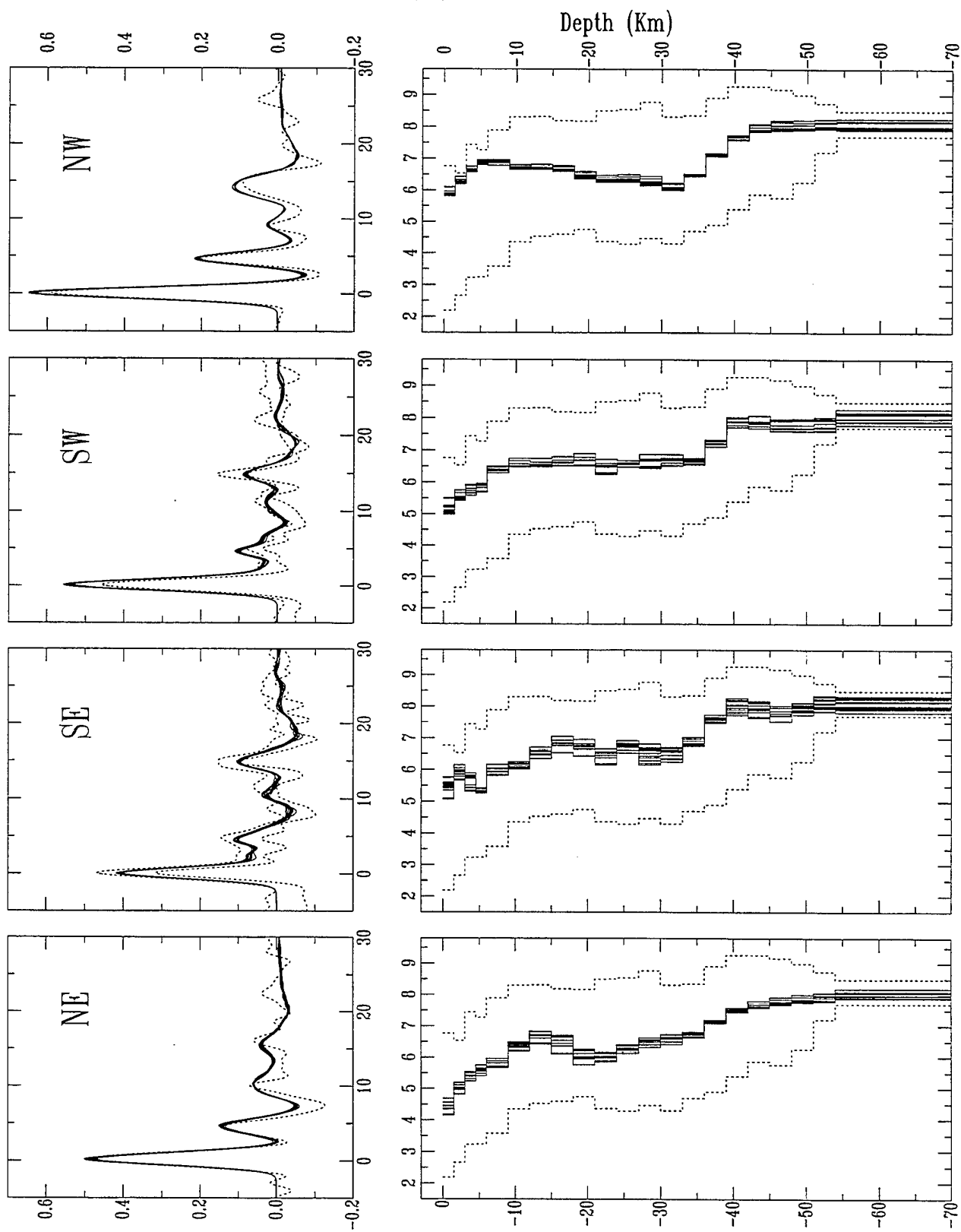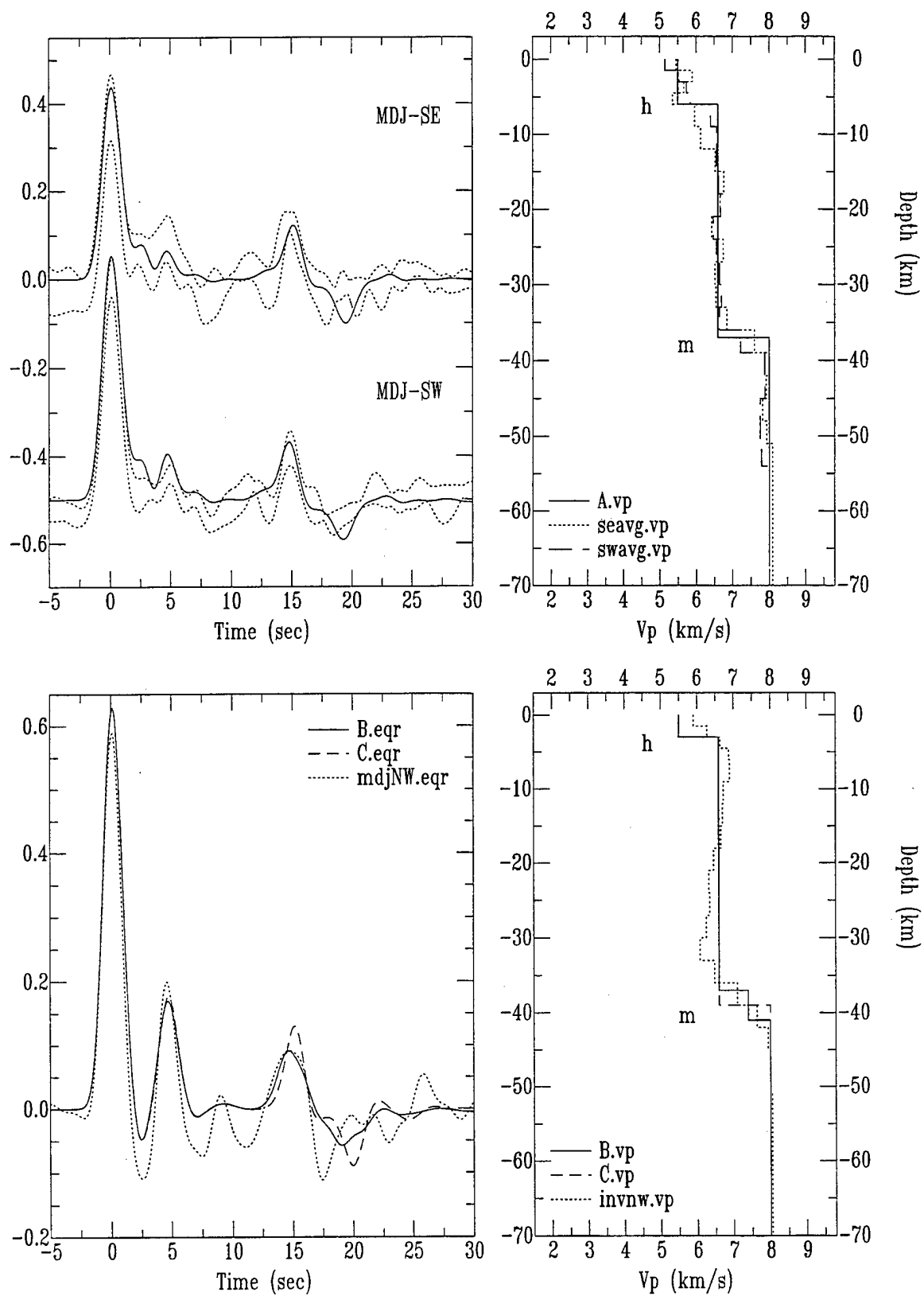
FIGURE 4a

135

FIGURE 4b

FIGURE 5

137

FIGURE 6

138

FIGURE 7

139

NE

(5) 38 0.061

SE

(6) 129 0.052

SSE

(5) 159 0.071

NW

(3) 309 0.065

Time (sec)

Time (sec)

FIGURE 8

FIGURE 9

FIGURE 10

NE

(7) 45 0.064

SE2

(8) 116 0.052

NW

(6) 295 0.074

Time (sec)

Time (sec)

FIGURE 11

143

FIGURE 12

144

FIGURE 13

145

FIGURE 14

146

FIGURE 15

147

FIGURE 16

FIGURE 17

148

NE

(5)   33 0.060

SE

(11) 134 0.061

SW

(2) 245 0.069

NW

(2) 281 0.075

Time (Sec)

Time (Sec)

FIGURE 18

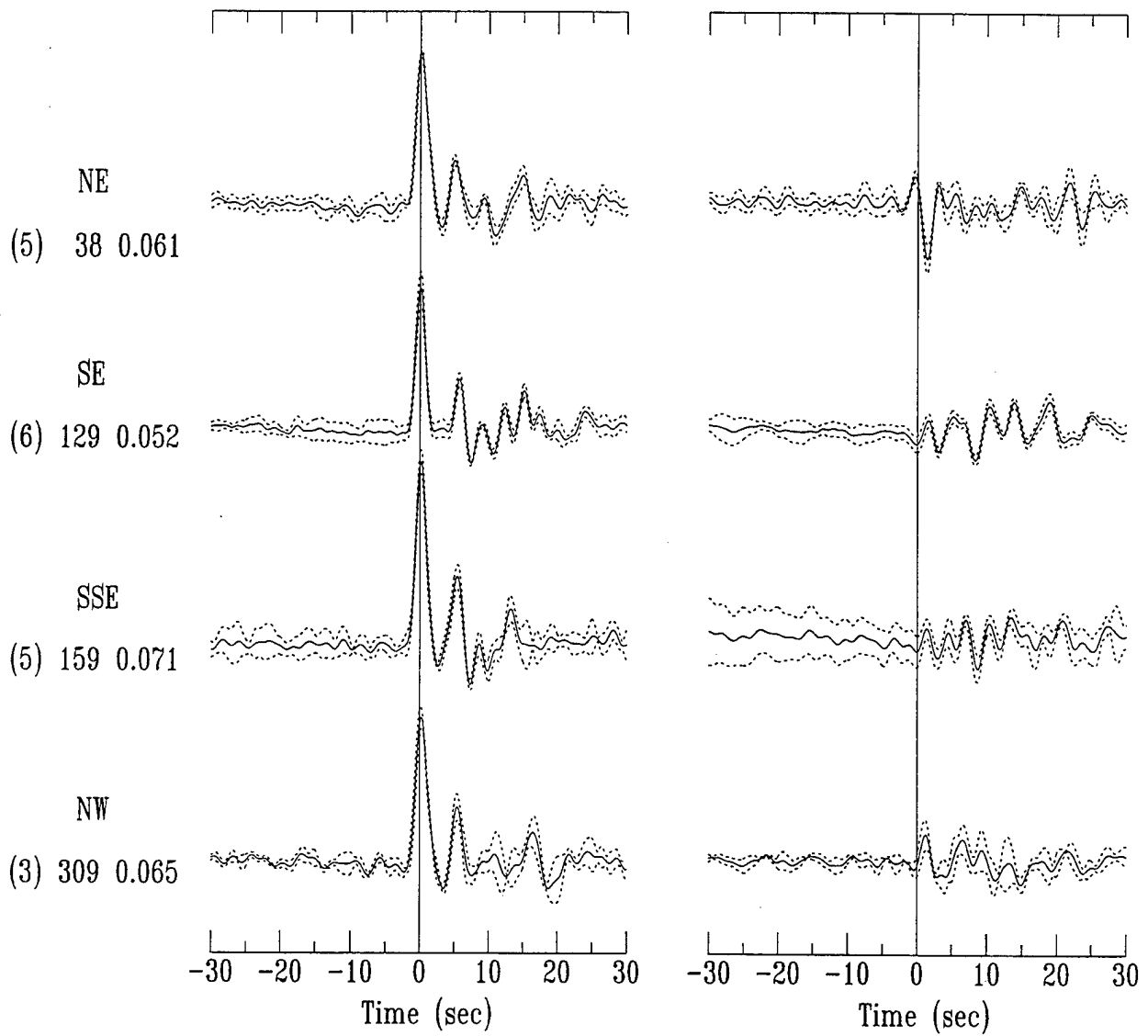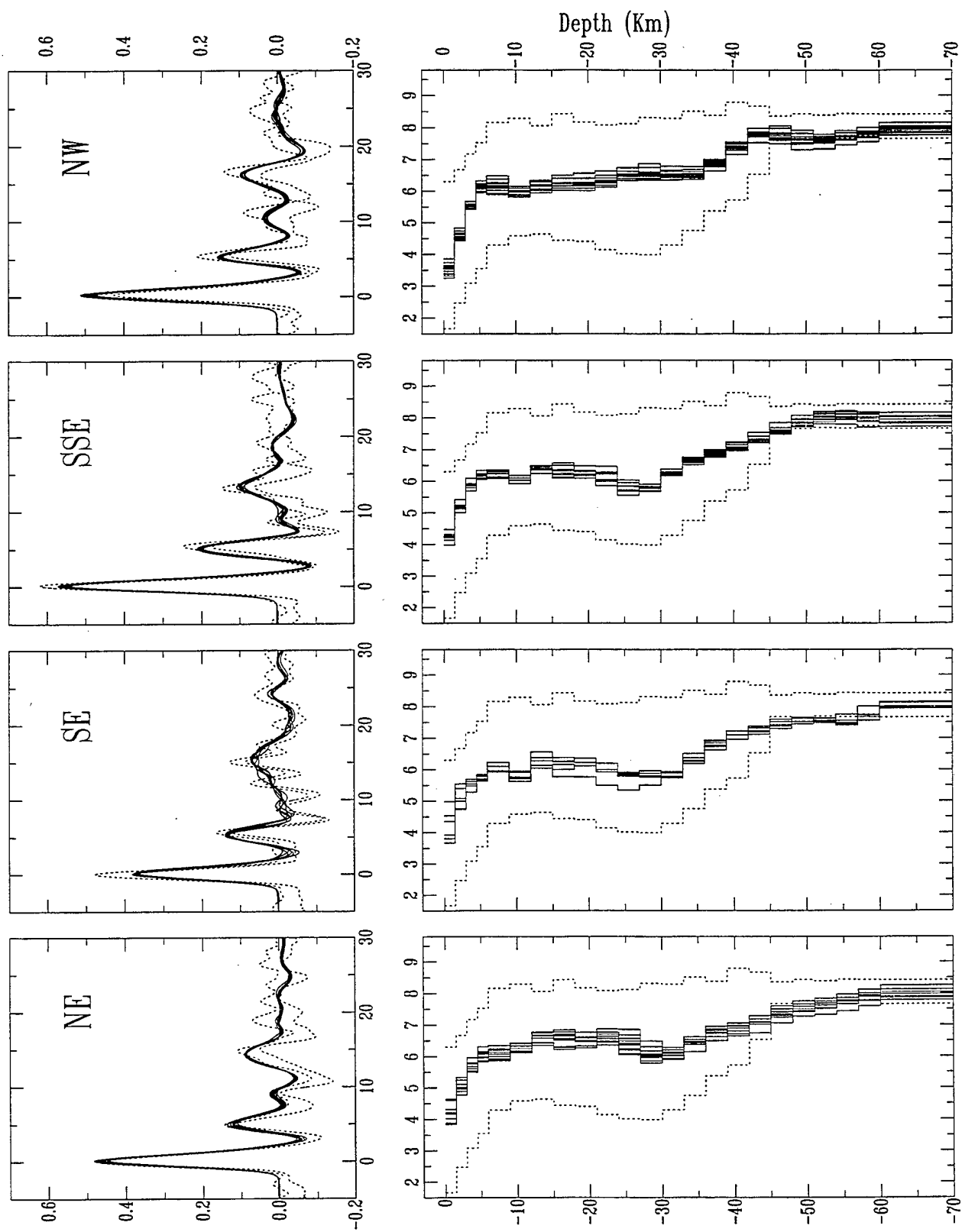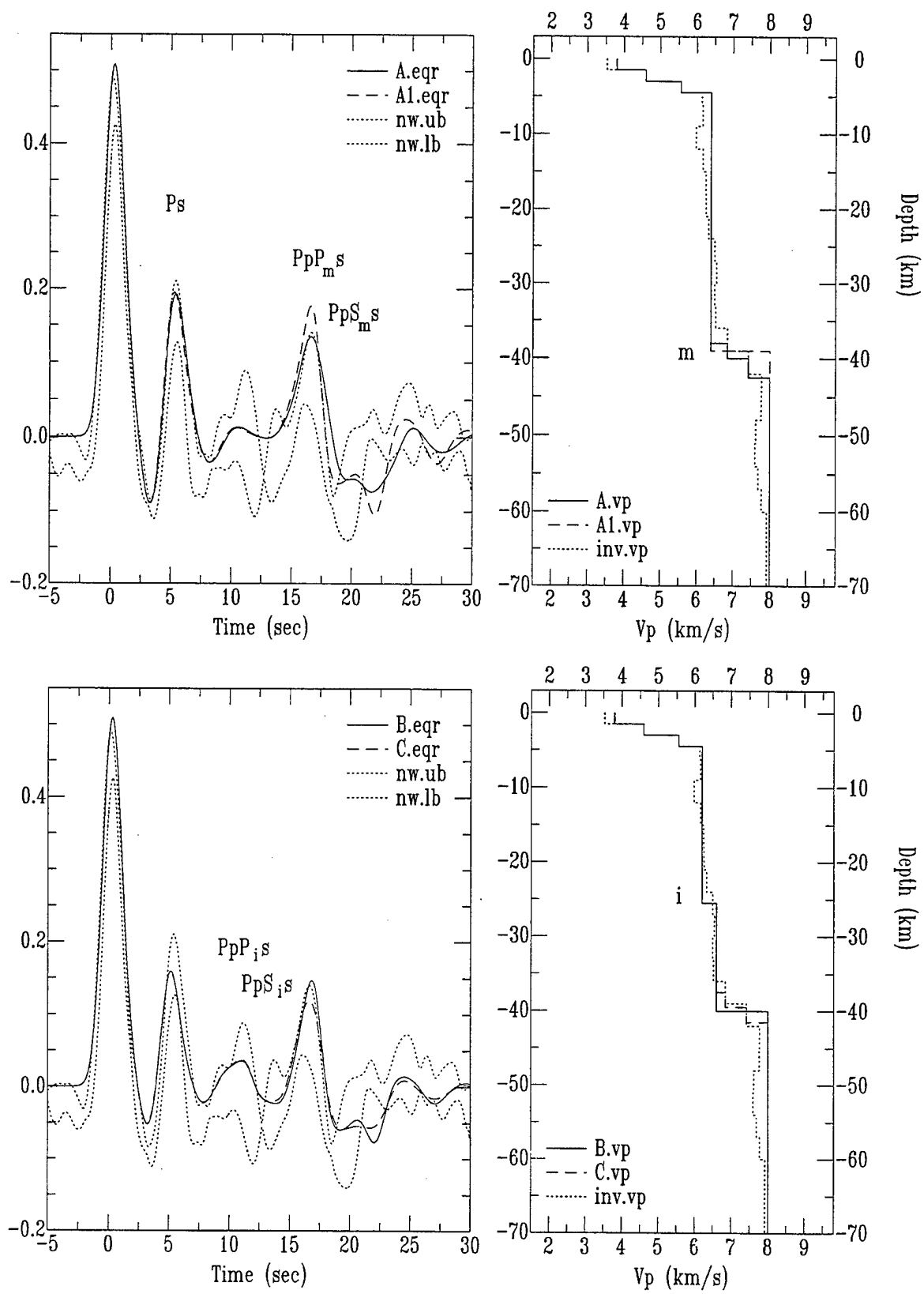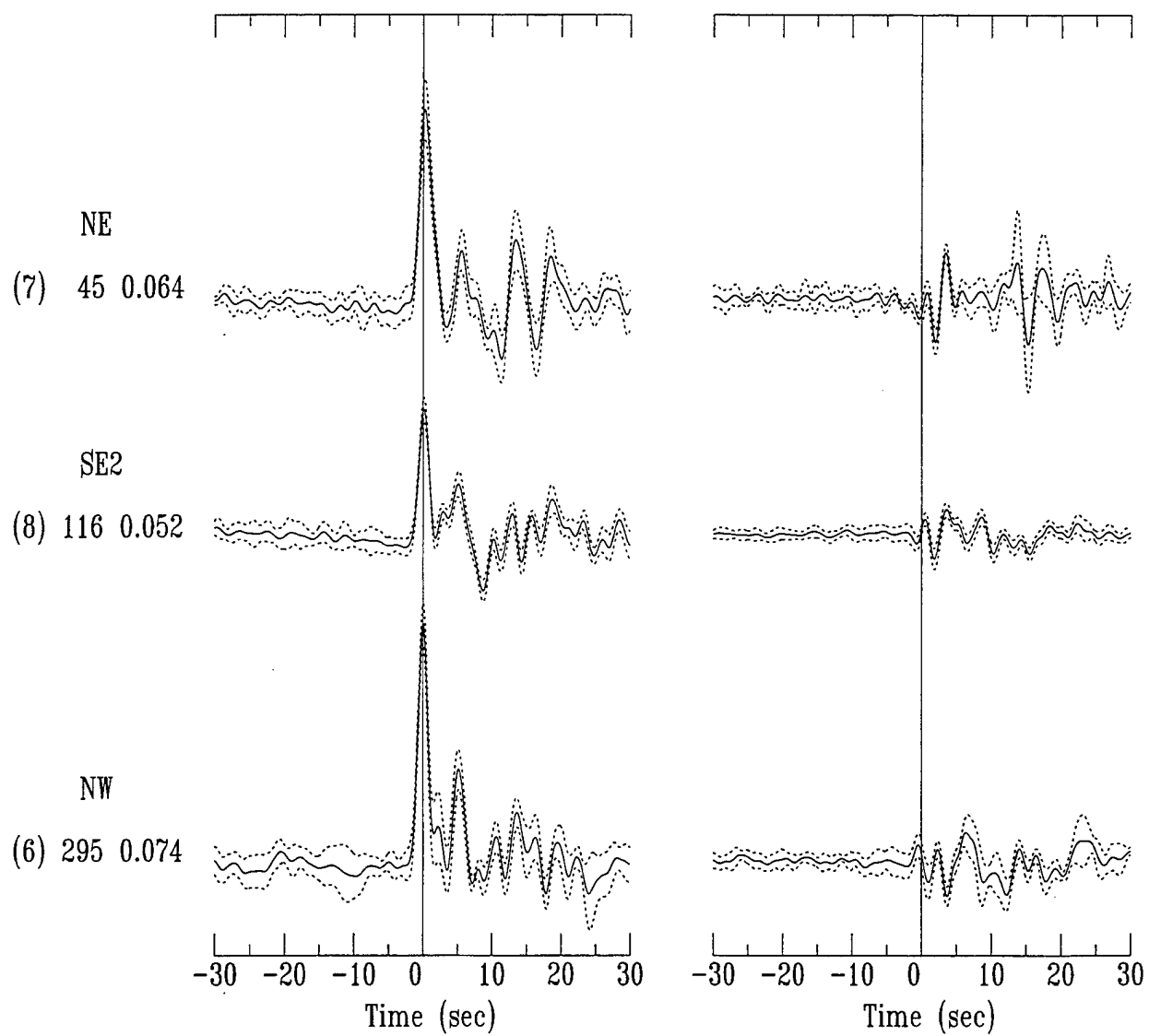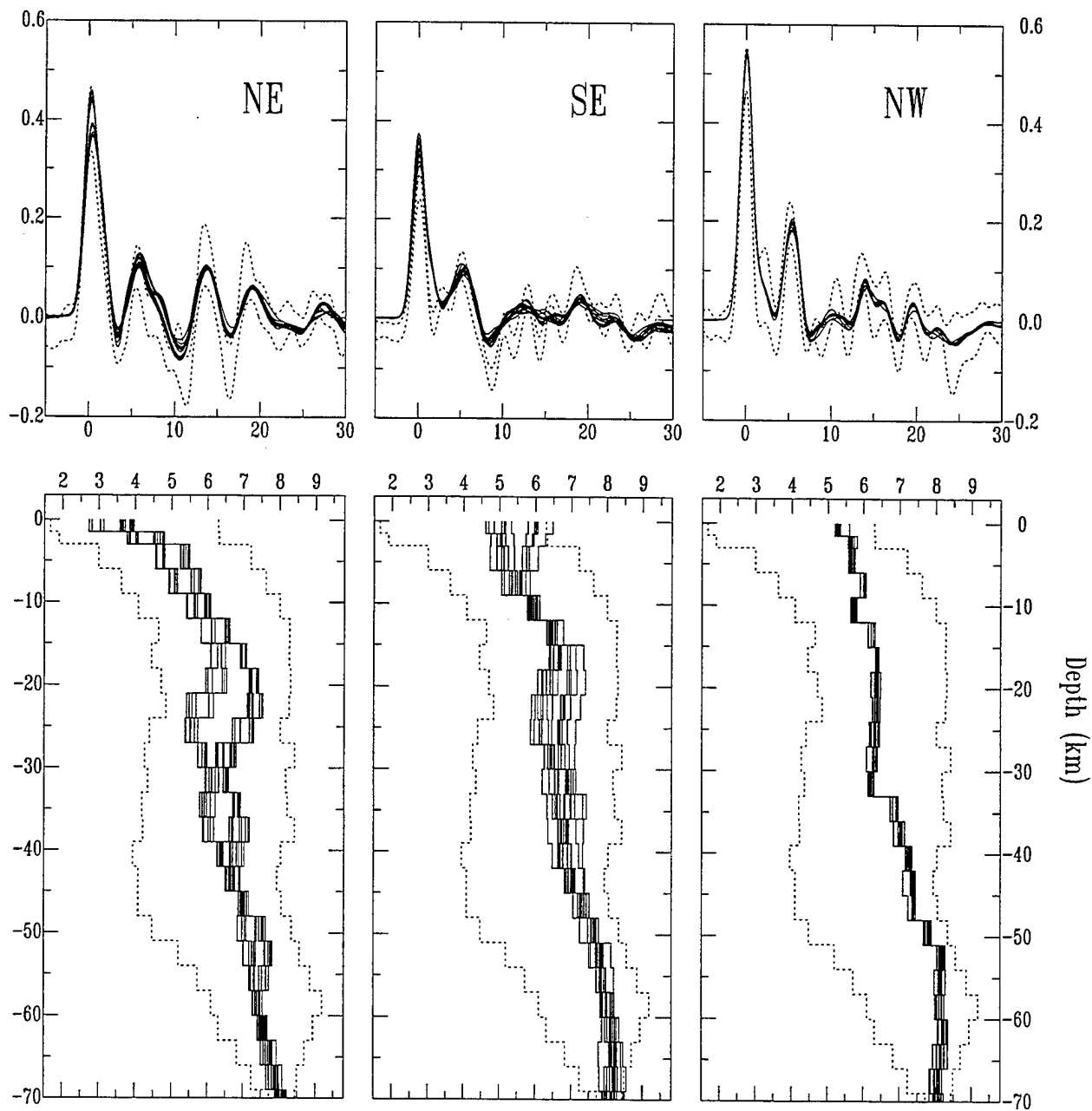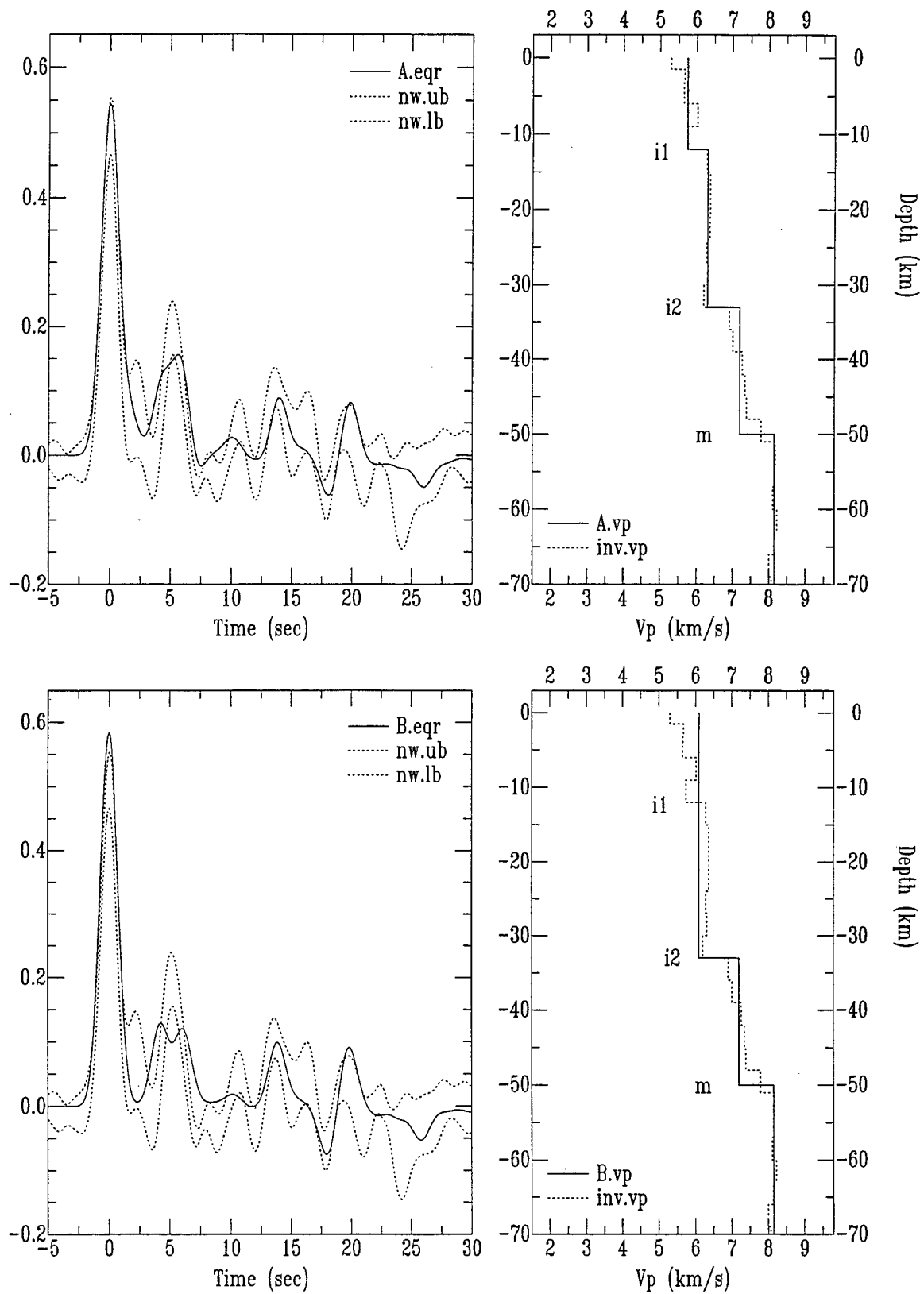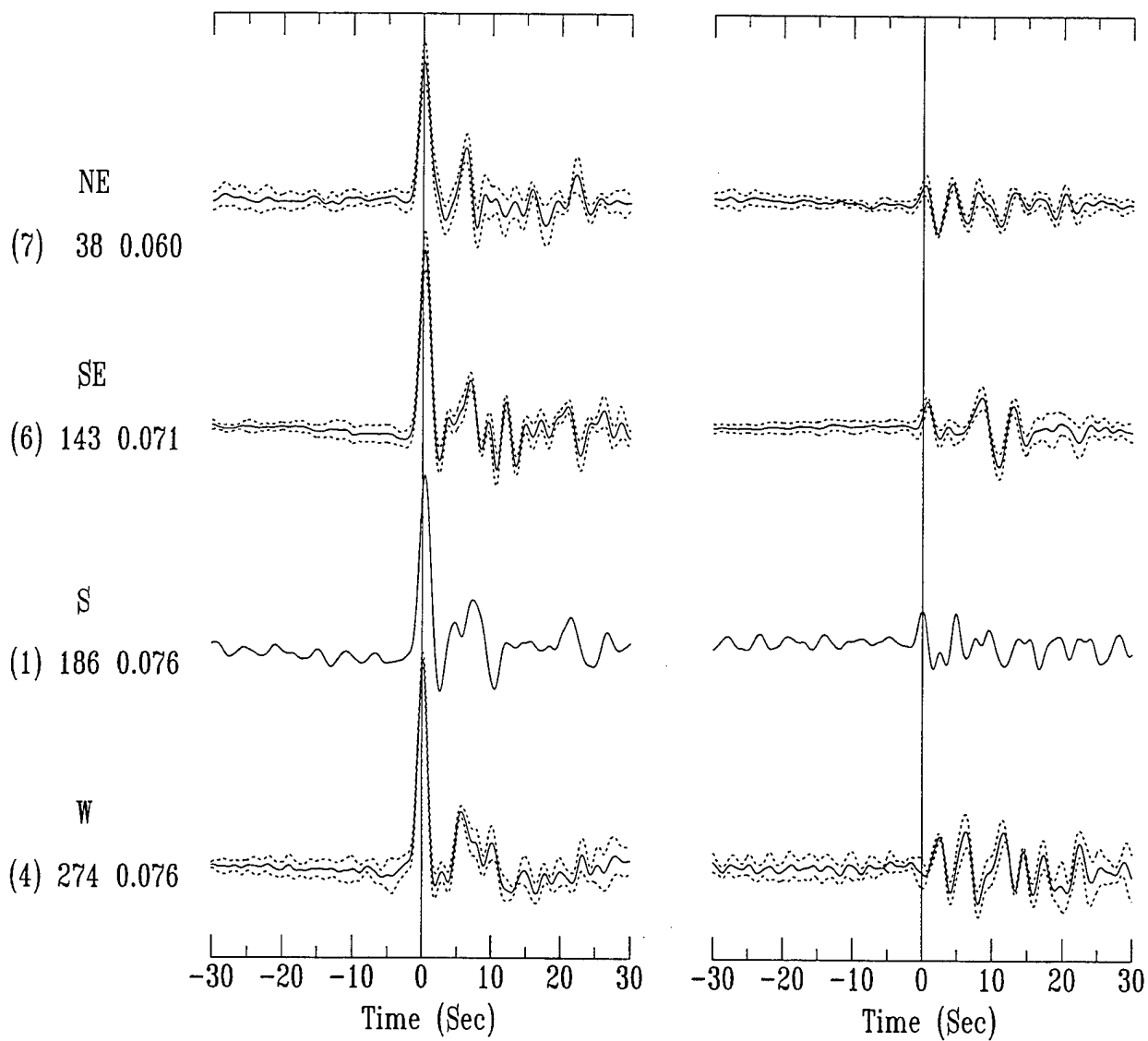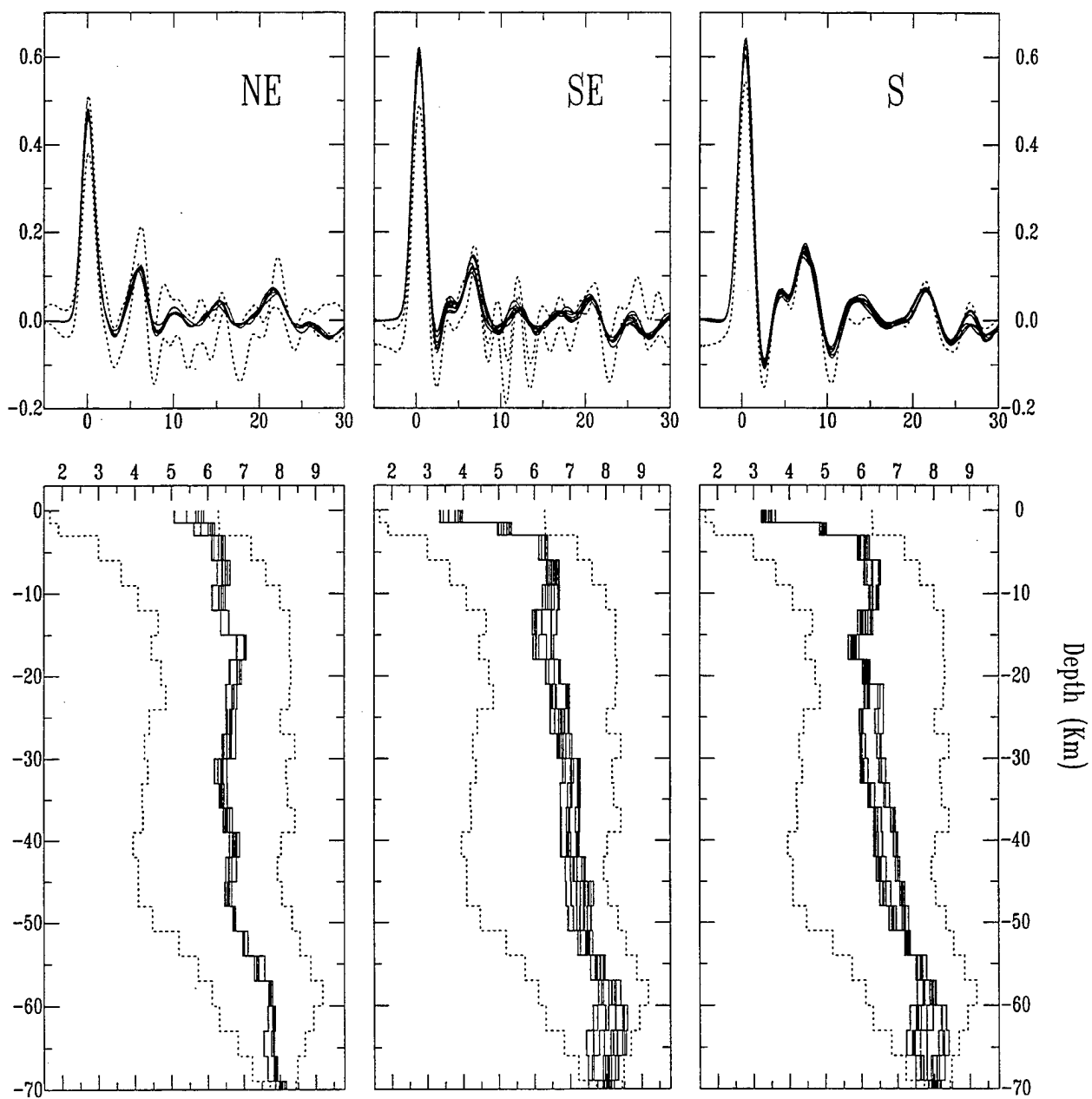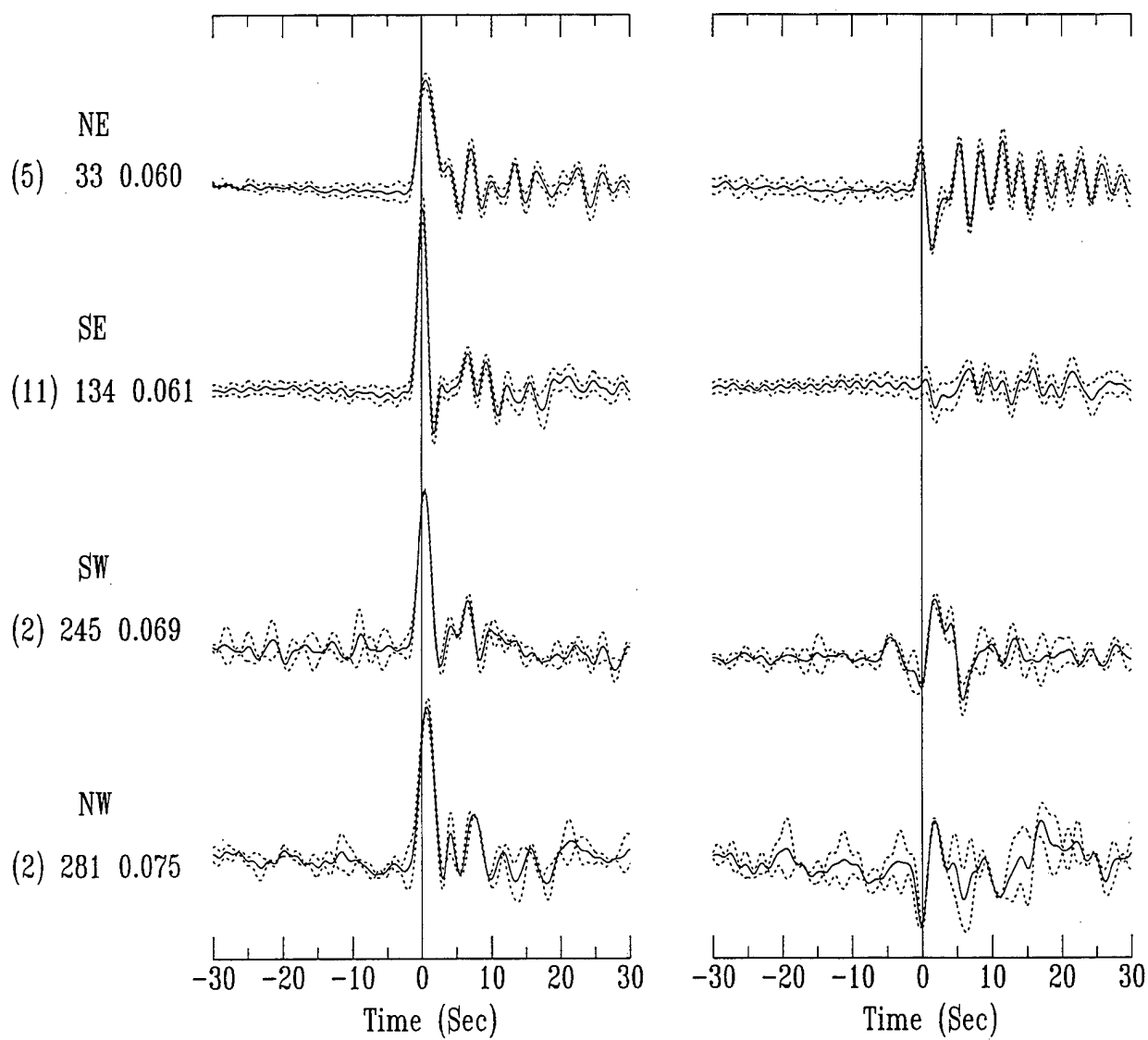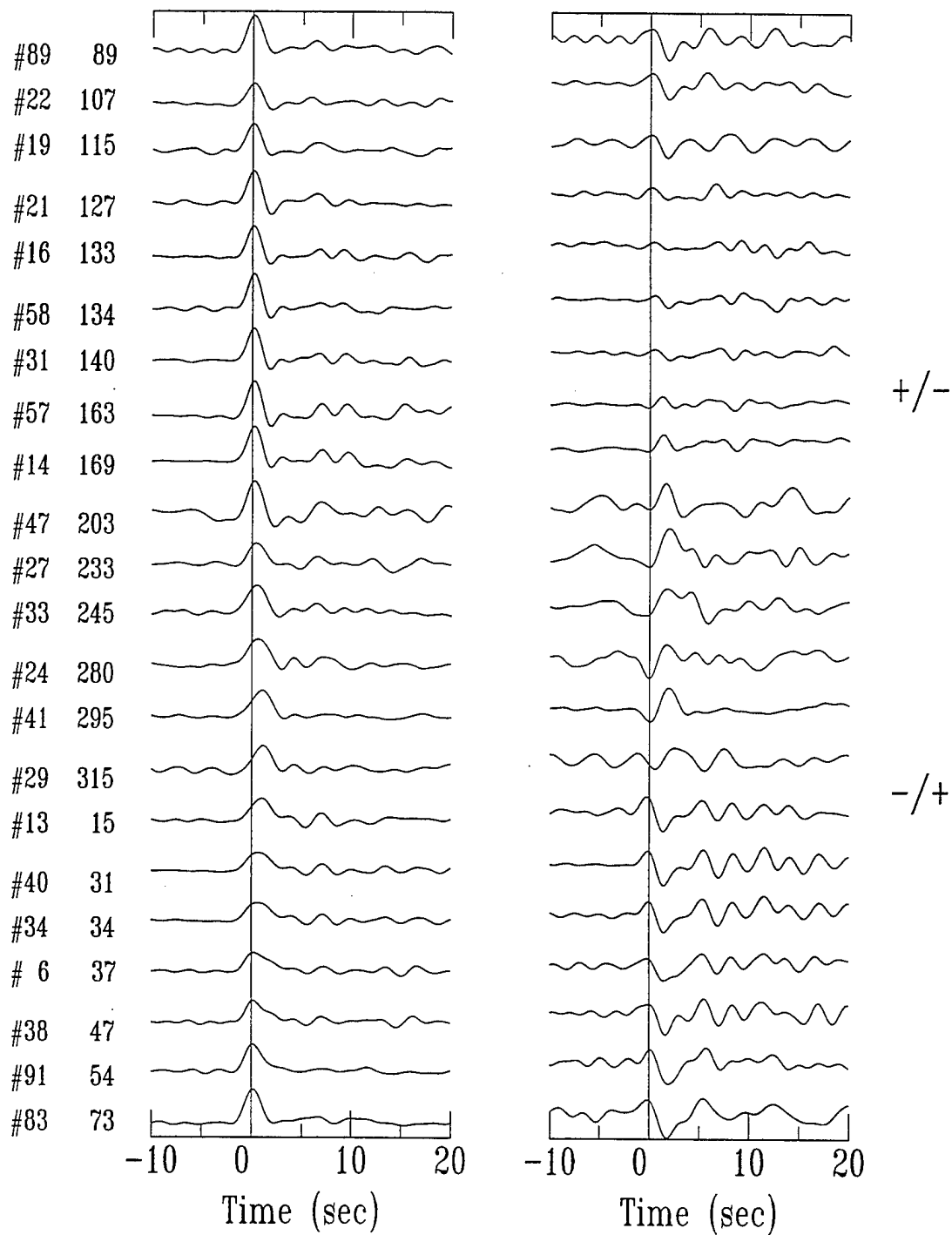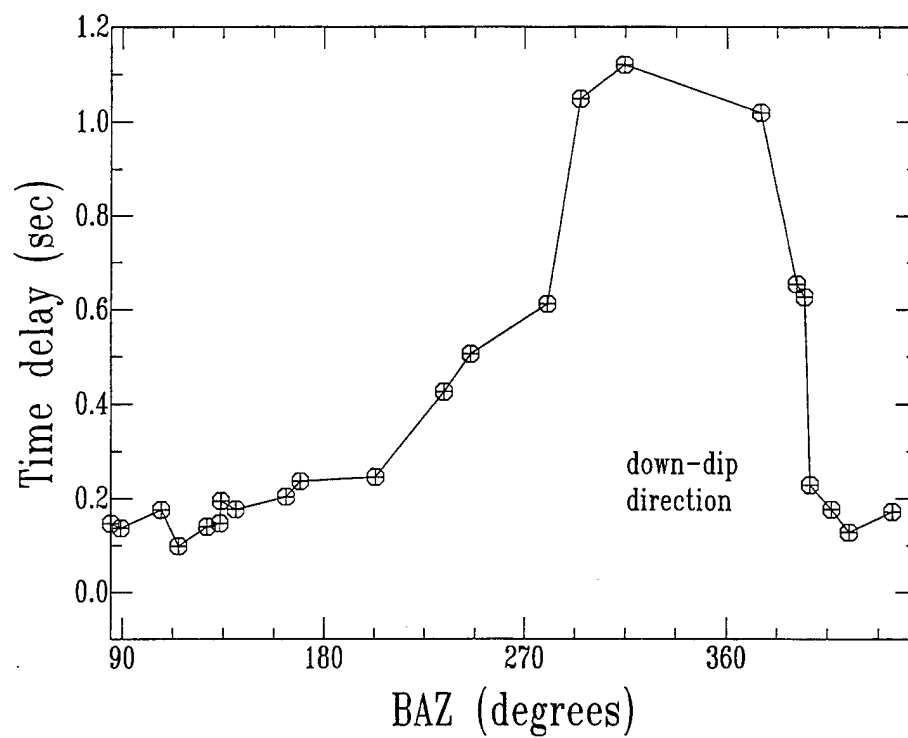| #89 | 89 |
#22	107
#19	115
#21	127
#16	133
#58	134
#31	140
#57	163
#14	169
#47	203
#27	233
#33	245
#24	280
#41	295
#29	315
#13	15
#40	31
#34	34
# 6	37
#38	47
#91	54
#83	73

+/−

−/+

Time (sec)   Time (sec)
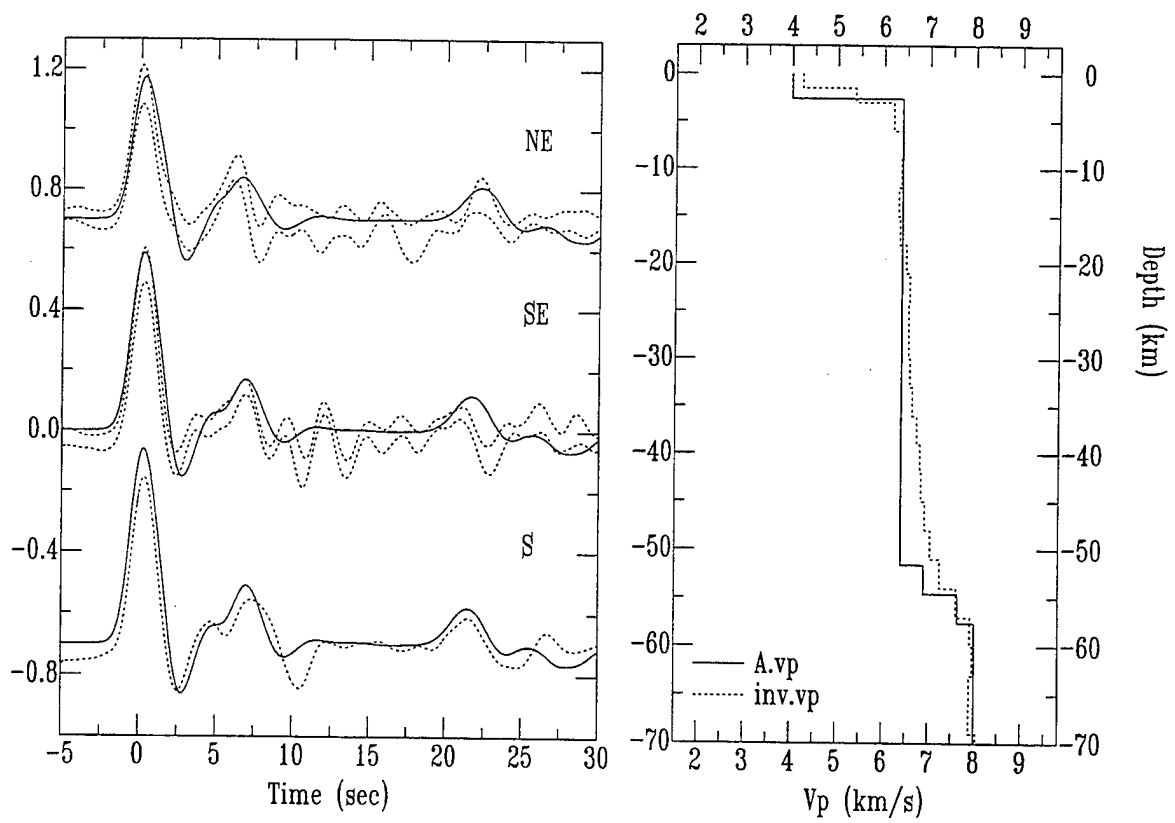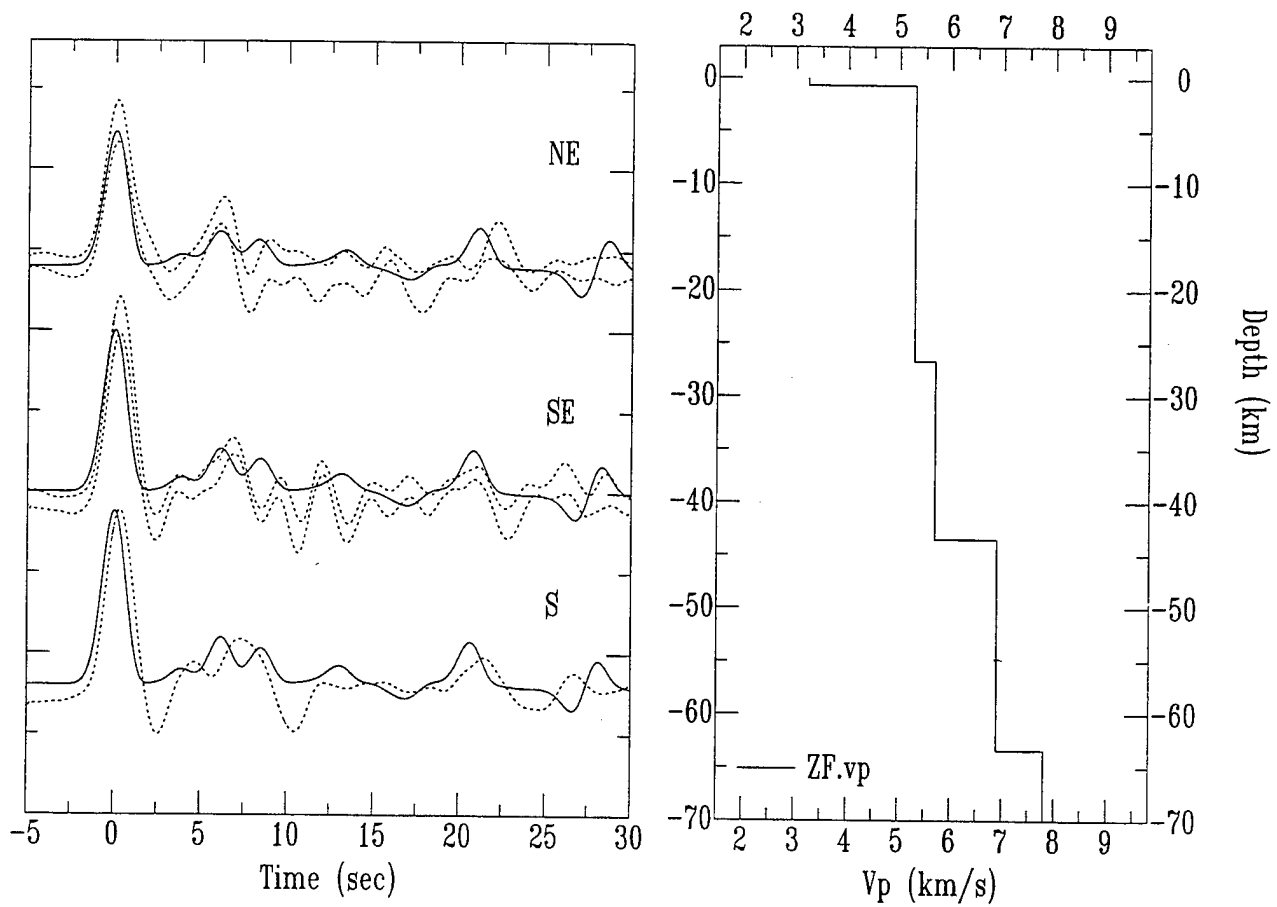
Figure 19

FIGURE 19

FIGURE 20
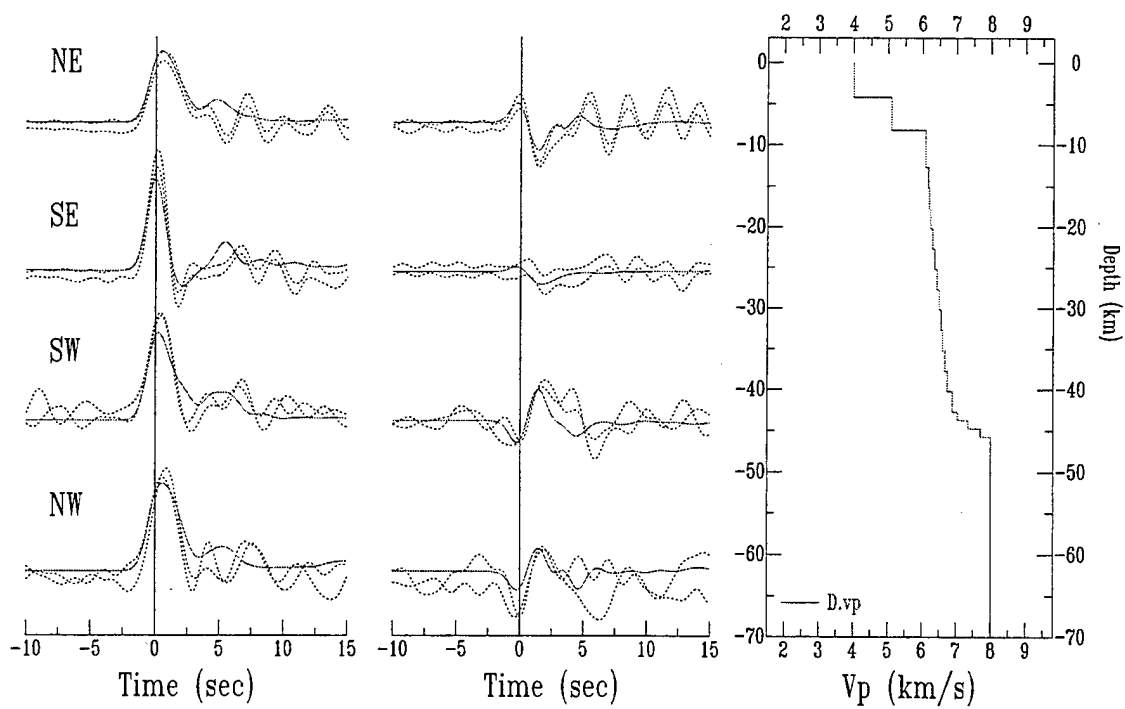
FIGURE 21

151
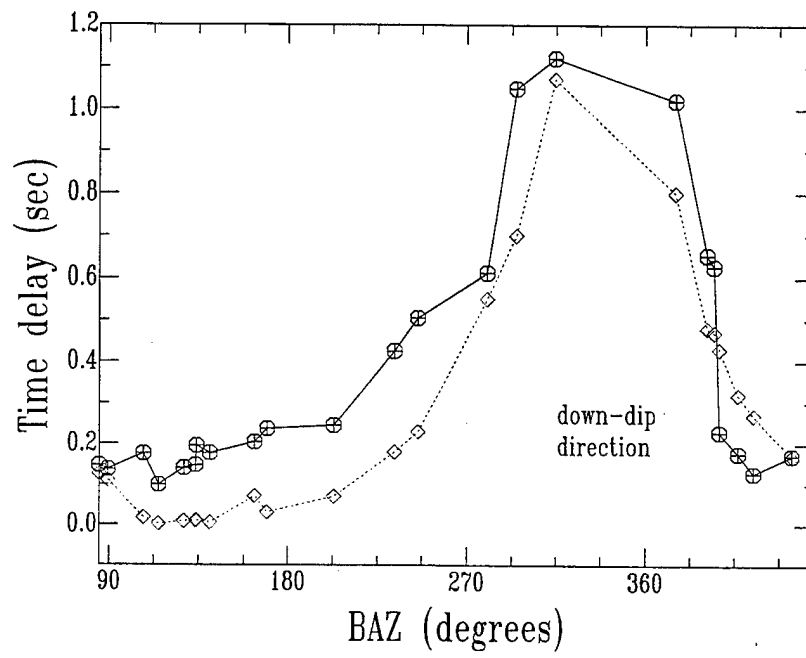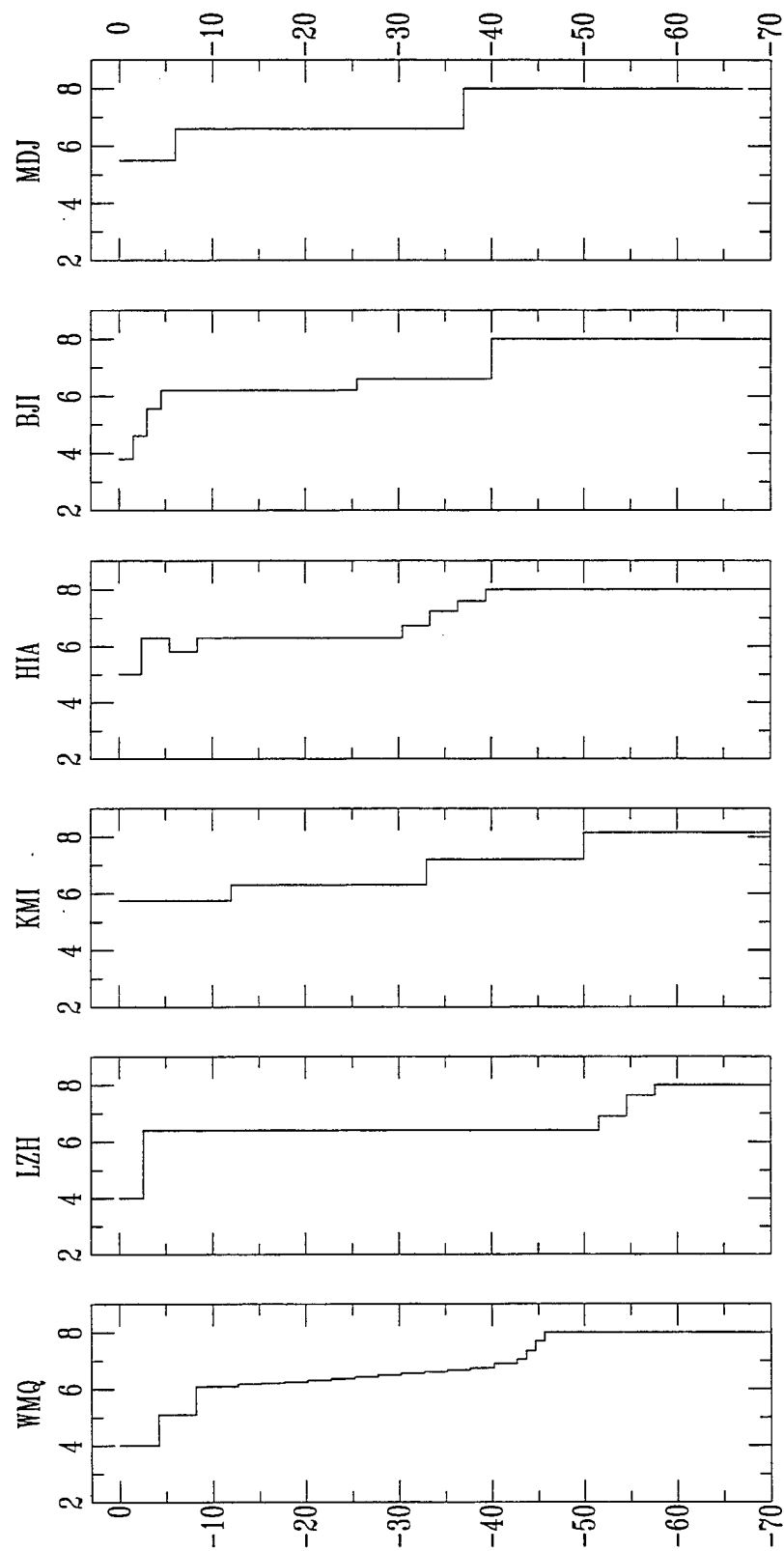
FIGURE 22

FIGURE 23
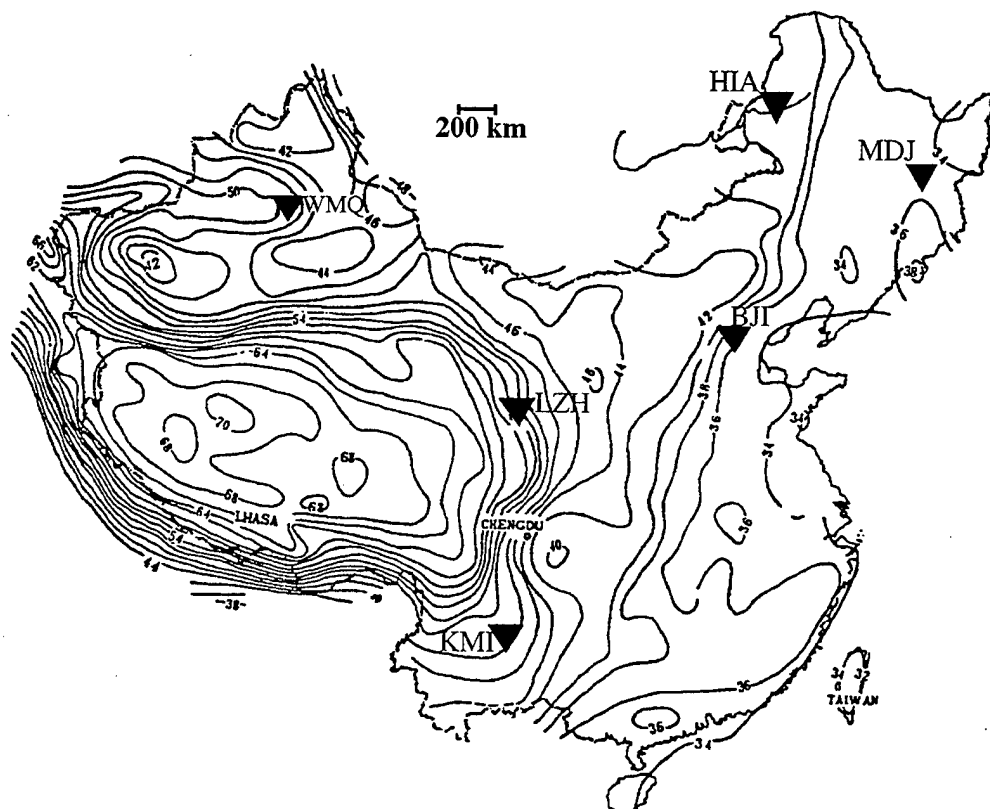
FIGURE 24

CALIBRATION OF $m_b(P_n)$, $m_b(L_g)$ SCALES AND TRANSPORTABILITY OF THE $M_o : m_b$ DISCRIMINANT TO NEW TECTONIC REGIONS

Keith F. Priestley, Department of Earth Sciences, Bullard Laboratories,

Cambridge University, Cambridge, CB3 0EZ United Kingdom

and

Howard J. Patton[1], Environmental Programs Directorate,

Lawrence Livermore National Laboratory, Livermore, CA 94551

ABSTRACT

We have developed $M_o : m_b$ relationships for earthquakes and explosions in central Asia using regional waveform data from the Chinese broadband, digital station, WMQ. Regional magnitude scales, $m_b(P_n)$ and $m_b(L_g)$, were established by (1) determining the attenuation rates of P_n and L_g waves, (2) calibrating the $m_b(P_n)$ against the teleseismic m_b, and (3) applying Nuttli's method to determine m_b from the L_g waves. Seismic moments for earthquakes and explosions were obtained by applying the Bolt and Herraiz (1983) method calibrated using CMT moments for earthquakes and regional moment estimates of the Soviet Joint Verification Experiment (JVE) explosion. The results show that $M_o : m_b(P_n)$ relationships for central Asian earthquakes and explosions are in excellent agreement with the relationships for western United States. This demonstrates that the $M_o : m_b$ discriminant is transportable to other regions and supports theoretical claims (Patton and Walter, 1993) that $M_o : m_b$ are directly comparable for explosions detonated in different emplacement media. Successful application depends upon correcting the $m_b(P_n)$ for the magnitude bias known to exist between the Shagan River test site and the Nevada Test Site (NTS). In general, region–specific m_b bias must be accounted for whenever regional magnitude scales are calibrated against teleseismic m_b, as pointed out by Douglas and Marshall (1996). Transporting $M_o : m_b(L_g)$ can be problematic because attenuation rates based on coda waves or L_g waves from earthquakes may not necessarily

---

[1]Present address: Geophysics Group, EES3, Los Alamos National Laboratory, Los Alamos, NM 87545

apply to L_g waves from explosions, and vice versa. This is demonstrated for the western United States where the coda Q measured from explosion data is much lower than the coda Q from earthquake data. We show that $m_b(L_g)$ for earthquakes located close to NTS is greatly over-estimated using the Q values determined from the coda of NTS explosions. This is apparently not a problem for L_g calibration in central Asia, perhaps because of differences in velocity and/or Q structures for the two regions. Other important considerations are the character of L_g propagation on short paths (< 400 km) for NTS explosions *vs.* long paths (1000 km) for East Kazakh explosions and the properties of coda wave spreading as a function of distance and velocity structures for different tectonic regions.

INTRODUCTION

Teleseismic discriminants for monitoring compliance of a Comprehensive Test Ban Treaty (CTBT) have traditionally relied upon a comparison of the short period (SP) teleseismic body wave magnitude m_b and the long period (LP) surface wave magnitude M_s. This discriminant has proven viable for events greater than about m_b 4.5 and the physical basis for this discriminant is now reasonably well understood (Douglas, *et al.*, 1971; Hudson and Douglas, 1975; Stevens and Day, 1985). To discriminate smaller earthquakes and explosions, important for a CTBT, regional-distance (< 2000 km) observations must be used. Challenges in developing LP:SP discriminants applicable to regional seismic data include: (1) suitable measures of SP and LP energy must be found for regional observations since conventional m_b and M_s are defined for teleseismic data, and (2) once SP and LP measures are chosen, the regional dependences of these measures must be understood in order to assess the transportability of the discriminant from one geologic region to another. Transportability is important because seismograms recorded at regional distances are complex, and it is not clear *a priori* how much of the observed complexity results from source differences and how much results from variations in the regional structure. Consequently, the utility of a discriminant in one region does not guarantee applicability elsewhere.

Regional magnitudes based on P_n, L_g and coda-wave amplitudes have been shown to be useful SP measures of the seismic source in North America (e.g., Nuttli, 1973; Vergino and Mensing, 1990; Mayeda, 1993). A suitable regional-distance LP measure is more problematic. Traditionally, M_s has provided a LP measure of the seismic source, but there are a number of difficulties in measuring M_s at regional distances, particularly for small events (Evernden *et al.*, 1971). Source and path effects can

make surface–wave amplitudes strongly frequency dependent. For example, M_s determined from 20–s period surface–wave amplitudes could differ substantially from M_s based on regional measurements of 10–s period surface–wave amplitudes because of nulls in the Rayleigh–wave spectrum caused by focal depth of crustal earthquakes. Seismic moment M_o is an alternate LP measure, which has the advantage over M_s that it is directly proportional to the seismic source size, free of complicating effects of the Green's function. Variants of LP:SP discriminants utilizing regionally determined body–wave magnitudes, $m_b(P_n)$, $m_b(L_g)$, or Richter magnitude M_L *versus* M_o have been proposed (e.g., Patton and Walter, 1993,1994; both cited hereafter as PW; Woods *et al.*, 1993). For North American events, $M_o : m_b$ relationships between earthquakes and explosions have been established for $m_b(P_n)$ down to 3.0 and for $m_b(L_g)$ down to about 4.0. These relationships show excellent separation between the earthquake and explosion populations, and they suggest that the separation will persist for even smaller events.

Furthermore, $M_o : m_b$ relationships for explosions appear to have little dependence on the source geology (PW). For the Nevada Test Site (NTS), all explosions plot on the same $M_o : m_b(P_n)$ relation, regardless of the emplacement medium (tuff, alluvium, or granite). Also, explosions detonated at the East Kazakh test site (KTS) plot on the same $M_o : m_b(L_g)$ relation as NTS explosions. The prospect of a single relationship for all nuclear explosions regardless of the emplacement geology is very exciting and important for global monitoring of a CTB.

The objectives of this study are to: (1) develop $m_b(P_n)$ and $m_b(L_g)$ scales for central Asian events using regional seismic data, (2) implement a simple algorithm for computing M_o using broadband regional seismic data, (3) determine $M_o:m_b$ relations for central Asian earthquakes and nuclear explosions, and (4) compare these relationships with those derived for North American events. It should be noted here that the algorithm in (2) is based on a method applied by Bolt and Herraiz (1983; hereafter cited as BH) to SP seismograms of Californian earthquakes. In its present form, it is not a means for retrieving M_o in an operational sense, and as such, does not constitute a procedure for discrimination *per se.* The problem of M_o estimation poses a number of practical challenges, but it is also the subject of much interest in the research community. Better methods are quickly becoming available for regional data (e.g., Patton and Zandt, 1991; Giardini *et al.*, 1993; Romanowicz *et al.*, 1993; Zhao and Helmberger, 1994; Ritsema and Lay, 1995).

157

DATA and ANALYSIS

Data: We have studied regional seismograms from 27 nuclear tests and 52 earthquakes (Fig. 1). Locations and origin times of explosions are those reported by Lilwall and Farthing (1990) based on joint epicenter determinations (see Table 1). The explosions include 26 events from KTS consisting of 17 from the Shagan test site (10 from the southwest area of Shagan, 4 from the transition zone, and 3 from the northeast area; Ringdal *et al.*, 1992), 9 explosions from the Degelen test site, and one explosion from the Chinese Lop Nor test site. The explosions range in size from m_b 4.6 to 6.2. Earthquake hypocentral parameters are summarized in Table 1 and are taken from the *Bulletin of the International Seismological Centre* (ISC). The earthquakes are located primarily in the central Asian fold belts and range in size from m_b 4.0 to 6.1. The teleseismic magnitudes (m_b and M_s) for earthquakes and explosions are from the ISC Bulletin. Also, Table 1 lists seismic moments for earthquakes and explosions and maximum likelihood estimates (MLE) of teleseismic m_b for explosions, as reported by a number of investigators.

All of the seismograms used in this study were recorded at the Chinese Digital Seismic Network (CDSN) station Urumqi (WMQ) which is located approximately 990 km from the Degelen Mountain test site, 960 km from the Shagan test site, and 240 km from the Lop Nor test site. Epicentral distances for earthquakes range from 200 to 1500 km. P_n is the first arrival for nearly all events studied. P_g is not well developed for the KTS explosions recorded at WMQ, as previously noted by Gupta *et al.*, (1992). In addition, many earthquakes do not have a clear P_g phase; 20 earthquakes showed little or no evidence of P_g on the World Wide Standard Seismogram (WWSS) SP passband. The L_g phase is prominent for explosions, with the first arriving wave packet having group velocities of about 3.6 km/s for KTS explosions. The L_g waves for the Lop Nor explosion show a high apparent group velocity ($\sim$ 3.8 km/s) assuming the ISC location. The earthquake L_g wavetrains show more variability between events than do the explosions, and for a few earthquake records, L_g was quite muted in the WWSS SP passband.

Determination of $m_b(P_n)$: We followed the procedure of Denny *et al.* (1987), who developed a $m_b(P_n)$ scale for the western United States (WUS). The broadband digital seismograms were filtered to simulate a WWSS SP seismogram (Fig. 2a) by deconvolving the CDSN broadband instrument response and convolving the WWSS SP response. We then picked the arrival times of P_n and P_g.

Picking P_g was difficult because of the variability of the phase. An average group velocity for the P_g phase based on the clearer picks is about 6.1 km/s. A window for the P_n amplitude measurement was chosen so that if the P_g phase was present, the window went from the P_n onset to the P_g arrival, and if P_g was absent, the window went from the P_n onset to a group velocity of 6.1 km/s.

Two measures of the P_n amplitude were taken. One was the maximum peak–to–peak amplitude, A_{p-p}, occurring in one continuous cycle anywhere within the measurement window; the second measure was an RMS amplitude, A_{rms}, using the entire window. Noise windows were also selected before the P_n onset, and noise levels were measured in the same way as the signals were. Generally, noise was not a problem for measuring P_n amplitudes, and no further analysis was carried out on the noise samples.

We assume that the relation between $m_b(P_n)$, A, and distance Δ is of the form

$$m_b(P_n) = a + \log A + b \log \Delta \qquad (1)$$

where a and b are constants to be determined. In (1) we follow Denny *et al.*, who found that observed scatter in the $m_b(P_n)$ amplitude measurements was reduced considerably by using the amplitude rather than the ratio of the amplitude to the period. We determined b by finding the value which removes the distance dependence and determined a so that the population mean of $m_b(P_n)$ equaled the mean of the teleseismic body–wave magnitude $m_b(P)$ from the ISC.

The results are shown in Fig. 3a for the peak–to–peak measurement. The KTS explosions are restricted in range, and neither they nor the Lop Nor explosion were used to estimate b. Linear least–squares fits gave the following results for a and b, respectively: -1.47 $\pm$ 0.26 and -7.33 $\pm$ 0.72 for peak–to–peak; -1.69 $\pm$ 0.25 and -7.43 $\pm$ 0.69 for RMS. In general, the explosion data fit reasonably well with the trend of the earthquake observations, and this led us to use a single distance correction for all events. Randall *et al.* (1996; also Phillips, pers. comm., 1996) made a similar study of P_n attenuation for WMQ, although their measurement window is a constant length of 10 s. Their attenuation rates are -1.27 $\pm$ 0.23 for zero–to–peak P_n amplitudes and -1.32 $\pm$ 0.23 for RMS amplitude. While these estimates are smaller than the decay rates reported here, the agreement is quite good considering the estimated uncertainties and the biases that could be introduced by differences in measurement window and epicenter selection. It is noteworthy that the amount of scatter in A_{rms} is not much less than the scatter in A_{p-p}, which is also consistent with Randall *et*

159

al.'s results. We decided to continue to analyze both measurements in parallel in our study.

The $m_b(P_n)$ formulae for earthquakes recorded at WMQ are

$$m_b(P_n) = 1.327 + \log(A_{p-p}) + 1.470\log(\Delta) , \qquad (2)$$

where the A_{p-p} is in μm, and for P_n A_{rms}

$$m_b(P_n) = 1.432 + \log(A_{rms}) + 1.693\log(\Delta) . \qquad (3)$$

The formulae for explosions are different by a small constant because the population mean of $m_b(P_n)$ based on A_{p-p} was 0.043 magnitude units (mu) greater than the mean of the teleseismic m_b and in the case of A_{rms} was 0.062 mu greater. The constant corrects for this so that both earthquake and explosion populations had zero mean with respect to the teleseismic m_b. $m_b(P_n)$ values are given in Table 2 and plotted against $m_b(P)$ in Fig. 3b. There is a suggestion that the magnitudes are not scaling one–to–one, and this may arise because ISC $m_b(P)$ is biased high for the smaller events, as we discuss later in the paper.

Determination of $m_b(L_g)$: We computed $m_b(L_g)$ using the Nuttli (1973) method, where $m_b(L_g)$ is defined in terms of the amplitude of the L_g phase with a period near 1 s observed on a WWSS SP instrument. $A(\Delta)$ is the amplitude of the third (3rd) largest peak of the L_g waves in the 3.2 to 3.6 km/s group velocity window. This amplitude is extrapolated back to an epicentral distance of 10 km by correcting for geometrical spreading and attenuation using the formula

$$A(10) = A(\Delta) \cdot (\Delta/10)^{\frac{1}{3}} \cdot [\sin(\Delta/111.1)/\sin(10./111.1)]^{\frac{1}{2}} \cdot \exp\gamma(\Delta - 10) . \qquad (4)$$

In this relation the $(\Delta/10)^{\frac{1}{3}}$ term accounts for group velocity dispersion when the measurements are made in the time domain. Nuttli concluded from empirical evidence that the exponent should be 1/3 corresponding to an Airy phase, rather than 1/2 corresponding to normally dispersed surface waves. Campillo *et al.* (1985) verified this conclusion using synthetic seismograms. The $[\sin(\Delta/111.1)/\sin(10./111.1)]^{\frac{1}{2}}$ term corrects for geometrical spreading, and the exponential term corrects for attenuation. γ is the attenuation coefficient for the L_g wave. Nuttli found that in central and eastern North America, a $m_b(P)$ 5.0 earthquake produced a 1 Hz L_g amplitude of 110 μm at a distance of 10 km, and therefore defined $m_b(L_g)$ as

160

$$\mathrm{m_b(L_g)} = 5.0 + \log(A(10)/110) \ . \tag{5}$$

We measured $\mathrm{L_g}$ amplitudes in two ways after correcting the broadband seismograms to a WWSS SP response (Fig. 2a). The first used the amplitude of the 3$^{\mathrm{rd}}$ peak down from the maximum, $A_{3\mathrm{rd}}$, as Nuttli did on analog records; the second used the RMS amplitude, A_{rms}, implemented by Patton (1988). The attenuation correction required by (4) is obtained from Q models based on the decay of $\mathrm{L_g}$ or coda waves from earthquakes or explosions. The attenuation is related to the Q model by the equation $\gamma = \pi/QUT$, where U is the group velocity, T is the wave period, and Q has the power law form $Q = Q_o f^\eta$, where Q_o is the Q at 1 Hz. We have adopted the Q model developed by Martynov, Rozhkov, and Priestley (unpublished results), who employed the methodology of Rautian and Khalturin (1978). The Q model is $Q = 400f^{0.6}$.

Q models for $\mathrm{L_g}$ and coda waves have been investigated for central Asia. Given *et al.* (1990) used data from small calibration shots to study $\mathrm{L_g}$ attenuation for a region about 300 km in radius around KTS, and reported $Q = 500f^{0.4}$. Sereno (1990) employed a generalized inversion method to recover source and path transfer functions for earthquakes and explosions in a region roughly 1000 km in radius around KTS. Trade–offs exist in his final results, and the frequency-independent model, $Q = 650$, gave the most consistent source amplitudes for different stations. Coda Q tomography results were reported by Xie and Mitchell (1991) using earthquake and explosion data. For tectonic paths, Q_o ranged from 400 – 500. Xie *et al.*, (1996) found Q_o of 400 – 450 for the tectonic areas around WMQ, where many earthquakes in this study occur. Xie *et al.* give Q_o values of 427 and 459 for coda waves and $\mathrm{L_g}$ waves, respectively, on the path between the Kirgizan seismic net stations and the Lop Nor test site, and 504 and 565 on the path between WMQ and KTS. The former path cuts through the tectonic areas of this study. A Q_o of 505 for the KTS–WMQ path translates into $\mathrm{m_b(L_g)}$ about 0.20 mu smaller than the estimates we obtain for explosions using Martynov *et al.*'s Q model.

The $\mathrm{L_g}$ A_{rms} had to be corrected for an effect of measurement window length, where the length is determined by group velocity and distance. As the distance increases, the length of the $\mathrm{L_g}$ window increases to accommodate the growing time separation between S-wave arrivals. We found that the A_{rms} decayed faster with distance than the $A_{3\mathrm{rd}}$ measurement because gaps between pulses of significant energy reduced the amplitude. By plotting $\log(A_{3\mathrm{rd}}/A_{rms})$ *vs.* distance, we were able to

161

establish an empirical correction for normalizing out the window effect.

In Fig. 4, we check consistency between our $m_b(L_g)$ and published values by plotting $m_b(L_g)$ from Ringdal *et al.* (1992) for explosions in common. Ringdal *et al.* measured $m_b(L_g)$ on far–regional L_g waves recorded on arrays in Germany and Norway using the peak amplitude of a RMS L_g envelope centered near 3.5 km/s (see Hansen *et al.*, 1990). They scaled their $m_b(L_g)$ to be consistent with the Nuttli magnitude. A plot of our $m_b(L_g)$ values from the A_{3rd} *vs.* those of Ringdal *et al.* should ideally be a line with unit slope and zero intercept. Fig. 4 shows that the magnitudes scale one-to-one with an average offset of only 0.03 mu. The $m_b(L_g)$ based on A_{rms} also scale well with the Ringdal *et al.* $m_b(L_g)$. The average offset between the RMS and 3rd peak $m_b(L_g)$ is 0.28 $\pm$ 0.06 mu, and agrees well with the offset of 0.22 mu found for NTS explosions (Patton, 1988). The $m_b(L_g)$ determined from A_{rms} show only slightly less variance than the 3rd peak magnitudes, also consistent with the NTS results.

Determination of seismic moment: Seismic moment M_o is a physically meaningful measure of the source size, and this is part of our motivation for using it to develop LP:SP regional discriminants. The use of M_o also reduces some of the complexity of investigating transportability of regional discriminants. We required a method for estimating M_o from regional seismograms when neither the crustal velocity structure nor the source mechanism are known, and when the signal–to–noise ratio for periods longer than $\sim$ 10 s may be poor. Since L_g is often the largest amplitude regional phase, we decided to estimate M_o using the method of Bolt and Herraiz (BH), who found that central California earthquakes obey the relation

$$\log M_o = a + b \log(C \cdot D \cdot \Delta^p) \; , \tag{6}$$

where C is the maximum peak–to–peak amplitude measured on a Wood–Anderson seismogram, D is the time duration between the S–wave arrival time and the time when the amplitude of the S–wave coda decreases to C/d, and Δ is the epicentral distance. Parameters a, b, d, and p are constants to be determined. The physical rationale for the form of the logarithmic term is that M_o is proportional to the LP spectral amplitude Ω_o (Keilis–Borok, 1960)

$$M_o = 4\pi\mu\beta \frac{\Delta\Omega_o}{2R_{\theta\phi}} \tag{7}$$

where μ is the rigidity, β is the shear wave velocity, and $R_{\theta\phi}$ is the source radiation pattern. Ω_o is the product of the pulse width and the amplitude and is closely related to the mean value of seismic energy arriving in the time window considered. For central California, BH found $a = 6.08 \pm 0.20$, $b = 1.22 \pm 0.14$, $d = 3$, and $p = 1$ for M_o in N–m and the amplitude measured in μm.

We adapted the method to digital, broadband waveform data by first converting the broadband seismograms to a Wood–Anderson response. We then measured the S–wave (L_g) arrival time, t_{L_g}, the absolute zero–to–peak amplitude of the L_g wave, C, in μm and the time $t_{1/3}$ at which the coda had fallen to one third of the peak amplitude. The duration D is then $t_{1/3}$ - t_{L_g}. Fig. 2b shows an example of these measurements on recordings of an earthquake.

An average of the product $(C \cdot D \cdot \Delta^p)$ for the N–S and E–W components was computed, and this value was plotted against the Harvard CMT M_o (Table 1). We determined values for a and b as a function of p ranging from 0.8 to 1.5. Since little difference in the quality of fit was found over this range of p, we chose $p = 1$, and the resulting fit to the data is plotted in Fig. 5. The linear relationship for central Asian earthquakes is

$$\log(M_o) \;=\; 7.05 \;+\; 1.12 \log\,[C \cdot D \cdot \Delta]\;, \tag{8}$$

for C in μm and M_o in N–m. For an abscissa value of 9.0, (8) gives a Log M_o of 17.13, while the BH formula gives 17.06. For the range of abscissa values in this application, the two formulae give quite similar M_o. M_o for all earthquakes are given in Table 2.

For the explosions, we used the isotropic seismic moment M_I of Ekstrom and Richards (1994) for calibration purposes (see Table 1). Ekstrom and Richards scaled the explosion moments relative to a value of 2.4×10^{16} N–m for the Soviet JVE (88258) based on a reverse–faulting tectonic release mechanism (Walter and Patton, 1990). Because of the limited number of explosions, we decided to use the same slope as the earthquakes' in (8), and the intercept value is set so that the calibration line passes through the Soviet JVE.

Studies of the Soviet JVE have been carried out by a number of investigators to characterize the seismic source (Walter and Patton, 1990; Langston, 1995; Xie et al., 1996). The most detailed source model is that of Langston who finds evidence for a spatially distributed source and suggests that explosion–driven faulting was a secondary source. Accounting for source time function and source complexities, Langston estimates an M_I of 1.1×10^{16} N–m for the Soviet JVE. The source

163

model favored by Walter and Patton is based on waveform model fitting to regional S–waves and surface waves and has a strike–slip mechanism with an M_I of 1.7×10^{16} N–m. Xie *et al.* obtained M_I estimates for many KTS explosions using a nonlinear inversion technique applied to L_g spectra. Their estimate of the M_I for the Soviet JVE is 1.3×10^{16} N–m. All of these studies report smaller M_I than the M_I for a reverse–faulting tectonic release model, and we decided to re-scale to a JVE M_I of 1.34×10^{16} N–m, the log mean of the estimates discussed above. The explosion moments are given in Table 2.

Fig. 6a is a plot of our moment estimates, $M_o(L_g)$, *vs.* various published seismic moment values from Table 1. The comparison is quite good down to the smallest event plotted, which is the Lop Nor explosion. The $M_o(L_g)$ for this explosion compares well with a model–based estimate (Wallace, pers. comm.,1996), even though it is estimated using the calibration for KTS explosions. Fig. 6b shows that $M_o(L_g)$ scales one–to–one with ISC M_S for earthquakes.

REGIONAL MOMENT: MAGNITUDE OBSERVATIONS

P_n relationships: In Fig. 7, we plot all of the KTS explosions for which we were able to measure M_I plus three explosions with M_I reported in Ekstrom and Richards (1994; no. 53 and 54) and in Stevens and McLaughlin (1988; no. 55). We also plot the Lop Nor explosion, where the $m_b(P_n)$ is reported by Wallace (pers. comm., 1996) based on amplitudes from Chinese stations beyond the P_n/P_g cross-over distance. Regression lines for the explosion and earthquake data are shown along with the resulting equations and uncertainties. A comparison of these results with the RMS results in part (b) indicates that the scatter is somewhat smaller for the $m_b(P_n)$ based on A_{rms}. Standard errors of the residuals are reduced more for the explosions, 0.17 *vs.* 0.13, than they are for the earthquakes, 0.31 *vs.* 0.29. This could be related to the fact that path variability is far less for KTS explosions.

The regression lines for NTS explosions and WUS earthquakes from PW are shown in Fig. 7 for comparison. The line for WUS earthquakes truncates at m_b 5.3 because that was the largest magnitude analyzed by PW. Since then, $m_b(P_n)$ has been measured for recent earthquakes, including the mainshock and aftershocks of the Little Skull Mountain sequence (Mayeda and Walter, 1996; Walter, pers. comm., 1996). M_o for larger events are available from a number of waveform modeling studies, all summarized in Mayeda and Walter (1996). M_o of smaller Little Skull Mountain earthquakes were

determined using the BH method. The new measurements are plotted in Fig. 7a.

Several interesting features are evident from the comparison of results in Fig. 7a. First, the explosions for both test sites have nearly the same slope (1.08 for KTS $vs.$ 1.12 for NTS), but are offset for the range of magnitudes in this study. Second, the slope of the earthquake $M_o : m_b$ relationship from PW appears to be underestimated since events with m_b greater than 5.2 generally plot well above a projection of the line. Third, the comparison of earthquake data for the two tectonic regions is good, although scatter in the observations is large.

We believe that the offset in the explosion results is caused by the test-site $m_b(P)$ bias between KTS and NTS (Nuttli, 1986,1987; Murphy et $al.$, 1991; Der et $al.$, 1985). Estimates of the magnitude bias between the Shagan River test site and NTS fall between 0.3 and 0.4 mu. Since $m_b(P_n)$ is calibrated against teleseismic m_b for both the WUS and central Asia, a bias existing in the teleseismic $m_b(P)$ will carry over into $m_b(P_n)$ scale. This is reflected by the results in Fig. 7a, where the offset is about 0.30 mu for a $\log M_o$ of 16.0 N–m.

L_g $relationships$: Fig. 8a shows the results for the 3rd peak measure and part (b) for the RMS measure. The RMS–based magnitudes were normalized to an equivalent 3rd peak measure by adding 0.28 mu, as was discussed earlier in the paper. The results for central Asia are very consistent for both measures, with no real differences in the scatter for either earthquakes (0.29 $vs.$ 0.27) or explosions (0.11 $vs.$ 0.10). We do not find significantly smaller scatter for the A_{rms}, as reported by Hansen et $al.$ (1990), probably because the window lengths are much shorter in this study.

The $M_o : m_b(L_g)$ relationships for KTS and NTS are quite similar. There is a suggestion that scaling rates are different; however, there are few KTS observations at small magnitudes where the differences are the greatest. At the larger magnitudes, the L_g relationships are not offset, as they are for $m_b(P_n)$. This is consistent with Nuttli's claim of regional transportability of the $m_b(L_g)$ scale.

The earthquake results in Fig. 8a show significantly more scatter than the explosion results do. The regression curve for central US (Herrmann, 1979; see PW) plots below the observations for central Asian earthquakes. However, even more extraordinary are measurements for the Little Skull Mountain earthquake sequence and other earthquakes located near NTS. $m_b(L_g)$ values were obtained using waveform data from the Lawrence Livermore NTS Network (LNN) and coda Q values determined from NTS explosions (Patton, 1988). The observations plot well below the earthquakes

for central Asia and central US. A comparison of the $m_b(P)$, $m_b(P_n)$, and $m_b(L_g)$ for the Little Skull Mountain mainshock, 5.5, 5.53, and 6.66, respectively, suggests that the discrepancy must arise from over–estimation of the $m_b(L_g)$. (Correction for the magnitude bias would only raise $m_b(P)$ and $m_b(P_n)$ by about 0.35 mu.)

Revised M_o : m_b relationships for P_n and L_g: In Fig. 9a, we have accounted for the magnitude bias between NTS and Shagan by adding 0.35 mu to $m_b(P_n)$ for all NTS explosions. This shifts the NTS relationship to the right, resolving the offset in Fig. 7. We have also added 0.35 mu to the $m_b(P_n)$ values for WUS earthquakes. This is justified by the fact that many of these earthquakes are located close to NTS or in areas of anomalous upper mantle attenuation. A regression line fitted through all of the WUS earthquakes captures the general trend, even though some large events may have saturated the m_b scale. Some earthquakes perhaps should not have been corrected for bias (e.g. those on the Colorado Plateau).

A new M_o : $m_b(L_g)$ relationship for WUS earthquakes is shown in Fig. 9b. This relationship is based on $m_b(L_g)$ computed for a Q model consistent with L_g and coda–wave attenuation in the WUS based on earthquake studies (see discussion below). In selecting the Q model, we took Q_o values averaging 225 on paths to the four LNN stations. The new M_o:m_b relationship now agrees well with the central US regression line plotted in Fig. 8a, but the comparison with central Asian observations is not as good.

DISCUSSION

The results presented in the preceding section are quite encouraging for the transportability of M_o : m_b relationships. In spite of great differences in material properties between the NTS and KTS, and possibly significant differences in testing practices, the agreement in Fig. 9 is excellent for explosions. The importance of regional calibration must be emphasized here since $m_b(P_n)$ scales developed for new tectonic regions depend on proper identification of regional phases, on calibration of P_n attenuation properties, and on determination of regional bias in the teleseismic m_b. Douglas and Marshall (1996) point out the susceptability of a regional magnitude scale to possible biases when the scale is calibrated against $m_b(P)$, and they emphasize the need for regional bias corrections to improve transportibility.

166

The earthquake results in Fig. 9 show larger differences between tectonic regions than explosions results do, but the disparities are remarkably similar for P_n and L_g. This fact suggests source effects, but propagation effects cannot be precluded yet and will be the focus of discussion in this section.

Our recent investigations are starting to make estimates of M_o based on regional recordings of LP surface-waves. The focus is on the CMT events in central Asia, and we utilize a method that perturbs the CMT source model in order to find a new model that minimizes the differences between observed and theoretical surface-wave amplitudes. Preliminary results suggest a systematic difference between the CMT M_o estimates and M_o estimated from regional data. The regional estimates are, on average, about a factor of 2 smaller. At this stage in our investigations, we have not determined the cause of these differences, although the Green-function responses utilized by the CMT and/or the regional solutions are possibilities. It is worth noting, however, that the regional estimates are based on Green functions for an earth model that approximates the average crustal thickness for our study area. If we were to use the regional M_o estimates for calibration in Fig. 5, new M_o:m_b relationships for central Asian earthquakes are in better agreement with WUS relationships for both $m_b(P_n)$ and $m_b(L_g)$.

Regional calibration and magnitude bias. Attenuation estimates of P_n and L_g waves are based on earthquake data for paths through tectonic areas. KTS is located in a more stable region, and this raises a concern that significant lateral heterogeneities in the crust and upper mantle could cause differences in propagation characteristics for earthquakes and explosions. Nevertheless, the calibration of L_g attenuation worked well for KTS explosions (see Fig. 4). Furthermore, a plot of $m_b(P)$ *vs.* 3rd peak $m_b(L_g)$ in Fig. 10a generally agrees with results of Nuttli (1986). Using ISC m_b, he found an average difference, $m_b(P) - m_b(L_g)$, of 0.036 ± 0.015 mu for Shagan River and 0.27 ± 0.03 mu for the Degelen Mountain site. Nuttli suggested that one cause for a larger bias at Degelen Mountain could be differences in the source coupling for either P or L_g waves. While the number of data are limited in this study, the trend of observations in Fig. 10a appears to be related more to magnitude than to test area.

In Fig. 10b, $m_b(L_g)$ is plotted *vs.* maximum likelihood estimates (MLE) of $m_b(P)$ for events at the Shagan test site (Ringdal *et al.*, 1992), at Degelen Mountain (Jih *et al.*, 1994), and for the Lop Nor explosion (Douglas *et al.*, 1993). The MLE estimates scale nearly one–to–one with

167

$m_b(L_g)$. The average difference, $m_b(P, MLE) - m_b(L_g)$, for the Shagan River explosions is 0.053 ± 0.040 mu, still in good agreement with Nuttli's estimate based on ISC m_b. However, the Degelen Mountain observations for small magnitudes are in good relative agreement with the larger Shagan River explosions as opposed to the results in Fig. 10a for ISC $m_b(P)$. This suggests that Nuttli's estimate of the magnitude bias for Degelen was too large, probably due to poor signal-to-noise and station selection in the ISC determination of $m_b(P)$.

We now employ the $m_b(L_g)$ results to check the P_n calibration. Fig. 10c shows that $m_b(P_n)$ and $m_b(L_g)$ scale one-to-one, as desired. All three explosions detonated in the NE area have significantly larger P_n amplitudes relative to L_g compared to tests in other areas. Excluding the three NE events, the average difference, $m_b(P_n) - m_b(L_g)$, is 0.164 ± 0.031 mu for the remaining 14 Shagan River explosions. This is 0.11 ± 0.05 mu larger than the results based on $m_b(P, MLE)$. Recalling that the raw $m_b(P_n)$ values were reduced by 0.043 mu to make the explosion population zero-mean with respect to the teleseismic m_b, the net $m_b(P_n) - m_b(P, MLE)$ offset is 0.15 ± 0.08 mu. Some or all of this offset could arise if the P_n attenuation correction was too large for the KTS–WMQ path. On the other hand, focusing of P_n waves is another possibility, as the following discussion illustrates.

The large P_n amplitudes for NE explosions are very curious in light of Ringdal *et al.* (1992) observations showing just the opposite effect for the teleseismic $m_b(P, MLE)$. They find the $m_b(P, MLE) - m_b(L_g)$ difference is -0.10 ± 0.047 mu based on roughly 25 NE explosions. Our study involved only three NE explosions, none in common with theirs, and they give an $m_b(P_n) - m_b(L_g)$ difference of $+0.57$ mu, which is a far larger effect and opposite in sign.

Israelsson (1992) reports that bias estimates for Shagan River show large variance from one teleseismic station to the next, and suggests that this is probably caused by wavefield distortions due to laterally-varying earth structures. Such wavefield distortions might be even stronger to regional-distance stations because velocity heterogeneities are probably greater for crust and upper mantle paths. WMQ may be sited at a P_n "bright spot" for KTS in general, and particularly for explosions detonated in the NE. Since the paths to WMQ are so similar, an effect of earth structures far away from KTS can be precluded, and focusing by heterogeneous earth structures very close to or in the source regions could cause large P_n amplitudes for explosions detonated in NE Shagan.

L_g enigma in the western US: The results in Fig. 4, Fig. 8a, and Fig. 10 highlight the problem

of calibrating L_g attenuation in geophysically distinct regions. To summarize, we found that the Nuttli method worked well for central Asian earthquakes and explosions using an attenuation model developed by Martynov et $al.$ based on the analysis of earthquake coda waves recorded at WMQ. It appears that coda waves from earthquakes can be used to calibrate the attenuation of L_g waves, even for the explosion sources whose paths lie partially outside the area sampled by earthquakes.

On the other hand, $m_b(L_g)$ calibration for the WUS appears to have failed miserably. As Fig. 11 shows, the coda Q_o measurements for explosions are systematically lower than the Q_o based on earthquake sources. This cannot be caused by a lateral heterogeneous Q distribution in the Basin and Range since the explosion paths sample many structures in common with the earthquake paths. Many of the stations plotted in Fig. 11 have Q_o measurements for earthquakes and explosions, and this fact precludes possible differences from other causes (e.g. site response). The variations are more likely caused by coda waves sampling different portions of the crust since the focal depths are very different for earthquakes and explosions. Such an effect was demonstrated very convincingly by Campillo et $al.$ (1985) for L_g waves using synthetic seismogram calculations and ray diagrams (see their Fig. 9) to illustrate the differences in sampling depths.

The effect of wave guides and source depth on coda wave spreading is an unsolved theoretical problem (Mayeda, pers. comm., 1996). Coda waves sample a volume of the earth surrounding the source and receiver, where, for explosions, the source and receivers are located near or on the earth's surface; for earthquakes, the source is located at depth in more competent media. It may be that depth sampling of coda waves is influenced by the depth of energy release for some crustal structures, as it is for L_g waves. In any case, the observations for the WUS suggest that coda waves generated by explosion sources sample more of the lower–Q, upper crust and earthquake codas sample more of the higher–Q, lower crust, at least for the near-regional distances represented in Fig. 11.

It is also interesting to note that Q_o observations in Fig. 11 tend to increase with distance. Two of the three stations with the smallest distances from NTS show much lower Q_o than stations at greater distance. The measurements for BKS suggest a similar trend for earthquakes, although DUG may violate the trend. An increase in apparent Q with distance might be expected for coda waves generated by shallow sources and composed mainly of surface waves attenuating rapidly at close range, while farther out, the codas are built up of body waves traveling deeper in the crust. Admittedly, lateral heterogeneities in Q structure could also be responsible for an apparent increase

of Q with distance.

Nuttli assumed that the Q_o determined from coda waves is applicable to L_g waves used for measuring $m_b(L_g)$. The equivalence of L_g Q and L_g coda Q has been supported by studies in several regions including the WUS (Mitchell, 1995). For comparison, Q_o measurements based on analysis of the L_g phase are also shown in Fig. 11. These results indicate that coda Q_o agree well with L_g Q_o for earthquakes in the Basin and Range, and both are significantly higher than the coda Q_o from explosions. The explosion coda Q_o is clearly not applicable to WUS earthquakes for the purpose of computing $m_b(L_g)$.

The question remains whether or not the low coda-wave Q_o applies to the propagation of L_g waves generated by explosions. Chavez and Priestley (1986) analyzed L_g waves from NTS explosions along a profile in northwest Nevada. The first station in their profile is about 200 km from NTS and the most distant is over 500 km away. Their Q model, derived from the decay of L_g waves along this profile, is $206f^{0.68}$, not significantly different from their results for earthquakes, $214f^{0.54}$. However, it is important to note that their model is not necessarily representative of the effective attenuation before the L_g waves reach the closest station. The propagation in the first 200 km distance from the source represents a significant fraction of the total path for many of the near–regional stations in Fig. 11. We suspect that propagation of shear waves out of the source region and into the L_g waveguide has a significant impact on amplitudes of near-regional L_g, and could lead to large differences in apparent Q for near-regional paths compared to long–range paths.

To our knowledge, there are no published L_g Q models based on the single–station method applied to NTS explosions, probably due to the fact that there is much uncertainty about the mechanisms responsible for L_g excitation. Present understanding of L_g excitation is best developed from NTS studies using detailed information about the emplacement conditions and earth structures. While not conclusive, these studies find that L_g waves with frequencies less than 1 or 2 Hz are generated by at least two principal mechanisms: (1) SV waves emanating directly from the source, and (2) near-source scattering of R_g waves into L_g by crustal heterogeneities (Gupta *et al.*, 1991; Gupta *et al.*, 1992; Patton and Taylor, 1995; Bennett *et al.* 1996).

SUMMARY

We have developed $M_o{:}m_b$ relationships for central Asian earthquakes and explosions using re-

gional seismograms recorded at the Chinese station, WMQ. Two magnitude scales, one for P_n waves and the other for L_g waves, were calibrated for the tectonic regions surrounding WMQ. We calibrated $m_b(P_n)$ against the teleseismic $m_b(P)$ reported by ISC, while $m_b(L_g)$ was calculated using the Nuttli (1973) method, where an absolute scale was set such that 110 microns of displacement at 10 km distance corresponds to an m_b 5.0. Phase amplitudes were measured in two ways for each scale, maximum A_{p-p} within a single cycle and A_{rms} for P_n, and A_{3rd} and A_{rms} for L_g. The different amplitude measures gave very similar results, and there were no significant differences in scatter.

We adhered to measurement windows following the procedures of Denny *et al.* (1987) for P_n and Nuttli (1973) for L_g. The use of appropriate measurement windows for P_n and L_g is an important consideration in calibrating m_b scales to new regions. Because of the complexity of regional seismograms, it is difficult to design windows for distances ranging 200 – 2000 km. For example, the decay of L_g A_{rms} had to be compensated for the increasing separation of L_g arrivals as the epicentral distance increases. Nuttli chose the velocity window, 3.6 – 3.2 km/s, to capture source–generated arrivals of L_g as much as possible, avoiding later–arriving, scattered waves.

The $M_o : m_b(P_n)$ relationships for central Asia agreed well with the relationships for earthquakes and explosions in the WUS, demonstrating the transportability of this LP:SP discriminant to other tectonic regions. The comparisons between explosions detonated in granite at KTS and explosions detonated in tuffs and alluviums at NTS are excellent and support the claim that $M_o : m_b$ relations for explosions are insensitive to the emplacement medium (PW). Another important point is that regional m_b scales tied to the teleseismic m_b will have to be investigated for possible effects of regional biases, as pointed out by Douglas and Marshall (1996). This was demonstrated very clearly for the $m_b(P_n)$ values of NTS explosions, which had to be corrected for the magnitude bias known to exist between the Shagan River test site and NTS.

$M_o : m_b(L_g)$ relationships for central Asia and WUS are in excellent agreement with those based on P_n waves. Very important is the fact that the $m_b(L_g)$ relations did not require correction for regional bias, supporting claims that magnitudes based on Nuttli's formula are indeed transportable. It is also important to note that P_n and L_g relationships for KTS and NTS explosions show closer agreement than earthquake relations for central Asia and WUS do. The reason for this is still under invetigation.

We found that $m_b(L_g)$ values for earthquakes located close to NTS are greatly over–estimated

using coda Q's determined from analysis of nuclear explosions. Coda Q measurements compiled from the literature show significantly lower values for NTS explosions compared to Q estimated from earthquake studies. Observations of L_g wave attenuation on inter–station paths are consistent with coda Q estimates based on earthquake data. The results of this study suggest that L_g attenuation on near–regional paths through the Basin and Range is greater for explosions than it is for nearby earthquakes, possibly due to differences in focal depth.

To conclude, we summarize (a) some issues arising from this work, (b) implications for CTB monitoring, and (c) topics requiring further study.

(1) $m_b(P_n)$ *calibration*: because the scale is calibrated against a teleseismic m_b, monitoring regions will have to be surveyed for m_b bias variations; Nuttli's $m_b(L_g)$ could provide a convenient method for doing this;

(2) $m_b(L_g)$ *calibration*: the use of chemical explosions has been proposed as a means to calibrate new regions; since source depth may be a factor controlling the decay of L_g amplitudes, future calibration experiments should collect data to study these effects more thoroughly; furthermore, modeling studies of regional phase and coda-wave propagation through complex media are needed to establish a physical basis;

(3) $M_o : m_b$ *discriminant*: a single relationship for nuclear explosions in any geologic environment simplifies identification under a CTB; while it is not ready for operational use, the discriminant is available for the study of special events failing conventional identification criteria;

(4) *Discrimination capabilities*: regional magnitude bias could be a factor affecting the performance of some regional discriminants; e.g., in the case where phase amplitudes are corrected for magnitude-dependent source effects or in the case of identification thresholds based on comparisons between earthquake and explosions located in disparate regions; further study of this topic is necessary.

Important sources of uncertainty in the results of this study arise from errors in earthquake locations and from inadequate regionalization of the attenuation rates of regional phases, which could have caused scatter in earthquake $M_o : m_b$ observations and possibly over-estimation of $m_b(P_n)$ for KTS explosions up to about 0.15 mu. We have noted there may be a source of systematic error in the M_o estimates used in this study. For central Asian earthquakes, the CMT M_o estimates are systematically larger than moments based on regional LP surface-wave amplitudes. This result is based on some

172

preliminary studies still in progress and will be reported on in a future paper. Also in the future, $M_o : m_b$ relationships must be established for other stations in central Asia to strengthen the empirical evidence for a single $M_o : m_b$ relationship for all nuclear explosions. The regionalization information needed to improve event location capability and reduce the scatter of discriminant observations is presently being collected by national laboratories and universities for key monitoring regions, including central Asia.

ACKNOWLEDGMENTS

REFERENCES

Bennett, T.J., K.L. McLaughlin, and M.E. Marshall (1996). The physical basis for the L_g/P discriminant, *Proceedings of the 18th Annual Seismic Research Symposium on Monitoring a Comprehensive Test Ban Treaty*, PL–TR–96–2153, 484 – 493.   ADA313692

Bolt, B.A., and M. Herraiz (1983). Simplified estimation of seismic moment from seismograms, *Bull. Seism. Soc. Am.*, **73**, 735 – 748.

Campillo, M., J. Plantet, and M. Bouchon (1985). Frequency – dependent attenuation in the crust beneath central France from L_g waves: data analysis and numerical modeling, *Bull. Seismo. Soc. Am.*, **75**, 1395 – 1411.

Chavez, D.E., and K.F. Priestley (1986). Measurement of frequency dependent L_g attenuation in the Great Basin, *Geophys. Res. Lett.*, **13**, 551 – 554.

Chung, D.H., and D. L. Bernreuter (1981). Regional relationships among earthquake magnitude scales, *Rev. Geophys. Space Phys.*, **19**, 649 – 663.

Denny, M.D, S.R. Taylor, and E.S. Vergino (1987). Investigation of m_b and M_s formulas for the western United States and their impact on the M_s/m_b discriminant, *Bull. Seism. Soc. Am.*, **77**, 987 – 995.

Der, Z., T. McElfresh, R. Wagner, and J. Burnetti (1985). Spectral characteristics of P waves from nuclear explosions and yield estimation, *Bull. Seism. Soc. Am.*, **75**, 379 – 390.

Douglas, A. and P. Marshall (1996). Seismic source size and yield for nuclear explosions, in *NATO Proceedings on Monitoring a Comprehensive Test Ban Treaty*, E.S. Husebye and A.M. Dainty, Editors, Kluwer Academic Publishers, 309 – 353.

Douglas, A., J.A. Hudson, and V.K. Kembhavi (1971). The relative excitation of seismic surface and body waves by point sources, *Geophys. J. R. astr. Soc.*, **23**, 451–460.

Douglas, A., P. Marshall, and K. Jones (1993). Body-wave magnitudes and locations of explosions at the Chinese test site, 1967 – 1989, *AWE Report No. O 12/93*, 19pp.

Evernden, J.F., W.J. Best, P.W. Pomeroy, T.V. McEvilly, J.M. Savino, and L.R. Sykes (1971).

Discrimination between small – magnitude earthquakes and explosions, *J. Geophys. Res.*, **76**, 8042 – 8055.

Ekstrom, G., and P.G. Richards (1994). Empirical measurements of tectonic moment release in nuclear explosions from teleseismic surface waves and body waves, *Geophys. J. Int.*, **117**, 120 – 140.

Giardini, D., E. Boschi, and B. Palombo (1993). Moment tensor inversion from MEDNET data to regional earthquakes of the Mediterranean, *Geophys. Res. Lett.*, **20**, 273 – 276.

Given, H., N. Tarasov, V. Zhuravlev, F. Vernon, J. Berger, and I. Nersesov (1990). High-frequency seismic observations in eastern Kazakhstan, USSR, with emphasis on chemical explosion experiments, *J. Geophys. Res.*, **95**, 295 – 307.

Gupta, I.N., T.W. McElfresh, and R.A. Wagner (1991). Near–source scattering of Rayleigh to P in teleseismic arrivals from Pahute Mesa NTS shots, in *Explosion Source Phenomenology*, American Geophysical Monograph 65, 151 – 159.

Gupta, I.N., W.W. Chan, and R.A. Wagner (1992). A comparison of regional underground nuclear explosions at east Kazakh and Nevada test sites, *Bull. Seism. Soc. Am.*, **82**, 352 – 382.

Gupta, I.N., and T.-R. Zhang (1996). Study of low frequency L_g from explosions at Nevada, Kazakh, Lop Nor, and Azgir test sites, *Proceedings of the 18$^{\text{th}}$ Annual Seismic Research Symposium on Monitoring a Comprehensive Test Ban Treaty*, PL–TR–96–2153, 328 – 337. ADA313692

Hansen, R.A, F. Ringdal, and P.G. Richards (1990). The stability of RMS L_g measurements and their potential for accurate estimation of the yields of Soviet underground nuclear explosions, *Bull. Seism. Soc. Am.*, **80**, 2106 – 2126.

Herrmann, R.B. (1979). Surface wave focal mechanisms for eastern North American earthquakes with tectonic implications, *J. Geophys. Res.*, **84**, 3543 – 3552.

Herrmann, R.B. (1980). Q estimates using the coda of local earthquakes, *Bull. Seism. Soc. Am.*, **70**, 447 – 468.

Hudson, J.A., and A. Douglas (1975). On the amplitudes of seismic waves, *Geophys. J. R. astr. Soc.*, **42**, 1039–1044.

Israelsson, H. (1992). Analysis of historic seismograms – RMS L_g magnitudes, yields, and depths of explosions at Semipalatinsk test range, *Phillips Laboratory Report No.* PL-TR-92-2117(I), 39pp. ADA256692

Jih, R.-S., and R.R. Baumstark (1994). Maximum–likelihood network magnitude estimates of low-yield underground explosions, *TBE-4617-3 / TGAL-94-02*, Teledyne–Brown Engineering, Arlington, VA.

Keilis – Borok, V.I. (1960). Investigation of the mechanism of earthquakes (English Translation), *Soc. Res. Geophys.*, **4**, 29.

Langston, C.A. (1995). Anatomy of regional phases and source characterization of the Soviet Joint Verification Experiment, underground nuclear explosion, *Bull. Seism. Soc. Am.*, **85**, 1416 – 1431.

Lilwall, R.C., and J. Farthing (1990). Joint epicentre determination of Soviet underground nuclear explosions 1973–89 at the Semipalatinsk test site, *AWE Report No. O 12/90*, 13pp.

Mayeda, K. (1993). $m_b(L_g Coda)$: A stable single station estimator of magnitude, *Bull. Seism. Soc. Am.*, **83**, 851 – 861.

Mayeda, K., and W.R. Walter (1996). Moment, energy, stress drop, and source spectra of western United States earthquakes from regional coda envelopes, *J. Geophys. Res.*, **101**, 11,195 – 11,208.

Mitchell, B.J. (1995). Anelastic structure and evolution of the continental crust and upper mantle from seismic surface wave attenuation, *Rev. Geophys.*, **33**, 441 – 462.

Mitchell, B.J., J.K. Xie, Y. Pan, and J. Ni (1993). L_g Q, L_g Coda Q, and yield estimation in Eurasia, *Proceedings of the 15th Annual Seismic Research Symposium*, 277 – 283. PL–TR–93–2160, ADA271458

Murphy, J.R., J.L. Stevens, D.C. O'Neill, B.W. Barker, K.L. Mclaughlin, and M.E. Marshall (1991). Development of a comprehensive seismic yield estimation system for underground nuclear explosions, *Phillips Laboratory Report No.* PL-TR-91-2161, 39pp. ADA240814

Nuttli, O.W. (1973). Seismic wave attenuation and magnitude relations for Eastern North America, *J. Geophys. Res.*, **78**, 876 – 885.

Nuttli, O.W. (1986). L_g magnitudes of selected east Kazakhstan underground explosions, *Bull. Seism. Soc. Am.*, **76**, 1241 – 1251.

Nuttli, O.W. (1987). L_g magnitudes of Degelen, east Kazakhstan, underground explosions, *Bull. Seism. Soc. Am.*, **77**, 679 – 681.

Patton, H.J. (1988). Application of Nuttli's method to estimate yield of Nevada Test Site explosions recorded on Lawrence Livermore National Laboratory's digital seismic system, *Bull. Seism. Soc. Am.*, **78**, 1759 – 1772.

Patton, H.J., and G. Zandt (1991). Seismic moment tensors of western U. S. earthquakes and implications for the tectonic stress field, *J. Geophys. Res.*, **96**, 18,245 – 18,259.

Patton, H.J., and W.R. Walter (1993). Regional moment : magnitude relations for earthquakes and explosions, *Geophys. Res. Lett.*, **20**, 277 – 280.

Patton, H.J., and W.R. Walter (1994). Correction to: 'Regional moment : magnitude relations for earthquakes and explosions', *Geophys. Res. Lett.*, **21**, 743.

Patton, H.J., and S.R. Taylor (1995). Analysis of L_g spectral ratios from NTS explosions: Implications for the source mechanisms of spall and the generation of L_g waves *Bull. Seism. Soc. Am.*, **85**, 220 – 236.

Randall, G.E., H.E. Hartse, W.S. Phillips, and S.R. Taylor (1996). Regional characterization of western China – II, *Proceedings of the 18th Annual Seismic Research Symposium on Monitoring a Comprehensive Test Ban Treaty*, PL–TR–96–2153, 80 – 87. ADA313692

Rautian, T.G., and V.I. Khalturin (1978). The use of coda for determination of the earthquake source spectrum, *Bull. Seism. Soc. Am.*, **68**, 923 – 948.

Ringdal, F., P.D. Marshall, and R.W. Alewine (1992). Seismic yield determination of Soviet underground nuclear explosions at the Shagan River test site, *Geophys. J. Int.*, **109**, 65 – 77.

Ritsema, J., and T. Lay (1995). Long–period regional wave moment tensor inversion for earthquakes in the western United States, *J. Geophys. Res.*, **100**, 9853 – 9864.

Romanowicz, B., D. Dreger, M. Pasyanos, and R. Uhrhammer (1993). Monitoring of strain release

in central and northern California using broadband data, *Geophys. Res. Lett.*, **20**, 1643 – 1646.

Sereno, T.J. (1990). Frequency-dependent attenuation in eastern Kazakhstan and implications for seismic detection thresholds in the Soviet Union, *Bull. Seism. Soc. Am.*, **80**, 2089 – 2105.

Singh, S., and R.B. Herrmann (1983). Regionalization of crustal coda Q in the continental United States, *J. Geophys. Res.*, **88**, 527 – 538.

Stevens, J.L., and S.M. Day (1985). The physical basis of m_b : M_s and variable frequency magnitude methods for earthquakes / explosion discrimination, *J. Geophys. Res.*, **90**, 3009 – 3030.

Stevens, J.L., and K.L. McLaughlin (1988). Analysis of surface waves from the Novaya Zemlya, Mururoa, and Amchitka test sites, and maximum likelihood estimation of scalar moments from earthquakes and explosions, *S-Cubed Report No.* SSS–TR–89–9953.

Vergino, E.S., and R.W. Mensing (1990). Yield estimation using regional $m_b(P_n)$, *Bull. Seism. Soc. Am.*, **80**, 656 – 674.

Walter, W.R., and H.J. Patton (1990). Tectonic release from the Soviet Joint Verification Experiment, *Geophys. Res. Lett.*, **17**, 1517 – 1520.

Woods, B.B., S. Kedar, and D.V. Helmberger (1993). M_L : M_o as a regional seismic discriminant, *Bull. Seism. Soc. Am.*, **83**, 1167 – 1183.

Xie, J., and B.J. Mitchell (1990). Attenuation of multiphase surface waves in the Basin and Range province, part I: L_g and L_g coda, *Geophys. J. Int.*, **102**, 121 – 137.

Xie, J., L. Cong, and B.J. Mitchell (1996). Spectral characteristics of the excitation and propagation of L_g from underground nuclear explosions in central Asia, *J. Geophys. Res.*, **101**, 5813 – 5822.

Zhao, L.S., and D.V. Helmberger (1994). Source estimation from broadband regional seismograms, *Bull. Seism. Soc. Am.*, **84**, 91 – 104.

FIGURE CAPTIONS

Figure 1. Location of seismograph station WMQ (solid triangle), earthquakes (open dots, CMT events; solid dots, all other earthquakes) and explosions (open stars) used in this study. The star south of station WMQ is the single Chinese explosion analyzed. Political boundaries are shown by heavy solid lines; tectonic boundaries are thin dashed lines. Elevations are shown as shades of gray in three intervals: -100 to 1000 m above sea level, no shading; 1000 to 3000 m, light gray; and above 3000 m, darker gray. Large bodies of water are shown by darkest gray areas.

Figure 2. Examples of the measurements made on seismograms of a regional earthquake (87005) recorded at the station WMQ. (a) The broadband response for WMQ was deconvolved from the data and the resulting displacement seismogram was convolved with a WWSS SP response. The inset shows an enlargement of the P–wave portion of the seismogram. The A_{p-p} for determining $m_b(P_n)$ is indicated by the horizontal bars; A_{rms} measurement was made over the P-wave window starting at the P_n onset to the arrival of P_g. For the $m_b(L_g)$, two vertical arrows denote the L_g group velocity time window over which the A_{3rd} and A_{rms} measurements are made. (b) Simulated Wood-Anderson seismograms were used to determine M_o. The duration is defined to be the time interval between the L_g arrival time and the time at which the amplitude drops to one third of the peak amplitude. These times are denoted by the two vertical arrows. The peak amplitude is indicated by C on each trace.

Figure 3. (a) Regression of P_n A_{p-p} corrected by ISC $m_b(P)$ vs. log distance. The earthquake data are denoted by the open circles and the explosion data by the asterisks. The line was obtained by linear least squares fit through the earthquake data. A_{p-p} is in units of meters; (b) A plot of $m_b(P_n)$ vs. ISC $m_b(P)$ for earthquakes and explosions. The solid line is unity.

Figure 4. Comparison of $m_b(L_g)$ measured at WMQ with $m_b(L_g)$ measured at arrays in Norway and Germany. The lines have unit slope and have been fit to the observations based on A_{3rd} at WMQ (open circles, solid line) and A_{rms} (circles with pluses, dashed line).

Figure 5. Plot of log scalar moment vs. $\log(C \cdot D \cdot \Delta)$. The regression line (solid line) is for the

179

earthquake data (open circles), where CMT M_o values from Table 1 are plotted. The dashed line for the explosion data (asterisks) has the same slope as the earthquakes, and the intercept is set so that the line passes through the moment of the JVE explosion, indicated by the star. The explosion M_o's are those of Ekstrom and Richards (1994) before re-scaling (see text). The amplitude, C, is measured in microns, the duration, D, in s, and the distance in km.

Figure 6. (a) Plot of log $M_o(L_g)$ from this study *vs.* log M_o from other studies cited in Table 1. Circle symbols are for earthquakes; open ones are earthquakes with CMT M_o, used for the calibration of BH method; circles with pluses are from Stevens and McLaughlin (1988); and the solid circle is from Xie *et al.* (1996). Explosions from Ekstrom and Richards are shown by asterisks; diamonds are from Stevens and McLaughlin; crosses are from Xie *et al.*,; and the solid star is from Wallace (pers. comm., 1996). (b) A plot of log $M_o(L_g)$ *vs.* ISC M_S for earthquakes. The least squares fit line is log $M_o = 0.98\ M_S + 12.07$.

Figure 7. (a) M_o:$m_b(P_n)$ from the A_{p-p} measurements. Open circles are central Asian earthquakes; asterisks are KTS explosions, and the star is the Lop Nor explosion. Solid circles indicate recent measurements for earthquakes that have occurred in the WUS since 1992, including 23Apr92 Joshua Tree, CA: $m_b(P_n)$ 6.29; 28Jun92 Landers, CA: 6.54; 29Jun92 Little Skull Mtn., NV: 5.53; 05Jul92 Little Skull Mtn., NV: 4.38; 02Sep92 St. George, UT: 5.81; 10Feb93 Pyramid Lake, NV: 4.41; 25Apr and 29Apr93 Cataract Creek, AZ: 5.07 and 5.68, respectively; 17May93 Eureka Valley, CA: 5.84; and 17Jan94 Northridge, CA: 6.14 (Walter, pers. comm., 1996). In addition, there are the 05Aug71 Massachusetts Mtn. earthquake on NTS: 3.98, and several other events located close to NTS. The triangles are aftershocks of the Little Skull Mtn. earthquake, where the M_o's were determined from the BH method. Solid lines are regression fits to central Asian data, and the dashed lines are the regression results reported by PW for the WUS, (b) M_o:$m_b(P_n)$ from the A_{rms} measurements.

Figure 8. (a) M_o:$m_b(L_g)$ from the A_{3rd} measurement of L_g. Open circles are central Asian earthquakes, and asterisks are KTS explosions. The solid star is Lop Nor. Solid circles are observations for the Little Skull Mtn. earthquake sequence, located on the southern boundary of NTS. The triangles are for other earthquakes located within 100 km of NTS. Regression lines are shown

as solid lines for central Asian earthquakes and explosions, and as dashed lines for central US earthquakes (Herrmann, 1979) and NTS explosions. (b) M_o:m_b(L_g) results based on the adjusted A_{rms} of L_g.

Figure 9. Revised M_o : m_b relationships for P_n and L_g. (a) For P_n, the NTS regression line has been shifted to the right 0.35 mu to account for the bias between NTS and KTS. All WUS earthquakes, including events from PW, are plotted as solid circles, and they have also been corrected for a 0.35 mu bias since many of them are located close to NTS. A regression line (dashed) has been fitted through all of the WUS earthquakes. (Note: a few events plotted off the top of the graph; see Fig. 7a.) (b) Same results plotted in Fig. 8a, except m_b(L_g) for earthquakes located near NTS were recomputed using higher Q_o values, as discussed in the text. The data points are shown as solid circles, and a regression line (dashed) was fit to these data.

Figure 10. (a) ISC m_b(P) *vs.* WMQ m_b(L_g) for explosions in this study. The symbols designate different test areas: solid circles, SW Shagan; circles with pluses, TZ Shagan; open circles, NE Shagan; up-side-down triangles, the Degelen test area; and the star, Lop Nor. The Shagan test areas were defined by Ringdal *et al.*. The line in this plot and in all of the others is $m_b = m_b(L_g)$. (b) Maximum likelihood estimates (MLE) of m_b(P) *vs.* WMQ m_b(L_g) for explosions in this study. (c) Peak–to–peak m_b(P_n) *vs.* m_b(L_g) for KTS explosions.

Figure 11. Summary of L_g coda Q_o measurements based on the "fp *vs.* tp" method of Herrmann (1980). The solid dots are 'point' measurements for NTS explosions, where all path lengths are approximately the same. The earthquake measurements are shown as lines, where the line spans the epicentral distances of events used to determine Q_o. The shaded region represents the range of Q_o and distance for studies of L_g wave attenuation. It is important to note that the Q measurements of L_g waves are based on inter–station analysis, and reflects loss of amplitude between receivers. The coda measurements, on the other hand, reflect losses in a larger volume of the crust, including in the source regions of earthquakes and explosions.

TABLE 1 – EVENTS IN THIS STUDY

(a) Earthquakes

Event No.	Year Jday	Da/Mo	Origin UTC	Lat °N	Lon °E	Depth km	m_b	M_S	Log M_o, N-m CMT°	Other
01	87005	05/Jan	22:52:46	41.95	81.32	15	5.8	5.8	17.616	17.028[†]
02	87024a	24/Jan	08:09:21	41.48	79.33	29	5.8	6.1	18.292	17.605[†]
03	87024b	24/Jan	08:59:35	41.31	79.37	33	4.3			
04	87025a	25/Jan	06:10:57	41.35	79.33	39	4.5			
05	87025b	25/Jan	22:49:14	41.36	79.38	45	4.5			
06	87026	26/Jan	05:28:41	41.32	79.17	33	4.4			
07	87028	28/Jan	00:01:41	41.42	79.28	33	4.6			
08	87045	14/Feb	23:03:15	41.39	79.59	43	4.4	4.0		
09	87054	23/Feb	22:31:07	41.34	79.41	49	4.6			
10	87062	03/Mar	09:41:31	41.34	79.29	10	5.1	5.0	16.617	
11	87094	04/Apr	17:45:14	42.53	80.09	33	4.0	4.1		14.828[†]
12	87130	10/May	20:19:33	44.25	79.68	33	4.5	4.0		15.439[†]
13	87217	05/Aug	10:24:18	41.32	82.09	14	4.8	4.5		
14	87261	18/Sep	21:58:40	47.11	89.53	25	5.4	5.3	17.107	16.649[†]
15	87263	20/Sep	03:54:07	42.83	77.66	51	4.6	4.2		15.377[†]
16	87289	16/Oct	18:30:49	44.10	82.70	39	4.8			14.872[†]
17	87351	17/Dec	12:17:23	41.83	83.13	33	5.1	4.6		
18	87356	22/Dec	00:16:39	41.32	89.62	21	5.8	5.3	17.330	
19	88039	08/Feb	17:49:20	43.79	83.81	10	4.4			
20	88061	01/Mar	15:45:39	40.24	77.70	59	4.3			
21	88075	15/Mar	15:55:23	42.23	75.51	19	4.4			15.342[‡]
22	88085	25/Mar	02:07:56	44.67	79.49	33	4.5			
23	88092	01/Apr	01:27:16	47.49	89.45	10	4.5	3.8		
24	88123	02/May	02:13:26	40.05	82.27	17	4.9	4.4		
25	88146a	25/May	00:05:23	40.46	77.81	31	4.7	4.1		
26	88146b	25/May	18:21:55	41.99	85.68	5	5.2	4.7		
27	88169	17/Jun	13:30:43	42.92	77.49	18	5.2	5.4	17.571	
28	88182	30/Jun	15:25:13	50.27	91.16	15	5.0	4.8		
29	88205	23/Jul	07:38:10	48.70	90.56	19	5.4	6.0	17.954	
30	88271	27/Sep	16:11:36	46.82	73.7	33	4.5			
31	88350	15/Dec	06:40:49	46.53	95.59	1	5.2	4.7	16.844	
32	88356	21/Dec	08:21:05	41.15	72.30	51	5.4	4.7		
33	89005	05/Jan	17:42:22	42.03	90.51	10	4.2			
34	89043	12/Feb	23:49:14	50.98	84.16	12	4.6			
35	89046	15/Feb	01:23:30	42.54	84.55	11	4.3			
36	89073	14/Mar	08:42:02	39.77	77.60	33	4.5			
37	89082	23/Mar	12:38:50	40.81	78.12	28	4.4			
38	89128	08/May	00:03:14	44.90	79.73	33	4.5	4.1		
39	89297a	24/Oct	13:33:28	41.76	82.26	11	4.6			

40	89297b	24/Oct	13:38:27	41.68	82.31	16	4.7		
41	89335	01/Dec	17:32:43	40.70	79.2	10	4.3		
42	90165	14/Jun	12:47:28	47.85	85.06	54	6.1	6.9	18.987
43	90215	03/Aug	09:15:04	47.97	84.97	16	6.0	6.2	18.297
44	90297	24/Oct	23:38:15	44.11	83.88	20	5.2	4.9	16.839
45	90316	12/Nov	12:28:50	42.94	78.07	9	5.8	6.3	18.517
46	90335	01/Dec	18:09:29	40.89	73.59	30	5.0	4.9	16.918
47	91056	25/Feb	14:30:28	40.36	78.98	21	5.5	6.1	18.121
48	91231	19/Aug	06:05:51	47.00	85.31	25	5.5	5.1	16.954
49	92359	24/Dec	05:09:47	42.15	72.24	36	5.2	5.1	17.114
50	93364	30/Dec	14:24:02	44.74	78.80	1	5.7	5.3	17.272
51	94129	09/May	09:14:12	40.26	78.94	46	4.8	4.7	16.592
52	94235	23/Aug	14:18:31	40.04	78.82	33	5.0	5.0	16.962

(b) Explosions

Event No.	Year Jday	Da/Mo	Origin UTC	Lat °N	Lon °E	Test Area[+]	m_b ISC	m_b MLE[@]	M_s ISC	Log M_I, N-m CMT[*]	Other
53	87071	12/Mar	01:57:19.6	49.929	78.824	SW	5.6	5.31[1]	3.9	15.826	15.460[†]
54	87093	03/Apr	01:17:10.3	49.910	78.786	SW	6.2	6.12[1]	4.8	16.551	16.169[†]
55	87126	06/May	04:02:08.1	49.777	77.984	DG	5.6	5.49[3]			14.920[†]
56	87157	06/Jun	02:37:09.2	49.837	78.065	DG	5.4	5.16[3]			14.629[†]
57	87171	20/Jun	00:53:07.1	49.927	78.740	SW	6.1	6.03[1]	4.5	16.111	15.638[†]
58	87198	17/Jul	01:17:09.2	49.769	78.035	DG	5.8	5.76[3]	4.8		15.583[†]
59	87214	02/Aug	00:58:09.2	49.877	78.873	SW	5.9	5.83[1]	4.3	16.111	15.436[†]
60	87347	13/Dec	03:21:07.2	49.957	78.792	SW	6.1	6.06[1]	4.7	16.377	15.901[†]
61	87354	20/Dec	02:55:09.1	49.774	77.975	DG	4.8		3.8		
62	87361	27/Dec	03:05:07.2	49.867	78.718	SW	6.1	6.00[1]	4.5	16.223	16.114[‡]
63	88044	13/Feb	03:05:08.2	49.932	78.878	TZ	6.1	5.97[1]	4.6	16.312	16.230[‡]
64	88094	03/Apr	01:33:08.1	49.909	78.918	TZ	6.0	5.99[1]	4.8	16.369	16.230[‡]
65	88113	22/Apr	09:30:09.4	49.824	78.102	DG	4.9				
66	88125	04/May	00:57:09.1	49.931	78.741	SW	6.1	6.09[1]	4.9	16.412	16.279[‡]
67	88166	14/Jun	02:27:09.0	50.034	78.964	NE	5.1	4.80[1]	4.1	15.114	14.845[‡]
68	88258	14/Sep	03:59:59.7	49.869	78.825	SW	6.1	6.03[1]	4.8	16.380	16.114[‡]
69	88273	29/Sep	07:00:02	41.52	88.15	LN	4.6	4.26[2]			14.415[*]
70	88292	18/Oct	03:40:09.2	49.802	78.002	DG	4.9				
71	88317	12/Nov	03:30:06.3	50.048	78.960	NE	5.4	5.24[1]	4.3	15.531	15.415[‡]
72	88328	23/Nov	03:57:09.0	49.765	78.029	DG	5.4	5.09[3]			15.255[‡]
73	88352	17/Dec	04:18:09.2	49.879	78.924	TZ	5.9	5.83[1]	4.7	16.423	16.114[‡]
74	89043	12/Feb	04:15:09.2	49.911	78.704	SW	5.8	5.86[1]	4.8	16.250	15.978[‡]
75	89048	17/Feb	04:01:09.2	49.849	78.064	DG	5.1	4.77[3]			
76	89189	08/Jul	03:47:00.0	49.869	78.775	SW	5.6	5.55[1]	4.3	15.954	15.544[‡]
77	89245	02/Sep	04:16:59.8	50.019	78.988	NE	5.1	4.94[1]	3.9	15.568	14.914[‡]
78	89277	04/Oct	11:30:00.2	49.751	78.005	DG	4.7		3.3		
79	89292	19/Oct	09:49:59.8	49.927	78.927	TZ	5.9	5.86[1]	4.8	16.328	16.000[‡]

Origin times, locations, and magnitudes of earthquakes from ISC Bulletin

Origin times and locations of East Kazakh explosions from Lilwall and Farthing (1990)

Origin time and location of the Lop Nor explosion from the ISC Bulletin

[@]Maximum likelihood magnitudes, [1] Ringdal et al. (1992); [2] Douglas et al. (1993);
[3] Jih and Baumstark (1994) - Note: The mle m_b of Jih and Baumstark plotted in Fig. 13b are reduced by 0.08 mu. This was necessary because a constant offset exists between their estimates of mle m_b and the AWE (Atomic Weapons Establishment) estimates, as determined from a regression analysis we performed on a data set of 50 Degelen Mountain explosions in common.

[+]SW - Southwest Shagan River test site; NE - Northeast Shagan River test site;
TZ - Transition zone Shagan River test site; DG - Degelen Mountain test site
LN - Lop Nor

Sources of M_o or M_I

◊ Harvard CMT solutions

∗ Ekstrom and Richards (1994)

‡ Xie *et al.* (1996)

⋆ Wallace, T. (pers. comm., 1996)

† Stevens and McLaughlin (1988) - Note: The seismic moments of Stevens and
McLaughlin were re-scaled in order to be consistent with our JVE moment estimate.
This was necessary because of the method used by the authors to estimate moment (see
their report for details). Based on six explosions in common with the Ekstrom and
Richards data set, an estimate of the correction factor is +0.24 log moment units.
This factor was applied to earthquakes and explosions moments alike for events no.
11, 12, 15, 16, 55, 56, and 58 plotted in Figs. 9 - 12.

TABLE 2 – MAGNITUDE AND SEISMIC MOMENT MEASUREMENTS

(a) Earthquakes

Event No.	Year Jday	Distance km	$m_b(P_n)$ p–p[†]	$m_b(P_n)$ rms	$m_b(L_g)$ 3rd[‡]	$m_b(L_g)$ rms	Log $M_o(L_g)$ N-m
01	87005	560.6	5.773	5.761	6.015	5.789	17.602
02	87024a	733.2	6.078	6.051	6.468	6.328	17.922
03	87024b	737.9	4.179	4.298	4.458	4.355	15.844
04	87025a	739.1	4.263	4.213	4.260	3.954	15.437
05	87025b	734.8	4.152	4.097	4.055	3.784	15.388
06	87026	752.7	4.106	4.170	4.206	3.946	15.442
07	87028	739.7	4.327	4.126	4.074	3.727	15.457
08	87045	717.5	4.359	4.353	4.431	4.050	15.727
09	87054	733.5	4.460	4.482	4.571	4.207	15.786
10	87062	742.6	4.796	4.752	5.152	4.996	16.532
11	87094	634.6	4.416	4.364	4.054	3.810	15.539
12	87130	644.0	4.114	4.135	4.221	4.017	16.095
13	87217	537.4	4.986	4.869	5.203	5.021	16.836
14	87261	392.7	5.372	5.454	5.250	4.993	17.549
15	87263	820.9	4.724	4.674	4.733	4.397	16.131
16	87289	402.1	4.377	4.345	4.394	4.158	16.071
17	87351	433.8	4.281	4.350	4.815	4.549	16.207
18	87356	319.6	5.710	5.808	6.272	5.832	17.638
19	88039	312.6	4.660	4.570	4.276	4.046	15.844
20	88061	917.5	4.193	4.310	4.098	3.722	15.575
21	88075	1007.9	4.305	4.347	4.467	4.121	15.816
22	88085	661.9	4.642	4.662	4.830	4.425	16.076
23	88092	430.1	4.432	4.379	4.644	4.356	16.346
24	88123	614.5	5.178	5.114	5.222	4.902	16.706
25	88146a	897.7	5.102	5.038	4.754	4.356	15.944
26	88146b	261.6	5.287	5.407	5.505	5.234	16.950
27	88169	832.7	5.614	5.573	5.851	5.544	17.466
28	88182	763.6	4.704	4.666	5.259	5.028	16.606
29	88205	585.5	6.119	6.041	6.427	6.150	18.016
30	88271	1145.1	4.569	4.419	4.495	4.201	15.747
31	88350	689.4	4.659	4.816	5.540	5.242	16.926
32	88356	1298.1	4.921	4.980	5.383	5.151	16.459
33	89005	304.0	4.414	4.441	4.308	4.071	16.132
34	89043	839.2	4.708	4.706	5.021	4.674	16.390
35	89046	292.6	4.688	4.610	4.378	4.219	16.084
36	89073	951.2	4.480	4.483	4.104	3.906	15.669
37	89082	856.7	4.663	4.538	4.274	4.029	15.665
38	89128	646.0	4.749	4.693	4.422	4.278	15.966
39	89297a	500.1	4.320	4.222	4.466	4.218	15.793
40	89297b	500.8	4.383	4.320	4.354	4.164	15.740

41	89335	781.5	4.334	4.353	4.134	3.800	15.924
42	90165	492.3	6.405	6.384	6.393	6.111	18.734
43	90215	507.3	6.295	6.191	6.312	5.963	18.486
44	90297	307.8	4.849	4.867	5.539	5.276	17.306
45	90316	785.7	6.142	6.217	6.202	6.037	18.156
46	90335	1205.2	4.880	4.909	5.698	5.269	16.762
47	91056	816.6	6.167	6.183	6.466	5.986	17.881
48	91231	399.6	5.488	5.338	5.246	5.025	17.428
49	92359	1272.3	5.280	5.235	5.602	5.373	17.022
50	93364	717.0	5.508	5.514	5.658	5.316	17.405
51	94129	825.2	5.007	5.028	4.711	4.498	16.531
52	94235	846.8	5.069	5.068	4.781	4.537	16.564

(b) Explosions

Event No.	Year Jday	Distance km	$m_b(P_n)$ p–p[†]	rms	$m_b(L_g)$ 3rd[‡]	rms	Log $M_o(L_g)$ N-m
53	87071	957.1	5.378	5.430	5.327	5.002	
54	87093	957.7	6.269	6.324	6.132	5.769	
55	87126	992.5	5.478	5.502	5.457	5.086	
56	87157	992.1	5.303	5.245	5.165	4.845	15.306
57	87171	961.4	6.199	6.232	6.085	5.766	16.114
58	87198	989.1	5.841	5.800	5.766	5.540	15.855
59	87214	950.6	5.935	5.980	5.830	5.499	15.978
60	87347	960.9	6.249	6.242	6.051	5.737	16.205
61	87354	992.8	4.636	4.628	4.483	4.186	
62	87361	958.2	6.101	6.110	5.881	5.676	16.127
63	88044	954.4	6.191	6.144	5.967	5.709	16.177
64	88094	950.6	6.094	6.203	5.980	5.607	16.182
65	88113	989.1	4.578	4.645	4.600	4.285	
66	88125	961.7	6.329	6.316	6.134	5.832	16.169
67	88166	957.5	5.360	5.231	4.772	4.511	14.865
68	88258	952.6	6.077	6.121	5.952	5.640	16.129
69	88273	258.3	4.55[*]		4.487	4.243	
70	88292	993.2	4.673	4.629	4.355	4.150	14.507
71	88317	958.8	5.718	5.564	5.156	4.870	15.320
72	88328	989.2	5.235	5.150	5.341	4.980	15.193
73	88352	948.0	6.017	6.074	5.758	5.432	15.849
74	89043	962.2	5.912	5.893	5.703	5.387	15.917
75	89048	993.0	4.852	4.905	4.741	4.488	14.788
76	89189	955.3	5.591	5.619	5.375	5.030	15.565
77	89245	955.1	5.364	5.224	4.812	4.438	14.849
78	89277	989.5	4.501	4.554	4.408	4.117	14.224
79	89292	951.4	5.818	5.935	5.694	5.322	15.903

† Maximum peak-to-peak wavelet amplitude
‡ Amplitude of 3rd peak down from maximum in the L_g window
⋆ Wallace, T. (pers. comm., 1996)

FIGURE 1

189

(a) WWSS Short-Period Response

3.6   3.2 km / s

Vertical

10 s A_{p-p}

Pn   Pg

50 s

(b) Wood-Anderson Responses

C

N - S

Lg $t_{1/3}$

C

E - W

50 s

Lg $t_{1/3}$

FIGURE 2

(a)

$$\log A_{p\text{-}p} - m_b(P) = -1.47 \log \Delta - 7.33$$
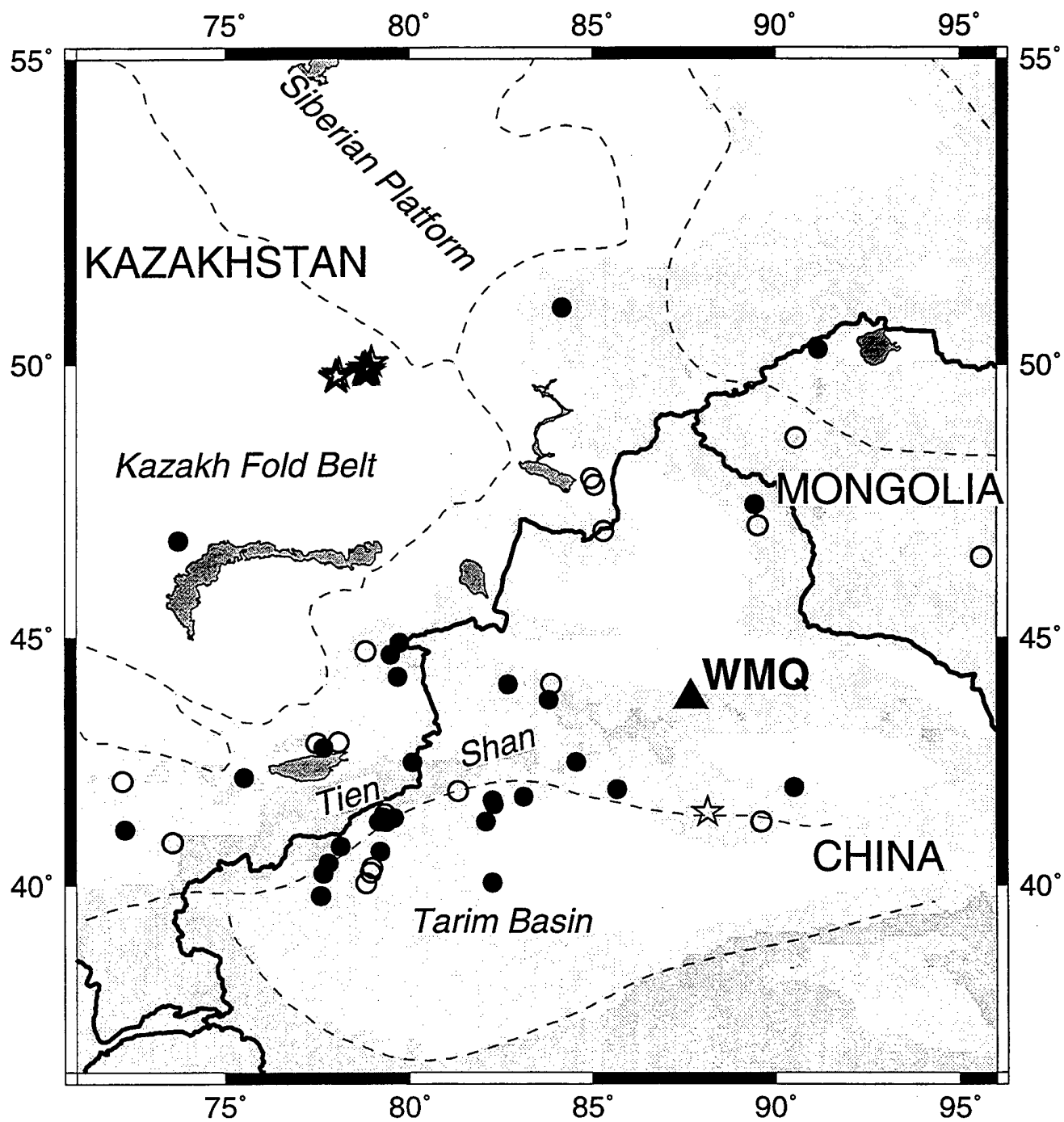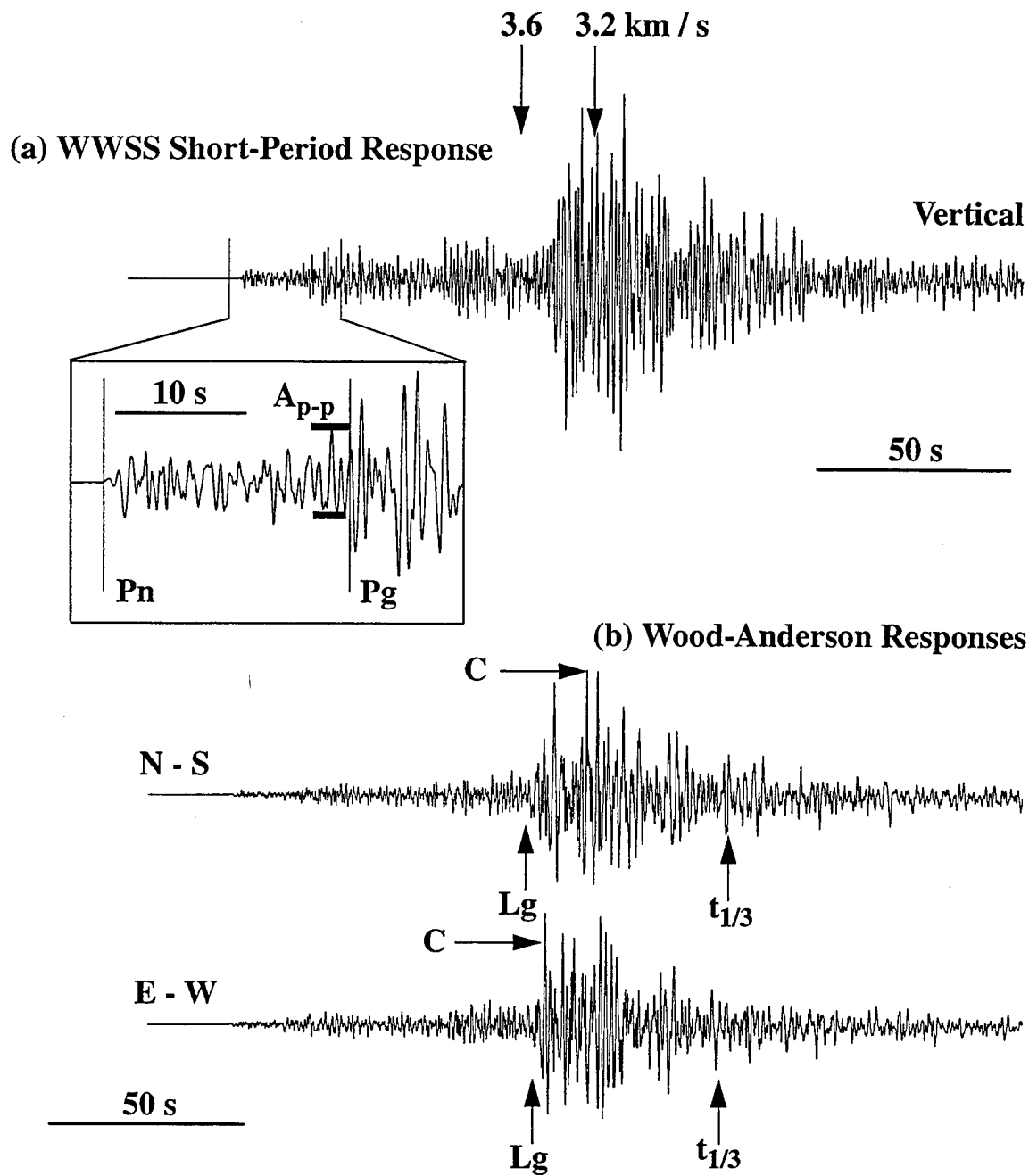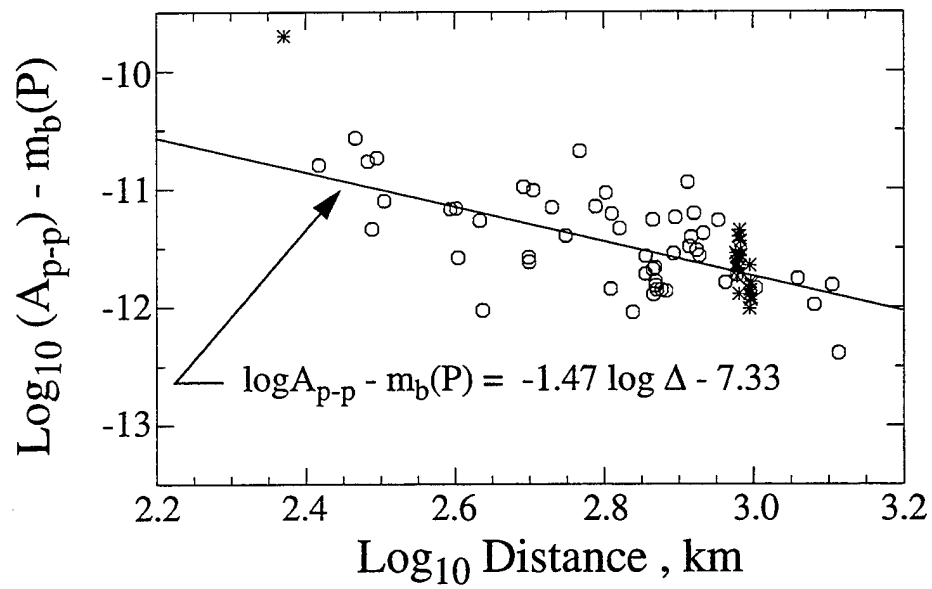
(b)
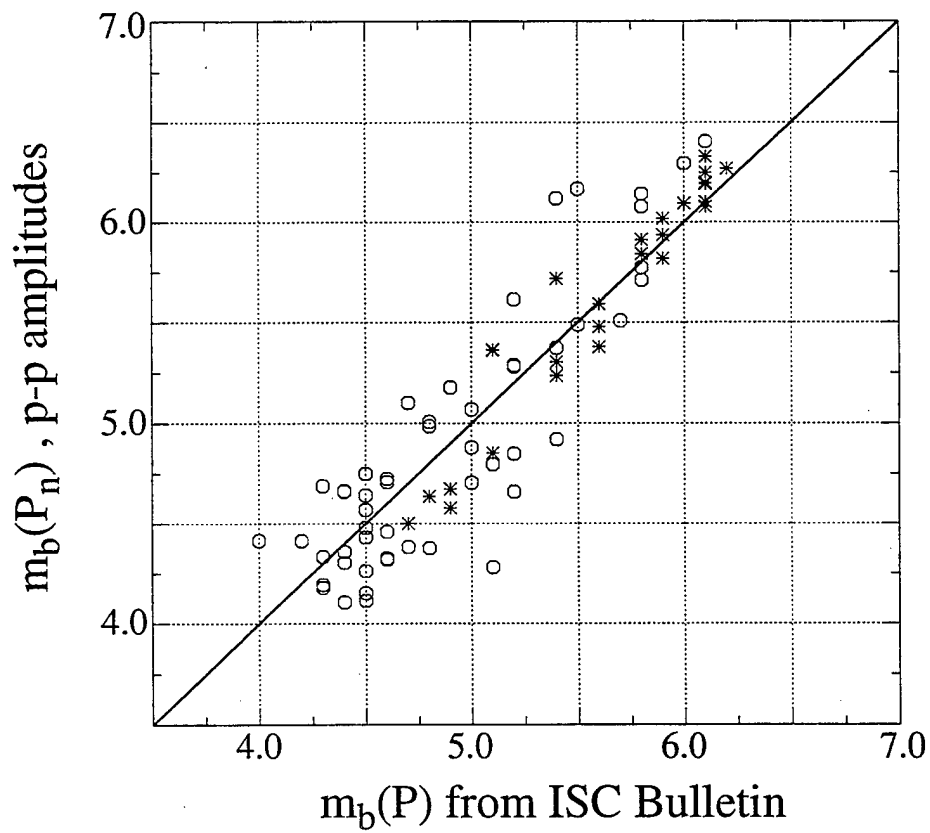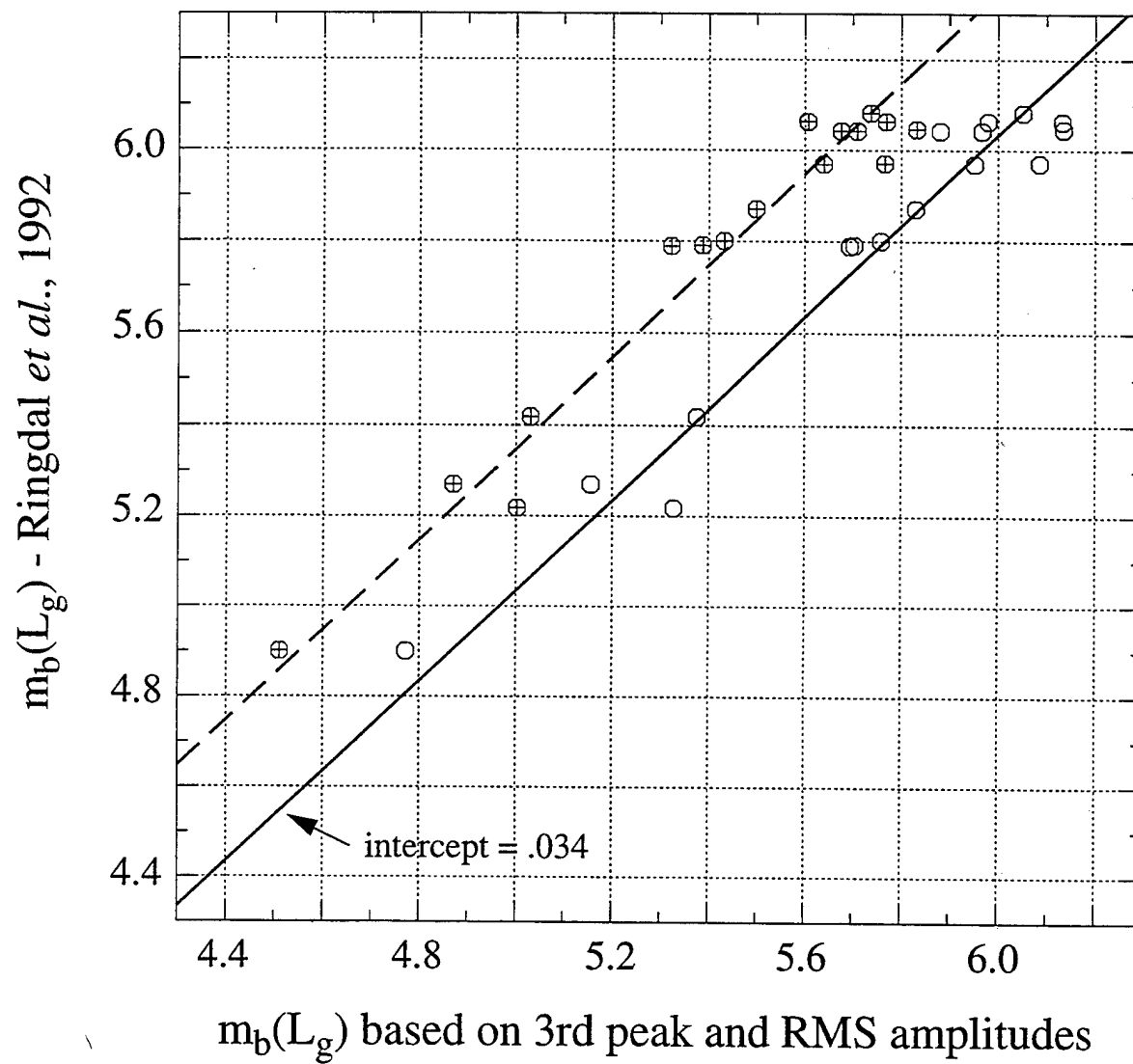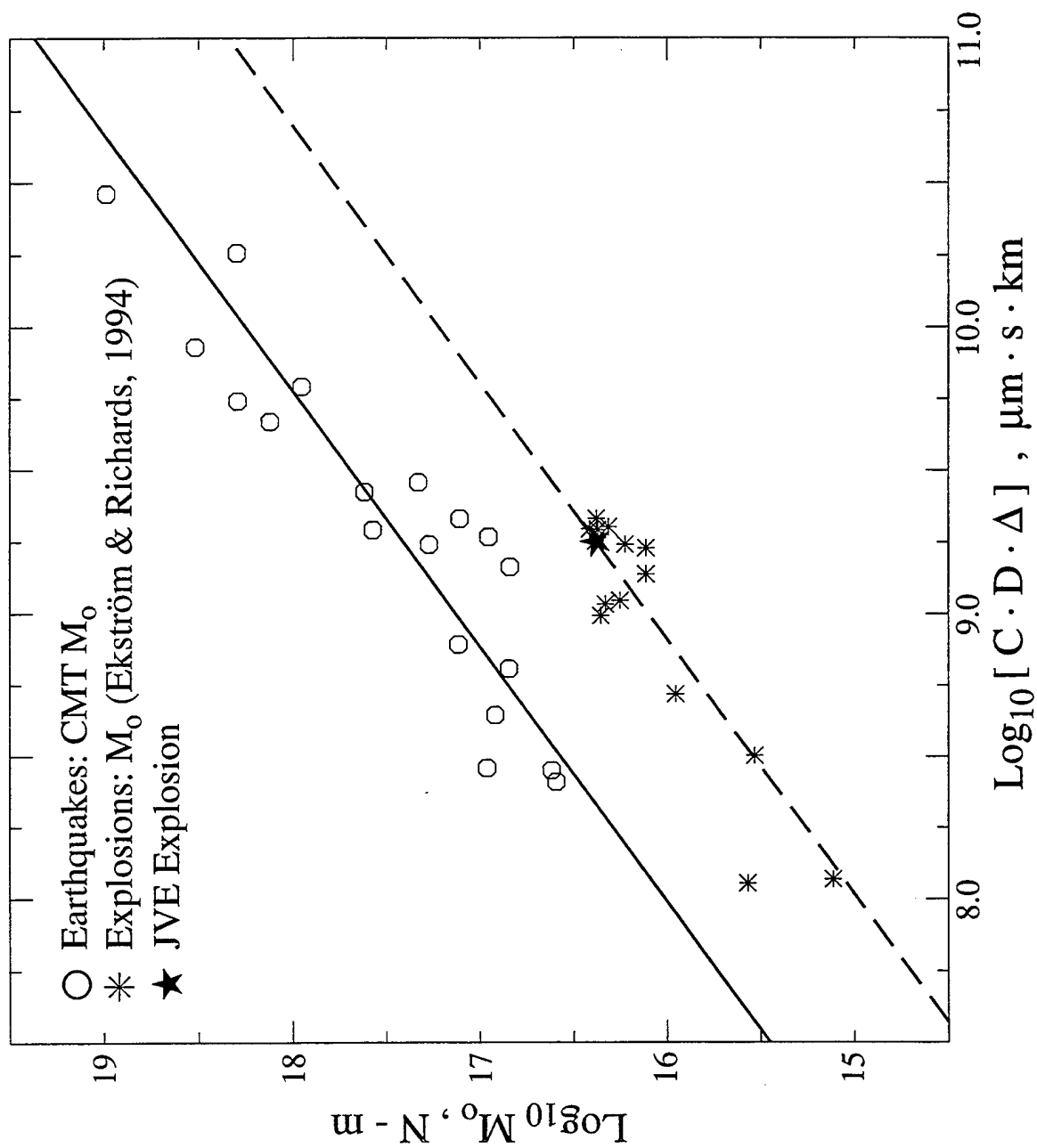
FIGURE 3

FIGURE 4
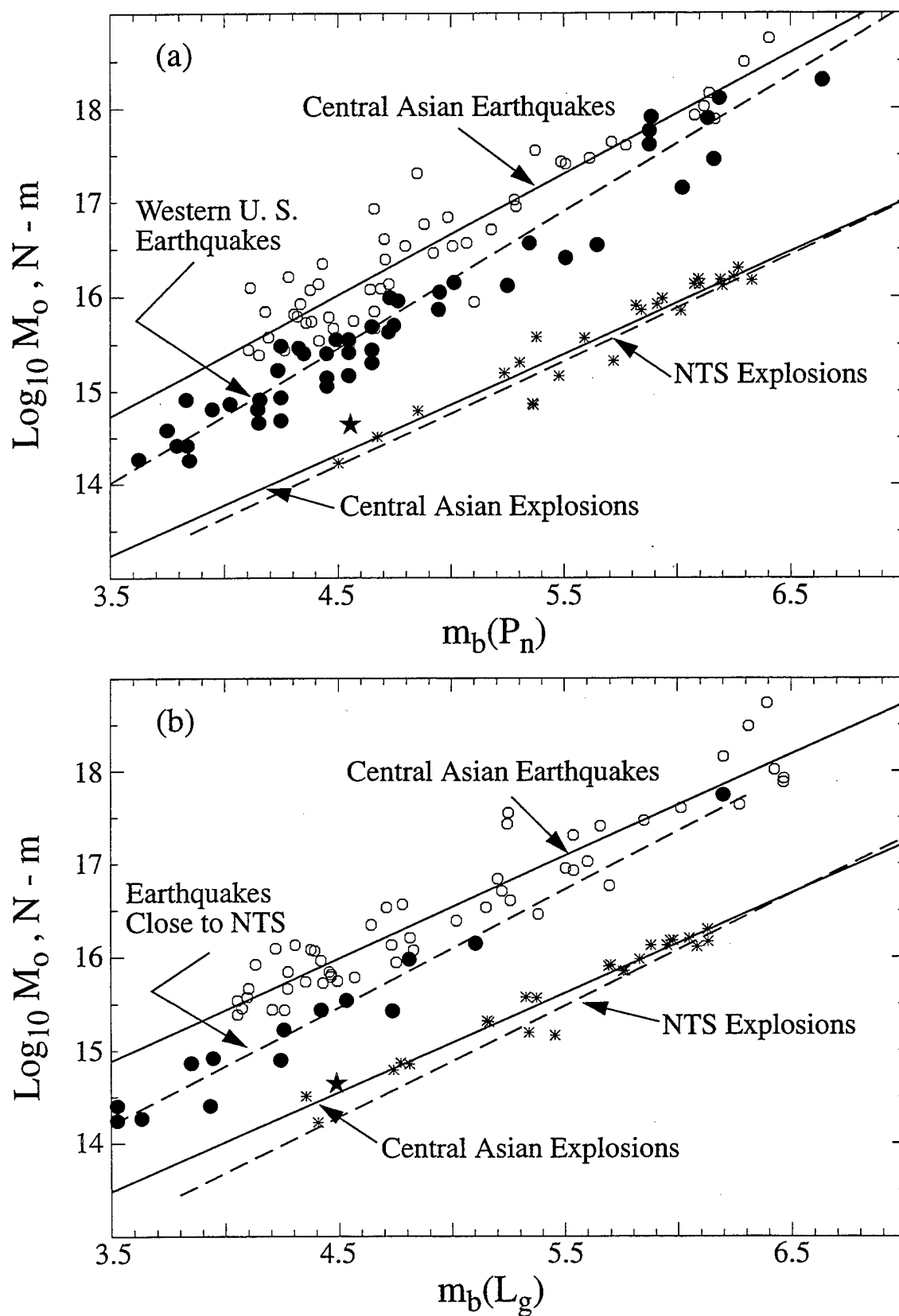
FIGURE 5
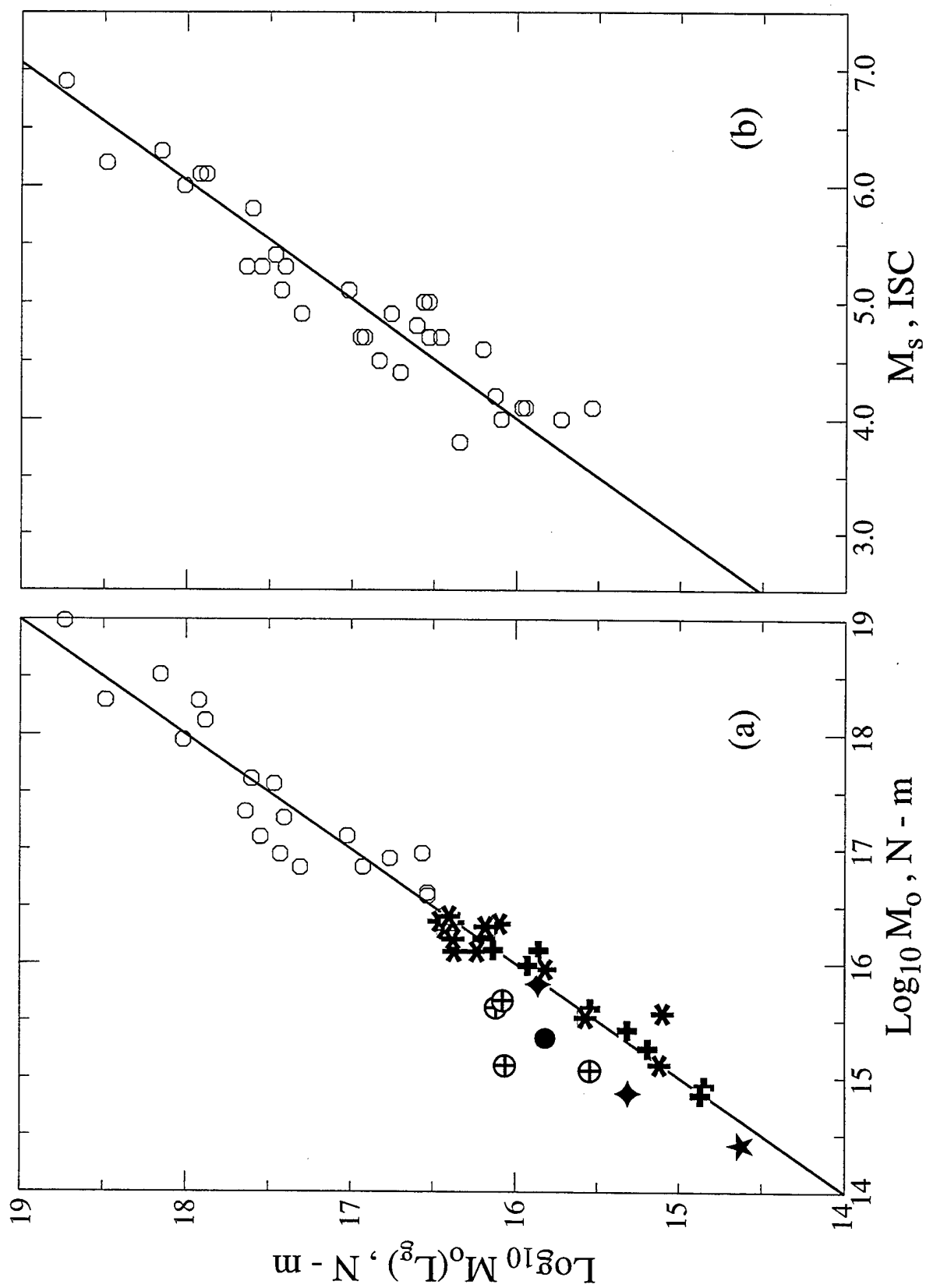
FIGURE 6
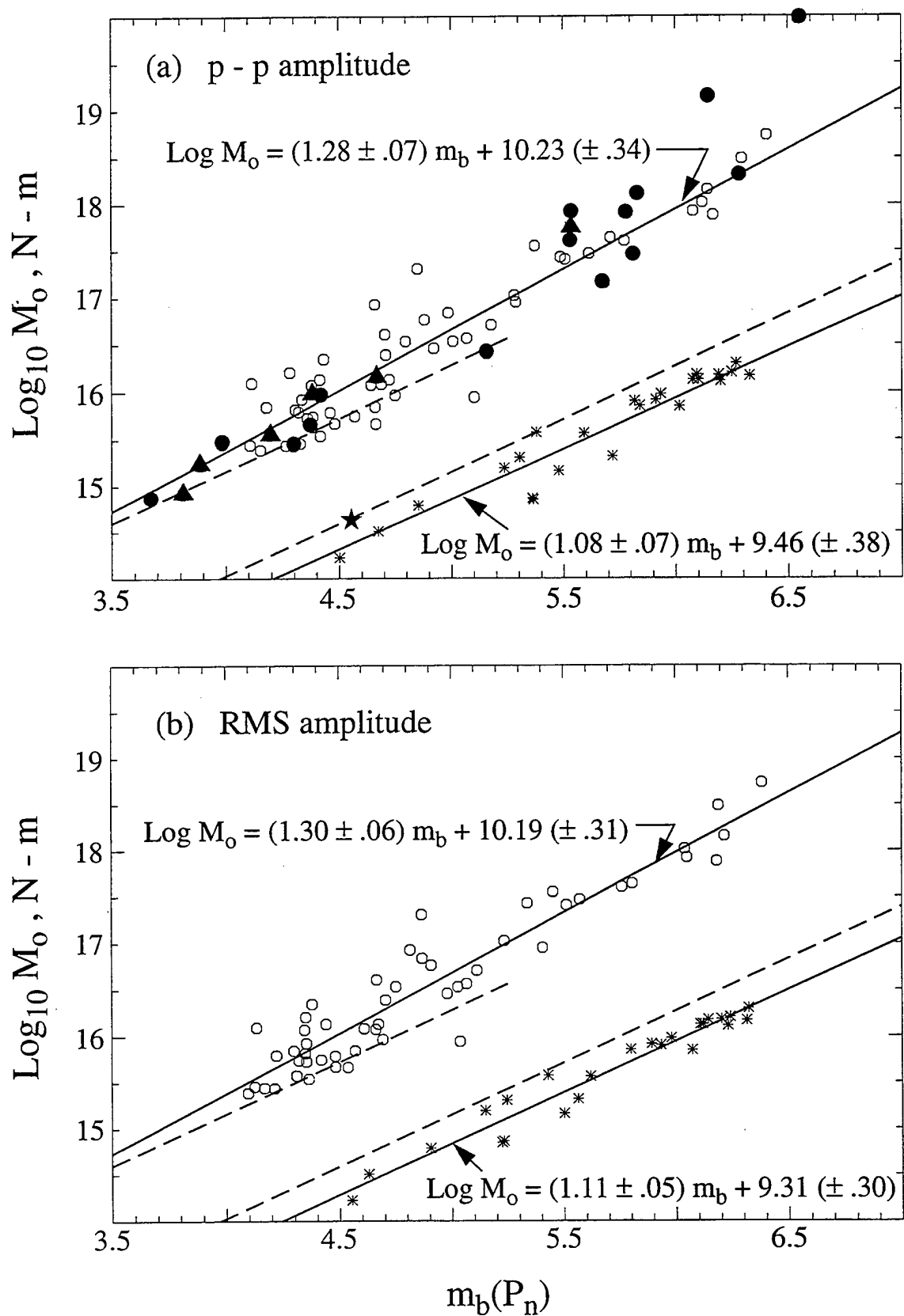
FIGURE 7
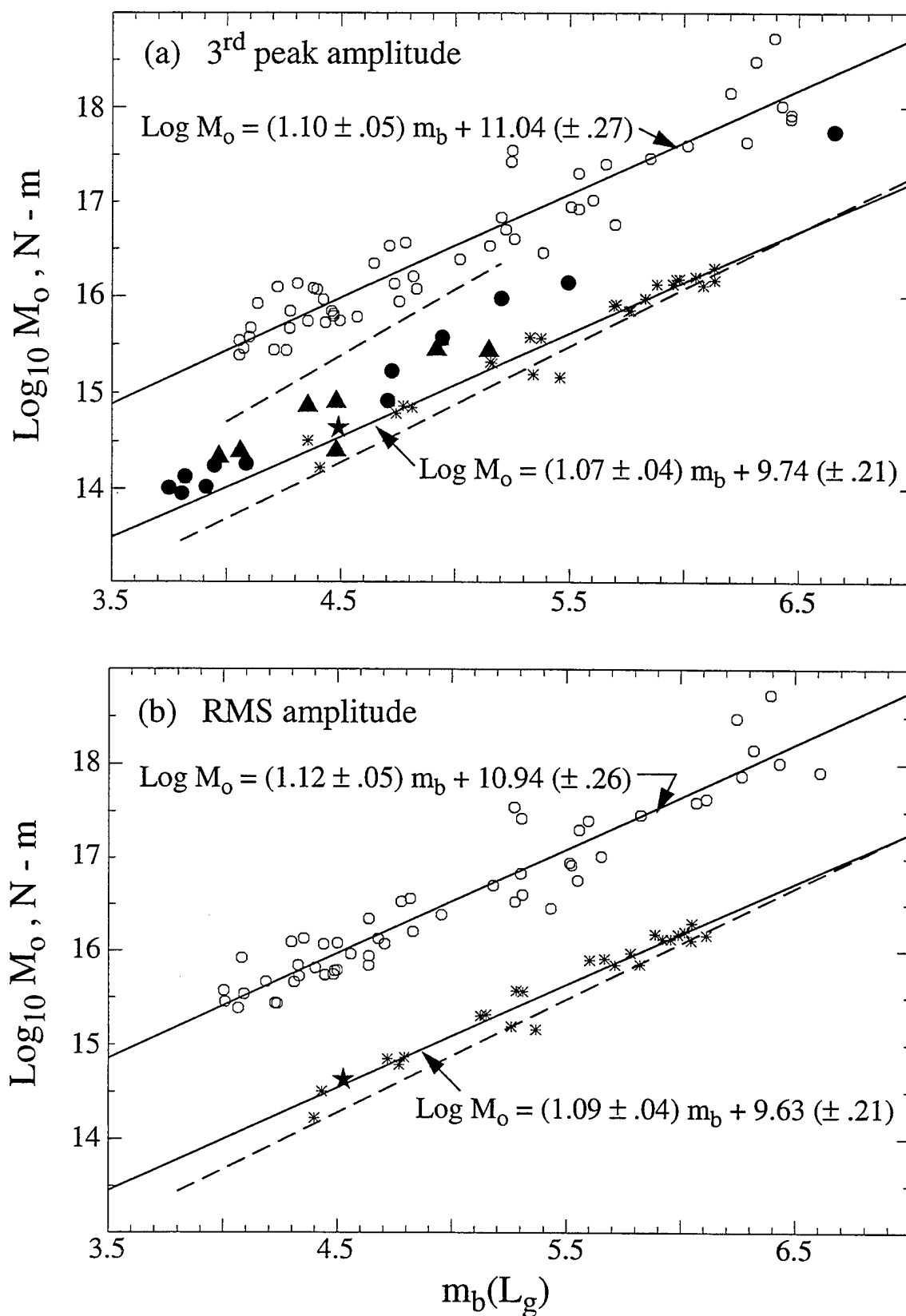
FIGURE 8

FIGURE 9
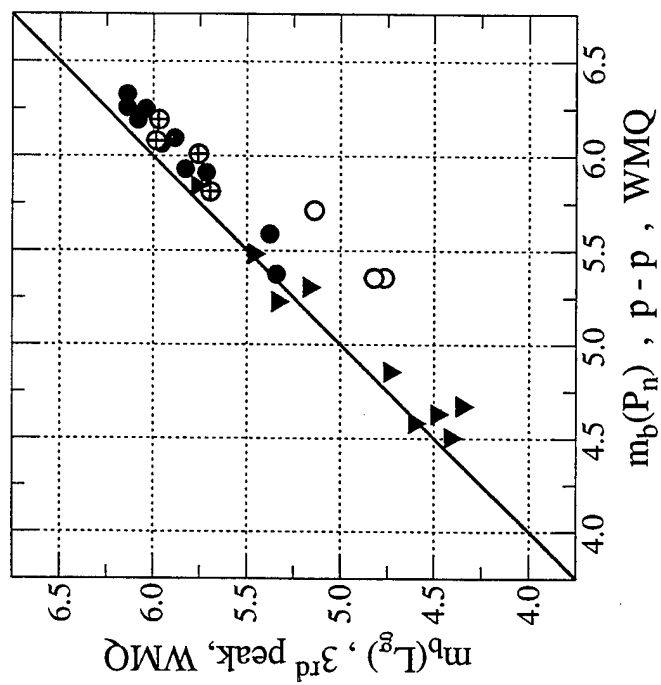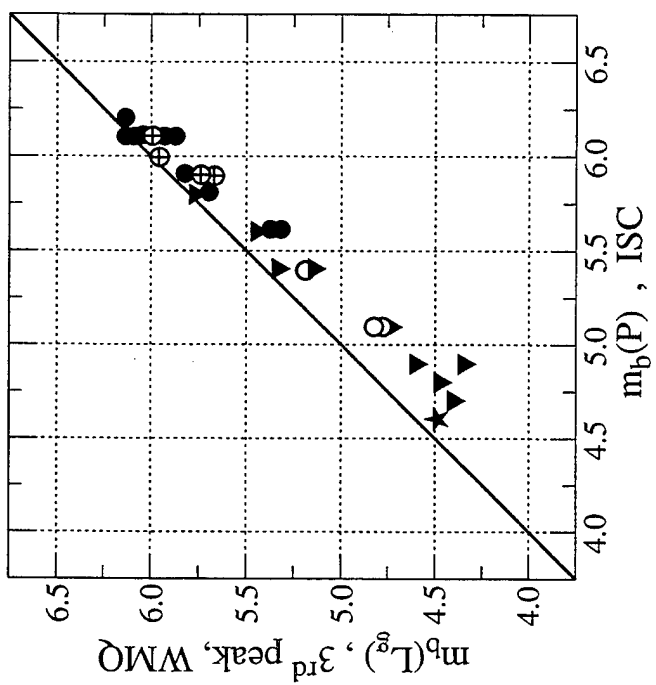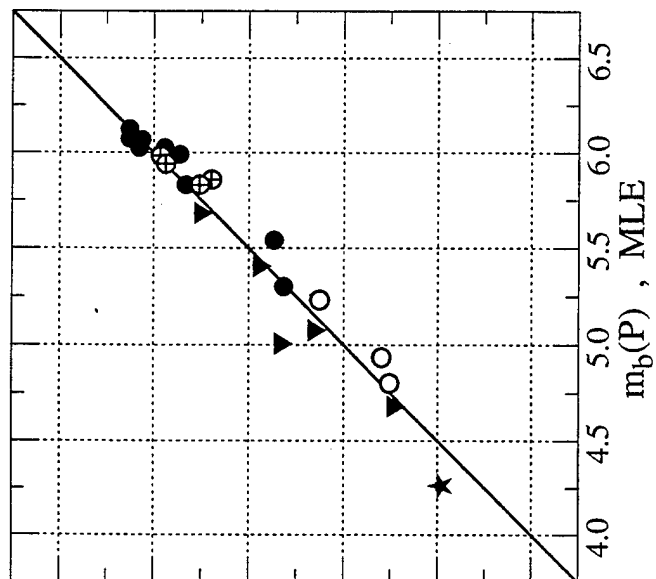
Figure 10
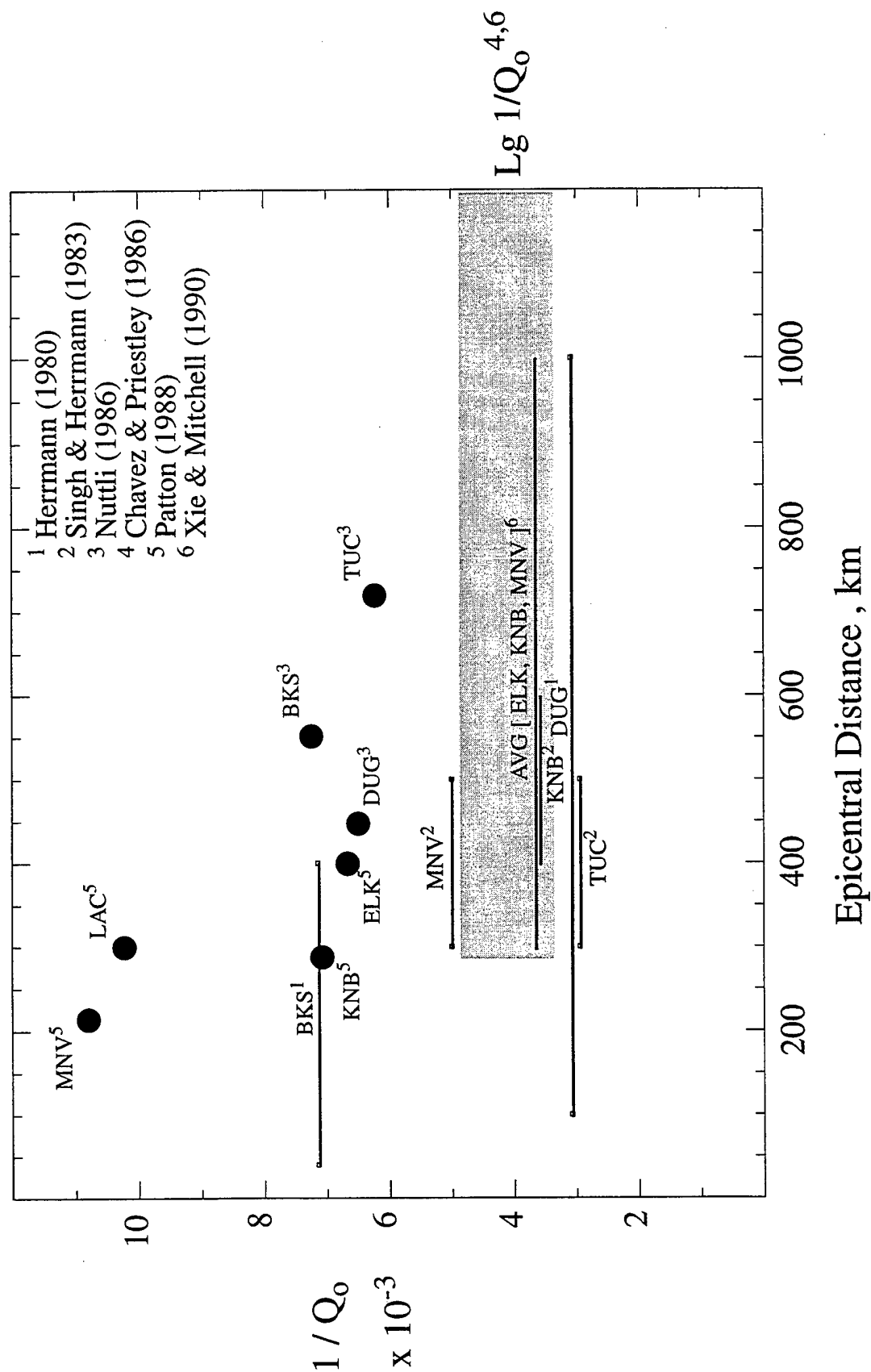
Lg Coda Q_o Measurements in the Western United States

1 Herrmann (1980)
2 Singh & Herrmann (1983)
3 Nuttli (1986)
4 Chavez & Priestley (1986)
5 Patton (1988)
6 Xie & Mitchell (1990)

Lg $1/Q_o$ [4,6]

Epicentral Distance , km

$1/Q_o$ x 10^{-3}

AVG [ELK, KNB, MNV][6]

FIGURE 11

THOMAS AHRENS
SEISMOLOGICAL LABORATORY 252-21
CALIFORNIA INSTITUTE OF TECHNOLOGY
PASADENA, CA 91125

AIR FORCE RESEARCH LABORATORY
ATTN: VSOE
29 RANDOLPH ROAD
HANSCOM AFB, MA 01731-3010

AIR FORCE RESEARCH LABORATORY
ATTN: RESEARCH LIBRARY/TL
5 WRIGHT STREET
HANSCOM AFB, MA 01731-3004

AIR FORCE RESEARCH LABORATORY
ATTN: AFRL/SUL
3550 ABERDEEN AVE SE
KIRTLAND, NM 87117-5776 (2 COPIES)

RALPH ALEWINE
NTPO
1901 N. MOORE STREET, SUITE 609
ARLINGTON, VA 22209

MUAWIA BARAZANGI
INSTITUTE FOR THE STUDY OF THE CONTINENTS
3126 SNEE HALL
CORNELL UNIVERSITY
ITHACA, NY 14853

T.G. BARKER
MAXWELL TECHNOLOGIES
8888 BALBOA AVE.
SAN DIEGO, CA 92123-1506

DOUGLAS BAUMGARDT
ENSCO INC.
5400 PORT ROYAL ROAD
SPRINGFIELD, VA 22151

THERON J. BENNETT
MAXWELL TECHNOLOGIES
11800 SUNRISE VALLEY DRIVE SUITE 1212
RESTON, VA 22091

JONATHAN BERGER
UNIVERSITY OF CA, SAN DIEGO
SCRIPPS INSTITUTION OF OCEANOGRAPHY IGPP, 0225
9500 GILMAN DRIVE
LA JOLLA, CA 92093-0225

ROBERT BLANDFORD
AFTAC
1300 N. 17TH STREET
SUITE 1450
ARLINGTON, VA 22209-2308

RHETT BUTLER
IRIS
1200 NEW YORK AVE., NW
SUITE 800
WASHINGTON, DC 20005

LESLIE A. CASEY
DOE
1000 INDEPENDENCE AVE. SW
NN-20
WASHINGTON, DC 20585-0420

CENTER FOR MONITORING RESEARCH
ATTN: LIBRARIAN
1300 N. 17th STREET, SUITE 1450
ARLINGTON, VA 22209

ANTON DAINTY
HQ DSWA/PMP
6801 TELEGRAPH ROAD
ALEXANDRIA, VA 22310-3398

CATHERINE DE GROOT-HEDLIN
UNIVERSITY OF CALIFORNIA, SAN DIEGO
INSTITUTE OF GEOPHYSICS AND PLANETARY PHYSICS
8604 LA JOLLA SHORES DRIVE
SAN DIEGO, CA 92093

DEFENSE TECHNICAL INFORMATION CENTER
8725 JOHN J. KINGMAN ROAD
FT BELVOIR, VA 22060-6218 (2 COPIES)

ZOLTAN DER
ENSCO, INC.
5400 PORT ROYAL ROAD
SPRINGFIELD, VA 22151

DIANE I. DOSER
DEPARTMENT OF GEOLOGICAL SCIENCES
THE UNIVERSITY OF TEXAS AT EL PASO
EL PASO, TX 79968

MARK D. FISK
MISSION RESEARCH CORPORATION
735 STATE STREET
P.O. DRAWER 719
SANTA BARBARA, CA 93102-0719

1

LORI GRANT
MULTIMAX, INC.
311C FOREST AVE. SUITE 3
PACIFIC GROVE, CA 93950

HENRY GRAY
SMU STATISTICS DEPARTMENT
P.O. BOX 750302
DALLAS, TX 75275-0302

I. N. GUPTA
MULTIMAX, INC.
1441 MCCORMICK DRIVE
LARGO, MD 20774

DAVID HARKRIDER
c/o EARTH RESOURCES LAB
MASSACHUSETTS INST. OF TECHNOLOGY
77 MASS AVE, BLDG E34
CAMBRIDGE, MA 02139

THOMAS HEARN
NEW MEXICO STATE UNIVERSITY
DEPARTMENT OF PHYSICS
LAS CRUCES, NM 88003

MICHAEL HEDLIN
UNIVERSITY OF CALIFORNIA, SAN DIEGO
SCRIPPS INSTITUTION OF OCEANOGRAPHY IGPP, 0225
9500 GILMAN DRIVE
LA JOLLA, CA 92093-0225

DONALD HELMBERGER
CALIFORNIA INSTITUTE OF TECHNOLOGY
DIVISION OF GEOLOGICAL & PLANETARY SCIENCES
SEISMOLOGICAL LABORATORY
PASADENA, CA 91125

EUGENE HERRIN
SOUTHERN METHODIST UNIVERSITY
DEPARTMENT OF GEOLOGICAL SCIENCES
DALLAS, TX 75275-0395

ROBERT HERRMANN
ST. LOUIS UNIVERSITY
DEPARTMENT OF EARTH & ATMOSPHERIC SCIENCES
3507 LACLEDE AVENUE
ST. LOUIS, MO 63103

VINDELL HSU
HQ/AFTAC/TTR
1030 S. HIGHWAY A1A
PATRICK AFB, FL 32925-3002

RONG-SONG JIH
HQ DSWA/PMP/CTBT
6801 TELEGRAPH ROAD
ALEXANDRIA, VA 22310-3398

THOMAS JORDAN
MASSACHUSETTS INSTITUTE OF TECHNOLOGY
EARTH, ATMOSPHERIC & PLANETARY SCIENCES
77 MASSACHUSETTS AVENUE, 54-918
CAMBRIDGE, MA 02139

LAWRENCE LIVERMORE NATIONAL LABORATORY
ATTN: TECHNICAL STAFF (PLS ROUTE)
PO BOX 808, MS L-200
LIVERMORE, CA 94551

LAWRENCE LIVERMORE NATIONAL LABORATORY
ATTN: TECHNICAL STAFF (PLS ROUTE)
PO BOX 808, MS L-221
LIVERMORE, CA 94551

LAWRENCE LIVERMORE NATIONAL LABORATORY
ATTN: TECHNICAL STAFF (PLS ROUTE)
LLNL
PO BOX 808, MS L-175
LIVERMORE, CA 94551

LAWRENCE LIVERMORE NATIONAL LABORATORY
ATTN: TECHNICAL STAFF (PLS ROUTE)
PO BOX 808, MS L-208
LIVERMORE, CA 94551

LAWRENCE LIVERMORE NATIONAL LABORATORY
ATTN: TECHNICAL STAFF (PLS ROUTE)
PO BOX 808, MS L-202
LIVERMORE, CA 94551

LAWRENCE LIVERMORE NATIONAL LABORATORY
ATTN: TECHNICAL STAFF (PLS ROUTE)
PO BOX 808, MS L-195
LIVERMORE, CA 94551

LAWRENCE LIVERMORE NATIONAL LABORATORY
ATTN: TECHNICAL STAFF (PLS ROUTE)
PO BOX 808, MS L-205
LIVERMORE, CA 94551

THORNE LAY
UNIVERSITY OF CALIFORNIA, SANTA CRUZ
EARTH SCIENCES DEPARTMENT
EARTH & MARINE SCIENCE BUILDING
SANTA CRUZ, CA 95064

ANATOLI L. LEVSHIN
DEPARTMENT OF PHYSICS
UNIVERSITY OF COLORADO
CAMPUS BOX 390
BOULDER, CO 80309-0309

JAMES LEWKOWICZ
WESTON GEOPHYSICAL CORP.
325 WEST MAIN STREET
NORTHBORO, MA 01532

LOS ALAMOS NATIONAL LABORATORY
ATTN: TECHNICAL STAFF (PLS ROUTE)
PO BOX 1663, MS F659
LOS ALAMOS, NM 87545

LOS ALAMOS NATIONAL LABORATORY
ATTN: TECHNICAL STAFF (PLS ROUTE)
PO BOX 1663, MS F665
LOS ALAMOS, NM 87545

LOS ALAMOS NATIONAL LABORATORY
ATTN: TECHNICAL STAFF (PLS ROUTE)
PO BOX 1663, MS D460
LOS ALAMOS, NM 87545

LOS ALAMOS NATIONAL LABORATORY
ATTN: TECHNICAL STAFF (PLS ROUTE)
PO BOX 1663, MS C335
LOS ALAMOS, NM 87545

IAN MACGREGOR
NSF
4201 WILSON BLVD., ROOM 785
ARLINGTON, VA 22230

GARY MCCARTOR
SOUTHERN METHODIST UNIVERSITY
DEPARTMENT OF PHYSICS
DALLAS, TX 75275-0395

KEITH MCLAUGHLIN
MAXWELL TECHNOLOGIES
8888 BALBOA AVE.
SAN DIEGO, CA 92123-1506

BRIAN MITCHELL
DEPARTMENT OF EARTH & ATMOSPHERIC SCIENCES
ST. LOUIS UNIVERSITY
3507 LACLEDE AVENUE
ST. LOUIS, MO 63103

RICHARD MORROW
USACDA/IVI
320 21ST STREET, N.W.
WASHINGTON, DC 20451

JOHN MURPHY
MAXWELL TECHNOLOGIES
11800 SUNRISE VALLEY DRIVE SUITE 1212
RESTON, VA 22091

JAMES NI
NEW MEXICO STATE UNIVERSITY
DEPARTMENT OF PHYSICS
LAS CRUCES, NM 88003

ROBERT NORTH
CENTER FOR MONITORING RESEARCH
1300 N. 17th STREET, SUITE 1450
ARLINGTON, VA 22209

OFFICE OF THE SECRETARY OF DEFENSE
DDR&E
WASHINGTON, DC 20330

JOHN ORCUTT
INSTITUTE OF GEOPHYSICS AND PLANETARY PHYSICS
UNIVERSITY OF CALIFORNIA, SAN DIEGO
LA JOLLA, CA 92093

PACIFIC NORTHWEST NATIONAL LABORATORY
ATTN: TECHNICAL STAFF (PLS ROUTE)
PO BOX 999, MS K6-48
RICHLAND, WA 99352

PACIFIC NORTHWEST NATIONAL LABORATORY
ATTN: TECHNICAL STAFF (PLS ROUTE)
PO BOX 999, MS K6-40
RICHLAND, WA 99352

PACIFIC NORTHWEST NATIONAL LABORATORY
ATTN: TECHNICAL STAFF (PLS ROUTE)
PO BOX 999, MS K6-84
RICHLAND, WA 99352

PACIFIC NORTHWEST NATIONAL LABORATORY
ATTN: TECHNICAL STAFF (PLS ROUTE)
PO BOX 999, MS K5-12
RICHLAND, WA 99352

GREG VAN DER VINK
IRIS
1200 NEW YORK AVE., NW
SUITE 800
WASHINGTON, DC 20005

TERRY WALLACE
UNIVERSITY OF ARIZONA
DEPARTMENT OF GEOSCIENCES
BUILDING #77
TUCSON, AZ 85721

DANIEL WEILL
NSF
EAR-785
4201 WILSON BLVD., ROOM 785
ARLINGTON, VA 22230

RU SHAN WU
UNIVERSITY OF CALIFORNIA SANTA CRUZ
EARTH SCIENCES DEPT.
1156 HIGH STREET
SANTA CRUZ, CA 95064

JAMES E. ZOLLWEG
BOISE STATE UNIVERSITY
GEOSCIENCES DEPT.
1910 UNIVERSITY DRIVE
BOISE, ID 83725

FRANK VERNON
UNIVERSITY OF CALIFORNIA, SAN DIEGO
SCRIPPS INSTITUTION OF OCEANOGRAPHY IGPP, 0225
9500 GILMAN DRIVE
LA JOLLA, CA 92093-0225

JILL WARREN
LOS ALAMOS NATIONAL LABORATORY
GROUP NIS-8
P.O. BOX 1663
LOS ALAMOS, NM 87545 (5 COPIES)

JAMES WHITCOMB
NSF
NSF/ISC OPERATIONS/EAR-785
4201 WILSON BLVD., ROOM785
ARLINGTON, VA 22230

JIAKANG XIE
COLUMBIA UNIVERSITY
LAMONT DOHERTY EARTH OBSERVATORY
ROUTE 9W
PALISADES, NY 10964